DEVELOPMENT OF CATALYST AND INTEGRATED HOLLOW FIBER CATALYTIC MEMBRANE REACTOR FOR REFORMING OF METHANE

YASOTHA KATHIRASER

NATIONAL UNIVERSITY OF SINGAPORE

2013

DEVELOPMENT OF CATALYST AND INTEGRATED HOLLOW FIBER CATALYTIC MEMBRANE REACTOR FOR REFORMING OF METHANE

YASOTHA KATHIRASER

(B. Eng. (Hons) UTM, M. Eng. UM, Malaysia)

A THESIS SUBMITTED

FOR THE DEGREE OF Ph.D. OF ENGINEERING

DEPARTMENT OF CHEMICAL AND BIOMOLECULAR ENGINEERING

NATIONAL UNIVERSITY OF SINGAPORE

2013

DECLARATION

I hereby declare that the thesis is my original work and it has been written by me in its entirety. I have duly acknowledged all the sources of information which have been used in the thesis.

This thesis has also not been submitted for any degree in any university previously.

YASOTHA KATHIRASER

27 August 2013

This thesis is dedicated to my late father and grandmother

Acknowledgements

I would like to take this privilege to express my heartfelt gratefulness and admiration to my supervisor, Prof. Sibudjing Kawi for his valuable and constructive advice, patient guidance and constant encouragement for my PhD. His far insights, kindness and knowledge inspire me for my future endeavors. I also sincerely thank Prof Kus Hidajat for his valuable advice for my research given during our group meeetings.

I would also like to take this opportunity to express my thankfulness and gratitude to all our group members, Dr. Usman Oemar, Dr. Yang Nai- Tao, Mr. Saw Eng Toon, Mr. Li Ziwei, Mr. Wang Zhigang, Dr. Kesada Sutthiumporn, Dr. Warintorn Thitsartarn, Dr. Thawatchai Maneerung, Dr. Mo Liuye, Ms. Ang Ming Li, Dr. Ni Jun, Mr. Gao Xingyuan and late Dr. Wu Xusheng for all their valuable assistance and giving me many good memories. I also would like to thank all staff members in ChBE Dept, Mdm Jamie Siew, Mr. Ang Wee Siong, Mr. Ng Kim Poi, Mr. Chia Phai Ann, Mr. Liu Zhi Cheng, Dr. Yuan Ze Liang, Mr. Mogan, Mr. Mao Ning and Ms. Alyssa Tay for all their kind help.

I am also very thankful to my good friends from Malaysia for their motivation. I am truly indebted forever to my beloved mother, sister, late father and grandmother for their enduring love and encouragement throughout my life. I feel fortunate for their all blessings to complete my thesis . But foremost of all, I thank the Almighty God for everything and showering his love and blessings in my life.

Last but not least, I would like to thank National University of Singapore for providing me scholarship and excellent professional environment for carrying out my research work.

Table of Contents

Summary

The recent discovery of shale gas extraction technology in the US for large-scale natural gas supply has resulted in a surging interest in this cleaner fuel for energy production. Natural gas (methane, being the main constituent) conversion to syngas has attracted global research efforts as it is a key intermediate for useful chemical production via Fischer Tropsch process. Several technologies that have prompted numerous researches in recent years for syngas production include CO_2 (dry) reforming of methane (DRM) and partial oxidation of methane (POM) reactions. Furthermore utilization of CO_2 with methane (two major greenhouse gas contributors) has very important environmental implications. However, the major concerns associated DRM reaction is its high endothermicity (ΔH^{o}_{298K} = 247 kJ.mol^{-1}), high carbon deposition rate and metal sintering which can cause catalyst deactivation. On the other hand, for POM reactions, the main concern stem from the requirement of the costly cryogenic air separation process for oxygen supply, besides the catalytic deactivation caused by metal sintering. This thesis investigates the development of an integrated membrane reactor system which is crucial for enhancing the transformation of methane in an energy efficient manner. The first part involves the development of active and stable Ni-based catalyst which was tested for DRM reaction due to its notoriety in causing deactivation of catalyst. The second part involves the development of a chemically stable mixed ionic and electronic conducting (MIEC) membrane for integration with the developed Ni-based catalyst in the oxidative CO_2 reforming of methane (OCRM) reaction. The OCRM reaction combines the merit of both DRM and POM, whereby with the presence of oxygen, the energy requirement can be minimized. Furthermore, oxygen produced via perovskite membrane system not only

eliminates the requirement for the cost-intensive cryogenic air separation, it also eliminates the requirement for external circuitry associated with solid oxide fuel cells.

In terms of catalyst development, interest lies in investigation on the catalytic activity of Ni supported on *in-situ* formed $LaAlO_3$ perovskite on alumina support. The viability of $LaAlO_3$–Al_2O_3 as a catalyst support is important due to their thermal stabilization property. Hence, the catalytic performance of the as prepared Ni/$LaAlO_3$-Al_2O_3 (NLA) catalyst was then compared with Ni/γ-Al_2O_3. Upon incorporation of 10 wt% Ni on the $LaAlO_3$-Al_2O_3 support, some of the Ni^{2+} species are shown to forcibly react with the underlying tetrahedral Al^{3+} sites to form inverse spinel structure instead of with the octahedral Al^{3+} sites to form the normal spinel structure. The remaining Ni^{2+} species have formed surface NiO species intercalated between the $LaAlO_3$ nanocrystallites on the support. There are several advantages of employing this approach to form this unique structure. Firstly, Ni sintering is found to be reduced. Secondly, phase transformation of γ-Al_2O_3 to α-Al_2O_3 is found to be prevented even at high reaction temperatures. Finally, whisker-like carbon filaments formed do not lead towards catalytic deactivation. Based on the good resistance of this catalyst, it was subsequently incorporated in the membrane reactor system developed in this research for methane conversion to syngas.

Regarding the membrane development, the goal lies in developing chemically stable mixed ionic and electronic conducting (MIEC) hollow fiber membrane. MIEC membranes in hollow fiber configuration generally exhibit many advantages compared to planar and tubular membranes, such as higher surface area/volume ratio and facile high temperature sealing. Generally, doped lanthanum cobaltites, $La_{1-x}Sr_xCoO_{3-y}$ (LSC) based

perovskites are known to possess mixed ionic–electronic conducting properties and high catalytic reactivities for oxygen reduction. It was reported that CO_2 tolerance of perovskite oxides doped with different B-site elements was in the order of Ga > Cr >Mn > Fe > Co. Therefore, presence of Ga in the LSCO membrane has good potential in terms of CO_2 resistivity. It was reported that the composition of $La_{0.6}Sr_{0.4}Co_{0.8}Ga_{0.2}O_{3-\delta}$ was found to be ideal as doping of Ga above 0.2 leads to formation of unknown phases which were postulated to be $LaSrGaO_4$. Furthermore, at this low level of Ga doping, the decrease in electronic conductivity can be anticipated to be within tolerable limits. Therefore based on the above considerations, the CO_2 tolerance of $La_{0.6}Sr_{0.4}Co_{0.8}Ga_{0.2}O_{3-\delta}$ (hereafter called LSCG) oxygen permeating hollow fiber membranes was studied. Oxygen permeation of LSCG was firstly tested under various conditions and sweep gases such as He, CH_4 and CO_2. An 80 h CO_2-stability test was then conducted at 900°C and 800°C. In this CO_2-stability study, He and CH_4 were intermittently used as sweep gases in order to study their effect on the O_2 flux of the CO_2 swept LSCG membrane. The LSCG membrane was found to retain its integrity despite being subjected to the harsh corrosive CO_2 environment.

The next step taken was to test the feasibility of the LSCG hollow fiber membrane in a membrane reactor setup. Hence the NLA catalyst developed in the first part of this research was integrated with the LSCG hollow fiber membrane and tested for POM reaction. The role of the catalyst in enhancing the methane conversion and the performance of the hollow fiber membrane system was investigated. Valuable insights on the morphological changes which took place on the membrane surface upon POM reaction, as well as upon exposure to H_2 and CO gases are discussed based on data from

elemental analysis techniques such as energy dispersive spectroscopy (EDX) and X-ray photoelectron spectroscopy (XPS). Based on the FESEM-EDX and XPS spectral analysis, presence of $SrCO_3$, CoO and Co_3O_4 can be detected on the external surface of the membrane after catalytic POM reaction, whereas the internal surface of the membrane is enriched with SrO, SrO_{1-x}, CoO and Co_3O_4 phases. Nevertheless, the crystalline perovskite structure and its inherent properties are retained and hence enabling oxygen permeability in the highly reducing environment. Using the results of POM reaction, the possible reaction pathways were postulated.

Prior to integrating the LSCG membrane reactor for the OCRM reaction, TPD studies using CO_2, H_2 and CO as probe gas was performed. The role of the membrane material in enhancement of methane conversion via study of adsorption and desorption of reactant and product species are crucial, as it would ultimately influence product distribution and H_2/CO ratio during the OCRM reaction. Finally, the LSCG hollow fiber membrane reactor integrated with NLA catalyst was successfully tested for OCRM reaction for 160 h of operation at 725°C. SEM-EDX, XPS and FTIR analysis indicate presence of adsorbed carbonate and CH_x species on the membrane surface. However, XRD of the bulk membrane confirms that the structural integrity of LSCG is retained despite the surface changes.

Keywords: CO_2 reforming of methane; Syngas production; $NiAl_2O_4$ inverse spinel structure; LSCG hollow fiber membrane; integrated LSCG membrane reactor, partial oxidation of methane, oxidative CO_2 reforming of methane

Nomenclature

Symbol	Description
BET	Brunauer Emmett Teller method
DRIFTS	Diffuse Reflectance Infra-red Spectroscopy
DRM	CO_2 (Dry) Reforming of Methane
EDX	Energy Dispersive X-Ray
FESEM	Field Emission Scanning Electron Microscope
FT-IR	Fourier Transform Infra-red
GC	Gas Chromatograph
MAS-NMR	Magic Angle Spin – Nuclear Magnetic Resonance
OCRM	Oxidative CO_2 Reforming of Methane
POM	Partial Oxidation of Methane
RWGS	Reverse Water Gas Shift
SEM	Scanning Electron Microscopy
SRM	Steam Reforming of Methane
TCD	Thermal Conductivity Detector
TEM	Transmission Electron Microscopy
TGA	Thermal Gravimetry Analysis
TPD	Temperature Programmed Desorption
TPR	Temperature Programmed Reduction
XPS	X-ray Photoelectron Spectroscopy
XRD	X-ray Diffraction

Symbol	Description	Unit
X_i	Reactant Conversion (i = CO_2; CH_4)	%
S_{CO}	Selectivity of CO	%
S_{H_2}	Selectivity of H_2	%
S_A	Membrane surface area	cm^2
J_{O_2}	Oxygen permeation flux	$mL.min^{-1}.cm^{-2}$
F_i	Flow rate of species (i= CH_4, O_2, CO_2, H_2O, H_2, CO)	$mL.min^{-1}$
A_m	Effective membrane area	cm^2
D_o	Outer diameter of hollow fiber membrane	mm
D_i	Inner diameter of hollow fiber membrane	mm
L	Effective length for O_2 permeation of hollow fiber membrane	mm
T	Temperature	°C
2θ	Angle	°

LIST OF TABLES

LIST OF FIGURES

CHAPTER 1

Introduction

1.1 Background

Hydrogen can be used in fuel cells as a power source and syngas can be converted into hydrocarbons via the Fischer–Tropsch synthesis. Increase of environmental restrictions forcing the reduction of exhaust emissions and interest in diminishing dependence on petroleum, associated with the continuous increase of probed natural gas reserves, are factors that justify the great deal of attention given to methane reforming processes [1]. Several methane reforming processes that have received considerable attention in research include CO_2 reforming of methane (DRM; $CH_4 + CO_2 \rightarrow 2CO + 2H_2$) and partial oxidation of methane (POM; $CH_4 + ½O_2 \rightarrow CO + 2H_2$). Although technological practice should minimize environmental impact, this is not always economically feasible. During the past decade, there has been increasing global concern over rise of anthropogenic CO_2 emissions into Earth's atmosphere, estimated to be circa $2x10^{15}$ g of carbon per annum [2]. Transformation of CO_2 with methane, the cheapest carbon-containing chemicals and the most problematic greenhouse gases, into more valuable compounds is one of the important subjects in energy and environmental research [3]. However, the major concern of the DRM reaction is its high endothermicity as well as catalytic deactivation caused by rapid carbon deposition and metal sintering [4-5]. Carbon deposition on the catalyst mainly comes from CO disproportionation ($2CO \rightarrow CO_2 + C$) and/or methane decomposition ($CH_4 \rightarrow 2H_2 + C$) [6]. Catalyst formulations typically comprise of metals such as Pt, Rh, Ru and Ni deposited or

incorporated into carefully engineered supports, doped with elements to improve thermal robustness or to achieve better activity [7]. Ni catalyst is industrially preferable, owing to its comparable reforming activity with noble metals, wide availability and low cost which is more appealing and practical from an industrial standpoint [8]. To maximize on the catalyst selection for the DRM reaction, the catalyst must be robust at high temperature and resistant to carbon deposition. Catalyst supports are usually ceramic solids such as γ-Al_2O_3 which has the distinction of having properties such as high surface area, mixture of acid-base properties, surface hydration/hydroxylation mechanisms, high mechanical strength and low cost [9]. Therefore, many researches on Ni supported on Al_2O_3 has been widely investigated for DRM reactions. Even though the Ni/Al_2O_3 catalyst is highly active, however the imminent catalyst deactivation from the acid surface during CO_2 reforming reaction as well as its phase transformation to the alpha phase leading to drop in activity is a major concern. The need to improve stability of Ni based catalysts for DRM reactions has prompted numerous investigations with structural modifications on *γ*-Al_2O_3 via presence of rare earth or alkaline based promoters.

On the other hand, even though the POM reaction is exothermic and has the advantage of rapid start-up and fast responses [10], it is however, still not industrially feasible due to the requirement of expensive cryogenic air separation processes for oxygen supply. Compared to conventional techniques, oxygen production via mixed ionic-electronic conducting (MIEC) ceramic based membranes offer substantial advantages as the process is effectively clean and flexible. Dense ceramic membranes exhibiting perovskite structure generally exhibit the greatest oxygen flux. Hollow fiber membrane configuration has been found to provide several advantages over conventional

disk or tubular membranes in terms of high surface area/unit volume for permeation coupled with facile sealing [11]. Several excellent studies on the development of hollow fiber membrane for air separation highlighted the development of dense membrane in the past 30 years [12-13]. Integration of these MIEC membranes with POM reaction has been an intense research focus in recent years in view of the tremendous benefit from integrated membrane reactor system, in which a single unit operation can ensure compactness of the process, hence minimizing cost [14-17].

However, the main challenge in this process lies in overcoming the poor chemical stability exhibited by perovskite oxides such as lanthanum strontium cobaltites, which exhibit high oxygen permeating properties but collapses under reducing and corrosive environment (during syngas production) [18]. Recently, gallium, niobium, molybdenum and tantalum have been used as hot B-site substitution cations for developments of high performance perovskite materials for catalytic membrane reactors. In fact, gallium is fixed valence state element, and exhibit high ionic conductivity but low electronic conductivity, low thermal expansion rates and good resistance to $CO_{2,}$ making them potential candidates as dopant in perovskite materials for use in catalytic membrane reactors [19].

Another viable process which can incorporate the merit of both the DRM and POM process for syngas production integrated in a sustainable catalytic hollow fiber membrane reactor system is via oxidative CO_2 reforming of methane (OCRM). In this process, oxygen permeated from the membrane can be supplied to enhance CO_2 reforming of methane. This process has great environmental implications in terms of utilizing both CO_2 and CH_4 in an oxygen-permeable membrane reactor system, hence

lowering the DRM energy requirement, besides rendering a sustainable process for syngas production. Besides, the product syngas ratio can be tailored by adjusting the amount of fuel, CO_2 and oxygen feed manipulation.

Hence, a key issue to solve involves engineering the synthesis of a highly active and stable Ni-based catalyst, preferably supported on cheap supports such as alumina and tested for DRM reaction, which is most notorious in causing imminent catalyst deactivation. The second issue is to develop a chemically stable hollow fiber membrane which can be integrated with the active and stable catalyst for methane conversion reactions such as POM, and more excitingly, OCRM, which is crucial for environmental sustainability in view of the escalating CO_2 emissions worldwide.

1.2 Research Objectives

The main objective of this thesis is to develop a highly active and stable methane reforming catalyst, which is integrated in a hollow fiber membrane reactor for stable performance in methane conversion to syngas. The research objectives are further subdivided as follows:

i) To synthesize a stable and active Ni catalyst supported on a thermally stable perovskite-oxide support ($Ni/LaAlO_3$-Al_2O_3) and is resistant for CO_2 reforming of methane reaction. Comparisons are made with Ni supported on γ-Al_2O_3 as well as Ni/La_2O_3 catalyst for DRM reaction. The structural formation of the catalyst shall be analyzed in depth and characterized with various techniques. Based on the performance of the catalyst in DRM reaction, further insights can be obtained.

ii) To develop a chemically stable hollow fiber membrane with the composition of $La_{0.6}Sr_{0.4}Co_{0.8}Ga_{0.2}O_{3-\delta}$ (LSCG) having good permeation properties and is resistant to CO_2. Doping with Ga has the potential to impart stability to the lanthanum strontium cobaltite compound due to its fixed valence state [20]. Ga also enhances the chemical stability of the material, which is an important property for use in catalytic membrane reactor systems [19]. Long term CO_2 stability test to be conducted.

iii) To integrate the synthesized $Ni/LaAlO_3$-Al_2O_3 (NLA) catalyst with the LSCG hollow fiber membrane reactor for catalytic POM reaction. Elemental analysis for determination of the phase compositional changes and analysis of reaction pathways.

iv) To integrate the NLA catalyst with the LSCG hollow fiber membrane reactor for long-term stability catalytic OCRM reaction in which CO_2 together with permeated oxygen from the membrane are used to reform methane into syngas. Further analysis on the membrane properties after long-term test stability test, include analysis on surface morphological changes as well as bulk structure XRD analysis for determination of membrane integrity.

1.3 Thesis Organization

This thesis consists of 9 chapters including introduction in this chapter. Chapter 2 presents a detailed literature review on reaction pathways and catalyst development for CO_2 reforming of methane reaction as well as an account of partial oxidation of methane and oxidative CO_2 reforming of methane. Chapter 3 presents the literature review on the

development of mixed ionic and electronic conducting membranes for oxygen separation from air, integrated membrane reactor systems for syngas production as well as recent development in the ceramic membrane reactor systems.

Chapter 4 presents the experimental methodology for catalyst synthesis and membrane fabrication as well as the reaction and permeation testing. Details on the characterization techniques are also presented.

Chapter 5 discusses the synthesis and reactivity of NLA catalyst for DRM reaction. Results from several characterization techniques such TPR, XRD, UV-VIS and NMR are presented, which show the formation of *inverse* $NiAl_2O_4$ spinel on the $LaAlO_3$-Al_2O_3 perovskite oxide support is presented. The main feature of the catalyst ability due to the inverse spinel structure to prevent phase transformation from gamma (γ) to alpha (α) unlike the transformation exhibited on the Ni/Al_2O_3 catalyst after 30h of DRM reaction is exhibited.

Chapter 6 presents the development of $La_{0.6}Sr_{0.4}Co_{0.8}Ga_{0.2}O_{3-\delta}$ (LSCG) hollow fiber membrane for oxygen separation from air. The morphology and structure of the hollow fiber is discussed. The permeation performance of the membrane was evaluated using various sweep gas such as He, CH_4 and CO_2. Long term resistance of the LSCG membrane with concentrated CO_2 as sweep gas and the effects of intermittent exposure to CH_4 and He is discussed.

Chapter 7 presents the successful integration of the NLA catalyst with the LSCG hollow fiber membrane for application in the POM reaction in the medium temperature range of 600-800°C. Valuable insights on the morphological changes which took place

on the membrane surface upon POM reaction are discussed based on several characterization techniques such as FESEM-EDX, XRD and XPS.

In chapter 8, surface reaction investigation on LSCG hollow fiber membrane surface using temperature programmed desorption techniques with H_2, CO and CO_2 are discussed. Successful integration of the NLA catalyst in LSCG hollow fiber membrane reactor for OCRM reaction and its long-term stability results are presented. Chapter 9 presents the main conclusions of this thesis as well as recommendations for follow-up works.

REFERENCES

[1] Araujo, J.; Zanchet, D.; Rinaldi, R.; Schuchardt, U.; Hori, C. Fierro, J. *App. Catal. B.* **2008**, *84*, 552-562.

[2] Hawkins, S.; Ravenscroft, M.; Rouniavilla, J.F.; Schulz, G. Editor, Ulmann's Encyclopaedia of Industrial Chemistry, *VCH* , **1989**, 169.

[3] Guo, J.; Hou, Z.; Gao, J.; Zheng, X. *Fuel*, **2008**, *87*, 1348-1354.

[4] Pan, W.; Song, C. *Catal. Today* **2009**, *148*, 232-242.

[5] Sutthiumporn, K.; Maneerung, T.; Kathiraser, Y.; Kawi, S. *Int. J. Hydrogen Energy* **2012**, *37*, 11195-11207.

[6] Zhu, T.; Flytzani-Stephanopoulos, M. *Appl. Catal. A: Gen.* **2001**, *208*, 403-417.

[7] Ghenciu, A. *Curr. Opin. Solid State Mater. Sci.* **2002**, *6*, 389.

[8] Pan, Y.X.; Liu, C.J. *Catal. Lett.* **2008**, *123*, 96-101.

[9] Chase, G.C.; Espe, M.P.; Evans, E.A.; Ramsier, R.D.; Reneker, D.H.; Tuttle, R.W.; Rapp, J. *US Patent 20100009267*, **2010**.

[10] Navarro, R.; Alvarez-Galvan, M.; Rosa, F.; Fierro, J. *Appl. Catal. A: Gen.* **2006**, *297*, 60-72.

[11] Liu, S.; Tan, X.; Shao, Z.; da Costa, J.C.D. *AIChE J.* **2006**, *52*, 3452-3461.

[12] Tan, X.; Li, K. Engineering aspects of MIEC hollow fiber membranes for oxygen production membrane engineering for the treatment of gases, Volume 2: Gas-separation Problems Combined with Membrane Reactors, Eds. E. Drioli and G. Barbierir, *Royal Society of Chemistry*, **2011**, 253-278.

[13] Zhang, K.; Sunarso, J.; Shao, Z.; Zhou, W.; Sun, C.; Wang, S.; Liu, S. *RSC Adv.* **2011**, *1*, 1661-1676.

[14] Kniep, J.; Lin, Y.S. *Ind. Eng. Chem. Res.* **2011**, *50*, 7941-7948.

[15] Wu, Z.; Wang, B.; Li, K. *Int. J. Hydrogen Energy* **2011**, *36*, 5334-5341.

[16] Wang, H.; Tablet, C.; Feldhoff, A.; Caro, J. *J. Membr. Sci*. **2005**, *262*, 20-26.

[17] Gong, Z.; Hong, L. *J. Membr. Sci.* **2011**, *380*, 81-86.

[18] Xu, S.J.; Thomson, W.J. *Ind. Eng. Chem. Res.* **1998**, *37*, 1290-1299.

[19] Dong, X.; Jin, W.; Xu, N.; Li, K. *Chem. Commun.* **2011**, *47*, 10886-10902.

[20] Kharton, V.V.; Viskup A.P.; Naumovich, E.N.; Lapchuk, N.M. *Solid State Ionics* **1997**, *104*, 67–78.

CHAPTER 2

Literature Review on Reaction Pathways and Catalyst Selection

2.1. CO_2 (dry) reforming of methane (DRM)

2.1.1. Overview of DRM process

In industrial practices, steam reforming of methane (SMR) is widely practiced for hydrogen/syngas production. However, in view of global climate change concerns, which has been increasingly attributed to greenhouse gas emission, i.e. CO_2 and CH_4 [1], CO_2 utilization has become a serious issue that need to tackled. Hence, CO_2 (dry) reforming of methane (DRM) has become an attractive solution. Reforming with CO_2, rather than steam, is attractive because it can be employed in areas where water is not available and it yields syngas with lower H_2/CO ratios, which is a preferable feedstock for the Ficher – Tropsch synthesis of long – chain hydrocarbons [2].

DRM involves a highly endothermic reaction (Equation 2-1). In fact, the thermodynamics and equilibrium characteristics of CO_2 reforming of methane are similar to the widely employed steam reforming of methane (Equation 2-2) except that the former reaction produces synthesis gas with lower H_2/CO ratio [1].

$$CO_2 + CH_4 \rightarrow 2CO + 2H_2 \qquad \Delta H°_{298} = 247 \text{ kJ.mol}^{-1} \qquad (2\text{-}1)$$

$$CH_4 + H_2O \rightarrow CO + 3H_2 \qquad \Delta H°_{298} = 228 \text{ kJ.mol}^{-1} \qquad (2\text{-}2)$$

Reverse water gas shift (RWGS) reactions which are likely to occur simultaneously (Equation 2-3) influences the product syngas ratio (H_2/CO), pushing it to

less than 1, since CO is produced more in this reaction. The steam produced enables steam/carbon gasification reaction to take place (Equation 2- 4).

$$CO_2 + H_2 \rightarrow CO + H_2O \qquad \Delta H°_{298} = 41 \text{ kJ.mol}^{-1} \qquad (2\text{-}3)$$

$$C + H_2O\ (g) \rightarrow CO + H_2 \qquad \Delta H°_{298} = 131 \text{ kJ.mol}^{-1} \qquad (2\text{-}4)$$

Carbon deposition is the main reason for catalyst deactivation originating from methane cracking (Equation 2-5) and Boudouard reaction (Equation 2-6).

$$CH_4 \rightarrow C_{ads} + 2H_2 \qquad \Delta H°_{298} = 75 \text{ kJ.mol}^{-1} \qquad (2\text{-}5)$$

$$2CO \rightarrow C_{ads} + CO_2 \qquad \Delta H°_{298} = 75 \text{ kJ.mol}^{-1} \qquad (2\text{-}6)$$

DRM poses the problem of severity in catalyst condition as there is no O_2 directly involved in gasifying the carbon deposited on the catalyst surface. In order to reduce the carbon present, carbon formed should be consumed by the reverse Boudouard reaction (Equation 2-6). Otherwise there will be a net carbon deposition which in practice would lead to catalyst deactivation and reactor blockages. Furthermore the formation of carbon (Equations 2-5 and 2-6) are more favourable at low temperatures. Therefore the DRM reaction temperature below 800°C mainly forms carbon - derived from both methane decomposition and Boudouard reactions. The formation of carbon eventually leads to the suppression of catalyst activity. In addition, the occurrence of RWGS reaction decreases the mole ratio of H_2/CO in the product stream. When the DRM reaction temperature is above 800 ºC, the deposition of carbon generated during CH_4/CO_2 reforming mainly

originates from CH_4 decomposition and the carbon species is more reactive than that generated from Boudouard reaction. Therefore, due to the presence of CO_2 in reforming process, the carbon formed can be easily oxidized. RWGS reaction also contributes to the slightly higher CO_2 conversion than CH_4 in DRM reaction.

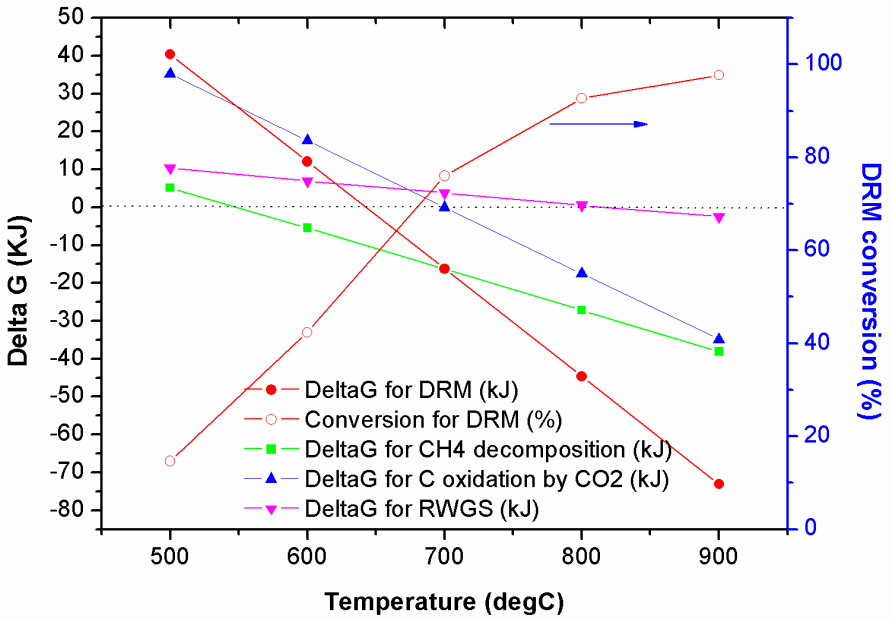

Figure 2-1 Spontaneity of reactions occurring in DRM at different temperatures [3]

Figure 2-1 shows the spontaneity of main and side reactions occurring in DRM at different temperatures ranging between 500 and 900°C using a CO_2/CH_4 feed ratio of l/l at 1 atm pressure. As discussed earlier, at the reaction temperature of 700ºC, the rate of methane decomposition is more spontaneous than the rate of carbon oxidation by CO_2, suggesting that the DRM reaction at high CO_2/CH_4 ratios (>1) and high temperatures can minimize carbon formation in DRM reaction. However, from an industrial point of view,

lower operating temperature, with CO_2/CH_4 ratios near unity is much preferred due to the cheaper operating cost.

2.1.2. Influence of process variables on reaction rates

Extensive investigations have been initiated to study the influence of process variables on the catalyst performance for DRM reaction. In order to gauge the dependence of the reaction rates for process parameters, these studies have been primarily aimed at designing and developing suitable catalysts and at the elucidation of the intrinsic kinetics of the DRM reaction. Catalyst property (Section 2.1.5. and 2.1.6. of this review) is a pre-requisite for efficient DRM operations. In order to achieve a compromise between economic feasibility and efficiency in process, it is of primary importance to accurately formulate the intrinsic kinetic models of the appropriate catalyst based on elementary steps, keeping in mind the influence of transport of reactants on reaction kinetics. Therefore, reaction kinetics is essential in order to optimize on the catalyst design based on the knowledge of the rate determining steps and kinetic trends.

2.1.3. General applicable models for DRM reactions

In this section, we shall cover the following models which are typically used for DRM reactions:

i) Power Law Model

ii) Eley Rideal (ER)

iii) Langmuir Hinshelwood- Hougen Watson (LHHW)

Among these models, Langmuir Hinshelwood Hougen Watson (LHHW) models have received greater attention (as shall be seen in Section 2.1.3.3) due to the conformity of most of the mechanistic steps proposed with experimental techniques for confirmation.

In this section, * shall be used to represent unoccupied active sites for all the mechanistic steps.

2.1.3.1. Power Law Models

Power-law models support the kinetic rate for DRM reaction in the form of:

$$r = k[P_{CH4}]^m[P_{CO2}]^n$$

Generally this simple model provides a rough estimation of the parameters required and do not represent the kinetics of the reaction in a wholesome manner applicable to a wide range of catalysts. Table 2-1 shows the value of these power-law rate coefficients for Ni-based catalysts based on the rate of CH_4 consumption.

Table 2-1 Kinetic rate law constants for Ni based catalysts in DRM reaction [3]

Catalyst	**r_{CH4}**		**r_{CO2}**		**r_{CO}**		**r_{H2}**	
	m	n	m	n	m	n	m	n
Ni/SiO_2	0.44	0.15	0.27	0.64	0.18	0.44	0.49	0.11
Ni/SiO_2	0.02 to 0.05	0.5 to 0.6	-	-	-	-	-	-
Ni/Al_2O_3	0.9 to 1.08	0.83 to 1.77	-	-	-	-	-	-
Ni/Al_2O_3	-	-	0.48	0.45	-	-	-	-
Ni/CeO_2-Al_2O_3	1.04 to 1.12	0.55 to 0.97	-	-	-	-	-	-
Ni/MgO	0.61 to 0.72	0.01 to 0.05	0.52 to 0.60	0.27 to 0.36	0.57 to 0.64	0.15 to 0.21	1.16 to 1.22	0.36 to 0.54
$La_{2-x}Sr_xNiO_4$	0.89 to 0.41	0.18 to 0.10	0.18 to 0.23	0.93 to 1.04	-	-	-	-

For most of the catalysts, the power constant for methane partial pressure (m) is close to unity, indicating that more methane is adsorbed on the species thus dominating the reaction. Whereas the power constant for CO_2 partial pressure (n) is generally much less, indicating the presence of CO_2 adsorptive term in the denominator. Based on the Pulse Surface Reaction Analysis (PSRA) results reported by Osaki et al. [4], Ni/SiO_2 catalysts were found to be hydrogen deficient on the surface, indicating its affinity to carbonaceous formation, i.e. fast decomposition of methane. This result shows that the presence of carbon due to the fast formation rate of carbon plays a part in suppressing the obtained orders of the DRM reaction.

Therefore the only advantage of these power-law models is the simplicity in application and parameter estimation. However, from different mechanistic schemes and over a wider range of partial pressure data, these models cannot sufficiently explain the various reaction mechanistic steps which take place on the catalyst surface. Since it is crucial to understand the mechanistic aspects of the DRM reforming reaction, more rigorous models such as Eley-Rideal (ER) type of models and Langmuir Hinshelwood-Hougen-Watson (LHHW) are used. Nevertheless, the power law model can be used for initial guess estimates in order to solve more complex models which require larger amount of data.

2.1.3.2. Eley-Rideal (ER) Models

Mark et al. [5] have shown the models based on the ER mechanism (ER I or ER II) as shown in following equations.:

Basic Reaction (B):

$$\text{a) } CH_4 + CO_2 \overset{k_{Ref}}{\Longleftrightarrow} 2CO + 2H_2$$

$$r_{Ref} = k_{Ref}\left(P_{CH_4}P_{CO_2} - \frac{{P_{CO}}^2{P_{H_2}}^2}{K_{Ref}}\right)$$

Eley-Rideal Model I (ER 1):

$$\text{a) } CH_4 + * \overset{K_{CH_4}}{\Longleftrightarrow} CH_4 - * \qquad K_{CH_4} = \frac{[CH_4 - *]}{P_{CH_4}[*]}$$

$$\mathbf{b)\ CH_{4-*} + CO_2 \overset{k_{Ref}}{\Longleftrightarrow} 2CO + 2H_2 + *} \qquad \mathbf{RDS}$$

$$r_{Ref} = \frac{k_{Ref}K_{CH_4}\left(P_{CH_4}P_{CO_2} - \frac{{P_{CO}}^2{P_{H_2}}^2}{K_{Ref}}\right)}{1 + K_{CH_4}P_{CH_4}}$$

Eley-Rideal Model II (ER II):

$$\text{a) } CO_2 + * \overset{K_{CO_2}}{\Longleftrightarrow} CO_2 - * \qquad K_{CO_2} = \frac{[CO_2 - *]}{P_{CO_2}[*]}$$

$$\mathbf{b)\ CO_2 - * + CH_4 \overset{k_{Ref}}{\Longleftrightarrow} 2CO + 2H_2 + *} \qquad \mathbf{RDS}$$

$$r_{Ref} = \frac{k_{Ref}K_{CO_2}\left(P_{CH_4}P_{CO_2} - \frac{{P_{CO}}^2{P_{H_2}}^2}{K_{Ref}}\right)}{1 + K_{CO_2}P_{CO_2}}$$

In ER model, one reactant is assumed to be associatively adsorbed on the catalyst surface at adsorption equilibrium. The slow and rate-determining step (RDS) is the reaction of the adsorbed species with the other reactant from the gas phase leading directly to the products. As both reactants can theoretically be the adsorbed species, both

resulting models (ER I and II) can be considered, i.e. gaseous CO_2 reacting with adsorbed CH_4 or gaseous CH_4 reacting with adsorbed CO_2.

There are not many literatures for ER formulated models for DRM reaction over Ni-based catalysts. Among the few, Akpan et al.[6] have conducted DRM studies over Ni/CeO_2-ZrO_2 catalyst in a packed bed tubular reactor. The kinetic model that best predicted their experimental rates was developed based on the ER formulation, assuming the methane dissociative adsorption as the rate-determining step. The validity of their ER kinetic model was tested against the experimental data and a satisfactory agreement between the model prediction and measured results was obtained. The reaction mechanism that they postulated was based on relevant literature data that they have compiled and are given as follows:

$$CH_4 + 2* \leftrightarrow CH_{3(*)} + H_{(*)}$$

$$CH_{3(*)} + * \leftrightarrow CH_{2(*)} + H_{(*)}$$

$$CH_{2(*)} + * \leftrightarrow CH_{(*)} + H_{(*)}$$

$$CH_{(*)} + * \leftrightarrow C_{(*)} + H_{(*)}$$

$$C_{(*)} + O_x \leftrightarrow CO + O_{x-1} + *$$

$$CO_2 + O_{x-1} \leftrightarrow O_x + CO$$

$$4H_{(*)} \leftrightarrow 2H_2 + 4*$$

$$H_2 + O_x \leftrightarrow O_{x-1} + H_2O$$

where * and O_x represent unoccupied active sites and lattice oxygen on their support surface, respectively. Richardson et al.[7] found that a simplified LH mechanism was

sufficient based on the rate determining reaction between adsorbed CH_4 and CO_2 to final products over Rh/Al_2O_3.

In order to analyse the differences between ER and LHHW models, Mark et al.[5] have conducted a comparison test study based on the ER and LHHW rate models for Ir/Al_2O_3 catalysts with 1:1 CH_4 and CO_2 mixture within 700-850^{0}C. Their results show that the fitting quality of the parameters for the models followed the order of ER 1 < LH < ER II. Fitting of the experimental rata based on the basic reaction equation (B) as shown in the beginning of this section, leads to an apparent activation energy of 230 kJ/mol (with only small standard deviation). From their model, Mark et al. [5] proposed that the reaction rate of DRM is determined by the dissociative adsorption of CH_4 due to the formation of active carbon and hydrogen species. However, in the fast second reaction step, which is thermodynamically controlled, the carbon species undergoes Reverse Boudouard reaction to form CO. Under higher reaction temperature region, they confirmed that methane decomposition was the RDS. However, for the other temperature regions, they found that neither the LH model nor the ER model could adequately describe the kinetics of CO_2 reforming over the whole temperature range. But among these 2 models, they postulated that the LH model appeared to provide a more-realistic reaction kinetic model of comparable fitting quality especially in the low temperature range of < 720^{0}C since methane decomposition controls at higher reaction temperature regime.

Based on the above discussion, there is less literature coverage on ER models for Ni-based catalysts and even further lack of experimental evidence in some studies pertaining to ER models which pose the ambiguity of gas phase reactions with a surface

adsorbed reactant for DRM reaction. On the other hand, LHHW models appear to have wider coverage in literature with greater applicability to Ni based catalysts and are therefore discussed more adequately in the next subsection.

2.1.3.3. Langmuir Hinshelwood Hougen Watson (LHHW) Models

Most of the reaction mechanisms proposed for the DRM reaction are based on the LHHW formalism. In the LHHW model it is assumed that one reaction step is slow and rate determining while the others are in thermodynamic equilibrium [5]. LHHW based kinetic models are usually derived from reaction mechanisms involving dissociative adsorption of the reactants CH_4 and CO_2 followed by rate-determining surface reaction of the adsorbed species to the final products, H_2 and CO.

Although the first reaction mechanism for DRM was proposed by Bodrov and Apel'baum [8] in 1967, however, in recent years most of the investigations for reaction mechanism were derived based on LH model which were referenced from the extensive LH steps presented by Xu and Froment [9] for their study on Ni/$MgAl_2O_4$ catalyst for steam reforming of methane (SRM) reactions.

The important postulations applicable for the DRM reaction based on the LHHW model of Xu and Froment [9] for SRM are as follows:

$$CH_4 + * \leftrightarrow CH_4*$$

$$CH_4* + * \leftrightarrow CH_3* + H*$$

$$CH_3* + * \leftrightarrow CH_2* + H*$$

$$CH_2* + * \leftrightarrow CH* + H*$$

$$CH^* + * \leftrightarrow C^* + H^*$$

$$CH_2^* + O^* \leftrightarrow CH_2O^* + *$$

$$CH_2O^* + * \leftrightarrow CHO^* + H^*$$

$$\mathbf{CHO^* + * \leftrightarrow CO^* + H^*} \quad \mathbf{(RDS)}$$

$$\mathbf{CO^* + O^* \leftrightarrow CO2^* + *} \quad \mathbf{(RDS)}$$

$$\mathbf{CHO^* + O^* \leftrightarrow CO_2^* + H^*} \quad \mathbf{(RDS)}$$

$$CO^* \leftrightarrow CO + *$$

$$CO_2^* \leftrightarrow CO_2 + *$$

$$2H^* \leftrightarrow H_2^* + *$$

$$H_2^* \leftrightarrow H_2 + *$$

where * represent unoccupied active sites on the catalyst surface.

Using the above mechanism steps, a LHHW model for DRM was developed with CH_4 dissociation proposed as the rate determining step by Zhang and Verykios [10] over Ni/CaO-Al_2O_3 catalyst. However Rostrup-Nielsen [11] countered on the proposed mechanism by Xu and Froment [9] by stating that methane dissociation is shown not to proceed via the adsorbed precursor state. Rostrup-Nielsen's [11] argument appeared to be more realistic as it is generally accepted that the activation of methane is rate determining. Furthermore, Xu and Froment [9] found that their result has negative heat of adsorption of steam which appears to deviate from the acceptable trend and therefore does not support their claim. This shows that there is generally no mutual agreement on the rate determining steps for LHHW models which shall be further described in the following sections.

Postulated LHHW models based on different RDS

Below are the key steps involved in DRM reaction:

a. Dissociation/activation of CH_4 and CO_2
b. Adsorption of elemental and intermediate C, H and O species on active sites
c. Formation of product species via surface reaction
d. Desorption of product species, i.e. CO, H_2, H_2O

Among these steps, CH_4 and CO_2 dissociation or activation are often considered to be the RDS. However, as we can see in the following sub-sections, several investigations done in recent years have unraveled various different steps to be the RDS. Table 2-2 presents a summary of the rate determining steps proposed in several studies.

i) CH_4 activation by metal – Ni as RDS

The initial and often rate determining step is dissociative chemisorption of CH_4 on the metal catalyst, i.e. breaking of one of the C-H bonds on CH_4 [12]. Kuijpers et al. [13] studied CH_4 dissociation and explained that it is a structure sensitive phenomenon, which may be a consequence of a change in the geometric active site distribution on the different metal surface structures. It was reported that the different faces of Ni crystallite surface indeed play an important role in the rate of CH_4 decomposition, whereby CH_4 decomposition decreases in the order of Ni(110) > Ni (100) > Ni (111) [3].

Several researchers, such as Zhang and Verykios [10] and Wang and Au [14], have proposed that CH_4 decomposition to be the rate determining step. Wei and Iglesia [15] also conducted a kinetic and isotopic assessment to investigate the mechanism of

DRM reaction on Ni/MgO catalysts. Their turnover rates and first order rate constant and activation energies were found to be similar to those measured for CH_4 decomposition, leading them to assert that C-H bond activation is the sole kinetically-relevant step in this reaction. Wei and Iglesia [15] further concluded that the mechanistic features on Ni surface resemble those previously established for supported noble metal catalysts (Rh, Pt, Ir, Ru).

It has been reported that hydrogen can be adsorbed on the Ni catalysts to form Ni-H species during the reforming reaction. Therefore, CH_4 dissociation is considered reversible since H_2 and Ni-H species can reach rapid equilibrium during the reforming reactions [3]. Hence, the subsequent sections shall further describe the different proposed RDS which differs from the generally accepted CH_4 decomposition.

ii) Surface reaction between adsorbed O or OH (from CO_2 or support surface)

Although there are several researchers suggesting that adsorbed O atoms are the key intermediate in the oxidation of adsorbed CH_x species, however surface OH groups are gaining more and more attention [3]. Li et al. [16] performed the investigation of methane adsorption on alumina by FT-IR spectroscopy and found that two hydroxyls with IR bands at 3750 and 3665 cm^{-1} were perturbed evidently by the adsorbed CH_4, hence resulting in two red shifted bands at 3707 and 3640 cm^{-1}. This result suggests that there is a weak interaction between methane and surface hydroxyls. This H-bridged bonding between the surface OH groups and the methane interaction has also been observed on Ir catalysts during CH_4 decomposition [3].

This is especially the case when the supporting materials are basic since the basic supports are expected to enhance the adsorption of CO_2. The principal pathway for CO_2 reduction occurs by the initial non-dissociative adsorption of CO_2 under reaction conditions on the basic support in the form of carbonates or bicarbonates, followed by H atom-assisted dissociation to produce CO and OH. By increasing the concentration of adsorbed OH species, the enhancement of the oxidation of surface adsorbed CH_x species from CH_4 decomposition can be achieved.

iii) Surface reaction between CH_x and O as RDS

When CH_4 dissociates on the metallic Ni site, various forms of CH_x species will be present, depending on the structure and property of the catalyst and the interaction of these species with the support. Osaki et al. [4] have proposed possible CH_4 dissociation steps during DRM based on PSRA technique. From their observation and proposed mechanistic steps, CO_2 firstly dissociates on the metal site as adsorbed CO and adsorbed O. CH_4, on the other hand, dissociates on the metallic Ni site and the adsorbed CH_x species reacts with adsorbed O, forming adsorbed CO and adsorbed H which later desorbs in the gas phase. Osaki et al. [17] also performed an *ab-initio* molecular orbital calculation for the PSRA calculation. Upon observation of rapid sharp H_2 response, they therefore excluded CH_4 dissociation as a rate determining step. They thus concluded from their PSRA study that the surface reaction between CH_x and O is rate determining and found that the two steps responsible for H_2 production are: i) dissociative adsorption of CH_4 to produce $2H_2$ and CH_x, followed by ii) subsequent production of $2H_2$ together with

CO by the surface reaction between CH_x and atomic O. For their study, an isotopic effect on the reaction of adsorbed hydrocarbon species with atomic oxygen was observed.

iv) Carbon oxidation as RDS

Several studies have proposed that the surface reaction between carbon and oxygen species to be the RDS [3]. Kroll et al. [18] using Ni/SiO_2 in their study found that the coke formation on their catalyst was highly dependent on the pre-treatment conditions whereby they found that reduction under reaction conditions produced less toxic filamentous carbon, whilst a pre-reduction under H_2 flow produced toxic encapsulating carbon. They conducted experiments to determine the kinetic isotopic effect (KIE) at 700°C (to minimize temperature gradient) and atmospheric pressure using predeuterated (CD_4) instead of light methane (CH_4) to measure KIEs. Their reaction mechanism scheme is proposed as follows:

C-H Activation: $CH_4 + *_1 \leftrightarrow C_{ads} + 2H_2$

This step was considered fast as no significant accumulation of CH_x or H_{ads} species was found, therefore leading to accumulation of dehydrogenated carbon monomers.

CO_2 Activation: $CO_2 + C_{ads} \leftrightarrow 2CO + *_1$

This activation step consists of two elementary steps shown below:

i. $CO_2 + *_2 \leftrightarrow CO + C_{ads}$

ii. **$C_{ads} + O_{ads} \rightarrow CO + *_{ads}$** **RDS**

The former elementary step was considered to be fast due to the observed isotopic equilibrium between CO_2 and CO. On the other hand, Kroll et al. [18] deduced from techniques such as Steady State Isotopic Transient Kinetic Analysis **(**SSITKA), Temperature Programmed Hydrogenation (TPH) and Temperature Programmed Oxidation (TPO) that the latter step to be rate determining as it required surface migration of species like adsorbed O and C. Using CH_4/CD_4 equilibration experiments, they also found evidence of isotopic H/D scrambling, leading them to suggest that water molecules interact reversibly with the catalytic surface, in the same manner as CO_2, as shown in the reaction step below:

$$H_2O + S_2 \leftrightarrow O_{ads} + H_2$$

Schuurman et al. [19] utilized transient kinetics to unravel the mechanisms of methane activation over Ni/SiO_2, $Ni/\alpha\text{-}Al_2O_3$, Ru/SiO_2 and $Ru/\gamma\text{-}Al_2O_3$. They coupled SSITKA with *in-situ* Diffuse Reflectance Infrared Fourier Transform Spectroscopy (DRIFTS) and utilized Temporal Analysis of Product (TAP) to correlate their findings. From methane pulsing using TAP, they found the release of hydrogen which was confirmed by Kroll et al. [18] The SSITKA and TAP experiments clearly revealed that CO was formed from direct and fast activation of CO_2 and oxidation of C monomer from CH_4 activation. The tailing response of CO gas phase in TAP reveals and further confirms that the reaction of surface C monomers with surface O atoms was rate determining.

v) Reverse Boudouard reaction as RDS

Generally CH_4 activation is often regarded as a first order reaction. Wang and Lu [20] did a comprehensive study on DRM over Ni/γ-Al_2O_3 catalyst and showed that CH_4 or CO_2 first involved chemisorption in the reaction and the CO formation step is the rate determining step from the reverse Boudouard reaction, as proposed in the following reaction mechanistic steps [20]:

$$CH_4 + * \rightarrow CH_4*$$

$$CO_2 + * \rightarrow CO_2*$$

$$CH_4* \rightarrow CH_3* + H$$

$$CH_3* \rightarrow CH_2* + H$$

$$CH_2* \rightarrow CH* + H$$

$$CH* \rightarrow C* + H$$

$$\mathbf{C* + CO_2* \rightarrow 2CO + 2*} \qquad \mathbf{(RDS)}$$

Wang and Lu [20] had observed that, with respect to the reaction rate on CH_4 or CO_2 partial pressure, methane showed first order and CO_2 exhibited first-order at lower partial pressures and zero order at high pressures. This observation shows that at higher partial pressures, CO_2 may not be the rate determining factor.

According to Gibson [21], one of the most powerful ways to activate inert CO_2 molecule for chemical reactions, is to form an active site-CO_2 complex via direct coordination method. CO_2 consists of C which is a Lewis acid center and O is a weak Lewis base. Therefore, a support with a strong Lewis base has the potential to form the active site-CO_2 complex. Therefore, using this criteria, Zhang et al. [22] conducted DRM

kinetic study over Ni-Co/Al-Mg-O bimetallic catalyst and postulated that CO_2 was activated due to the presence of Lewis base center in their catalyst support, i.e. MgO. This activated CO_2 was assumed to undergo a slow reaction with the carbon from CH_4 decomposition. Zhang et al. [22] also proposed that reaction of activated CO_2 with surface hydrogen species to form CO and adsorbed hydroxyl group (from RWGS reaction), could also be rate determining. However, in their final modeling, reverse Boudouard reaction was taken as the sole RDS to correlate with their kinetic data.

vi) Two (2) Step- Single Site RDS: CH_4 activation by metal Ni and CH_xO decomposition as RDS

There are many studies reporting the formation of CH_xO species as the Most Abundant Reaction Intermediate (MARI) species, leading to postulation that CH_xO decomposition is the kinetically relevant step. The following rate equation has been proposed by Bradford and Vannice [23]:

$$r_{CH_4} = \frac{k_1 P_{CH_4} P_{CO_2}}{\left(\frac{k_{-1}K}{k_7}\right) P_{CO} P_{H_2}{}^{(4-x)/2} + \left[1 + \left(\frac{k_1}{k_7}\right) P_{CH_4}\right] P_{CO_2}}$$

where $k_i = k_i L$, L = total number of active sites and K is a lumped equilibrium constant:

$$K = \left(\frac{K_8}{K_2 K_4 K_6}\right)$$

The addition of promoters, such as alkali or alkaline oxides, onto catalyst surface has been used to improve the performance of catalysts by increasing the basicity of the supporting materials. The kinetic results showed that the added metal oxides changed the reaction order in CH_4 from negative to positive and that in CO_2 from positive to negative.

This observation implies that the surface of a nickel catalyst incorporating basic metal oxides is abundant in adsorbed CO_2, whereas the surfaces devoid of these oxides are abundant in adsorbed CH_4 [24]. The coverage of nickel with CO_2 is most likely unfavorable to CH_4 decomposition and, as a result, the carbon deposition is decreased.

Nandini et al. [25] performed the DRM reaction over 13.5Ni-2K/10CeO_2-Al_2O_3 catalyst and found that their reaction sequence involved methane adsorption and dissociation, nondissociative carbon dioxide adsorption, promotion of carbon dioxide dissociation by adsorbed hydrogen atoms, interaction of the adsorbed CH_x fragments with surface hydroxyl groups, and irreversible CH_xO decomposition. The proposed irreversibility of CH_xO was valid under circumstances of no net methane formation, and hence, this formed the basis of their claims to be the RDS.

Luo et al. [26] investigated the mechanism of DRM reaction over Ni supported on La_2O_3/5A catalyst based on CH_4/CD_4 kinetic isotopic studies. From their observation, C-H cleavage was found to be O assisted, and further confirmed that decomposition of CH_xO to CO and H_2 to be the rate determining step. They have deduced three possible ways for C-H cleavage in DRM :

i. $CH_4 \leftrightarrow C_x + 4H$

ii. $CH_x + O \rightarrow CO + xH$

iii. **$CH_xO \rightarrow CO + xH$** **RDS**

Luo et al. [26] suggest that step (i) was reversible as they did not observe IR bands circa 3000 cm^{-1} which indicated the absence of CH_x adsorbed species, and hence postulated that this could be a result of fast CH_x interaction with surface oxygen species.

Step (ii) was postulated to be rather facile based on their observation from the isotopic CH_4 pulsing with CO_2. They also observed CD_3CHO in the CD_3I chemical trapping, which indicates presence of HCO on the sample surface, which was further confirmed by the presence of broad and weak IR bands in the range of 2700-3000 cm^{-1} characterizing CH_xO species (where x=1-3). Hence, based on these observations, they concluded that CH_xO decomposition is the RDS.

The proposed DRM mechanism of Luo et al. [26] is as follows:

$$CH_{4,g} \rightarrow CH_{4,*}$$

$$CO_{2,g} \rightarrow CO_{2,*}$$

$$CH_{4,s} \rightarrow CH_{x,*} + (4\text{-}x)H_{,*}$$

$$CO_{2,*} \rightarrow CO_{,*} + O_{,*}$$

$$HCOO_{,*} \rightarrow HCO_{,*} + O_{*}$$

$$HCOO_{,*} \rightarrow CO,* + OH_{,*}$$

$$CH_{x,*} + O_{,*} \rightarrow CH_xO_{,*}$$

$$CH_{4,*} + O_{,*} \rightarrow CH_xO_{,*} + (4\text{-}x)H_{,*}$$

$$CH_{x,*} + OH_{,*} \rightarrow CH_xO_{,*} + H_{,*}$$

$$\mathbf{CH_xO_{,*} \rightarrow CO_{,*} + xH_{,*}} \qquad \mathbf{RDS}$$

$$H_{,*} + OH_{,*} \rightarrow H_2O_{,*}$$

From these mechanistic steps, Luo et al. [26] have shown that CH_x decomposition on Ni^0 is postulated to be assisted by oxygen generated in CO_2 dissociation via CH_xO formation (x=1, 2). The CO_2 adsorbed on basic sites dissociates with or without H

species from CH_4 decomposition to give CO and O or CO and OH. Therefore, the RDS is the decomposition of CH_xO to CO and H.

vi) Multiple rate determining steps

Cui et al. [27] concur that operating temperature zone plays an important part in the determination of RDS. They employed transient kinetic methods to prove their claim. They found that the E_a for CH_4 and CO_2 were 31.1 and 40.5 kJ/mol respectively below 650°C, and 89.1 and 88.6 kJ/mol respectively above 650°C. These results suggest that the reforming mechanism might be varied below 650°C and constant above 650°C. They concluded that the activation energies of CH_4 dissociation and CO_2 conversion, together with the reaction orders of CH_4, CO_2, H_2, and CO, showed that the reaction mechanism can be divided into three regions: 550–575°C, 575–650°C, and 650–750°C. The reaction was constant in the low and high temperature regions but varied with temperature in the middle region. The dissociation of CH_4 into CH_x species and hydrogen species on the Ni active sites reached equilibrium state above 650°C. It was found that the surface oxygen species originating from CO_2 dissociation became removable and they moved to Ni active sites to react with CH_x species above 575^{o}C. The reaction rate of CH_x with CO_2 was lower than that of CH_4 dissociation above 650°C, leading to the durative carbon deposition on the Ni/Al_2O_3 catalyst throughout the DRM reaction. CO competed with CH_4 on the Ni active sites and inhibited the dry reforming below 650°C; and CO was desorbed rapidly above 650°C. Since the formation of hydrogen was a rapid step due to the equilibrium with Ni–H in the reforming reaction, therefore CH_4 dissociation was the RDS in the temperature region of 550–575°C. The reaction between CH_x and CO_2 became the RDS in 650–750°C. The restraining steps were switched from the former two

steps to the latter one in the temperature region of 575–650°C. Therefore, based on their observations, the reaction temperature obviously altered the reaction steps, including the amount of Ni–H on catalyst, the removability of the oxygen species, and desorption of CO from catalysts. The variation of the reaction steps with the temperature lead to the alternations of the reforming mechanism and the RDS in the different temperature regions.

Table 2-2 Summary of kinetic reaction models developed for DRM [3]

Catalyst	Rate Model	Temp Range (^oC)
Ni/Al_2O_3, Ni/CaO-Al_2O_3	$r_{ref} = \frac{aP_{CH_4}P_{CO_2}{}^2}{(a + bP_{CO_2}{}^2 + cP_{CH_4})^2}$ **RDS: *–CH_4 → *–C + $2H_2$**	500-850
Ni-Rh-Al_2O_3	$r_{ref} = \frac{k_1 K_{CH_4} K_{CO_2} (\frac{p_{CH_4} p_{CO_2}}{p_{H_2}{}^{0.5}} - \frac{p_{H_2}{}^{1.5} p_{CO}{}^2}{K_{ref}})}{(1 + \frac{p_{CH_4}}{p_{H_2}{}^{0.5} K_{CH_4}} + p_{CO_2} K_{CO_2})^2}$ $k_1 = 3.59 \times 10^{21} \exp\left(\frac{332.04 \pm 52.40}{RT}\right)$ $K_{CH4} = 2.89 \times 10^{-8} \exp\left(\frac{-109.68 \pm 57.53}{RT}\right)$ $K_{CO2} = 3.53 \times 10^{-8} \exp\left(\frac{-125.39 \pm 39.11}{RT}\right)$ **RDS: *–CH_3 + *-CO_2 → 2CO + $2H_2$ + 2***	505-625
Ni/SiO_2, MoS_2 and WS_2	$r_{ref} = \frac{k_{ref}\sqrt{K_{CH_4} K_{CO_2} P_{CO_2} P_{CH_4}}}{(1 + \sqrt{K_{CH_4} P_{CH_4}} + \sqrt{K_{CO_2} P_{CO_2}})^2}$ **RDS: CH_x-* + O-*→CO + x/$2H_2$ + 2***	600-800
Ni/La/Al_2O_3	$r_{ref} = \frac{k_{ref} P_{CH_4} P_{CO_2}}{(1 + K_1 P_{CH_4} + K_2 P_{CO})(1 + K_3 P_{CO_2})}$ K_{ref} = 0.00445mol.s^{-1}.$g_{catalyst}{}^{-1}$.atm^{-2} , K_1= 0.52 atm^{-1}, K_2=10 atm^{-1}, K_3= 27 atm^{-1} **RDS: C-* + O-* → CO + 2***	700-900
Ni/Al_2O_3, Ni/CeO_2-Al_2O_3	$r_{ref} = \frac{k_{ref} P_{CH_4} P_{CO_2}}{(1 + K_{CH_4} P_{CH_4})(1 + K_{CO_2} P_{CO_2})}$ Ni/Al_2O_3 : k_1 = 0.2-0.32 (umol.g_{cat}.s kPa), K_1 = 8.2 x10^{-4}-3.5x10^{-2} kPa, K_2= 0.43-4.3 kPa Ni/CeO_2-Al_2O_3: k_1 = 0.21-1 (umol.g_{cat}.s kPa), K_1 = 1.3 x10^{-10}-7.6x10^{-10} kPa, K_2= 0.9-22.8 kPa **RDS: C-* + O-*→ CO + 2***	500-700

Catalyst	Rate Model	Temp Range (^oC)
Ni–Co/Al_2O_3, Ce–Co–Ni/Al_2O_3	$-r_{CH4} = \frac{k_{rxn}\sqrt{P_{CH_4}}\sqrt{P_{CO_2}}}{(1+\sqrt{K_{CH_4}P_{CH_4}})(1+\sqrt{K_{CO_2}P_{CO_2}})}$ $k_{rxn} = A\exp\left(\frac{-E_a}{RT}\right)$ $K_{CH4} = \exp\left(\frac{\Delta S_{ads,CH4}}{R}\right)\exp\left(\frac{-\Delta H_{ads,CH4}}{RT}\right)$ $K_{CO2} = \exp\left(\frac{\Delta S_{ads,CO2}}{R}\right)\exp\left(\frac{-\Delta H_{ads,CO2}}{RT}\right)$ **RDS: C-*$_1$ + O-*$_2$ → CO-*$_2$ + *$_1$**	650–750
Ni-Co/Al-Mg-O	$r_{CH4} = \frac{k_1 P_{CH_4} P_{CO_2}}{(1+K_1 P_{CH_4})(1+K_2 P_{CO_2})}$ k_1 = 0.2 – 0.32 μmol/g.cat.skPa^2 K_1= 0.00082-0.035 kPa^{-1} K_2= 4.3-0.43 kPa^{-1} **RDS: *-C + *-CO_2 → 2CO + 2***	500-700
Ni-Co/Al-Mg-O	$-r_{CH4} = \frac{aP_{CH_4}P_{CO_2}}{bP_{CH_4}+cP_{CO_2}+dP_{CH_4}P_{CO_2}}$ $a=C_{MT}C_{ST}K_1k_2K_3k_4$ $b=K_1k_2$ $c=C_{ST}K_3k_4$ $d=C_{ST}K_1K_3k_4$ **RDS: *-CO_2 + M-C → 2CO + M + ***	650-750
Supported Ni	$r_{ref} = \frac{k_1 P_{CH_4} P_{CO_2}}{\left(\frac{k_{-1}\mathbf{K}}{k_7}\right)P_{CO}P_{H_2}^{(4-x)/2} + \left[1+\left(\frac{k_1}{k_7}\right)P_{CH_4}\right]P_{CO_2}}$ $k_i=k_iL$, L = total number of active sites and **K** is a lumped equilibrium constant: $\mathbf{K} = \left(\frac{K_8}{K_2K_4K_6}\right)$ Ni/TiO_2 : k_1=0.003-0.042, k_7=0.77-5.35, k_{-1} **K** =0-5.38 Ni/MgO: k_1=0.031-0.085, k_7=20.45-33.58, k_{-1} **K** =0.153-0.167 **RDS: Methane Dissociation and CH_xO decomposition**	400-450, 500-550

Catalyst	Rate Model	Temp Range (^{o}C)
Ni-K/CeO_2-Al_2O_3	$r_{CH_4} = \frac{k_{1L}P_{CH_4}}{\left[\left(k_{1L}P_{CH_4}P_{CO}/k_{7L}K_aP_{CO_2}\right) + \left(K_bP_{CO_2}P_{H_2}^{\frac{1}{2}}/P_{CO}\right) + \left(k_{1L}P_{CH_4}/k_{7L}\right) + 1\right]}$ $k_{1L} = 1292 \pm 465 \exp\left(\frac{-12894 \pm 366}{T}\right)\ \left(\frac{gmol}{gcat}.s.atm\right)$ $k_{7L} = (3.8 \pm 0.1)e-3 \exp\left(\frac{-220 \pm 25}{T}\right)\ \left(\frac{gmol}{gcat}.s\right)$ $K_a = (7.4 \pm 4.4)\exp\left(\frac{-4145 \pm 663}{T}\right)\ (atm^{-2})$ $K_b = 2.3e7\exp\left(\frac{-15998 \pm 2808}{T}\right)\ (atm^{-2.5})$ And $c = 5.8\exp\left(\frac{8605}{T}\right)$ **RDS_1 : *–CH_4 → *–C + 2H_2** **RDS_2 : $CH_xO_{,s}$ → $CO_{,s}$ + x$H_{,s}$**	600–800
Ni/La_2O_3	$r_{CH_4} = \frac{K_1k_2K_3k_4P_{CH_4}P_{CO_2}}{K_1k_2K_3P_{CH_4}P_{CO_2} + K_1k_2P_{CH_4} + K_3k_4P_{CO}}$ $K_1k_2 = 2.61\times10^{-3}\exp\left(\frac{-4300}{T}\right)(mol/g\,s)(kPa)^{-1}$ $K_3 = 5.17\times10^{-5}\exp\left(\frac{-8700}{T}\right)(kPa)^{-1}$ $k_4 = 5.35\times10^{-1}\exp\left(\frac{-7500}{T}\right)(mol/g\,s)$ **RDS_1 : *–CH_4 → *–C + 2H_2** **RDS_2 : $La_2O_2CO_3$ + C–* → La_2O_3 + 2CO + ***	650–750

2.1.4. Catalyst selection

Catalysts are of prime importance in syngas production. From industrial standpoint, it is desirable to operate the process at a relatively lower temperature and with a CO_2/CH_4 ratio close to unity. This necessitates the use of a catalyst which can endure the severe conditions imposed by the DRM reactions, such as carbon resistant, thermally stable (to prevent sintering), as well as can give good catalytic performance especially at the thermodynamically favourable conditions [28].

The knowledge of the relation between the catalytic and solid state properties of catalysts is crucial for the systematic design of more efficient preparations. In the pursuit of these relations formulation of catalyst systems which can yield experimental data facilitating such generalizations is a great benefit. If one tries to correlate bulk properties with the rates of reactions occurring at the surface it is necessary that the systems are isostructural. As the surface represents a discontinuity of the crystal, the bulk properties have the same relationship with the surface properties [29].

According to Rostrup-Nielsen [30], the desired catalyst properties are described as the following:

i) Surface dehydrogenation sites that can enhance the dissociation of methane to CH_x species and remove H species from the intermediate to form hydrogen;

ii) Surface CO_2 adsorption sites that promote the activation or participation of CO_2 to remove C species derived from the decomposition of CH_4;

iii) Adjacent surface sites that will facilitate the reaction between C species and activated CO_2 molecules so that the overall reaction rate can be improved;

iv) Adjacent surface sites that will facilitate the reaction between C species and activated CO_2 molecules so that the overall reaction rate can be improved;

v) Thermal stability that can retain catalyst physical and mechanic properties thus phase transitions and crystal transformation could be avoided at high reaction temperatures, such as 1023 K;

vi) Uniform and stable dispersion of active components with small particle sizes while suppressing carbon formation or other undesired reactions. This is due to the fact that the ensemble area required for carbon formation from active sites is larger than those required for reforming.

2.1.4.1. Choice of Metal

Generally, CH_4 is only adsorbed on the metal in a dissociated form to produce hydrogen and hydrocarbon species CH_x (x=0–4). Values of x are dependent on the metal substrate and the reaction temperature. If $x \approx 0$, it indicates that carbon deposition occurs on the metal surface. Both CH_x and H atoms are attached to the metal active sites. The large majority of the adsorbed hydrogen species are then recombined, producing hydrogen molecules that subsequently desorb into the gaseous phase [31].

Most of the group VIII transition metals have promising catalytic performance for this reaction. Noble metals such as Rh, Ru, Pd, Pt and Ru are known to reduce carbon

deposition. Nickel is one metal which has comparable activity to noble metals compared to other non-noble metals [1]. The only problem is that Ni can easily deactivate and sinter. However, noble metals are high in cost, for e.g. Rh is about 2000 times more expensive than Nickel. Hence, considering the high cost and limited availability of these precious metals, it is more attractive to develop a suitable nickel catalyst with a good support to tackle the issue of carbon deposition. It is therefore, practical to develop Ni-based catalysts for DRM reaction from the view point of cost and availability.

2.1.4.2. Choice of Supports

From a fundamental point of view, the presence of several metal elements in a common structure permits the adjustment of the local electronic properties, imposes well defined coordinations, limits the extent of oxidation–reduction phenomena, and may stabilize the whole catalyst by retarding sintering [32]. Mixed oxide based precursors for catalyst supports fit well in providing this aspect for catalyst synthesis.

The forms of active components present in heterogeneous catalysts are of importance to catalysis. A supported catalyst usually consists of an active component dispersed on a support with a highly specific surface. It was postulated by Xie and Tang [33] that, an active component dispersed on a support may end up in one of three forms:

a) it may retain its chemical identity as a separate crystalline or amorphous phase;
b) it may form a new stoichiometric compound with the support or additive, or
c) it may dissolve in the support to give a solid solution.

The investigation of secondary components such as supports and promoters has attracted significant attention.

2.1.5. Nickel supported on mixed oxides or in form of perovskite type oxides

As reported by Ruckenstein and Hu [34], DRM activity was depends on nature of the support. They found that activity and selectivity of the catalyst was in the order of Ni/Al_2O_3>Ni/SiO_2>Ni/TiO_2. However, the activity and selectivity of the reduced NiO/Al_2O_3 catalyst increased rapidly with initial reaction time but decreased subsequently due to metal sintering and carbon deposition over $NiO\text{-}Al_2O_3$.

Spinel oxide Ni-based catalysts also have already been applied for DRM The substoichiometric spinel structures present the properties to be an active catalyst: high dispersion of NiO into the spinel, stability of the structure at low temperature, formation of Ni phase in the same temperature area than the catalytic reaction and presence of Ni oxide to limit the growing of the particles probably by formation of interaction between nickel metal out of the structure and Ni oxide of the structure [35, 36].

Formation of spinel structures such as $NiAl_2O_4$ compounds in the Ni/Al_2O_3 as a result of high temperature calcinations leads to strong metal support interaction [37]. The presence of this compound strengthens the Ni-O bond in $NiAl_2O_4$ compared to NiO crystal. However, the bulk structure however, is difficult to reduce and has lower activity at lower temperatures. On the other hand, surface spinel structures are more desirable as they are more activity. Wang and Lu [38] have reported the high activity and stability of Ni/Al_2O_3 catalyst compared to Ni/CeO_2 catalyst due to strong metal support interactions. Nevertheless, it has been reported by Bhattacharya and Chang [39] that, transformation to

α-phase take place at high temperatures resulting in catalyst deactivation.

Many different types of supports such as SiO_2, ZrO, CaO, La_2O_3, MgO etc. have been studied by different groups. In addition, various types of promoters have been used to further enhance the desirable properties of the Ni catalyst and suppress carbon formation [40]. These promoters include addition of rare earth metals, basic elements and other metal additives to form bimetallic structures. Novel supports such as perovskite based oxides have also been considered.

Various efforts have been undertaken by many researchers to synthesize various types of Ni based catalysts in order to obtain a catalyst that is active, stable and selective for the reforming of methane reactions. These catalysts should be able to mitigate the problems highlighted in the preceding section. The catalyst forms investigated include Ni supported on oxides, mixed oxides, as well as being incorporated in perovskite type oxides (ABO_3). Irreversible carbon formation upon reaction is one of the major problem afflicting catalysts. In this regard, catalysts which provide unfavourable conditions for carbon formation, thereby increasing its activity and stability are much desired.

Composite oxides form a class of oxides in which a low surface area carrier (e.g. lanthana) is dispersed on a high surface area carrier (e.g. alumina). Alumina is known to have two types of acid sites: Lewis and Brönsted. The number, strength and type of acid sites in a composite oxide can be easily controlled by varying its composition [41].

The salient features of some Ni based catalyst which are supported on different types of support and promoted by various promoters are summarized in Table 2-3 based on several literature findings [3].

Table 2-3

Summary of Ni supported catalyst for DRM

Catalyst Ni (wt%)	Activation	S.A (m^2/g) .	Metal particle size (nm)	T [ºC]	Metal-support interaction	Lattice oxygen	CH_4/CO_2 (ml/min)	DRM Activity			Stability (% Coke) And Type of Carbon	Remark	Ref
								Conv. CH_4 [%]	Conv. CO_2 [%]	H_2/ CO			
Ni Supported Catalyst													
10% Ni/γ-Al_2O_3	Air, 850 °C, 4h H_2, 327°C, 2.5 h	150.2	-	550	-	-	67.8/67.8	8.7	36.6	-	-	Highest methane conversion obtained on Ni/CeO_2, but with deactivation. Doping K and Li enhanced catalyst stability and no carbon deposition was observed.	42
10%Ni/α-Al_2O_3	Air, 850 °C, 4h H_2, 327°C, 2.5 h	3.3	-	550	-	-	67.8/67.8	8.4	34.7	-	-		42
10%Ni/La_2O_3	Air, 850 °C, 4h H_2, 327°C, 2.5 h	3.2	-	550	-	-	67.8/67.8	4.4	24.3	-	-		42
10%Ni/γ-Al_2O_3 (CO-IM)	Air, 600 °C, 5h H_2, 700°C, 1 h	90.9	24	700	NiAl(CO-IM)> NiAl(SG-IM)> NiAl(SG)	-	13.2/11.6 /41.6	-	-	-	38	Small size of metallic Ni particles is a key factor to prevent coke formation	43
10%Ni/γ-Al_2O_3 (Sol-gel-IM)	Air, 600 °C, 5h H_2, 700°C, 1 h	171.1	9.9	700		-	13.2/11.6 /41.6	88	88	-	0		43
10%Ni/γ-Al_2O_3 (Sol-gel)	Air, 600 °C, 5h H_2, 700°C, 1 h	183.2	-	700		-	13.2/11.6 /41.6	-	-	-	1.2		43
7% Ni/Si_3N_4	Air, 400 °C, 5h H_2, 700°C, 1 h	23	-	800	Strong interaction between metal and basic support	-	40/40	95	91	-	-	Combination of high intrinsic activity with the improved properties of silicon nitride support make Ni/Si_3N_4 catalyst superior to other high temperature catalysts	44
Ni supported Catalyst with Promoter													
14%Ni/Al_2O_3 0.5wt%K, Ca, Mn and Sn as promoter	Air, 850°C, 10h H_2, 850°C, 14 h	209~17 0	5-7	750	Strong interaction for Ni-Sn and Ni-Ca	-	149.2	84.7	90.8	0.97	6% After 30 h operation	Severe pretreating condition produced a high metal–alumina interaction	45

Catalyst Ni (wt%)	Activation	S.A (m^2/g).	Metal particle size (nm)	T [°C]	Metal-support interaction	Lattice oxygen	CH_4/CO_2 (ml/min)	DRM Activity			Stability (% Coke) And Type of Carbon	Remark	Ref
								Conv. CH_4 [%]	Conv. CO_2 [%]	H_2/ CO			
5wt.%Ni/CaO-Al_2O_3	Air, 900°C, 10h H_2, 750°C, 1.5 h	6.61	-	750	Strong interaction	-	100	62~64	65-68	-	5% after 50h	The strong metal support interactions is due to the presence of Ca	46
8.8%Ni/γ-Al_2O_3	Air, 550 °C H_2, 700°C, 2h	158.6	9.79	800	Promoted catalysts have stronger interaction between Ni and the support than 13.5Ni/Al_2O_3 catalyst	-	29.2/29.2	88.7	82.7	1.1	0.3	Incorporation of K and CeO_2 (or MnO) onto the catalyst significantly reduced coke formation due to partial coverage of the surface of nickel by patches of promoters and increase in CO_2 adsorption	47
13.5%Ni-2%K/ 10%CeO_2-Al_2O_3	Air, 550 °C H_2, 700°C, 2h	127.2	9.3	700		-	29.2/29.2	62.4	62.7	1.0	trace		47
13.5%Ni-2%K/ 5%MnO-Al_2O_3	Air, 550 °C H_2, 700°C, 2h	123.8	9.69	700		-	29.2/29.2	59.5	60.0	0.98	<0.1		47
5%Ni/$BaTiO_3$	Air, 700 °C, 2 h	-	-	750	Strong interaction between NiO and $BaTiO_3$	-	50/50	85.2	84.9	-	5.93	Catalytic activity and stability; and carbon resistance can be improved with addition of rare earth oxide	48
5%Ni-La/$BaTiO_3$	Air, 700 °C, 2 h	-	-	750		-	50/50	88.2	88.9	-	3.2		48
5%Ni–$BaTiO_3$	Air, 700 °C, 2 h	-	-	750		-	50/50	89.0	90.0	-	7.2		48
5%Ni–0.75wt% La–$BaTiO_3$	Air, 700 °C, 2 h	-	-	750		-	50/50	91.3	91.9	-	0.67		48
10%Ni/γ-Al_2O_3 5 wt.% K_2O as promoter	Air, 500 °C, 2 h H_2, 500°C, 2h	-	-	700	Interaction reduced due to addition of K	-	6/6/48	88	88	-	<1 mg/g non-structured carbon	Presence of K hinders the accumulation of coke, which is due to ability of K to gasify coke without any structural modification of nickel	49
10%Ni-La_2O_3/γ-Al_2O_3	Air, 750 °C, 2 h H_2, 700°C, 2h	233.43	-	800	-	-	50/50	83	90	-	100h: 6.73	Metallic Ni < 15 nm can effectively suppress carbon formation	50

Catalyst Ni (wt%)	Activation	S.A (m^2/g).	Metal particle size (nm)	T [°C]	Metal-support interaction	Lattice oxygen	CH_4/CO_2 (ml/min)	DRM Activity			Stability (% Coke) And Type of Carbon	Remark	Ref
								Conv. CH_4 [%]	Conv. CO_2 [%]	H_2/ CO			
10%Ni-La_2O_3/Al_2O_3	Air, 750 °C, 2 h H_2, 700°C, 2h	76.67	-	800	-	-	50/50	93	90	-	55h: 17.46	suppress carbon formation of carbon filaments, resulting in a better activity and stability	50
10%Ni-La_2O_3/α-Al_2O_3	Air, 750 °C, 2 h H_2, 700°C, 2h	38.09	-	800	-	-	50/50	87	80	-	100h: 12.41		50
8%Ni/SiO_2	Air, 800 °C, 3 h H_2, 800°C, 1h	-	-	800	Ca strengthen the interaction between Ni and α-Al_2O_3	-	25/25	66.6	73.2	-	66.68	Ca improved Ni dispersion, strengthened interaction between Ni and Al_2O_3, and retarded the sintering	51
8%Ni/α-Al_2O_3	Air, 800 °C, 3 h H_2, 800°C, 1h	-	54.3	800		-	25/25	69.5	75.4	-	10.4		51
8%Ni/γ-Al_2O_3	Air, 800 °C, 3 h H_2, 800°C, 1h	-	-	800		-	25/25	77.2	81.0	-	8.08		51
8%CaNi/α-Al_2O_3	Air, 800 °C, 3 h H_2, 800°C, 1h	-	-	800		-	25/25	84.8	85.5	-	9.96		51
8%CaNi/γ-Al_2O_3	Air, 800 °C, 3 h H_2, 800°C, 1h	-	-	800		-	25/25	72.6	79.0	-	10.36		51
Ni-CaO-ZrO_2	Air, 600 °C, 5 h H_2, 600°C, 1 h	227.1	-	700	Strong interaction between NiO and ZrO_2	-	40/40	75	85	0.91	-	Carbonaceous species from CH_4 decomposition could be eliminated by the lattice oxygen of ZrO_2	52
33%Ni-La-Al_2O_3	Air, 750 °C, 3 h H_2, 650°C	149.4	26: 4h reacted	700	La strengthen the interaction between Ni and Al_2O_3	-	50/50/200	49	63	-	0.9% (250min)	Presence of La increases metallic dispersion, conversion and stability during reaction.	53
33%Ni-4%La-Al_2O_3	Air, 750 °C, 3 h H_2, 650°C	141.1	11.3: 4h reacted	700		-	50/50/200	59	65	-	0.2 (250min)		53
33%Ni-8%La-Al_2O_3	Air, 750 °C, 3 h H_2, 650°C	130.9	12.1: 4h reacted	700		-	50/50/200	65	70	-	0.15 (250min)		53
33%Ni-12%La-Al_2O_3	Air, 750 °C, 3 h H_2, 650°C	150.0	24.3: 4h reacted	700		-	50/50/200	55	62	-	0.25 (250min)		53

Catalyst Ni (wt%)	Activation	S.A (m^2/g).	Metal particle size (nm)	T [°C]	Metal-support interaction	Lattice oxygen	CH_4/CO_2 (ml/min)	DRM Activity			Stability (% Coke) And Type of Carbon	Remark	Ref
								Conv. CH_4 [%]	Conv. CO_2 [%]	H_2/ CO			
10%Ni//γ-Al_2O_3	Air, 550 °C, 5 h H_2, 750°C, 1 h	185	-	750	Strong interaction between Ni and $MgAl_2O_4$	-	20/20	31.8	29.2	0.88	42.5	Interactions between Ni and $MgAl_2O_4$ produce a highly dispersed active Ni species for high activity and coke resistance and sintering	54
10%Ni/MgO-γ-Al_2O_3	Air, 550 °C, 5 h H_2, 750°C, 1 h	120	-	750		-	20/20	76.7	88.4	0.9	4.5		54
10%Ni/$MgAl_2O_4$	Air, 550 °C, 5 h H_2, 750°C, 1 h	78.5	10.4 (reduced) 11.8 (used)	750		-	20/20	31.8	29.2	0.88	42.5		54
10%Ni/γ-Al_2O_3	O_2 300 °C H_2, 700°C, 2 h	145	-	700	-	-	10/10/20	66	68	-	14.9	Ni– Al_2O_3 aerogel catalysts showed a low coking rate due to highly dispersed metal particles.	55
10%Ni/ 5%(mol)Mg-La_2O_3	Air, 800 °C, 5 h H_2, 650°C, 0.5 h	-	8-10	600	Ni and Mg formed the strongest interaction among all catalysts, probably due to solid state interaction	Ni/Sr-La_2O_3 > Ni/Mg-La_2O_3> Ni/La_2O_3	1 :1	37	33	-	10 (after 10h)	Presence of lattice oxygen promotes C-H activation, resulting in high H_2 production	56
10%Ni/ 5%(mol)Sr-La_2O_3	Air, 800 °C, 5 h H_2, 650°C, 0.5 h	-	12-15	600			1 :1	78	59	-	40 (after 10h)		56
5%Ni/ γ-Al_2O_3	H_2, 800°C, 5 h	125.4	5.8	700	B_2O_3 reduces interaction between Ni and Al_2O_3	-	12.5/12.5	69	72	0.8	9.9 (after 65 h)	High amount and strong basicity of surface OH from B_2O_3 suppressed carbon deposition by reacting with surface carbon from methane decomposition	57
5%Ni/ 1%B_2O_3-Al_2O_3	H_2, 800°C, 5 h	91.8	6.2	700		-	12.5/12.5	60	64	0.8	32.0 (after 65 h)		57
5%Ni/ 5%B_2O_3-Al_2O_3	H_2, 800°C, 5 h	69.5	7.1	700		-	12.5/12.5	69	72	0.8	13.0 (after 65 h)		57
5%Ni/ 10%B_2O_3-Al_2O_3	H_2, 800°C, 5 h	73.3	9.1	700		-	12.5/12.5	63	64	0.7	33.5 (after 65 h)		57

2.1.6. Summary of catalyst properties

(i) Surface acidity-basicity

The surface acidity-basicity of the catalyst support has a significant influence not only on the metal-support interaction but also on the adsorption and reactions of methane and carbon dioxide. Strong acidity may be detrimental to the efforts to reduce coke formation. One example is silica-supported catalysts where the acidic silica support plays little role in improving carbon deposition, as both CO_2 and CH_4 are activated by metal active sites. The supports with basicity are expected to enhance the adsorption of CO_2 and as well as concentration of surface adsorbed OH groups. Furthermore, the increase of the concentration of adsorbed CO_2 is suggested to reduce carbon formation via CO disproportionation. Mizuhara et al. [58] have found that a support with larger acidity is more prone to carbon deposition. On the other hand, Yamazaki et al. [59] claimed that the support basicity was essential to suppress carbon deposition.

The addition of promoters, such as alkali or alkaline oxides, onto the catalyst surface has been used to improve the performance of catalysts during DRM reaction by increasing the basicity of the supports. For instance, Pan et al. [60] found that Ga_2O_3, which was introduced as the promoter onto SiO_2, activated adsorbed CO_2 to form surface carbonate and bicarbonate species. The activated CO_2 should react much more easily with the deposited carbon than the linearly or physically adsorbed CO_2. Consequently, Ga_2O_3-promoted SiO_2-supported Ni catalyst showed higher stability and coke resistance for CO_2 reforming of methane than Ni/SiO_2 catalyst (as shown in Table 2-3). Figure 2-2 shows the activation of adsorbed CO_2 on SiO_2-Ga_2O_3catalyst.

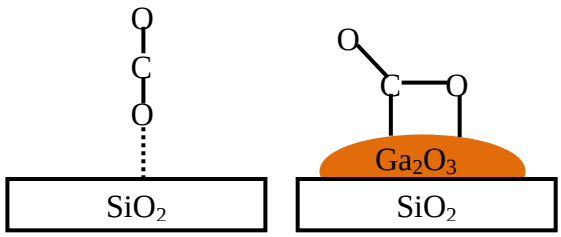

Figure 2-2 Activation of adsorbed CO_2 on SiO_2-Ga_2O_3 catalyst [60].

The reaction kinetic results for DRM showed that the added basic metal oxides play a role in changing the reaction order of the reactants implying that the surface of a nickel catalyst incorporating basic metal oxides is abundant in adsorbed CO_2 [3]. The coverage of nickel with CO_2 is most likely unfavourable for CH_4 decomposition and, as a result, carbon deposition is decreased.

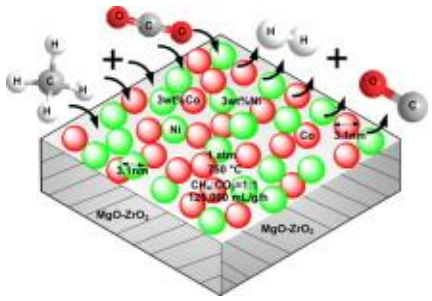

Figure 2-3 Synergetic bimetallic effect and surface basicity to prevent coke [61]

Fan et al. [61] found that the constant activity of bimetallic Ni-Co catalyst had high degree of reducibility due to the synergetic effect between Ni and Co (TPR analysis), the inhibition of metal from being oxidized as well as the surface basicity to inhibit coke formation (XPS analysis). The reaction diagram is illustrated in Figure 2-3. Their catalyst

showed impressive restoration of catalytic activity after being used in DRM reaction and regenerated using air. The catalytic activity of their used catalyst was restored to achieve comparable catalytic performance as that of fresh catalyst. The catalytic performance of monometallic nickel and cobalt catalysts was improved through the synergized effect of both Ni and Co components in the bimetallic catalyst which showed better activity and regenerability.

(ii)Surface oxygen

Previous investigations on DRM reaction have shown that the adsorbed O atoms derived from direct decomposition of CO_2 or the oxycarbonate species derived from the reaction between CO_2 and basic La_2O_3 support are the key intermediates in the oxidation of adsorbed CH_x ($0 \leq x < 4$) species originated from CH_4 decomposition on the active Ni sites.

Our research group [56] recently investigated the effect of promotional rare earth over the catalytic DRM performance on Ni-La_2O_3 catalysts. The Ni-La_2O_3 catalyst doped with a small amount of Sr significantly improved the catalytic performance even at low temperatures of 600^0C with low carbon deposition, due to the highly mobile surface oxygen species which enabled C-H bond activation. These surface oxygen species can adsorb CO_2 molecules to form bidentate carbonate species, which react with surface carbon species, thus resulting in higher CO_2 conversion and lower carbon formation.

Another recent study from our research group [62] also demonstrated that the presence of β-oxygen on Y_2O_3 surface helps to dissociate CH_4. Since the amount of β-oxygen is very little, a small amount of oxygen in the feed is required to regenerate the □-

oxygen in order to maintain the stability of the regenerate the β-oxygen in order to maintain the stability of the catalyst. Figure 2-4 shows the DRM reaction mechanism of carbon removal on Pd-Ni/Y_2O_3 catalyst.

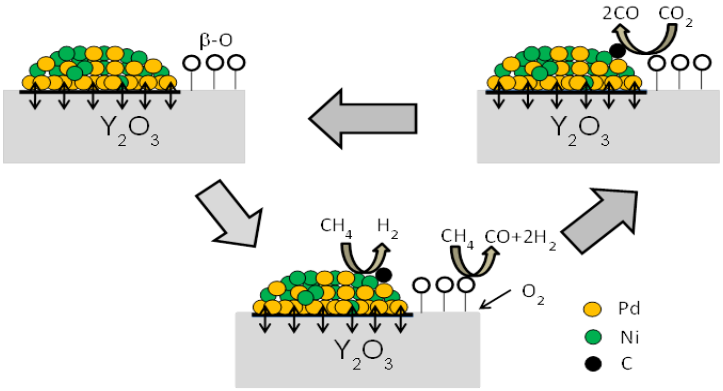

Figure 2-4 Mechanism of carbon removal on Pd-Ni/Y_2O_3 catalyst [62]

(iii)Lattice oxygen

Valderrama et al. [63] studied the partial substitution of La^{3+} with Sr^{2+} in $La_{1-x}Sr_xNiO_3$ perovskite structure for DRM reaction. They found that this substitution decreases the oxidation state of Ni favouring its reduction and produced solids with the spinel type structure, due to the increase on vacancies that facilitate the mobility of the oxygen toward the surface of the solid. The redox processes on the perovskite structure occur through intermediary species and they are not reversible. The high activity observed on these precursory solids in the DRM reaction is due to the presence of Ni^0 during the course of the reaction and to the formation of $La_2O_2CO_3$ that allows the oxidation of methane, the regeneration of La_2O_3, and the suppression of carbon deposits [63].

A recent study by our research group [64] on the performance of partially-substituted $LaSrNiO_3$ perovskite catalysts in DRM reaction show that lattice oxygen species in these perovskite catalysts play an important role in the activation of C-H bond

of CH_4 molecule and reduce the carbon formation by reacting with CO_2 to form $La_2O_2CO_3$. The Cu-substituted $LaSrNiO_3$ catalyst initially has high CH_4 conversion due to the high amount of accessible Ni and the availability of mobile lattice oxygen species. However, due to the weak metal-support interaction, these Ni particles could agglomerate to form bigger Ni particle size, causing lower catalytic stability. On the contrary, although the Fe-substituted $LaSrNiO_3$ catalyst has initial low DRM activity due to the lower reducibility of Fe and less mobility of lattice oxygen species, but it shows high catalytic stability in DRM reaction (as shown in Figure 2-5) due to: (1) stronger metal-support interaction, hindering thermal agglomeration of Ni particles and (2) the presence of the abundant lattice oxygen species which are less active for C-H bond activation but active to form $La_2O_2CO_3$.

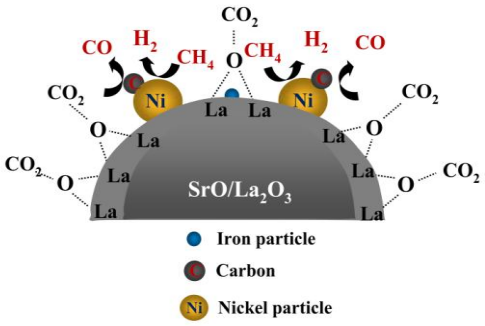

Figure 2-5 Schematic diagram of carbon removal on SrO/La_2O_3 support [64]

(iv)Hydroxyl groups

The participation of OH groups in the oxidation of these CH_x species in DRM reaction has not been considered as important as those observed in steam reforming of methane reaction because of the low surface coverage of OH. However, DFT calculations indicated that the free energy barriers for the oxidation of CH_x species by OH groups are

slightly lower than the oxidative reactions by O atoms [3]. The present study by our research group [57] demonstrated that by altering the concentration and acidity/basicity of surface OH groups by addition of B_2O_3, carbon formation in DRM reaction can be significantly suppressed, and thus the catalytic performance of Ni-based catalysts for DRM reaction can be promoted (as shown in Table 2-3). The reaction mechanism over these borated-alumina supported Ni-based catalysts has been proposed based on the ample characterization and catalytic reaction data, clearly elucidating the reaction pathway whereby metal nickel catalyses CH_4 and CO_2 activation and decomposition, followed by OH groups oxidizing surface carbon species derived from CH_4 decomposition. Figure 2-6 shows the schematic of carbon removal with addition of B_2O_3 to Ni/Al_2O_3 catalyst surface which was found to increase the concentration of surface basic OH species [57].

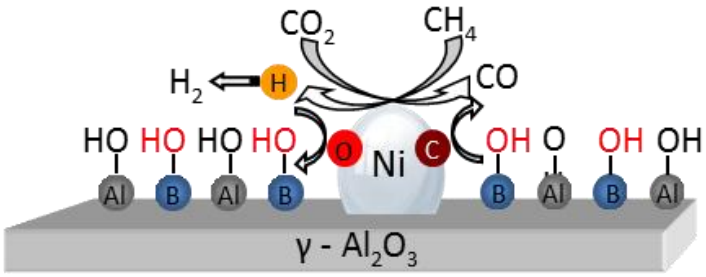

Figure 2-6 Mechanism of carbon suppression on Ni/B_2O_3-Al_2O_3 catalyst [57]

(v)Metal-support interaction

Effective DRM catalysts are those with metal-support combinations that can promote the catalyst activity. The experiment carried out by Hou [65] showed that on Ca-promoted Ni/α-Al_2O_3 catalysts, the addition of Ca improved the dispersion of Ni, strengthened the interaction between Ni and Al_2O_3, and retarded the sintering.

Moreover, the high activity and high resistant to coking and sintering of 10%Ni/$MgAl_2O_4$ in the DRM reaction has been ascribed to the strong interactions between Ni and $MgAl_2O_4$, producing a highly dispersed active Ni species [66]. However, very strong metal-support interaction may lead to the catalyst difficult to be reduced. Thus, an appropriate metal-support interaction should be suggested for good performance and stability of a catalyst.

The recent study from our research group [67] shows that the type of metal precursor has a great effect on metal support interaction. The Pd-Ni/Y_2O_3 catalyst synthesized from $PdCl_2$ precursor (denoted as Pd(C)-Ni/Y_2O_3) has excellent stability than the Pd-Ni/Y_2O_3 catalyst from $Pd(NO_3)_2$ precursor (denoted as Pd(N)-Ni/Y_2O_3). The presence of chloride ion in the catalyst helps to form metal support interaction between Pd and Y_2O_3, resulting in higher metal dispersion. The catalyst activity is also enhanced due to the small metal particle size and formation of Pd-Ni alloy. Figure 2-7 shows the different structure of Pd-Ni/Y_2O_3 catalyst synthesized from $PdCl_2$ and $Pd(NO_3)_2$ precursors.

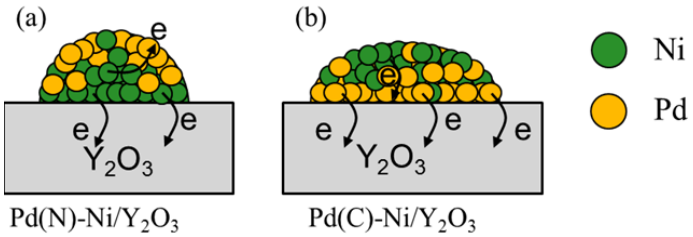

Figure 2-7 Metal support interaction derived from catalyst precursor [67]

2.2. Partial Oxidation of Methane (POM)

POM reaction is also an attractive technology for syngas/hydrogen production. The syngas product ratio from POM is 2.0 compared to 1.0 from DRM reaction.

The reactions, which occur during POM to syngas are enlisted as follows [68]:

Main reaction:

POM: $CH_4 + ½\ O_2 \rightarrow CO + 2\ H_2$ $\Delta H°_{298} = -35.7$ kJ/mol (6-7)

Side reaction :

Decomposition: $CH_4 \leftrightarrow C + 2H_2$ $\Delta H°_{298} = 74.9$ kJ/mol (2-8)

Boudouard: $2CO \leftrightarrow C + CO_2$ $\Delta H°_{298} = -172.4$ kJ/mol (2-9)

Combustion: $CH_4 + 2\ O_2 \rightarrow CO_2 + 2\ H_2O$ $\Delta H°_{298} = -803$ kJ/mol (2-10)

Water-Gas Shift: $CO + H_2O \leftrightarrow CO_2 + H_2$ $\Delta H°_{298} = -41.2$ kJ/mol (2-11)

Several key advantages of POM reaction compared to SRM as summarized by York et al. [69] are as follows:

- Mildly exothermic – hence enables fast start up. Morever, when used in combination with SRM or DRM, enhances efficiency.
- Ideal H_2/CO ratio of 2.0 for further chemical synthesis via Fischer Tropsch reaction.

However, just like DRM, this process is not yet commercially practiced, in view of the high costs involved for oxygen production via conventional cryogenic technologies. The POM process operating at a very low contact time (about millisecond), is of great practical importance [70]. However, in this process a high methane conversion (> 90%) coupled with very high space velocity (≥ 500,000 $cm^3g\text{-}1h^{-1}$) leads to production of a large

amount of heat in a small catalyst zone, even at very high product selectivity. Hence this leads to "hot spot" formation (which is difficult to control) and ultimately resulting in the deactivation of a thermally unstable catalyst [71]. Even a small loss in the selectivity due to catalyst deactivation is expected to make this process highly hazardous / out of control.

Furthermore, using air as an oxygen source is not a feasible method as downstream processes may not be able to tolerate large volumes of nitrogen. Hence, in order to render the POM process more feasible, inexpensive and compact oxygen supply distributed along the reactor channel is highly desirable. This, coupled with a thermally stable and carbon resistant catalyst is of utmost importance. Recent advances in alternative technologies such as ceramic dense membrane, which can deliver high O_2 fluxes at high temperatures holds a promising future for the POM reaction and furthermore, controlled distribution in oxygen supply, can even minimize the hot spot formation along the membrane reactor [72]. This review is covered in Chapter 3.

2.3. Combination of DRM and POM – Oxidative CO_2 Reforming of Methane

The carbon deposition and catalyst deactivation from sintering and thermal deactivation faced by DRM reaction on Ni-based catalyst can be minimized via structural or promotional modifications. However, the high energy requirements of this process still prevail. In order to enable sustainable operation of this process, combining POM with DRM offers the benefit of minimizing the high energy requirements. This "mixed" reaction is called oxidative CO_2 reforming of methane (OCRM). Hence, the heat effects of reaction can be controlled directly by adjusting the feed proportions of oxygen, fuel and CO_2. In order to counter the effects of high cost of O_2 production, this process is more

efficient to be conducted in a ceramic membrane reactor [73]. This review is presented in Chapter 3.

In terms of catalyst selection, a carbon resistant and thermally stable catalyst is a pre-requisite, in addition to high activity [70]. Most often, a catalyst that can withstand the severe operating conditions of DRM reaction can suit for the POM and OCRM reactions as well, as long as they have the above-mentioned properties.

According to Choudhary et al. [70], the following reactions can occur during OCRM reaction depending on the process conditions:

Main reactions:

POM: $CH_4 + ½\ O_2 \rightarrow CO + 2\ H_2$ $\Delta H_r = -5$ kcal/mol (2-12)

DRM: $CH_4 + CO_2 \rightarrow 2\ CO + 2\ H_2$ $\Delta H_r = 61$ kcal/mol (2-13)

SRM: $CH_4 + H_2O \rightarrow CO + 3\ H_2$ $\Delta H_r = 54$ kcal/mol (2-14)

Side reactions:

$CH_4 + 2\ O_2 \rightarrow CO_2 + 2\ H_2O$ $\Delta H_r = -192$ kcal/mol (2-15)

$CH_4 + 1½\ O_2 \rightarrow CO + 2\ H_2O$ $\Delta H_r = -124$ kcal/mol (2-16)

$CO + H_2O \rightarrow CO_2 + H_2$ $\Delta H_r = -8$ kcal/mol (2-17)

$CO_2 + H_2 \rightarrow CO + H_2O$ $\Delta H_r = 8$ kcal/mol (2-18)

Reactions (2-15) and (2-16) are the combustion and partial combustion reactions which can produce the required energy. Both reactions (2-17) and (2-18) are the water gas shift (WGS) and the reverse water gas shift (rWGS) reactions, respectively which occur depending on the process temperature. Due to the complex reaction pathways, several reactions can occur at the same time.

REFERENCES

[1] Bradford, M.C.J.; Vannice, M.A. *Catal. Rev.* **1999**, *42*, 1-42.

[2] Gadalla, A.; Bower, B. *Chem. Eng. Sci.***1988**, *43*, 3049-3062.

[3] Kathiraser, Y.; Ni, J.; Oemar, U.; Saw, E.T.; Kawi, S. Mechanistic and kinetic aspects for CO_2 reforming of methane over Ni based catalysts, *Submitted to Ind. Eng. Chem. Res.*

[4] Osaki, T.; Masuda, H.; Mori, T. *Catal. Lett.* **1994**, *29*, 33.

[5] Mark, M.F.; Mark, F.; Maier, W.F. *Chem. Eng. Technol.* **1997**, *20*¸361.

[6] Akpan, E.; Sun, Y.; Kumar, P.; Ibrahim, H.; Aboudheir, A. Idem, R. *Chem. Eng. Sci.* **2007**, *62*, 4012.

[7] Richardson, J.T.; Paripatyadar, S.A. *Appl. Catal.* **1990**, *61*, 293.

[8] Bodrov, I.M.; Apel'baum, L.O. *Kinet. Catal.* **1967**, *8*, 379.

[9] Xu, J.; Froment, G.F. *AIChE J.* **1989**, *35*, 88.

[10] Zhang, Z.L.; Verykios, X.E. *Catal. Today*, **1994**, *21*, 589.

[11] Rostrup-Nielsen, J.R. *Adv. Catal.* **2004**, *47*, 65.

[12] Luntz, A.C.; Harris, J. *Surf. Sci.* **1991**, *258*, 397.

[13] Kuijpers, E.G.M.; Breedijk, A.K.; van der Wal, V.J.J.; Geus, J.W. *J. Catal.* **1983**, *81*, 429.

[14] Wang, H.Y.; Au, C.T. *Catal. Lett.* **1996**, *38*, 77.

[15] Wei, J.; Iglesia, E. *J. Catal.* **2004**, *224*, 370.

[16] Li, C.; Yan, W.; Xin, Q. *Catal. Lett.* **1994**, *24*, 249.

[17] Osaki, T.; Horiuchi, T.; Suzuki, K.; Mori, T. *Appl. Catal. A: Gen.* **1997**, *155*, 229.

[18] Kroll, V.C.H.; Tjatjopoulos, G.J.; Mirodatos, C. *Stud. Surf. Sci. Catal.* **1998**, *119*, 753.

[19] Schuurman, Y.; Kroll, V.C.H.; Aparicio, P.F.; Mirodatos, C. *Catal. Today*, **1997**, *38*, 129.

[20] Wang, S.B.; Lu, G.Q.; Millar, G.J. *Energ. Fuel* **1996**, *10*, 896.

[21] Gibson, D.H. *Chem. Rev.* **1996**, *96*, 2063-2096.

[22] Zhang, J.; Wang, H.; Dalai, A.K. *Ind. Eng. Chem. Res.* **2009**, *48*, 677.

[23] Bradford, M.C.J.; Vannice, M.A. *Appl. Catal. A:Gen.* **1996**, *142*, 97.

[24] Horiuchi, T.; Sakuna, T.; Fukui, T.; Kubo, Y.; Osaki, T.; Mori, T. *Appl. Catal. A:Gen.* **1996**, *144*, 111.

[25] Nandini, A.; Pant, K.K.; Dhingra, S.C. *Appl. Catal. A:Gen.* **2006**, *308*, 119.

[26] Luo, J.Z.; Yu, Z.L.; Ng, C.F.; Au, C.T. *J. Catal.* **2000**, *194*, 198.

[27] Cui, Y.; Zhang, H.; Xu, H.; Li, W. *Appl. Catal. A:Gen.* **2007**, *331*, 60.

[28] Luo, J.Z.; Yu, Z.L.; Ng, C.F.; Au, C.T. *J. Catal.* **2000**, *194*, 198-210.

[29] Fierro, J.L.G. *Catal. Today* **1990**, *8*, 153-174.

[30] Rostrup-Nielsen, J.R. *Aspects of CO_2 Reforming of Methane*, In: Curry-Hyde, J.E.; Howe, R.F., Editor. Natural Gas Conversion II. Lausanne, Switzerland: *Elsevier Science B.V.* **1994,** 25-42.

[31] Fan, M.S.; Abdullah, A.Z.; Bhatia, S. *ChemCatChem.* **2009**, *1*, 192-208.

[32] Delmon, B. *J. Therm. Anal. Calori.* **2007**, *90*, 49-65.

[33] Xie, Y.; Tan, Y. *Adv. Catal.***1990**, *37*, 1-43.

[34] Ruckenstein, E.; Hu, Y.H. *J. Catal.* **1996**, *162*, 230-238.

[35] Sahli, N.; Petit, C.; Roger, A.C.; Kiennemann, A.; Libs, S.; Bettahar, M.M. *Catal. Today* **2006**, *113*, 187-193.

[36] Corthals, S.; Van Nederkassel, J.; Geboers, J.; De Winne, H.; Van Noyen, J.; Moens, B.; Sels, B.; Jacobs, P. *Catal. Today* **2008**, *138*, 28-32.

[37] Chen, Y.G.; Ren, J. *Catal. Lett.***1994**, *29*, 39-48.

[38] Wang, S.; Lu, G.Q. *Appl. Catal. B: Environ.* **1998**, *19*, 267-277.

[39] Bhattacharyya, A.; Chang, V.W. *Stud. Surf. Sci. Catal.* **1994**, *88*, 207-213.

[40] Xu, G.; Shi, K.; Gao, Y.; Xu, H.; Wei, Y. *J. Mol. Catal. A: Chem.* **1999**, *147*, 47-54.

[41] Subramaniam, M.; Chattha, M.; Peters, C.J. *J. Mol. Catal.* **1991**, *69*, 235-245.

[42] Barroso-Quiroga, M.M.; Castro-Luna, A.E. *Int. J. Hyd. Energ.* **2010**, *35*, 6052-6056.

[43] Tang, S.; Ji, L.; Lin, J.; Zeng, H.C.; Tan, K.L., Li, K. *J. Catal.* **2000**, *194*, 424-430.

[44] Shang, R.; Guo, X.; Mu, S.; Wang, Y.; Jin, G.; Kosslick, H.; Schulz, A.; Guo, X.Y. *Int. J. Hyd. Energ.* **2011**, *36*, 4900-4907.

[45] Luna, A.E.C.; Iriarte, M.E. *Appl. Catal. A:Gen.* **2008**, *343*, 10-15.

[46] Lemonidou, A.A.; Vasalos, I.A. *Appl. Catal. A:Gen.* **2002**, *228*, 227-235.

[47] Nandini, A.; Pant, K.K.; Dhingra, S.C. *Appl. Catal. A:Gen.* **2006**, *308*, 119-127.

[48] Xiancai, A.; Wu, M.; Lai, Z.; He, F. *Appl. Catal. A:Gen.* **2005**, *290*, 81-86.

[49] Juan-Juan, Román-Martínez, M.C.; Illán-Gómez. M.J. *Appl. Catal. A:Gen.* **2004**, *264*, 169-174.

[50] Xu, J.; Zhou, W.; Wang, J.; Li, Z.; Ma, J. *Chin. J. Catal.* **2009**, *30*, 1076-1084.

[51] Hou, Z.; Yokota, O.; Tanaka, T.; Yashima, T. *Appl. Catal. A:Gen.* **2003**, *253*, 381-387.

[52] Sun, N.; Wen, X.; Wang, F.; Peng, W.; Zhao, N.; Xiao, F.; Wei, W.; Suna, Y.; Kang, J. *Appl. Surf. Sci.* **2011**, *257*, 9169-9176.

[53] Martinez, R.; Romero, E.; Guimon, C.; Bilbao, R. *Appl. Catal. A:Gen.* **2004**, *274*, 139-149.

[54] Guo, J.; Lou, H.; Zhao, H.; Chai, D.; Zheng, X. *Appl. Catal. A:Gen.* **2004**, *273*, 75-82.

[55] Kim, J.H.; Suh, D.J.; Park, T.J.; Kim, K.L. *Appl. Catal. A:Gen.* **2000**, 197, 191-200.

[56] Sutthiumporn, K.; Kawi, S.; *Int. J. Hyd. Energ.***2011**, *36*, 14435-14446.

[57] Ni, J.; Chen, L.; Lin, J.; Kawi, S. *Nano Energy*, **2012**, *1*, 674-686.

[58] Mizuhara, Y.; Miyasita, Y.; Fujita, T.; Ishihara, T.; Takita, Y. *Preprint of Spring Annual Meeting of Chem. Soc. Jpn.* **1992,** 3C441.

[59] Yamazaki, O.; Nozaki, T.; Omata, K.; Fujimoto, K. *Chem. Lett.* **1992**, *21*, 1953-1954.

[60] Pan, Y.X.; Kuai, P.; Liu, Y.; Ge, Q.; Liu, C.J. *Energ. Environ. Sci.* **2010**, *3*, 1322.

[61] Fan, M.S.; Abdullah, A.Z.; Bhatia, S. *Appl. Catal. B:Environ.* **2010**, *100*, 365.

[62] Oemar, U.; Hidajat, K.; Kawi, S. *Appl. Catal. A: Gen.* **2011**, *402*, 176.

[63] Valderrama, G.; Goldwasser, M.R.; de Navarro, C.U.; Tatibouet, J.M.; Barrault, J.; Dupeyrat, C.B.; Martinez, F. *Catal. Today* **2005**, *107-108*, 785.

[64] Sutthiumporn, K.; Maneerung, T.; Kathiraser, Y.; Kawi, S. *Int. J. Hydrogen Energy* **2012**, *37*, 11195-11207.

[65] Hou, Z.; Yokota, O.; Tanaka, T.; Yashima, T. *Appl. Catal. A: Gen.* **2003**, *253*, 381.

[66] Guo, J.; Lou, H.; Zhao, H.; Chai, D.; Zheng, X. *Appl. Catal. A: Gen.* **2004**, *273*, 75.

[67] Oemar, U.; Hidajat, K.; Kawi, S. *Submitted to Appl. Catal. B: Environ.*

[68] Lødeng, R; Bjørgum, E.; Enger, B.C.; Eilertsen, J.S.; Holmen, A.; Krogh, B.; Rønnekleiv, M.; Rytter, E. *Appl. Catal. A: Gen.* **2007**, 333, 11-23.

[69] York, A.P.E.; Xiao, T.; Green, M.L.H. *Top. Catal.* **2003**, 22, 345-358.

[70] Choudhary, V.R.; Mammon, A.S.; Sansare, S.D. *Angew. Chem. Int. Ed. Engl*. **1992,** *31*, 1189-1190.

[71] He, S.; Wu, H.; Yu, W.; Mo, L.; Lou, H.; Zheng, X. *Int. J. Hyd. Energ.* **2009**, *34*, 839–843.

[72] Ambrosini, A., Garino, T., Nenoff, T.M. *Solid State Ionics* **2006**, *177*, 2275–2279.

[73] Yang, N.T.; Kathiraser, Y.; Kawi, S. *Int. J. Hyd. Energ.* **2013**, *38 (11)*, 4483-4491.

CHAPTER 3

Literature Review on MIEC Membranes and Integrated Membrane Reactors

3.1. Ceramic membranes for oxygen production from air

3.1.1. Concept of Mixed ionic-electronic conducting (MIEC) ceramic membranes

Presently at industries, oxygen production is mainly by cryogenic distillation of air. This is a very energy and cost intensive process. Alternatively, pressure swing adsorption is used where nitrogen from compressed air at high pressure is preferentially adsorbed on materials such as activated carbon. After removal of the oxygen-enriched air, the pressure is reduced to desorb nitrogen. Pressure swing adsorption is more economical at a smaller scale but it has the disadvantage of being a batch process.

Ceramic membranes have been intensely researched in recent years to provide an economical alternative to current methods of oxygen production [1]. Dense mixed-ionic and electronic conducting membranes are capable in performing oxygen separation, where an oxygen partial pressure across the membrane is created for permeation and oxygen transport occurs via hopping ions to neighboring vacant site in the crystal lattice [2]. At high temperatures, oxygen molecules on the high oxygen pressure side are adsorbed on the membrane surface and dissociated into oxygen ions, which further migrate through the bulk to the opposite membrane side, where they are recombined with electrons to form oxygen molecules [2]. Oxygen ions must possess sufficient thermal energy to overcome the energy barrier when they hop from one crystallographic site to another. As oxygen ions are transported across the membrane, counter-transport of electrons is necessary to maintain charge neutrality. This oxygen transport mechanism is as shown in Figure 3-1.

The formation of oxygen vacancies can be representing using the Kroger-Vink notation [3]:

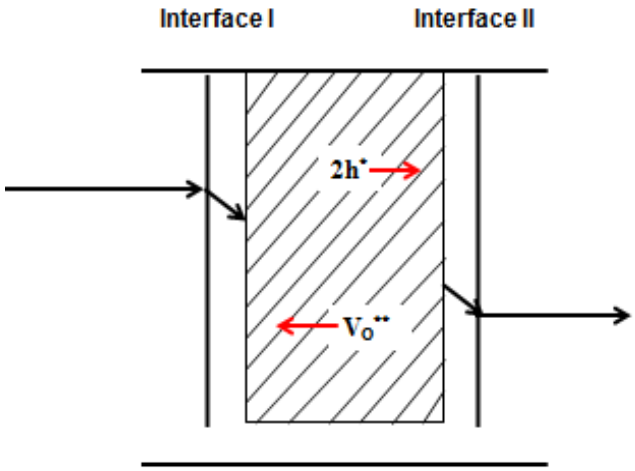

Figure 3-1 Oxygen transport mechanism

$$\frac{1}{2}O_2 + V_O^{\cdot\cdot} \overset{k_f}{\rightarrow} O_O^x + 2h^* \quad ; \quad O_O^x + 2h^* \overset{k_r}{\rightarrow} \frac{1}{2}O_2 + V_O^{\cdot\cdot} \qquad (3\text{-}1)$$

where $V_o^{``}$ represents oxygen vacancy, O_o^x for lattice oxygen and h^* for electron hole.

Based on the notation above on the formation of oxygen vacancies, oxygen is transported via the hopping of oxygen ions via thermal activation to neighboring vacant site in the crystal lattice when an oxygen partial pressure across the membrane is present. This process is accompanied by a counter flux of electrons or electron holes. In addition, besides bulk transport, oxygen transport occurs across the interface between the perovskite and the gas phase [4]. Moreover, it requires neither external electrical circuitry nor electrodes to operate. Therefore this dense mixed ionic and electronic conducting (MIEC) membrane is more practical and economical for use in a membrane reactor. Generally, MIEC oxygen-permeating membranes are usually dense structures that exhibit perovskite

crystal structure with 100% selectivity to oxygen [3]. This is a significant advantage in terms of technical and safety point of view for industrial realization.

3.1.1.1. Perovskite

Figure 3-2 and Figure 3-3 illustrates the ideal perovskite structure, with the general formula of ABO_3. This symmetric lattice compound has a cubic crystal structure. A-site metal ions are located at the corners of the cube, B-site metal ions are in the center and the oxygen atoms are situated in faces' centers. As the B-site ions are enclosed in O_6 octahedral, they can be represented as BO_6. Perovskite stability requires the presence of a BO_3 skeletal subunit and taking into account geometry, B-site cations must possess a radius greater than 0.051 nm to achieve octahedral coordination [5]. The BO_3 subunit can become distorted by A-site cation and under conditions of high distortion, orthorhombic or rhombohedra lattice geometries can occur [5].

To determine whether perovskite structure has been preserved, Goldschmidt tolerance factor is employed:

$$t = \frac{R_A + R_o}{\sqrt{2}(R_B + R_o)} \tag{3-2}$$

where R_A, R_B and R_o are the respective ionic radii of the lattice constituents.

Geometrically, the ratio of the bond length of A–O bond and the bond length of B–O bond is $\sqrt{2}$: 1 for an ideal perovskite [6]. The ideal cubic structure has a tolerance factor of 1 and perovskite stability requires $0.75 < t < 1$. To ensure stable twelvefold coordination for A-site lattice, A-site cation must possess a radius greater than 0.09 nm. In principle, higher oxygen permeation flux is favored by a cubic structure as in proceeding from cubic

to orthorhombic structure, the number of crystallographically equivalent sites, which favors ionic transport, decreases [5].

A summary of conditions required for fast ion conductivity in perovskite materials include the following [7] High concentration of mobile charge carriers (i.e. O^{2-})

- Sufficient crystallographic sites for the charge carriers, i.e. high oxygen vacancy concentration
- Low mean value of metal-oxygen bonding energy of perovskite oxide
- An open structure which can facilitate oxygen ion mobility (i.e. high lattice free volume)
- Critical cation saddle point for greater O^{2-} migration.

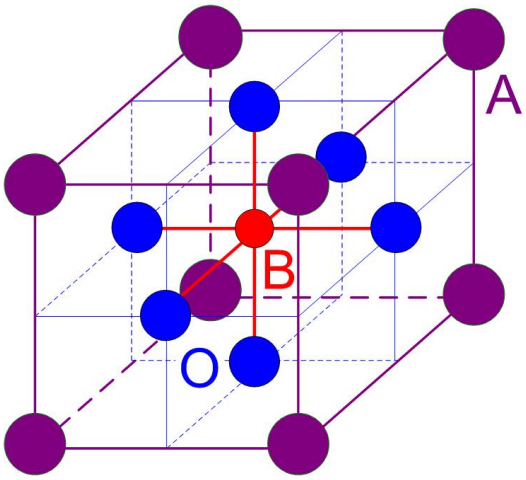

Figure 3-2 The unit cell view of the ideal perovskite structure [8]

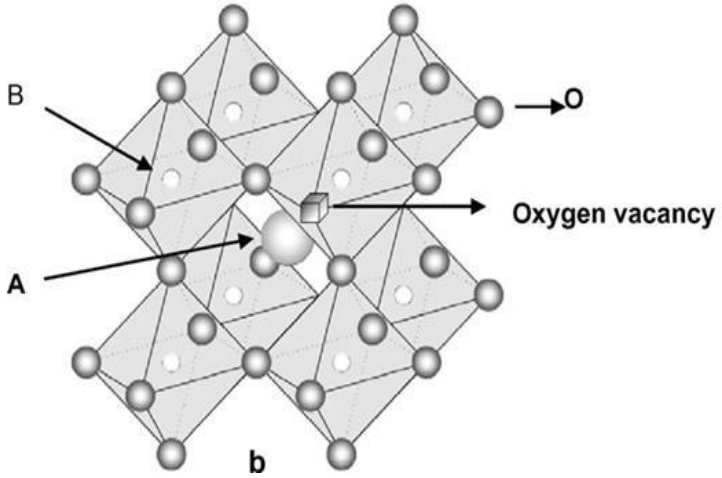

Figure 3-3 Overview of the ideal perovskite structure [8]

Perovskites are non-stoichiometric oxides. When A- and/or B-site metal ions are doped with ions of different charges, oxygen vacancies are created for charge neutralization. The deficiency of oxygen caused by an excess of metals thus, bring about oxygen transport across the membrane structure. As a counter-transport of electrons is required to maintain charge neutrality, the perovskite structure has to exhibit both ionic and electronic conductivity. As the conductivity of a perovskite material depends upon the products of their defect component concentration, charge and mobility, the relative concentration of ionic defects, electrons and electron holes is altered at different oxygen partial pressures and temperatures [3]. Hence, the effectiveness of the membrane in performing oxygen separation is highly dependent on the experimentally-chosen temperature and partial pressures.

3.1.1.2. Solid defect theory

According to the second law of thermodynamics, defects will be present in solid compounds unless at absolute zero condition. These defects are mainly caused by the

entropy effect and impurities present in the compound. The entropy effect is where the presence of defects will cause an increase in entropy and result in the compound having a minimal Gibbs free energy [3].

In general, defects can be classified as electronic effects and structural defects. Electronic defects are attributed to the intrinsic ionization or excitation of electrons from valence to conduction bands or their formation to fulfill the electric neutrality criteria [3]. For instance, at high temperature, when the transition metal, such as Fe2+, gain sufficient energy, it will transit to Fe3+ resulting to an electronic defect. As for structural defects, it can be further classified into one dimensional defect, two dimensional defect and three dimensional defect, namely point defects, line defects and plane defect respectively. However, the main defect that contributes to the migration oxygen anions across a perovskite compound is point defect.

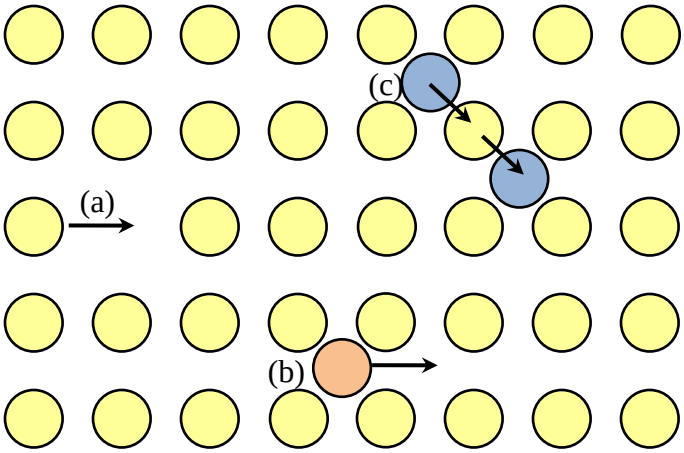

Figure 3-4 Illustrations of various lattice diffusion mechanisms via (a) vacancies (b) interstitials and (c) lattice diffusions [3]

Point defects are changes which occur at atomic level and involve only a single lattice and its immediate vicinity [3, 5]. With reference to Figure 3-4, there are generally

three types of common point defects, (a) the formation of empty regular atoms or ions sites (vacancies), (b) the creation of atoms or ions in the interstices between regular atom sites (interstitials) and (c) presence of foreign atoms which will push neighboring atoms, where lattice diffusions of ionic compounds will occur inside the perovskite crystals.

Figure 3-5 shows two popular point defect, (a) Frenkel disorder and (b) Schottky disorder. Frenkel disorder occurs when a vacancy is formed due to atoms or ions leaving its regular site and become interstitial atoms or ions; whereas Schottky disorder occurs when there is an equal number of a cation and anion vacancy [3].

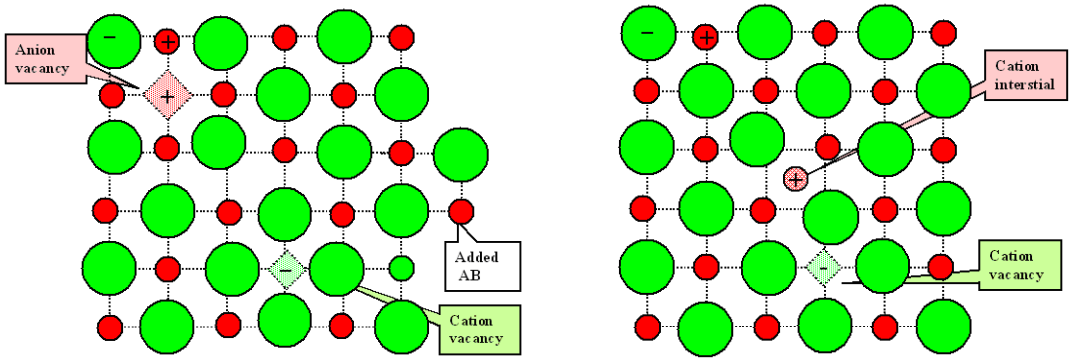

a) b)

Figure 3-5 Illustrations of two important point defect in oxides (a) Frenkel disorder and (b) Schottky disorder [8]

3.1.2. Oxygen transport through MIEC membranes

An oxygen partial pressure is required as the driving force for oxygen separation. Oxygen transport occurs from the high to low oxygen chemical potential side and is accompanied by a counter-transport of electrons. The rate of oxygen permeation can be bulk-diffusion limited or surface-exchange limited, as illustrated in Figure 3-6.

Higher oxygen fluxes are obtained when either or both ionic conductivity are increased. At afixed total conductivity, the flux is maximum when ionic and electronic transference numbers are equal, i.e. 0.5. Hence, it is important to maximise the product of mobility and concentration of ionic and electronic charge carriers in the appropriate ranges of temperature and oxygen partial pressures for the required application [9].

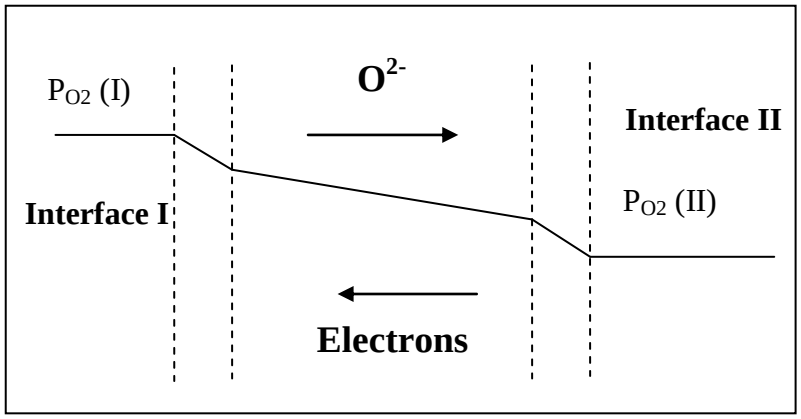

Figure 3-6 Overview of the oxygen permeation process

The oxygen flux is dependent on the perovskite crystal defects and the oxygen partial pressure across a dense perovskite-based MIEC membrane that will directly affect and will be limiting the transport mechanism. With reference to Figure 3-6, the oxygen transport through the membrane will involve and can be limited by the following three progressive steps [10]:

(1) The surface-exchange reaction on Interface I

(2) The simultaneous bulk-diffusion of O2- ions and electron/electron holes in the bulk phase

(3) The surface-exchange reaction on Interface II

To allow separation of oxygen from the feed side to the permeate side as shown in Figure 3-6, the oxygen molecules are first disassociated on the membrane surface to form

O^{2-} ions after which they migrate through the membrane via oxygen vacancy defect sites [11]. The occurrence of these oxygen vacancy defect sites arises from the partial substitution of the metal cations (B of the ABO_3) with other cations with lower valencies. Equilibration of the perovskite oxide at reduced oxygen partial pressure can also result in vacancies [12]. Oxygen molecules cannot diffuse through directly as the membrane is too tight and dense. The flux of the oxygen ions is compensated by the simultaneous flux of electrons in the opposite direction. When the O^{2-} ions reaches the permeate side, they will release their electrons and combine to form back oxygen molecules.

Thus MIEC membranes are suitable for oxygen separation as they are able to conduct both ions and electrons without the use of electrodes. The ability to conduct ions is due to the disordering of the oxygen vacancies which occurs only at a high temperature [12]. However, it requires a driving force, i.e. an oxygen partial pressure gradient on both sides of the membranes [13].

Oxygen transport is also affected by microstructure such as grain boundary diffusion and order-disorder phenomena, roughness or porosity of the membrane surface. However, these influences depend on characteristic of the measured sample (preparation method, grain size, etc) as well as the experimental conditions employed (temperatue, sweep gas, partial pressure of oxygen gradient across the membrane).

3.1.2.1. Bulk-diffusion limited

The Wagner theory [14] is used to describe oxygen flux in relatively thick membrane, where the diffusion process is limited by bulk-diffusion. The equations are derived by assuming the existence of local equilibrium between two charged species.

$$J_{O_2} = \frac{1}{4^2 F^2 L} \int_{\mu_{O_2(II)}}^{\mu_{O_2(I)}} t_i t_e \sigma_t \ d\mu_{O_2}$$

$$t_i = \frac{\sigma_i}{\sigma_i + \sigma_e} = \frac{\sigma_i}{\sigma_t} \qquad (3\text{-}3)$$

where J_{O2} is the oxygen flux; F is the Faraday constant; L is the membrane thickness; t_i and t_e are the ionic and electronic transfer numbers and $\sigma_{i,}$ σ_e and σ_t are the ionic, electronic and overall conductivity.

Equation 3-3 shows the inverse relation between oxygen flux and membrane thickness. Thus, in fabricating the hollow fiber for oxygen separation, the fiber is made thin to minimize bulk resistance.

3.1.2.2. Surface-exchange diffusion limited

When membrane thickness is reduced, surface-exchange reaction becomes the limiting factor in oxygen flux movement. Hence, the Wagner theory discussed above does not apply. Surface-exchange reactions are expected to be composed of sequential steps such as adsorption from gas phase, charge transfer reaction between adsorbed species and the bulk [15]. Wagner's equation is valid only when bulk transport is the limiting factor for diffusion of oxygen across the membrane. However, surface processes might have an influence over the rate of oxygen permeation. The gradient in O_2 chemical potential will be partially consumed by surface exchange kinetics at the interfacial zones of the membrane and partially by bulk diffusion in middle zone [16]. If the membrane is sufficiently thick, bulk diffusion is generally the rate determining step. When the thickness

of the membrane is decreased, mixed control will be dominating. On the other hand, for ultrathin membranes, surface exchange reactions will control the process.

Using the Nernst equation, the apparent potential η is related to the partial pressure drop across the membrane [17].

$$\eta = \frac{RT}{4F} \ln[(P'_{O_2}) / (P''_{O_2})] \tag{3-4}$$

where P'_{O_2} and P''_{O_2} refer to the oxygen partial pressure on each side of the membrane, R is the gas constant, T is the temperature and F is Faraday's constant.

For surface-exchange diffusion limited membranes, the membrane resistance is described as the resistance of the surface of the membrane as a result of oxygen exchange process. Hence, using an analogy of an equivalent electrode resistance, R_E is assigned equally to both high and low pressure surfaces [17]. The ionic current density, J_{O2-} through the membrane thickness, L, and ionic conductivity, σ, can be expressed as follows:

$$J_{O^{2-}} = \frac{\eta}{2R_E} = \frac{\eta}{\frac{2D}{\sigma k}} \tag{3-5}$$

The latter expression follows from an expansion of R_E in terms of surface exchange coefficient, k, and diffusion coefficient, D [17].

3.1.3. Membrane configuration

Membrane separation processes may involve different membrane configurations such as tubular, hollow fiber or disk shaperd. Besides increase in operating temperature and an increase in the differential pressure, the geometry of the membrane systems is another factor for increasing O_2 permeation as it can affect the surface area of the

membranes [18]. The larger the surface area of the ceramic membranes, the more easily the oxygen ions can penetrate the ceramic membranes.

Tubular membrane is a tube in shell design where the membrane is commonly found on the inside of tube. Although there is good control of feed stream flow, tubular membrane possesses low membrane area to volume ratio and therefore, it has high hold up volume and requires large space. In most studies [19], disc-shaped membranes are utilized as they can be easily fabricated using conventional static-pressing method. Several sheets of membrane can be stacked onto each over for large scale air separation process. However, problems such as pressure resistance and high temperature sealing are faced and these discourage their usage [20].

Recently, hollow fiber ceramic membranes are gaining industrial importance. These fibers are prepared by phase inversion spinning or sintering method. In hollow fiber membranes, air can enter either in lumen or shell side. The advantages of hollow fiber membranes include its larger area to volume ratio compared to disk or tubular membranes, it high packing density and low energy operating costs as well as high temperature facile sealing. Therefore, higher flux deliverance of these perovskite hollow fibre membranes brings the process to one a step closer toward large scale applications [21, 22].

3.1.3.1. Hollow fiber membrane fabrication via phase inversion method

Phase inversion process is an important means to prepare asymmetric hollow-fiber membranes as shown in Figure 3-7. Even though it is commonly used to prepare polymeric hollow-fiber membranes, the process can be modified to prepare inorganic hollow-fiber precursors. The formation of asymmetric hollow fiber membranes consists of

seven important steps: (1) dope preparation, (2) degas, (3) metering, (4) spinning, (5) evaporation (in the air gap region), (6) coagulation, and (7) solvent exchange [23].

If liquids are used as bore fluids, the internal coagulation process starts immediately after the extrusion from a spinneret, and the fiber goes through the external coagulation. Usually water is the preferred external coagulant because of its low cost and being environmental friendly. The proper choice of the internal coagulant is, therefore, becoming very important because the rate of demixing (i.e. phase separation) and the resultant inner skin morphology strongly depends on the chemistry and composition of the internal coagulant [23]. The molecular sizes and solubility parameters of solvents, internal and external coagulants play an important role on membrane morphology. With proper control over the parameters in the phase inversion process, hollow fiber membranes can be fabricated with minimal defects [24].

Subsequently, the fiber precursors are heated to remove the polymer and sintered to a porous or dense structure. Compared to other methods, such as dry spinning, or wet spinning, a system of inorganic material and binder, depositing fibers from the gas phase to a substrate, pyrolyzing the polymers etc., the combined phase inversion and sintering technique is simple and requires no expensive equipment.

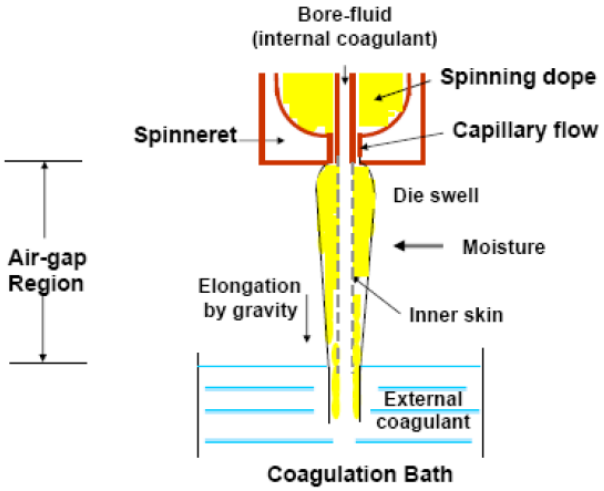

Figure 3-7 A schematic diagram for spinning single layer hollow fiber setup [23]

More important, because the cross section of the hollow-fiber membranes prepared by phase inversion is asymmetric (that is, a thin dense layer integrated with a porous substrate) the resistance to oxygen permeation is thus lowered [25**].** Such a highly asymmetric structure is more favourable for oxygen permeation than the sandwiched structure since it not only has lower diffusion resistance to oxygen ions from the single dense layer but also possesses a larger surface area for oxygen exchange reactions [26].

3.1.4. Development of MIEC perovskite materials for catalytic membrane reactors

Since the pioneering efforts by Teraoka et al. [27] to develop the $La_{1-x}A_xCo_{1-y}Fe_yO_{3-\delta}$ materials for oxygen permeation, much research effort in this area has been intensified for the past nearly three decades. Teraoka et al. [27] partially doped Sr^{2+} on the La^{3+} to yield a solid solution with the general formula $La_{1-x}Sr_xCo_{1-y}Fe_yO_{3-\delta}$ (x=0-1, y=0-1), where d denotes the average number of vacant oxygen sites per unit cell. δ is called the level of nonstoichiometry. In this class of materials the charge compensation mechanism

due to introduction of aliovalent Sr-cations involves creation of oxygen vacancies which lead to oxidation of a fraction of Co^{3+} to Co^{4+} which leads to high concentrations of mobile ionic and electronic charge carriers at elevated temperatures (>700°C) [28]. It was shown that the oxygen semipermeability increased with increasing strontium content. Apart from fast oxygen diffusion in the bulk of the material, perovskite oxides also exhibit significant rate of oxygen exchange with its surrounding [29].

For instance, incorporation of Sr^{2+} in a $LaCoO_3$ host lattice can be represented in Kröger-Vink notation as follows:

$$SrCoO_3 \xrightarrow{LaCoO_3} Sr'_{La} + Co'_{Co} + 3O^x_O \qquad (3\text{-}6)$$

Charge compensation occurs through an increase in net valency of transition metal at the B-site. Equation 3-6 represents the one of the possible charge compensation mechanisms. The second mechanism involves the formation of oxygen vacancies [13].

$$2Co'_{Co} + \frac{1}{2}O^x_O \leftrightarrow Co^x_{Co} + V^{"}_O + 3O^x_O \qquad (3\text{-}7)$$

The mechanism of charge compensation which occurs depends on temperature and oxygen partial pressure [13].

Since Teraoka's pioneering work, many further studies have taken place to find improved materials. Cobalt-rich compounds with high concentrations of aliovalent dopants can combine high oxygen semipermeability and have reasonable chemical stability. However, no materials have reached potential for industrial application, due to the twin requirements of high permeation and good stability. In any case, the doped lanthanum cobaltite family, $La_{0.6}Sr_{0.4}Co_{0.2}Fe_{0.8}O_{3-\delta}$ still gains attention since it is mechanically strong.

In terms of materials studied to substitute cobalt, such as $La_{1-x}Sr_xFeO_{3-\delta}$ (x=0.1, 0.2) [30] $La_{1-x}Ca_xCrO_{3-\delta}$ [31], they generally display significantly lower oxygen permeation fluxes, than those containing Co.

Recently, gallium, niobium, molybdenum and tantalum have been used as hot B-site substitution cations for developments of high performance perovskite materials for catalytic membrane reactors. In fact, gallium is fixed valence state element, and exhibit high ionic conductivity but low electronic conductivity, low thermal expansion rates and good resistance to CO_2, making them potential candidates for catalytic membrane reactors [32]. Studies on $La_{1-x}Sr_xFe_{1-y}Ga_yO_{3-\delta}$ ($x \geq 0.40$; $y \leq 0.60$) [33] showed that with increasing Sr concentration, Ga solubility decreased. The maximum solid solubility of Ga cations at x=0.70 was about 0.31 (y = 0.31). When the concentration of Sr was higher than this maximum value, segregated phase of $SrLaGa_3O_7$ was observed. Thus, doping with gallium resulted in an increase of unit cell volume and decrease of thermal expansion as well as total conductivity of $La_{1-x}Sr_xFe_{1-y}Ga_yO_{3-\delta}$. Therefore, these results demonstrate that upto an increase of Sr=0.7, the oxygen ionic conductivity of $La_{1-x}Sr_xFe_{1-y}Ga_yO_{3-\delta}$ is positive and further increase leads to deterioration of conductivity performance.

Shao et al. [34] developed $Ba_{0.5}Sr_{0.5}Co_{0.8}Fe_{0.2}O_{3-\delta}$ (BSCF) by substituting the Sr at A-site with Ba and found that besides improving structural stability, oxygen permeability was also modified. However, this material is not stable at the medium temperature due to low valence stability of cobalt, and suffers in structural deterioration to a cobalt rich hexagonal $Ba_{0.5\pm0.1}Sr_{0.5\pm0.1}CoO_{3-\delta}$ phase, which are poor oxygen conductors [35].

Table 3-1 shows the performance summary of several MIEC membrane developed by researchers.

Table 3-1

Performance summary of MIEC perovskite for O_2 permeation

Perovskite	Shape	Thickness mm	Temperature (°C)	O_2 flux $mol \cdot cm^{-2} \cdot s^{-1}$	Note	Ref
$Ba_{0:5}Sr_{0:5}Co_{0:8}Fe_{0:2}O_{3-\delta}$	Disk	1.5	950	$1.17x10^{-6}$		33
$SrCo_{0.33}Fe_{0.67}O_{3-\delta}$	Disk	1.0	800-1000	$(0.89\sim2.06) \times10^{-6}$		36
$LaCo_{0.8}Cr_{0.2}O_{3-\delta}$	Disk	1.4	885	$(0.4\sim0.8)\times10^{-7}$		37
$LaFe_{1-x}Ni_xO_{3-\delta}$ (x=0.2-0.5)	Disk	1.0	800-1000	$(0.43\sim8.6) \times10^{-8}$		38
$LaCo_{0.7}Fe_{0.1}Ni_{0.2}O_{3-\delta}$	Disk	1.0	800-1000	$(1.68\sim3.20)\times10^{-9}$		39
$La_{0.8}Sr_{0.2}Co_{0.8}Fe_{0.2}O_{3-\delta}$	Disk	0.5	800-1000	$(2.5\sim8.3)\times10^{-7}$		40
$LaGa_{1-x}Ni_xO_{3-\delta}$(x=0.2-0.6)	Disk	1.0	800-1000	$(1.9\sim6.6)\times10^{-}$		2
$La_{0.8}Sr_{0.2}Ga_{0.6}Fe_{0.4}O_{3-\delta}$	Disk	0.5	800-1000	$(0.43\sim0.83)\times10^{-6}$		40
$Ba_{0.5}Sr_{0.5}Fe_{0.8}Cu_{0.2}O_{3-\delta}$	Disk	1.1	750	$4.24x10^{-7}$		41
$BaCo_{0.7}Fe_{0.2}Ta_{0.1}O_{3-\delta}$	HF		950	$3.2x10^{-6}$	U shaped -250h stability	42
$La_{0.6}Sr_{0.4}Co_{0.2}Fe_{0.8}O_{3-\delta}$	HF		1000	$1.6x10^{-6}$		43
$BaCo_xFe_yZr_{1-x-y}O_{3-\delta}$	HF		950	$2.8x10^{-6}$		44
$La_{0.6}Sr_{0.4}Co_{0.2}Fe_{0.8}O_{3-\alpha}$	HF		1000	$4.24x10^{-5}$	Packed as module of 7 membrane pieces-260h stability	45
$La_{0.6}Sr_{0.4}Co_{0.2}Fe_{0.8}O_{3-\delta}$	HF		850	$6.32x10^{-7}$	H_2SO_4 modification	46

Perovskite	Shape	Thickness mm	Temperature (°C)	O_2 flux $mol \cdot cm^{-2} \cdot s^{-1}$	Note	Ref
$La_{0.6}Sr_{0.4}Co_{0.2}Fe_{0.8}O_{3-\delta}$	HF		1050	$1.93x10^{-6}$	H_2SO_4 modification	46
$La_{0.6}Sr_{0.4}Co_{0.2}Fe_{0.8}O_{3-}$□	HF		950	$2.5x10^{-6}$	Honey comb structure for UT dense layer	47
$SrCo_{0.9}Nb_{0.1}O_{3-\alpha}$	HF		900	$3.8x10^{-6}$	Stability test 250h	48
$Ba_{0.5}Sr_{0.5}Co_{0.75}Zr_{0.05}Fe_{0.2}O_{3-\alpha}$	HF		700-950	$(0.35\text{-}3.07)x10^{-6}$		49
$Ba_{0.5}Sr_{0.5}Co_{0.7}Zr_{0.1}Fe_{0.2}O_{3-\alpha}$	HF		700-950	$(0.30\text{-}2.66)x10^{-6}$		49
$Ba_{0.5}Sr_{0.5}Co_{0.6}Zr_{0.2}Fe_{0.2}O_{3-\alpha}$	HF		700-950	$(0.20\text{-}2.44)x10^{-6}$		49
$La0.6Sr0.4Co0.2Fe0.8O_{3-\delta}$	HF		850-900	$(0.4\text{-}1.0)x10^{-7}$		50
$SrCo_{0.9}Nb_{0.1}O_{3-\delta}$	HF		900	$2.9x10^{-5}$		48
$Ba_{0.5}Sr_{0.5}Co_{0.8}Fe_{0.2}O_{3-\delta}$	HF		950	$3.5x10^{-6}$		51
$Ba_{0.5}Sr_{0.5}Co_{0.8}Fe_{0.2}O_{3-\delta}$	HF		950	$1.1x10^{-5}$	PEI binder and Pd surfaces modification	51
$Ba_{0.5}Sr_{0.5}Co_{0.8}Fe_{0.2}O_{3-\delta}$	HF		950	$1.3x10^{-6}$	One end dead	52
$La_{0.6}Sr_{0.4}Co_{0.2}Fe_{0.8}O_{3-\delta}$	HF		1000	$1.4x10^{-6}$	Ag modification	53
$Ba_{0.5}Sr_{0.5}Co_{0.8}Fe_{0.2}O_{3-\delta}$	HF		900	$2.5x10^{-6}$	Ag modification	54
$Ba_{0.5}Sr_{0.5}Co_{0.8}Fe_{0.2}O_{3-\delta}$	HF		700	$6.7x10^{-7}$	Ag modification	54
$La_{0.6}Sr_{0.4}Co_{0.2}Fe_{0.8}O_{3-\delta}$	HF		850	$1.5x10^{-7}$	Pd modification	55

3.1.5. POM in catalytic membrane reactors

Production of syngas via catalytic hydrocarbon conversion reactions such as partial oxidation of methane (POM) has been widely investigated since CH_4, the main component of natural gas is widely available. The mildly exothermic POM reaction has garnered much attention, as it is estimated to reduce costs to about 30% compared to the industrial steam reforming of methane [56]. The main difficulty for POM reaction, however, stems from the requirement of the costly cryogenic air separation process for purified oxygen supply, since N_2 presence in air is not tolerable for downstream processes [57]. In this context, integrated catalytic membrane reactor system for simultaneous production of oxygen for supply in the POM reaction holds much promise**.** This system is compact and hence minimizes extra cost incurred from additional unit operational requirements for the process. For reactions such as POM, it is necessary to use pure oxygen as the oxidant since it is difficult to separate nitrogen and methane in the downstream process. An additional advantage of the membrane reactor is that lattice oxygen may be more selective compared to molecular O_2 for partial oxidation reactions. It has been demonstrated for several oxidation reactions that electrochemically supplied O^{2-} showed better performance in improving selectivity and conversions compared to gas phase molecular O_2 [58].

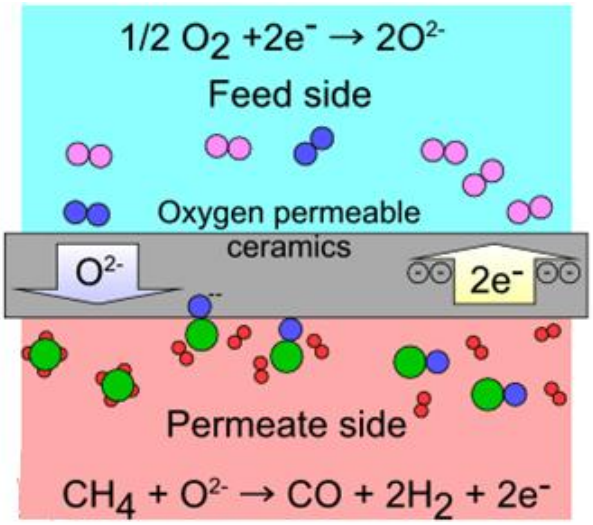

Figure 3-8 A schematic for MIEC membrane operation for POM reaction [59]

Based on the Figure 3-8, reduction of oxygen molecules into O^{2-} ions take place on the membrane surface (feed side) via surface exchange reaction, whereby the O^{2-} ions diffuse through the dense membrane and reacts with the feed gas of methane (permeate side) on the catalyst bed, forming the H_2:CO syngas product. Balachandran et al. [60] conducted investigation on $La_{0.2}Sr_{0.8}Co_{0.2}Fe_{0.8}O_{3-\delta}$ (LSCF) and $SrCo_{0.8}Fe_{0.2}O_{3-\delta}$ (SCF) tubular membranes and found that upon introduction of methane at 850°C, the membrane broke to several pieces. This is attributed to the stress induced by expansion inside the membrane surface which is exposed to the methane gas, and the inability of the membrane to replenish the oxygen sufficiently. The SCF membrane exhibits considerable flux under air/He environment. However, upon exposure to syngas, two types of cracks occur. The first occurred when the reaction just started and the membrane broke into several pieces. The second type of crack occurred days after reaction, where a large crack was formed parallel to the tube axis. Therefore, they attributed the first type of crack as a consequence

of oxygen gradient in membrane from reaction to air side, and the second type of fracture was a result of chemical decomposition [60].

It was also found by Hendriksen and co-workers that the perovskite structure might be disrupted at an oxygen partial pressure of as high as 10^{-8} atm [62]. For reactions such as syngas production, the oxygen partial pressure can be about as low as 10^{-19} atm and cobalt ion is intrinsically unstable under such reducing atmostphere. Thus, cobalt ions maybe reduced to metal and cause the perovskite MIEC membrane to undergo phase change; hence affecting the membrane's oxygen permeability [60]. Secondly, cobalt-based perovskite compound usually have high thermal expansion coefficient [63]. This will induce higher stress on the internal structure of the membrane if exposed to asymmetric atmosphere [64]. However, from several literatures, it was found that cobalt-based perovskite compound give high oxygen permeation fluxes when compared to similar perovskite compounds without cobalt [34]. In addition, under controlled and stringent partial oxygen pressure condition, cobalt-based perovskite MIEC membranes are able to operate with comparable stability. For example, Dong et al. [65] successfully conducted POM reaction for more than 500h in a BSCF membrane reactor. The membrane stability was attributed to facile kinetics of phase changes in the material which prevent membrane fracture. Tsai et al. [66] successfully conducted long-term POM experiments using $La_{0.2}Sr_{0.8}Co_{0.2}Fe_{0.8}O_{3-\delta}$ to generate syngas at 850°C for 850 h despite post-reaction analysis revealing some morphological and compositional changes on the membrane surface. Therefore, cobalt-based perovskite MIEC membranes are still attracting attention and widely researched.

3.1.6. Stability of MIEC membranes under CO_2 atmosphere

Global escalating CO_2 emission has recently captured world-wide attention in view of the global warming phenomenon. Hence, CO_2 capture and storage as well as utilization are gaining prominence to battle this issue. The role of oxygen membranes in this aspect include for use in oxy-fuel combustion [32] as well as oxidative CO_2 reforming of methane [67]. The main concern regarding CO_2 presence is its susceptibility for carbonate formation on the membrane surfaces hence leading to performance deterioration.

However, in recent years, remarkable improvements have been made with regards to membrane stability in either syngas or CO_2 environments. Table 3-2 compiles features of several MIEC membrane under CO_2 and syngas environments.

Table 3-2

Performance summary of MIEC perovskite under corrosive/reductive environments

Perovskite	Shape	Thickness mm	Temperature (ºC)	O_2 flux $mol \cdot cm^{-2} \cdot s^{-1}$	Atmosphere	Note	Ref
$La_{0.6}Sr_{0.4}Co_{0.8}Fe_{0.2}O_{3-\delta}$	HF		950	$6.8x10^{-7}$	100%CO_2	Only 1.4micron layer erosion observed - 100 hr of CO_2 exposure	68
$BaCo_xFe_yZr_zO3_{3-\delta}$	HF		800-900	$2.23x10^{-6}$-$1.67x10^{-6}$	10%CO_2/He	Decrease to negligible in 30 mins	69
$BaCo_xFe_yZr_zO3_{3-\delta}$	HF		800	-	50%CO_2/He	Impairment of perovskite structure to a depth of 30μm after 10 h exposure	
$Sr(Co_{0.8}Fe_{0.2})_{0.8}Ti_{0.2}O_{3-\delta}$	HF		950	$1.4x10^{-6}$ to $1x10^{-6}$ (at 400h)	100% CO_2	Flux stabilize to *ca*. $1x10^{-6}$ from 100-400h	70
$SrFe_{0.8}Nb_{0.2}O_{3-\delta}$	Disk	1.0	900	$2x10^{-7}$	100%CO_2	Stable for 200h	71
$BaCo_{0.4}Fe_{0.4}Nb_{0.2}O_{3-\delta}$	Disk	1.0	800-900	$5x10^{-7}$	100% CO_2	Decrease to negligible in 1 hr	72
$(Pr_{0.9}La_{0.1})_2(Ni_{0.74}Cu_{0.21}Ga_{0.05})O_{4+\delta}$	HF		975	$7.3x10^{-7}$	50%CO_2/He	Stable for 200 h	73
$La_{0.6}Sr_{0.4}Co_{0.2}Fe_{0.8}O_{3-\delta}$	Disk	1.0	900	$1.5x10^{-7}$	100%CO_2	Stable for 200 h	74
$La_{0.6}Ca_{0.4}Co_{0.8}Fe_{0.2}O_{3-\delta}$	Disk	1.0	850-900	$7.4x10^{-8}$-$1.1x10^{-7}$	100%CO_2	Stable for 200 h	75
$La_{0.85}Ce_{0.1}Ga_{0.3}Fe_{0.65}Al_{0.05}O_{3-\delta}$	Disk	1.0	950	$6.54x10^{-7}$	100%CO_2	Stable for 50h	76
$La_{0.2}Sr_{0.8}Fe_{0.2}Co_{0.8}O_x$	Tubular		850		80%CH_4/He	Membrane broke into several pieces	60
$La_{0.80}Sr_{0.20}MnO_{3-\delta}$ (LSM-ScSZ)/NiO-ScSZ	Disk	1.0	920-1060	$1.9x10^{-7}$-$1.35x10^{-6}$	10%CH_4/Ar	Dual phase POM with CH_4 Conv: 54-99%; CO selec	77
$La_{0.7}Sr_{0.3}FeO_{3-\delta}$	HF		950	$5.1x10^{-6}$	30%H_2/He		78
$La_{0.7}Sr_{0.3}FeO_{3-\delta}$	HF		950	$2.83x10^{-6}$	5%H_2/He		78
$SrCo_{0.8}Fe_{0.1}Ga_{0.1}O_{3-\delta}$	HF		900	$2.5x10^{-6}$	100% CH_4	Stable for 100 h test	79

Perovskite	Shape	Thickness mm	Temperature (ºC)	O_2 flux $mol \cdot cm^{-2} \cdot s^{-1}$	Atmosphere	Note	Ref
$La_{0.7}Sr_{0.3}FeO_{3-\delta}$	HF		950	$3x10^{-6}$	100% CH_4	No Catalyst; CH_4 Conv increase from 20 -80% (from 0-50hr); CO Selec decrease from 98-10% (from 0-50hr)	78
$Ba_{0.5}Sr_{0.5}Co_{0.8}Fe_{0.2}O_{3-\delta}$	Disk	1.8	875	8.6×10^{-6}	50%CH_4/He	$LiLaNiO_x$ /γ-Al_2O_3 Catalyst for POM 500 h operation stable with CH_4 Conv:>97; CO Selec:>95	65
$La_{0.4}Ba_{0.6}Fe_{0.8}Zn_{0.2}O_{3-\delta}$	Disk	0.5	900	$3x10^{-6}$	17.5-100 % CH_4 (bal Ar)	Ni-Cat for POM-Stable for 500h CH_4 Conv: ~100%; CO Selec:~100%	80
$SrCoFeO_x$	Disk	1.0	900	$1.8x10^{-6}$	50%CH_4/He	POM using 10wt%Ni/Al_2O_3 cat CH_4 Conv:~90%; CO Selec: 97%	81
$Ba_{0.5}Sr_{0.5}Fe_{0.8}Zn_{0.2}O_{3-\delta}$	Disk			$1.9x10^{-6}$	50%CH_4/He	100mg Ni Catalyst for POM with 100h operation; CO Selec:97%	82
$BaCe_{0.1}Co_{0.4}Fe_{0.5}O_{3-\delta}$	Disk	1.0	950	$7x10^{-6}$	100%CH_4	POM using LiLaNiO/□-Al_2O_3 cat CH_4 Conv:99%;CO Selec: 93%	83
$Ba_{0.5}Sr_{0.5}Co_{0.8}Fe_{0.2}O_{3-\delta}$	Tubular		875	$6x10^{-6}$	100%CH_4	POM using LiLaNiO/□-Al_2O_3 cat stable for 500 h CH_4 Conv:94%;CO Selec: >95%	18
$La_{0.2}Sr_{0.8}MnO_{3-\delta}$ (LSM80)-$Ce_{0.8}Gd_{0.2}O_{2-\delta}$(CGO20)/dense YSZ-Ag composite/porous YSZNi(0) composite	Tubular		900		33%CH_4/He	POM using 50%NiO/YSZ cat with CH_4 Conv:97%; CO Selec:94%	84
$BaCo_{0.7}Fe_{0.2}Nb_{0.1}O_{3-\delta}$-$Ce_{0.8}Gd_{0.2}O_{3-\delta}$	Disk	1.0	875	$1.4x10^{-5}$	Coke Oven Gas	Ni/$Ce_{0.75}Zr_{0.25}O_2$/Mg_3(Al)O catalyst for PO-COG with CH_4 Conv:99%; CO Selec:91%	85
$Ba_{0.9}Co_{0.7}Fe_{0.2}Nb_{0.1}O_{3-\delta}$	Disk	1.0	875	$5.2x10^{-6}$	30%CH_4/He	NiO/MgO Cat for POM 400h operation stable,CH_4 Conv:93%;CO Selec:95%	86
$SrFeCo_{0.5}O_x$	Disk	2.0	800		80% (CH_4+CO_2)/Ar	150l/gcat.h Pt/ZrO_2 Cat for Oxy-DRM CH_4 Conv:43-18%at 14h	87
$Ba_{0.5}Sr_{0.5}Co_{0.8}Fe_{0.2}O_x$	Disk	2.0	800		80% (CH_4+CO_2)/Ar	150l/gcat.h Pt/ZrO_2 Cat for Oxy-DRM CH_4 Conv:42-25%at 14h	87

REFERENCES

[1] Li, N.N.; Fane, A.G.; Ho, W.S.W.; Matsuura, T. Editors, Advanced membrane technology and applications, *Wiley*, **2008**.

[2] Kharton, V.V; Yaremchenko, A. A.; Kovalevsky, A.V.; Viskup, A. P.; Naumovich, E.N.; Kerko, P. F. *J. Memb. Sci.***1999**, *163*, 307-317.

[3] Sunarso, J.; Baumann, S.; Serra, J.M.; Meulenberg, W.A.; Liu, S.; Lin, Y.S.; da Costa, J.C.D. *J. Memb. Sci.* **2008**, *320*, 13-41.

[4] Geffroy, P.M.; Bassat, J.M.; Vivet, A.; Fourcade, S.; Chartier, T.; Gallo, P.D.; Richet, N. *Catal. Lett.* **2002**, *78*, 129-137.

[5] Sammells, A.F.; Mundschau, M.V. Non porous inorganic membranes, *Wiley VCH*, **2006**, 1-291.

[6] Hashim, S.M.; Mohamed, A.R.; Bhatia, S. *Adv. Coll. Int. Sci.* **2010**, *160*, 88-100.

[7] Cook, R.L.; Sammells, A.F. *Solid State Ionics*, **1991**, *45*, 311-321]:

[8] Hong, C.S.; Chu, S.Y.; Su, W.C.; Chang, R.C.; Nien, H.H. et al. *J. Appl. Phys.***2007**, *101*, 054117(1-7)

[9] Burggraaf, A.J.; Cot, L. *Fundamentals of inorganic membrane science and technology*, Elsevier Science, **1996**, 435-515.

[10] Li, W.; Liu, J.J.; Chen, C.S. *J. Memb. Sci.* **2009**, *340*, 266-271.

[11] Metcalfe, A.T. *J. Solid State Electrochem.* **2006**, *10*, 604-616.

[12] Bouwmeester, H.J.M. *Catal. Today* **2003**, *82*, 141-150.

[13] Bouwmeester, H.J.M.; Burggraaf, A.J. Dense ceramic membranes for oxygen separation. *Elsevier Science B.V* **1996**.

[14] Lin, Y.S.; Wang, W.; Han, J. *AIChE J.* **1994**, *40*, 786-798.

[15] Chen, C.S.; Boukamp, B.A.; Bouwmeester, H.J.M.; Cao, G.Z.; Kruidhof, H.; Winnubst, A.J.A.; Burggraaf, A.J. *Solid State Ionics*, **1995**, *76*, 23-28.

[16] Bouwmeester, H.J.M.; et al *Solid State Ionics*, **1994**, *72*, 185-194

[17] Kilner, J.A. Ion-conducting membranes: Membrane separations. *Imperial College of Science, Technology and Medicine, London,* **2003**.

[18] Wang, H.H.; Cong, Y.; Yang, W.S. *Catal. Today* **2003**, *82*, 157-166.

[19] Dyer, P.N.; Richards, R.E.; Russek, S.L.; Taylor, D.M. *Solid State Ionics*, **2000**, *134*, 21-33.

[20] Tan, X.; Liu, Y.; Li, K. *AIChE J.* **2005**, *51*, 1991-2000.

[21] Tan, X.; Liu, Y.; Li, K. *Ind. Eng. Chem. Res.* **2005**, *44*, 61-66.

[22] Schiestel, T.; Kilgus, M.; Peter, S.; Caspary, K.J.; Wang, H.; Caro, J. *J. Memb. Sci.* **2005**, *258*, 1-4.

[23] Chung, T.S. Fabrication of hollow fiber by phase inversion, *John. Wiley & Sons, Inc.* **2002.**

[24] Kesting, R.E.F.; Cruse, A.; Murphy, M.K..; Handermann, A.C.; Malon, R.F.; Moore, M.D. *J. Appl. Polym. Sci.* **1990**, *40*, 1557-1574.

[25] Liu, S.; Tan, X.; Shao, Z.; Diniz da Costa, J.C. *AIChE J.* **2006**, *52*, 3452-3461.

[26] Tan, X.; Liu, N.; Meng, B.; Liu, S. *J. Memb. Sci.***2011**, *378*, 308-318.

[27] Teraoka, Y.; Zhang, H.M.; Furukawa, S.; Yamazoe, N. *Chem. Lett.* **1985**, 1743-1746.

[28] Misuzaki, J. *Solid State Ionics* **1992**, *52*, 79-91.

[29] Carter, S.; Selcuk, A.; Chater, R.J.; Kajda, J.; Kilner, J.A.; Steele, B.C.H. *Solid State Ionics* **1992**, *53-56*, 597-605.

[30] van Hassel, B.A.; ten Elshof, J.E.; Bouwmeester, H.J.M. *Appl. Catal. A:Gen.* **1994**, *119*, 279-291.

[31] Sakai, N.; Horita, T.; Yokokawa, H.; Dokiya, M.; Kawada, T. *Solid State Ionics* **1996**, *86-88*, 1273-1278.

[32] Dong, X.; Jin, W.; Xu, N.; Li, K. *Chem. Commun.* **2011**, *47*, 10886-10902.

[33] Kharton, V.; Shaulo, A.; Viskup, A.; Avdeev, M.; Yaremchenko, A.; Patrakeev, M.; Kurbakov, A.; Naumovich, E.; Marques, F. *Solid State Ionics,* **2002**, *150*, 229-243.

[34] Shao, Z.P.; Yang, W.S.; Cong, Y.; Dong, H.; Tong, J.H.; Xiong, G.X. *J. Memb. Sci.* **2000**, *172*, 177-188.

[35] Liang, F.Y.; Jiang, H.Q.; Luo, H.X.; Caro, J.; Feldhoff, A. *Chem. Mater.* **2011**, *23*, 4765-4772.

[36] Aasland, S.; Tangen, I.L.; Wiik, K. ; Ødegård, R. *Solid State Ionics,* **2000**, *135*, 713-717.

[37] Kharton, V.V.; Kovalevsky, A.V.; Tikhonovich, V.N.; Naumovich, E.N.; Viskup, A.P. *Solid State Ionics*, **1998**, *110*, 53-60.

[38] Kharton, V.V.; Viskup A.P.; Naumovich, E.N.; Tikhonovich, V.N. *Mat. Res. Bull.* **1999**, *34*, 1311-1317.

[39] Kharton, V.V.; Viskup A.P.; Bochkov, D.M.; Naumovich, E.N.; Reut, O.P. *Solid State Ionics*, **1998**, *110*, 61-68.

[40] Ishihara, T.; Yamada, T.; Arikawa, T.; Nishiguchi, H.; Takita, Y. *Solid State Ionics*, **2000**, *135*, 631-636.

[41] Efimov, K.; Halfer, T.; Kuhn, A.; Heitjans, P.; Caro, J.; Feldhoff, A. *Chem. Mater.* **2010**, *22*, 1540-1544.

[42] Liao, Q.; Zheng, Q.; Xue, J.; Wei, Y.; Wang, H. *Ind. Eng. Chem. Res.* **2012**, *51*, 15217-15223.

[43] Wang, Z.; Yang, N.T.; Meng, B.; Tan, X.; Li, K. *Ind. Eng. Chem. Res.* **2009**, 48, 510-516.

[44] Liang, F.; Jiang, H.; Schiestel, T.; Caro, J.. *Ind. Eng. Chem. Res.* **2010**, *49*, 9377-9384.

[45] Tan, X.; Pang, Z.; Li, K. *J. Memb. Sci.* **2008**, *310*, 550-556.

[46] Wang, Z.; Liu, H.; Tan, X.; Jin, Y.; Liu, S. *J. Memb. Sci.* **2009**, *345*, 65-73.

[47] Liu, N.; Tan, X.; Meng, B.; Liu, S. *Sep Purif. Technol.* **2011**, *80*, 396-401.

[48] Meng, B.; Wang, Z.; Liu, Y.; Tan, X.; da Costa, J.C.D.; Liu, S. *Sep. Purif. Technol.* **2011**, *78*, 175-180.

[49] Meng, X.; Yang, N.; Meng, B.; Tan, X.; Ma, Z.F.; Liu, S. *Ceram. Int.* **2011**, *37*, 2701-2709.

[50] Li, K.; Tan, X.; Liu, Y. *J. Memb. Sci.* **2006**, *272*, 1-5.

[51] Leo, A.; Smart, S.; Liu, S.; da Costa, J.C.D. *J. Memb. Sci.* **2011**, *368*, 64-68.

[52] Wei, Y.; Tang, J.; Zhou, L.; Li, Z.; Wang, H. *Chem. Eng. J.* **2012**, *183*, 473-482.

[53] Tan, X. Wang, Z.; Liu, H.; Liu, S. *J. Memb. Sci.* **2008**, *324*, 128-135.

[54] Leo, A.; Liu, S.; da Costa, J.C.D. *J. Memb. Sci.* **2009**, *340*, 148-153.

[55] Yacou, C.; Sunarso, J.; Lin, C.X.C.; Smart, S.; Liu, S.; da Costa J.C.D. *J. Memb. Sci.* **2011**, *380*, 223-231.

[56] Koh, A.; Chen, L.; Johnson, B.; Khimyak, T.; Leong, W.; Lin, J. *Int. J. Hyd. Energ.* **2013,** Article in press.

[57] Li, Q.; Zhu, X.; He, Y.; Yang, W. *Catal Today* **2010**, *149*, 185-190.

[58] Nagamoto, H.; Hayashi, K.; Inoue, H. *J. Catal.* **1990**, *126*, 671-673.].

[59] Hitoshi, T. *Energy and Resources*, **2005**, *26*, 260-263.

[60] Balachandran, U.; Dusek, J.T.; Mieville, R.L.; Poeppel, R.B.; Kleefisch, M.S.; Pei, S.; Kobylinski, T.P.; Udovich, C.A.; Bose, A.C. *Appl Catal A Gen*. **1995,** *133*,19-29.

[61] Pei, S.; Kleefisch, M.S.; Kobylinksi, T.P.; Faber, J.; Udovich, C.A.; Zhang-McCoy V.; Dabrowski, B.; Balachandran, U.; Mieville, R.L.; Poeppel, R.B. *Catal. Lett*. **1995**, *30*, 201-212.

[62] Hendriksen, P.V.; Larsen, P.H.; Mogensen, M.; Poulsen, F.M.; Wiik, K. *Catal. Today* **2000**, *56*, 283-295.

[63] Jin, W.; Li, S.; Huang, P.; Xu, N.; Shi, J.; Lin, Y.S. *J Membr Sci*. **2000**, *166*, 13-22.

[64] Zeng, P.; Chen, Z.; Zhou, W.; Gu, H.; Shao, Z.; Liu, S. *J. Memb. Sci.* **2007**, *291*, 148-156.

[65] Dong, H.; Shao, Z.; Xiong, G.; Tong, J.; Sheng, S.; Yang, W. *Catal Today*. **2001**, *67*, 3-13.

[66] Tsai, C.Y.; Dixon, A.G.; Ma, Y.H.; Moser, W.R.; Pascucci, M.R. *J. Am. Ceram. Soc.* **1998**, *81*, 1437-1444.

[67] Slade, D.A.; Duncan, A.M.; Nordheden, K.J.; Stagg-Williams, S.M. *Green Chem.* **2007**, *9*, 577-581.

[68] Tan, X.; Liu, N.; Meng, B.; Sunarso, J.; Zhang, K.; Liu, S. *J. Memb. Sci.* **2012**, *389*, 216– 222.

[69] Czuprat, O.; Arnold, M.; Schirrmeister, S.; Schiestel, T.; Caro, J. *J. Memb. Sci.* **2010**, *364*, 132-137.

[70] Li, J.L.; Zeng, Q.; Liu, T.; Chen, C.S. *Sep. Purif. Technol.* **2011**, *77*, 76-79.

[71] Yi, J.; Schroeder, M.; Martin, M. *Chem. Mater.* **2013**, *Just Accepted*.

[72] Yi, J.; Schroeder, T.; Weirich, T.; Mayer, J. *Chem. Mater.* **2010**, *22*, 6246-6253.

[73] Wei, Y.; Ravkina, O.; Klande, T.; Wang, H.; Feldhoff, A. *J. Memb. Sci.* **2013**, *429*, 147-154.

[74] Klande, T.; Ravkina, O.; Feldhoff, A. *J. Memb. Sci.* **2013**, *Just Accepted.*

[75] Efimov, K.; Klande, T.; Juditzki, N.; Feldhoff, A. *J. Memb. Sci.* **2012**, *389*, 205-215.

[76] Dong, X.; Zhang, G.; Liu, Z.; Zhong, Z.; Jin, W.; Xu, N. *J. Memb. Sci.* **2009**, *340*, 141-147.

[77] Wu, Z.; Wang, B.; Li, K. *Int J Hydrogen Energy* **2011**, *36*, 5334-5341.

[78] Tan, X.; Shi, L.; Hao, G.; Meng, B.; Liu, S. *Sep. Purif Technol*. **2012**, *96*, 89-97.

[79] Yang, N.T.; Kathiraser, Y.; Kawi, S. *J Membr Sci*. **2013**, *428*, 78-85.

[80] Gong, Z.; Hong, L. *J. Memb. Sci.* **2011**, *380*, 81-86.

[81] Kniep, J.; Lin, Y.S. *Ind. Eng. Chem. Res.* **2011**, *50*, 7941-7948.

[82] Luo, H.X.; Yu, L.H.; Chen, X.Z.; Wang, H.H.; Caro, J. *Chin. Chem. Lett.***2009**,*20*, 250-252.

[83] Li, Q.; Zhu, X.; He, Y.; Yang, W. *Catal. Today* **2010**, *149*, 185-190.

[84] Yin, X.; Hong, L.; Liu, Z.L. *J. Phys. Chem. C.* **2007**, *111*, 9194-9202.

[85] Cheng, H.; Lu, X.; Hu, D.; Zhang, Y.; Ding, W.; Zhao, H. *Int. J. Hyd. Energ.* **2011**, *36*, 528-538.

[86] Song, S.; Zhang, P.; Han, M.; Singhal, S.C. *J. Memb. Sci.* **2012**, *415-416*, 654-662.

[87] Faraji, S.; Nordheden, K.J.; Stagg-Williams, S.M. *Appl. Catal. B:Environ.* **2010**, *99*, 118-126.

CHAPTER 4

Experimental Methodology

4.1. List of Chemicals

- Lanthanum (III) nitrate hexahydrate (99.9%, Sigma Aldrich)
- Gamma-Aluminium oxide anhydrous (Merck)
- Nickel (II) nitrate hexahydrate (ACS Reagent, Merck)
- Strontium nitrate (ACS Reagent, ≥ 99.0%, Sigma Aldrich)
- Cobalt (II) nitrate hexahydrate (ACS Reagent, ≥ 98%, Sigma Aldrich)
- Gallium (III) nitrate hydrate (99.99%, PURATREM, Strem Chemicals)
- Citric acid (CA) (99.5+%, Merck)
- Ethylene glycol anhydrous (99.8%, Sigma Aldrich)
- N-methyl pyrollidone (Merck)
- Polyethersulfone (PESf, Radel A-300, Ameco Performance)
- Silver paste (DAD 87)
- Silicone sealant (Dow Corning)

4.2. Catalyst preparation

4.2.1. Synthesis of $LaAlO_3$-Al_2O_3 support

The *in-situ* formed $LaAlO_3$ on Al_2O_3 perovskite-oxide support were prepared by the conventional wet impregnation method. 21 mol% $La(NO_3)_3.6H_2O$ (Sigma Aldrich) were introduced to 79 mol% of γ-Al_2O_3 (Merck). The reactants were dissolved in DI water and stirred and heated to 55°C. Upon drying, the catalyst support was dried overnight at 100°C. The supports were calcined at 900°C for 6 hours to facilitate solid state diffusion for perovskite phase formation. Preliminary X-ray diffraction (XRD) analysis showed that La_2O_3 precipitates were not formed, suggesting sufficient La incorporation at the calcination conditions employed.

4.2.2. Synthesis of Ni supported on $LaAlO_3$-Al_2O_3

Ni was impregnated on the calcined $LaAlO_3$-Al_2O_3 supports and calcined at 400°C for 1 h (for nitrate decomposition) and further to 600°C for 5 h. For reference and comparison, Ni was also impregnated on pure γ-Al_2O_3 and La_2O_3 supports and further calcined in the same way. The catalysts prepared are thus designated as NA, NLA and NL (Ni/ γ-Al_2O_3, Ni/ $LaAlO_3$-Al_2O_3, and Ni/La_2O_3) respectively and characterized and tested for DRM reaction. Initial tests were based on 10wt% Ni loading. Subsequently, 5wt% Ni loading was used and further incorporated for POM and OCRM testing in catalytic hollow fiber membrane reactor studies.

4.3. Hollow fiber membrane preparation

4.3.1. Synthesis of LSCG composite perovskite

The $La_{0.6}Sr_{0.4}Co_{0.8}Ga_{0.2}O_{3-\delta}$ (LSCG) composite perovskite was synthesized via an ethylene glycol – citric acid complexation method. Citric acid (CA) (99.5+%) from Merck was used as the chelating agent and dissolved in ethylene glycol and water. Lanthanum (III) nitrate hexahydrate, strontium nitrate, cobalt (II) nitrate hexahydrate and gallium (III) nitrate hydrate were then dissolved together with the above solution at 50°C. Upon full dissolution of all required chemicals reagents, the solution was heated up to 80°C to allow the solvent to evaporate until gel-like or viscous solution is obtained. Subsequently the gel was allowed to auto-combust in an oven at 100°C. The composite material was further calcined at 950°C for 5 h in a furnace with a ramping rate of 2 °C/min under static air to obtain the perovskite phase. Finally the calcined powders were ball-milled followed by sieving using a mesh with the size of 125 μm to ensure that fine particles are obtained.

4.3.2. Preparation of LSCG hollow fiber membranes

Polyethersulfone (PESf, Radel A-300, Ameco Performance) and N-methyl-2-pyrrolidone (NMP, Merck) were used as binder and solvent respectively. 75% DI water-25% NMP and tap water were used as the internal and external coagulants, respectively, when fabricating the hollow fibre precursors. The LSCG hollow fiber membranes were fabricated by a phase inversion-sintering method. As such, the PESF and NMP were mixed with the LSCG powder in a ratio of 1:4:9 (mass ratio). The spinning solution was stirred together for 72 h and the solution was degassed prior to spinning. An air-gap distance of 2 cm was used and the membranes spun were allowed to free fall into the external coagulant. After spinning, the green LSCG hollow fiber membranes were left in

the external coagulant bath overnight in order to allow sufficient solvent-non solvent exchange to take place. The membranes were then dried at room temperature and straightened out on a PVC board for at least 3 days. Finally, the LSCG hollow fiber membranes were calcined in a vertical furnace at 2°C/min to 1175 °C for 5 h. Gas tightness test was conducted for each membrane prior to oxygen permeation testing.

4.4. DRM testing of catalyst in packed bed reactor

A micro-catalytic reactor in a single pass, steady-state plug flow mode was used for the catalytic DRM reaction as shown in Figure 4-1. 50 mg of NA, NLA and NL catalyst bed was packed in between quartz wool layer in the reactor placed in a Carbolite furnace. The catalyst bed was reduced under 10mL/min H_2 (in 10mL/min N_2) flow for 30 minutes at 600°C. CH_4 (10mL/min) and CO_2 (10 mL/min) were then introduced from the gas manifold for reaction at 700°C. The product gases were analysed by an on-line HP 6890 GC (Agilent) equipped with a TCD using Porapak Q and Molecular Sieve 5A packed columns.

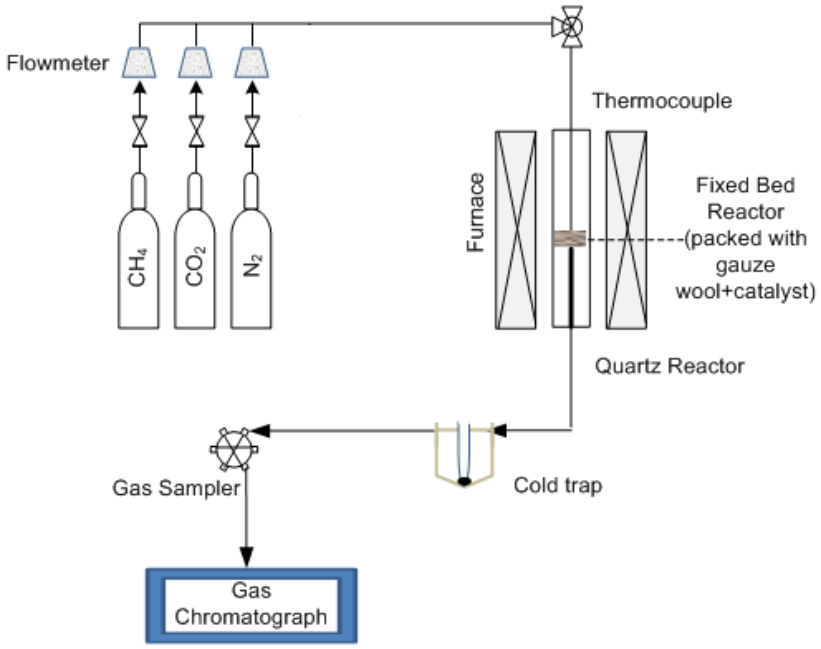

Figure 4-1 Experimental test rig for DRM packed bed reaction testing

4.5. Oxygen permeation testing of LSCG hollow fiber membrane

Figure 4-2 shows the schematic of the apparatus used for oxygen permeation testing setup for the LSCG hollow fiber membrane. Each end of the hollow fiber was adhered to a quartz tube (with an inner diameter of 8 mm) using a high temperature silicone sealant (Dow Corning). Air was fed at a constant flow rate of 100 $mL \cdot min^{-1}$ from the tube side of the hollow fiber membrane reactor. Firstly, purified helium as sweep gas was fed at varying flow rates of 20, 40, 60 80 and 100 $mL \cdot min^{-1}$ on the shell side. Subsequently, using the flow rate with the highest effect on the permeation with helium as sweep gas, purified CH_4 and CO_2 were then used as sweep gases to conduct further permeation studies. The testing temperature range was between 650°C to 950°C. In order to test the oxygen concentration in the sweep gas, the shell side gas outlet was connected to a gas chromatography (GC6890N, Agilent), and analyzed by a thermal conductivity

detector (TCD) using a Hayesep D 100/120 column. The effluent flow rates from the permeate side were also measured by using soap bubble flow meter.

The corrected O_2 fluxes were subtracted using the following formula:

$$J_{O_2} = \frac{V(x_{O_2} - (21/78)x_{N_2})}{A_m} \tag{4-1}$$

where V is the permeate gas flow rate (mL·min^{-1}); x_{O2} and x_{N2} are the % concentrations of O_2 and N_2 in the permeate; A_m (cm^2) is the effective membrane area, $A_m = \pi(D_o - D_i)L / \ln(\frac{D_o}{D_i})$ where D_o, D_i, and L are the outer and inner diameter as well as the effective length for oxygen permeation of the hollow fiber membrane, respectively.

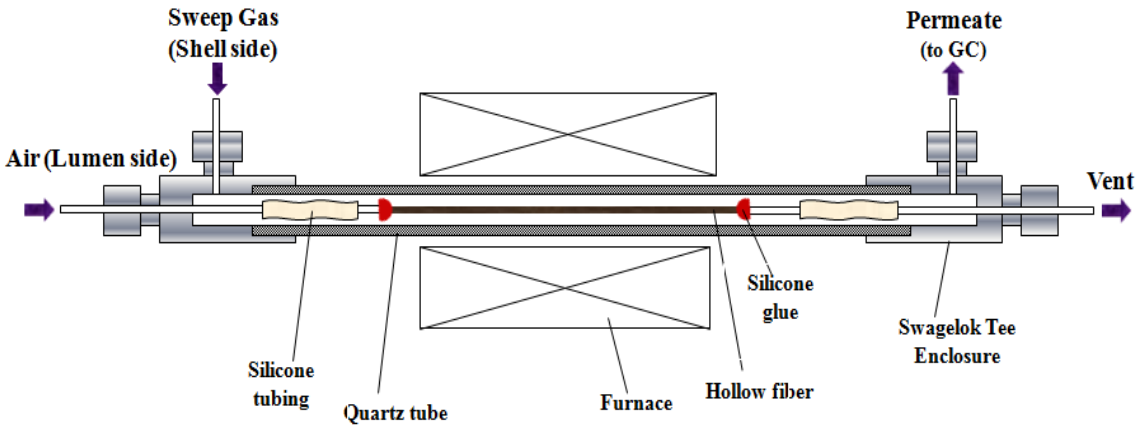

Figure 4-2 Apparatus for hollow fiber oxygen permeation setup

4.6. POM reaction and sweep with H_2:CO gas mixture in LSCG hollow fiber membrane reactor

Figure 4-3 shows the schematic of the catalytic membrane reactor setup. Two ends of the sintered fiber were adhered by silicone glue (Dow Corning) to quartz tube. 0.2g of 5% Ni/$LaAlO_3$-Al_2O_3 catalyst was spread on the quartz wool packed around the hollow fiber in the mid-section corresponding to the optimal heated length in the furnace which has a total length of 15 cm (Carbolite MTF 10/15/130/3216P1). For the blank POM reaction with only the bare membrane, the same configuration was used except that no catalyst was packed.

The 5% Ni/$LaAlO_3$-Al_2O_3 catalyst was firstly pre-reduced under H_2 flow at 600°C for 30 minutes. Silver paste was coated on all parts of the membrane surface except 4.5 cm of the mid-section which is the approximated length of the optimal heating zone of the furnace. The purpose of coating the Ag paste on the external surface of the membrane (apart from the central heated area) was to create a barrier to minimize permeation from other parts which are not within the central heating zone. Hence in this way, a more accurate estimation of the O_2 flux from POM reaction can be determined. Air flowrate of 100mL.min^{-1} was introduced to the lumen side, whereas the reactant was introduced on the shell side (25% CH_4/He, 10 mL.min^{-1}). The furnace was heated up from room temperature to 600°C at a rate of 2.5°C.min^{-1}. POM reaction testing was conducted at the interval of 25°C and held for 3 hours for each interval. Reaction testing was carried out in the medium temperature regime of 600°C to 800°C. In order to calculate the reactant conversion and products in the effluent stream, the shell side gas outlet was connected to a gas chromatography (GC6890N, Agilent), and analyzed by a thermal conductivity

detector (TCD) using a Hayesep D 100/120 column. For the exposure to 50% H_2:CO gas mixture (in helium), the sweep gas in the shell side consists of 2.5mL.min^{-1} H_2, 2.5mL.min^{-1} CO and 5mL.min He^{-1}. Air was introduced at a rate of 100mL.min^{-1} in the lumen side and the experiment was conducted in the same way as the POM reaction.

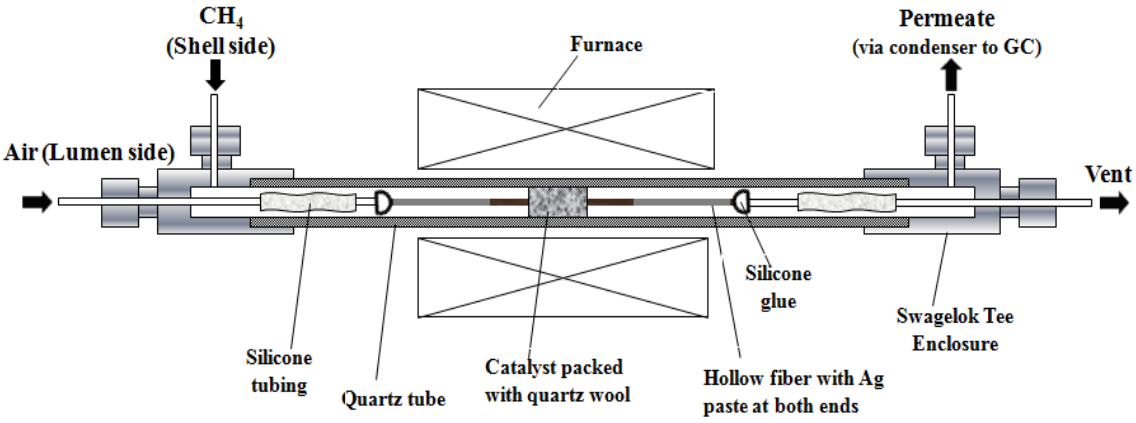

Figure 4-3 Schematic for catalytic LSCG membrane reactor setup for POM

The conversion of CH_4 (X_{CH_4}), selectivity of CO (S_{CO}) and H_2 (S_{H_2}) and the O_2 permeation flux (J_{O_2}) are defined respectively as follows:

$$X_{CH_4}(\%) = \frac{F_{CH_4,in} - F_{CH_4,out}}{F_{CH_4,in}} x\,100\,\% \tag{4-2}$$

$$S_{CO}(\%) = \frac{F_{CO,out}}{F_{CO,out} + F_{CO_2,out}} x\,100\,\% \tag{4-3}$$

$$S_{H_2}(\%) = \frac{F_{H_2,out}}{2(F_{CH_4,in} - F_{CH_4,out})} x\,100\,\% \tag{4-4}$$

$$J_{O_2}\ (\text{mL.min}^{-1}.\text{cm}^{-2}) = \frac{F_{O_2}}{S_A} \tag{4-5}$$

$$F_{O_2} = \frac{1}{2}F_{CO,out} + F_{CO_2,out} + \frac{1}{2}F_{H_2O,out} + F_{O_2,out} \tag{4-6}$$

$$F_{H_2O,out} = 2(F_{CH_4,in} - F_{CH_4,out}) - F_{H_2,out} \tag{4-7}$$

where F_i is the flow rate of species *i*, in mL.min^{-1}, S_A is the membrane surface area in cm^2. Using the same formula for conversion of CH_4, the H_2 and CO conversions were similarly calculated for the LSCG membrane swept with 50% H_2:CO (in helium) gas mixture.

Carbon balance is in the range of (100±10)% and calculated using the following formula:

$$\text{Carbon balance} = \frac{F_{CH_{4,out}} + F_{CO_{out}} + F_{CO_{2,out}}}{F_{CH_{4.in}}} \tag{4-8}$$

Leakage from GC and valve system was found to be ~ 0.5% of the O_2 flux and was constant throughout the experiments. The corrected O_2 fluxes were subtracted using the formula shown in Equation (4-1).

4.7. OCRM reaction in LSCG hollow fiber membrane reactor

OCRM reaction was carried out in the similar configuration as POM reaction in LSCG hollow fiber membrane reactor setup. Two ends of the sintered fiber were adhered by silver paste (DAD-87) to quartz tubes. Prior to be packed in the hollow fiber membrane reactor, the 5% Ni/$LaAlO_3$-Al_2O_3 catalyst was firstly pre-reduced under H_2 flow at 600°C for 30 minutes. Then 0.18 g of the reduced catalyst was spread on the quartz wool packed

around the hollow fiber in the mid-section stage. Air flowrate of 100mL.min^{-1} was introduced to the lumen side, whereas the reactants were introduced to the catalyst bed on the shell side (3.2 mL.min^{-1} of CH_4 and 2.7 mL.min^{-1} of CO_2). Helium was used as a diluent with a flowrate of 6.8 mL.min^{-1}. OCRM reaction testing was carried out from 650°C to 800°C at the interval of 25°C and held for 3 hours for each interval. Based on the reaction results, the optimal temperature was then chosen (725°C in this study) for long-term stability tests.

The conversion of the reactants, X_i (where i is CH_4 and CO_2), selectivity of CO (S_{CO}) and H_2 (S_{H_2}) are defined respectively as follows:

$$X_i\ (\%) = \frac{F_{i,in} - F_{i,out}}{F_{i,in}} x100\% \tag{4-9}$$

$$S_{CO}\ (\%) = \frac{F_{CO,out}}{(F_{CH_4,in} - F_{CH_4,in}) + (F_{CO_2,in} - F_{CO_2,out})} x100\% \tag{4-10}$$

$$S_{H_2}(\%) = \frac{F_{H_2,out}}{2(F_{CH_4,in} - F_{CH_4,out})} x\,100\% \tag{4-11}$$

The oxygen permeation flux is calculated based on Equations 4-5 to 4-7.

4.8. Characterization Techniques

The characterization methods as well as the equipments used are described in this section.

4.8.1. X-ray diffraction (XRD)

XRD analysis is known widely for its importance as a "fingerprint" in the identification of materials. From the XRD, parallel planes of atoms intersect the unit cells and thereby define the directions and distances in the crystal, providing vital information

on the crystallinity and lattice parameters referred to as Miller indices. A Shimadzu XRD-6000 powder diffractometer as well as a Bruker D8 were the available equipments for carrying out this test. The X-ray source used was the Cu target K-α ray. The measurement conditions were under 40 kV voltage and 30 mA current using the following parameters: divergence slit: 1.0000 (deg), scattering slit: 1.0000 (deg) and receiving slit: 0.30000 (mm). A scanning speed of $1°min^{-1}$ was employed over an angular range of $20°<2\theta<80°$.

4.8.2. H_2- Temperature programmed reduction (H_2-TPR)

H_2-Temperature programmed reduction (H_2-TPR) was conducted using a Quantachrome ChemBET 3000 TPR system which was equipped with a thermal conductivity detector (TCD) connected to a moisture trap. Typically, about 0.03g of Ni impregnated catalyst sample was placed in a U-tube holder and first degassed (to remove water and other contaminants) at 300^oC for 2 hours by flushing with N_2 gas at a flowrate of 80 mL/min. Upon degassing, the probe gas mixture consisting of 5% H_2/N_2 at a flow rate of 50 ml/min was passed through the sample. The sample was heated from ambient conditions to 1000^oC to obtain TPR profiles for the reduction process of the catalysts.

4.8.3. Temperature programmed desorption (TPD)

Temperature programmed desorption (TPD) on the fresh LSCG hollow fibers were carried out using O_2, CO_2, CO and H_2 as probe gases. The oxygen mobility in the crystalline lattice of the hollow fiber membranes was tested via O_2-TPD using a Quantachrome ChemBET 3000 system. Typically, about 0.2 g of LSCG hollow fiber sample was crushed and degassed at 150°C for 1 h under 80 $mL \cdot min^{-1}$ of He flow. Upon

degassing, the sample was cooled down for baseline stabilization. The TPD profiles were obtained by heating the sample under He flow at 10°C/min to 1000°C.

For CO_2, CO or H_2-TPD studies, about 0.25g of crushed sample was firstly outgassed at 300°C to remove any moisture. After that, the sample was cooled down to room temperature and exposed to continuous flow of CO_2, CO or H_2 for 1 hour. After flushing the physisorbed gases with He at room temperature, TPD experiment was conducted upto 950°C under helium with a ramp rate of 10°C.min^{-1}. The sample effluent was analyzed by a quadrupole mass spectrometer (OMNISTAR, Balzers) which operates with a Faraday detector on SEM emission mode.

4.8.4. Braunner Emmet Teller (BET) surface area analysis

The BET surface area of the H_2 reduced catalysts (600°C for 30 minutes) were measured using Micromeritics ASAP 2010 analyzer at 77 K by the nitrogen adsorption and desorption isotherms. Prior to analysis, about 0.04 g of the samples were degassed at 300°C for 12 hours to remove all surface impurities and moisture. The weights of the samples were re-measured to determine the net weight of sample after degassing. After that, a glass rod was placed into the sample cell for reduction of dead space. The sample cell was then placed into the analysis station with liquid nitrogen at 77.4 K as adsorbate. The sample cells were immersed into a flask containing liquid nitrogen to maintain the low temperature of 77.4K throughout the analysis.

4.8.5. UV-Visible Diffuse Reflectance Spectroscopy (UV-DRS)

UV-Visible diffuse reflectance spectroscopy (UV-DRS) analysis was conducted for the NA and NLA catalysts and their respective supports via a Shimadzu 3600 UV-Vis

NIR Spectrophotometer equipped with an integrating sphere. The scanning range was 200-800 nm at medium scanning speed. Barium sulphate was used as the reference spectra. Spectra was recorded under ambient conditions.

4.8.6. ^{27}Al-MAS Nuclear Magnetic Resonance (NMR)

^{27}Al NMR measurements for NA and NLA catalysts with their respective supports were performed on a Bruker Avance-400 spectrometer equipped with a 4 mm HR Magic Angle Spinning (MAS) probe operating at a resonance frequency of 104.3 MHz. The NMR peak positions reflect the chemical environment and nucleic positions of the atoms within the molecule. The spectra were recorded with a spinning rate of 10 kHz, scan width of 52083 Hz for 100 scans in total.

4.8.7. X-ray photoelectron spectroscopy (XPS)

X-ray photoelectron spectroscopy (XPS) was used to obtain information on the chemical composition and binding energy of the elements. A Kratos AXIS spectrometer with a spatial resolution of 30 µm equipped with an Al K α ($h\upsilon$= 1486.6eV; 1 eV = 1.6302 x 10^{-19} J) X- ray source was used to obtain the XPS spectra. A standard calibrated value C1 s hydrocarbon peak at 284.5 eV was used as reference. XPS peak 4.1 software package was used to fit all spectra by subtracting Shirley (for transition metals) or linear background (for other elements) with a peak width at half maximum of 1-2.

4.8.8. High Resolution Transmission Electron Microscopy (HR-TEM)

In order to prepare sample for TEM analysis, about one droplet of ultrasonically-dispersed suspension of the sample in ethanol was dripped on-to a copper grid and dried at

atmospheric conditions prior to analysis. In the operation of TEM, the specimen is exposed to an electron beam and part of the electron beam is transmitted. An objective lens was used to focus the transmitted portion into an image which is enlarged and projected for visual observation. In order to obtain the particle sizes of the reduced and fresh catalysts, TEM images were obtained via a JEM 2010F TEM equipment operated at an acceleration voltage of 200 kV.

4.8.9. Thermal gravimetry analysis (TGA)

Thermal gravimetry coupled with differential thermal analysis (TGA-DTA) of the spent catalyst was carried out in a Shimadzu DTG-60 analyzer to determine the amount of carbon accumulation during the catalytic reaction. About 0.015g of the sample was placed in a basket hanging on the arm of the electronic balance (equipped with a thermocouple) of the analyzer; and heated in air to 800^{o}C by ramping to a rate of 10^{o}C/minute.

4.8.10. Scanning Electron Microscopy – Energy Dispersive Spectroscopy (SEM-EDX)

The morphologies of the used catalysts as well as calcined LSCG perovskite powder and LSCG hollow fiber membranes were examined through a SEM coupled to an EDX (SEM-EDX, Jeol, JSM-670F). The samples were degassed under vacuum condition in order to remove impurities. Platinum coating (about 10 nm thickness) was carried out at 20 mA for 45 seconds. EDX mode was used to analyze composition of the membrane surface.

4.8.11. Fourier Transform Infrared Spectroscopy (FTIR)

The nature of acid sites on the NA and NLA catalysts were carried out by Fourier transform infrared spectroscopy (FTIR, Bruker Vertex 70 SN_1253) via pyridine adsorption for the NA and NLA catalysts. Measurements were conducted *in-situ* using a Harricks dome cell equipped with KBr windows. Before analysis, the samples were reduced under H_2/He flow at 600°C for 30 mins. Pyridine (Py) adsorption was carried out at 25°C for 30 min using He to carry the Py moieties (vaporized with heating gun) to the sample chamber. After that, physisorbed Py was removed with He prior to analysis. IR spectra were recorded with He evacuation at 25°C, 100°C, 200°C and 300°C.

FTIR analysis was also conducted for the fresh and post-reacted (after long-term stability) LSCG membranes. The LSCG membrane (fresh and post-reacted) was firstly ground and diluted with KBr prior to placement in a Harricks dome cell equipped with KBr windows. Upon outgassing at 250°C and cooling down to room temperature, the sample spectrum was recorded. In order to study the effect of CO_2 or CO on the post-reacted samples, CO or CO_2 was firstly adsorbed on the membrane surface and the temperature was ramped up to 600°C. Upon cooling down to room temperature and flushing with He gas, desorption was carried out under He with spectra recorded at each interval of 100°C up to 600°C (the maximum cell temperature).

CHAPTER 5

Inverse $NiAl_2O_4$ on $LaAlO_3$-Al_2O_3: Unique catalytic structure for stable CO_2reforming of methane

In this chapter, Ni supported on $LaAlO_3$-Al_2O_3 (NLA) perovskite-oxide was synthesized for syngas production via DRM and compared with Ni supported on γ-Al_2O_3 (NA) and La_2O_3(NL). The formation of $LaAlO_3$ perovskite oxide structure involves interaction with octahedral sites of the alumina support, resulting in the enforced Ni-Al interaction with the underlying tetrahedral Al^{3+} sites when Ni was impregnated. As a result, the inverse $NiAl_2O_4$ spinel structure was formed and it positively affects the catalytic activity. Catalytic studies show that NLA exhibited the most stable catalytic performance with the lowest carbon deposition. Furthermore, XRD of spent NA catalyst showed phase transformation of support from γ-Al_2O_3 to α-Al_2O_3. Therefore, the enhanced stability of the NLA catalyst throughout the 30-hour DRM reaction is attributed to the enhanced lattice stability imparted by the inverse spinel structure and $LaAlO_3$ nanocrystallites on the alumina support, both of which aid in minimizing agglomeration of Ni particles.

5.1. Introduction

Transformation of CO_2 with methane, both notorious greenhouse gases via CO_2 dry reforming of methane (DRM) into more valuable compounds is one of the important subjects in catalysis research [1]. However, the major concern of the DRM reaction is catalytic deactivation caused by rapid carbon deposition [2-4]. Carbon deposition on the

catalyst mainly comes from CO disproportionation ($2CO \rightarrow CO_2 + C$) and/or methane decomposition ($CH_4 \rightarrow 2H_2 + C$) [5]. These two side reactions, which occur and generate carbon deposits, eventually would destroy the catalyst particles and block the reactor, hence leading to catalytic deactivation [6]. Noble metal catalysts are primarily suited to counter catalytic deactivation. However, due to their enormous cost, Ni catalyst is the preferable choice, owing to its comparable reforming activity, wide availability and low cost which is more practical from an industrial standpoint [7-8]. In this regard, improvement of resistance to carbon deposition and prevention of sintering is still a hot topic in the DRM reactions [9].

Catalyst supports are usually ceramic solids [10]. Al_2O_3 as a support has the distinction of having properties such as high surface area, mixture of acid-base properties, surface hydration/hydroxylation mechanisms, high mechanical strength and low cost [11]. Even though the Ni/Al_2O_3 catalyst is highly active, however imminent catalyst deactivation from the acid surface during DRM reaction is a major concern [12]. Generally for Ni catalysts, surface carbons are accepted as key reaction intermediates in the conversion of hydrocarbon to syngas [13]. Besides reacting with surface oxygen atoms to form CO, surface carbon atoms can also diffuse to subsurface octahedral sites or combine with other surface carbon atoms to form graphene islands. Thus, subsurface octahedral sites have been reported to entice carbon build up [13]. The need to improve stability of Ni based catalysts for DRM reactions has prompted numerous investigations with structural modifications on γ-Al_2O_3 via presence of rare earth or alkaline based promoters such as La_2O_3 [14], Yb_2O_3 [15], Ce-ZrO_2 [16], Mg [17] and K [18] to improve the catalysts support affinity towards CO_2 adsorption. Several researchers have tried

mitigating carbon nucleation sites by binding the octahedral sites via introduction of boron [12], Sn [19], and Au [20].

Among the alkaline based promoters that have been investigated, La has the potential to react with Al^{3+}, thereby enabling binding with the octahedral Al^{3+} cations via formation of $LaAlO_3$ to take place at the appropriate loading and calcination temperatures. However, for DRM reactions, most of the studies have focused on introduction of slight basicity in the form of small amounts of La in order to obtain a well dispersed La on the alumina support [14].

There are a number of studies which have reported on the $LaAlO_3$ perovskite formation on the alumina support. Phase transformation to α-Al_2O_3 has been observed to take place during high temperature operations *ca.* 1000-1050°C [22]. Hence, these studies were conducted to prove that via introduction of La, thermal stabilization of γ-Al_2O_3 can be successfully achieved [23-27]. Interaction of La^{3+} with Al^{3+} leads to nucleation of $LaAlO_3$ microdomains on the surface of alumina support structure [26-28]. Bettman et al.[28] stressed that the formation of $LaAlO_3$ perovskite involved only octahedral aluminium and a strongly bound surface layer involving La species which were located in limited 'active sites' of alumina. They confirmed that La species which were located in other sites of Al_2O_3 precipitated as La_2O_3 as the number of active site decreased due to sintering upon calcination at high temperatures. Oudet et al.[25] demonstrated that the coherence of the interfacial structure of $LaAlO_3$-γ-Al_2O_3 was due to the common coordination of octahedral aluminium cations on both sides of the interface. By this strong anchoring to form $LaAlO_3$, subsequent atomic diffusion leading to phase transformation to α-Al_2O_3 could be hindered. Their postulations were verified by Beguin

et al.[26] who showed that the microdomains of $LaAlO_3$ on γ-Al_2O_3 surface would lock the highly reactive coordinative unsaturated Al ions into a thermally stable structure. Imai et al.[29] on the other hand, studied the effect of Al introduction to La_2O_3 and concluded that $LaAlO_3$ formation provided a stabilization effect as La_2O_3 was catalytically active for oxidative coupling of methane reactions. Recently, Yang [30] from BASF suggested the viability of *in-situ* formed $LaAlO_3$-Al_2O_3 as a catalyst support due to their thermal stabilization property.

The above observations on the thermal stabilization effect of $LaAlO_3$ on Al_2O_3 have been extensively studied. However, most of them relate to the aspect of material synthesis and have not been fully investigated for catalytic applications. Stabilizing effect is indeed an important material property which can be capitalized to enhance catalytic performance in terms of activity and stability. Hence, in this paper, investigation on the catalytic activity of Ni supported on *in-situ* formed $LaAlO_3$ perovskite in equilibrium with the alumina layer ($LaAlO_3$-Al_2O_3) is reported. Comparisons are made with Ni supported on γ-Al_2O_3 in order to illustrate the differences observed. Upon incorporation of 10 wt% Ni on the $LaAlO_3$-Al_2O_3 support, some of the Ni^{2+} species are shown to forcibly react with the underlying tetrahedral Al^{3+} sites to form inverse spinel structure instead of with the octahedral Al^{3+} sites to form the normal spinel structure. The remaining Ni^{2+} species have formed surface NiO species intercalated between the $LaAlO_3$ nanocrystallites on the support. There are several advantages of employing this approach to form this unique structure. Firstly, Ni sintering is found to be reduced. Secondly, phase transformation of γ-Al_2O_3 to α-Al_2O_3 is found to be prevented during the

prolonged reaction hours. Finally, whisker-like carbon filaments formed do not lead towards catalytic deactivation.

5.2. Results and discussion

5.2.1. X-ray diffraction studies

Figure 5-1 shows the XRD profiles of the fresh NA, NLA and NL catalysts as well as reduced catalysts with their phases defined. Based on the characteristic *d*-spacing and diffraction angles from references in the Powder Diffraction (PDF) database [31], the crystalline phases of the structures were identified and summarized (Table 5-1).

From Figure 5-1 (a), NiO and γ-Al_2O_3 phases can be observed for the NA catalyst. In addition, peaks corresponding to *d*- spacing values at 2.41 (37.2°), 2.00 (45.5°) and 1.43 (65°) are detected. These *d*- spacing values are similar to the value of $NiAl_2O_4$ phase (i.e., 2.40 (37°), 2.01 (45°) and 1.42 (65.5°)). The interaction between nickel and alumina support is complex; namely, Ni^{2+} could disperse on the surface of Al_2O_3, or diffuse into the bulk structure of Al_2O_3 to different extents and form nickel aluminate, $NiAl_2O_4$ [32]. However, from the XRD spectra and the estimated *d*-spacing values, it is highly possible that the surface amorphous $NiAl_2O_4$ spinel species was predominantly formed on the NA catalyst.

As for the NLA catalyst, only NiO and $LaAlO_3$ peaks, with a small reflection of (440) plane of γ-Al_2O_3 are observed. Based on the stoichiometric ratio of La to Al (1:1) formation of $LaAlO_3$, it is clear that in this study not all aluminium atoms participated in the thermally induced (via high temperature calcination of 900°C) solid state formation of $LaAlO_3$ [33].

From Figure 5-1(a), upon H_2 reduction, a noticeable decrease in the peak intensity at ca. 37° can be observed for the NA catalyst. This reduction could have taken place possibly from $NiAl_2O_4$ and NiO species. However, from Figure 5-1 (b), for the reduced NLA catalyst, only Ni and $LaAlO_3$ peaks can be seen.

It can be observed that the XRD pattern of NL exhibit characteristic reflections of La_2O_3, NiO and $LaNiO_3$ (Table 5-1). However, upon reduction, as can be seen from Figure 1c, the $LaNiO_3$ peaks have disappeared, suggesting that the Ni-La interaction could be completely destroyed upon reduction, resulting in the participation of only Ni dispersed on the La_2O_3 support in the catalytic activity.

Table 5-1 XRD phase references from Powder Diffraction (PDF) database [31]

Phase	**PDF No.**
$LaAlO_3$	#00-031-0022
γ-Al_2O_3	#00-050-0741
α-Al_2O_3	# 00-001-1296
NiO	#00-001-1258
Ni	#00-001-1258
$NiAl_2O_4$	#00-001-1299
La_2O_3	# 00-024-0054
$LaNiO_3$	# 00-88-0633

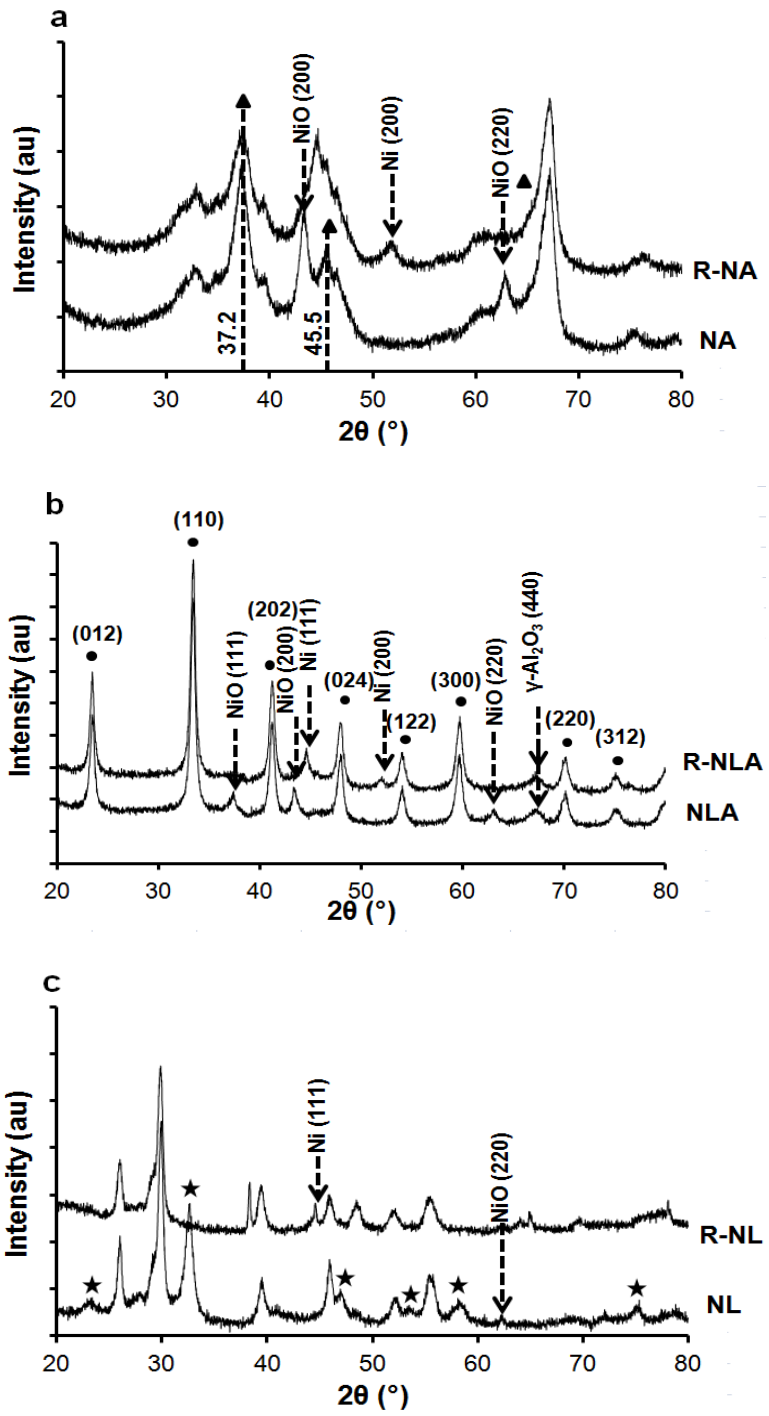

Figure 5-1 XRD patterns for fresh and reduced (R) catalysts; (a) NA and R-NA; (b) NLA and R-NLA; and (c) NL and R-NL. The symbols represent: ▲: amorphous surface $NiAl_2O_4$ spinel conjoined with Al_2O_3 phases (broadened lattice; ■ $LaAlO_3$ *R*3m phase; ★: $LaNiO_3$ phase.

5.2.2. H_2-TPR profiles

In order to investigate the existence of nickel aluminate on both NA and NLA catalysts, H_2-TPR was carried out for the synthesized catalysts and the result is shown in Figure 5-2. It is known that the reduction temperatures lower than 500°C correspond to NiO that interacts weakly with the support [34]. Temperatures above 500°C relate to Ni interacting with bulk phase of the support. For the NL catalyst, the reduction profiles between 300-500°C correspond to the free NiO and amorphous NiO phase. The higher temperature peaks between 500-650°C suggest the reduction of the transition phases of $LaNiO_3$ into metallic Ni° [35]. This result tallies with the XRD results indicating presence of Ni in the form of NiO and $LaNiO_3$.

On the other hand, for the NA catalyst, there are two peaks coinciding at 515°C and 695°C, suggesting that there is medium-strength interaction of Ni with the alumina support. Implicitly for Al_2O_3 based supports, reduction temperatures above 600°C denote reduction of highly amorphous surface $NiAl_2O_4$ spinel [36], whilst those above 800°C relate to bulk $NiAl_2O_4$ reduction. Moreover, since the predominant reduction peak appears at *ca.* 695°C (i.e., 72% of total H_2 consumption), the Ni species on the reduced NA catalyst was in the form of amorphous surface $NiAl_2O_4$ and this result is in good agreement with the XRD results.

TPR profile of NLA catalyst clearly shows the reduction of free NiO species, weak and strongly bound Ni species. Explicitly, presence of amorphous surface $NiAl_2O_4$ is indicated with reduction peak at 699°C (59% of total H_2 consumption). However, this amorphous surface $NiAl_2O_4$ species was not clearly observed by XRD, since the peaks are more likely to be dwarfed by the presence of the more crystalline $LaAlO_3$ diffraction

peaks. To confirm the H_2-TPR result and presence of surface $NiAl_2O_4$ species in NLA catalyst, further characterizations such as UV-VIS and ^{27}Al-MAS NMR were conducted and discussed in the subsequent sections. This is an interesting phenomenon since reduction of the amorphous spinel-like structure is more dominant compared to the other peaks even in the presence of $LaAlO_3$ nano-crystallites on the support.

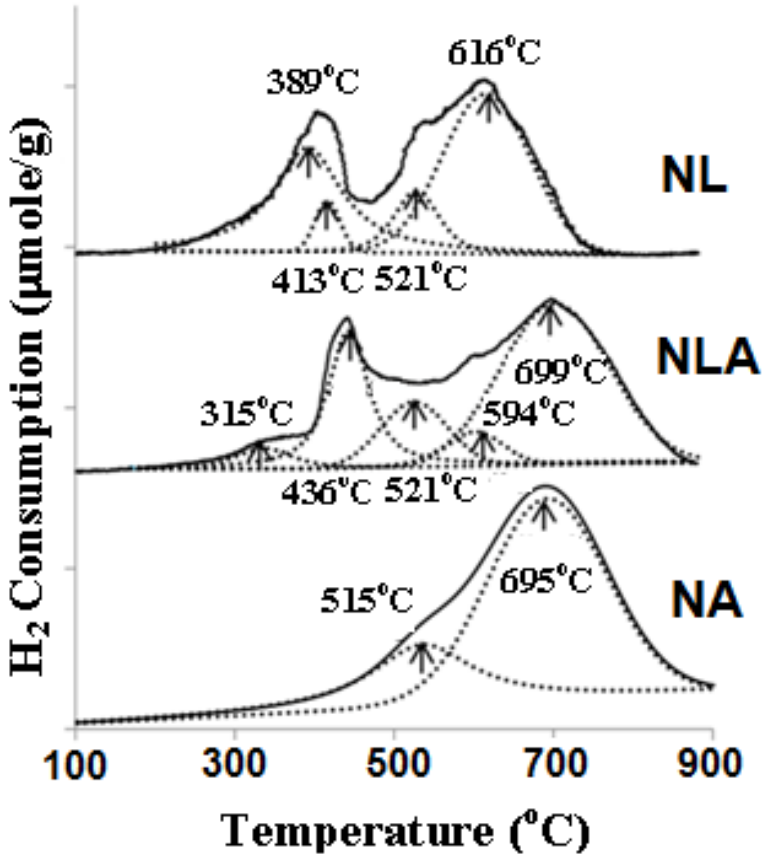

Figure 5-2 H_2-TPR profiles for fresh catalysts

5.2.3. Textural and physicochemical properties

Table 5-2 shows the textural and physicochemical parameters of the reduced catalysts, as well as metallic particle sizes. The data show that the reduced NA catalyst has the highest surface area. However, the surface area of NLA catalyst was

comparatively lower due to the incorporation of La in the support to form the $LaAlO_3$-Al_2O_3 perovskite-oxide phase. The presence of $LaAlO_3$ nanocrystallites on the NLA catalyst inevitably provoked a loss in surface area due to diminution of pore size diameter which occurs when La is incorporated into the alumina network [37]. The reduced NL catalysts exhibited the lowest surface area.

The Ni° particle sizes by TEM observation (Figure 5-11) and summarized in Table 5-2 are in the order of NA<NLA<NL. It is worth noting that there is correlation between the Ni particle size and surface area of the catalyst. Namely, the bigger Ni° particle sizes are obtained on a catalyst with lower surface area. NA has the smallest average Ni° particle size due to the surface interaction to form the amorphous $NiAl_2O_4$ spinel structure. Even though H_2-TPR analysis indicates presence of amorphous $NiAl_2O_4$ spinel structure as well on the NLA catalyst, the average Ni° particle size is greater than NA. This is due to presence of $LaAlO_3$ phase which reduces the dispersion of Ni° on alumina, hence leading to larger average particle size compared to NA. NL has the largest average Ni° particle size and due to its lowest surface area among all the catalysts.

Table 5-2 Textural and physicochemical parameters of reduced (R) catalysts

Sample	S_{BET}[a] (m^2/g)	Average Ni° particle size[b] (nm)
R- NA	78	5.2±1.3
R- NLA	29	8.4±3.5
R- NL	14	10.6±2.8

a) Determined from application of BJH method to experimental isotherms

b) Determined from TEM measurement of reduced catalysts

5.2.4. XPS analysis for La chemical state

It has been reported that $LaAlO_3$ nanocrystallites are surface bound on the alumina surface upon solid state reaction of La with Al at a calcination temperature of 900°C [38]. The La coordination in NLA and NL catalysts has been investigated via XPS. Figure 5-3 shows a main XPS peak in the binding energy (BE) range of 833-835 eV. NL shows the La $3d_{5/2}$ spectra at the BE of 834.3 eV corresponding to the characteristic binding energy of La_2O_3. The characteristic BE for $LaAlO_3$ is 833.8 eV [39-40]. The La $3d_{5/2}$ spectra of the NLA catalyst observed at 834.7 eV slightly differs from the standard $LaAlO_3$ due to strong local concentration of lanthanum inherent to tridimensional growth of $LaAlO_3$ nano-crystallites on the alumina [38]. This result suggests that $LaAlO_3$ nanocrystallites are present on the surface of the alumina support.

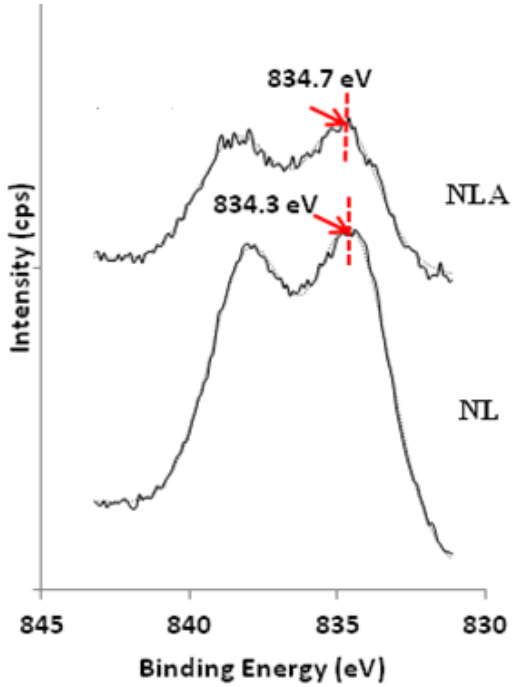

Figure 5-3 XPS La $3d_{5/2}$ profiles for NL, NLA and NLAO catalysts

5.2.5. UV-DRS analysis for NA and NLA catalyst

In order to further investigate the Al^{3+} and Ni^{2+} coordination in the NLA and NA catalysts, UV-DRS analysis was performed. Figure 5-4 (a) shows prominent bands in the wavenumber region of 250-400 nm for γ-Al_2O_3 (278 nm) and $LaAlO_3$-Al_2O_3 (dual bands at 281 and 306 nm) supports. Based on literature [41], UV absorption band of 270 nm was observed for γ-Al_2O_3. It is concurred that increase in wavenumber upon La addition leads to a change in coordination of Al^{3+} due to interaction with La^{3+} [37].

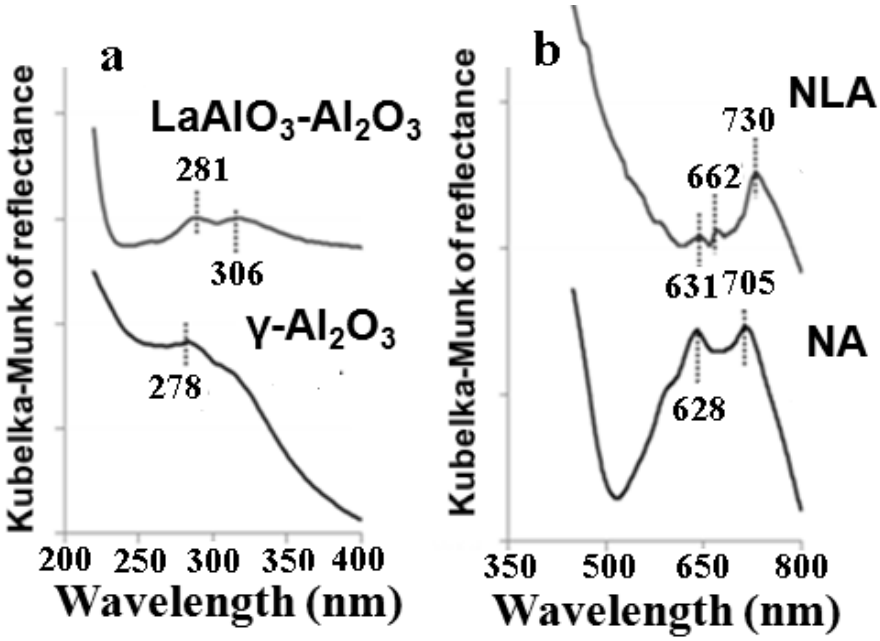

Figure 5-4 UV-DRS data for (a) γ-Al_2O_3 and $LaAlO_3$-Al_2O_3 supports (b) NA and NLA catalyst.

Figure 5-4 (b) shows spectral information with respect to Ni^{2+} coordination of the NA and NLA catalysts. As discussed in Sections 5.2.1 and 5.2.2, Ni mostly exists as amorphous surface $NiAl_2O_4$ spinel structure upon being supported on γ-Al_2O_3. As for the

NLA catalyst, although not apparent on XRD data, however, H_2-TPR behaviour suggests presence of this spinel structure similar to NA catalyst. Figure 5-4 (b) shows that for the NA catalyst, absorption bands at 628 and 705 nm are observed. On the other hand, the NLA catalyst shows an obvious intense absorption band at 730 nm with minor edges at 631 and 662 nm. It was reported that absorption bands at 714-769 nm correspond to Ni^{2+} in octahedral (O_h) position whereas those at 626 nm correspond to Ni^{2+} in tetrahedral (T_d) position [42].

Although the exact absorption values slightly differ in literature [42-45], however, they are in general agreement that Ni^{2+} in T_d environment have more pronounced peaks in the region of 600-640 nm due to the d-d electronic transition of the T_d-Ni^{2+} cations, and Ni^{2+} in O_h environment dominates more in the region above 720 nm. Also a red-shift to above 640 nm shows lower tendency to T_d environment. These results suggest that majority of Ni^{2+} exist in Td environment for NA catalyst, and O_h environment for NLA catalyst. Based on UV-DRS spectra, this confirms that for the NA catalyst, amorphous surface $NiAl_2O_4$ spinel structure in the *normal coordination* is formed which corresponds to its reduction peak *ca.* 700°C from H_2-TPR profile. However, for the NLA catalyst, presence of majority Ni^{2+} in O_h environment gives evidence that this could be due to presence of amorphous surface $NiAl_2O_4$ spinel structure in the *inverse coordination*.

$NiAl_2O_4$ is known to exist in both normal spinel $(Ni^{2+})[Al_2{}^{3+}]O_4$ and to an inverse spinel, $(Al^{3+})[Ni^{2+}Al^{3+}]O_4$ coordination depending on the degree of inversion [46]. In this process, the larger Ni^{2+} ions which occupy T_d sites in a normal spinel move to O_h sites in an inverse spinel while half of the smaller Al^{3+} ions move in the opposite direction. Hence, in this regard, the tendency of inverse spinel formation in NLA as compared to

NA could be reverted to the fact, that most of the octahedrally coordinated Al^{3+}cations have reacted with La^{3+} to form the perovskite-oxide support, hence the availability of tetrahedrally coordinated Al^{3+} to react with Ni^{2+} is more probable forming the inverse spinel configuration.

Thus, the UV-DRS results suggest that Ni^{2+} is prone to form inverted spinel structure in $LaAlO_3$-Al_2O_3 compared to conventional γ-Al_2O_3 structure. ^{27}Al-MAS NMR was conducted and discussed in the next section to confirm the coordination of Al^{3+} species for both NA and NLA catalysts with their respective supports in order to correlate to the findings from UV-DRS results.

5.2.6. ^{27}Al-MAS NMR for NA and NLA catalyst

Figure 5-5 shows the ^{27}Al-MAS NMR spectra for the NLA catalyst-support pair versus the NA catalyst-support pair. Based on the coordination structure of γ-Al_2O_3 from literature, the four-coordinated Al-O (IV) occurs at about 50-80 ppm and the six-coordinated Al-O (VI) occurs at about -10 to 15 ppm [47]. As indicated in Figure 5-5, T_d and O_h sites can be observed for both the support catalyst pairings of NA and NLA.

For the γ-Al_2O_3 support, the O_h and T_d peaks are located *ca.* 10.4 ppm and 66.3 ppm, respectively. Upon impregnation with Ni, the peaks shift to the right at 9.0 and 65.5 ppm respectively, indicating that Ni could have interacted with both the O_h and T_d sites. However, for the $LaAlO_3$-Al_2O_3 support, the O_h and T_d peaks can be seen at *ca.* 13.7 and 65.2 ppm respectively. The sharp crystalline chemical shift at 13.7 ppm is due to the formation of $LaAlO_3$, which we have verified based on spectra of the pure phase $LaAlO_3$ (not shown). Upon Ni impregnation, no change was observed for the O_h site, but

chemical shift occurred to the left (deshielding) for the T_d sites. It has been reported that deshielding of electron field of T_d Al atoms in metal supported alumina as opposed to pure active alumina indicates migration of metal ions in the alumina matrix [48].

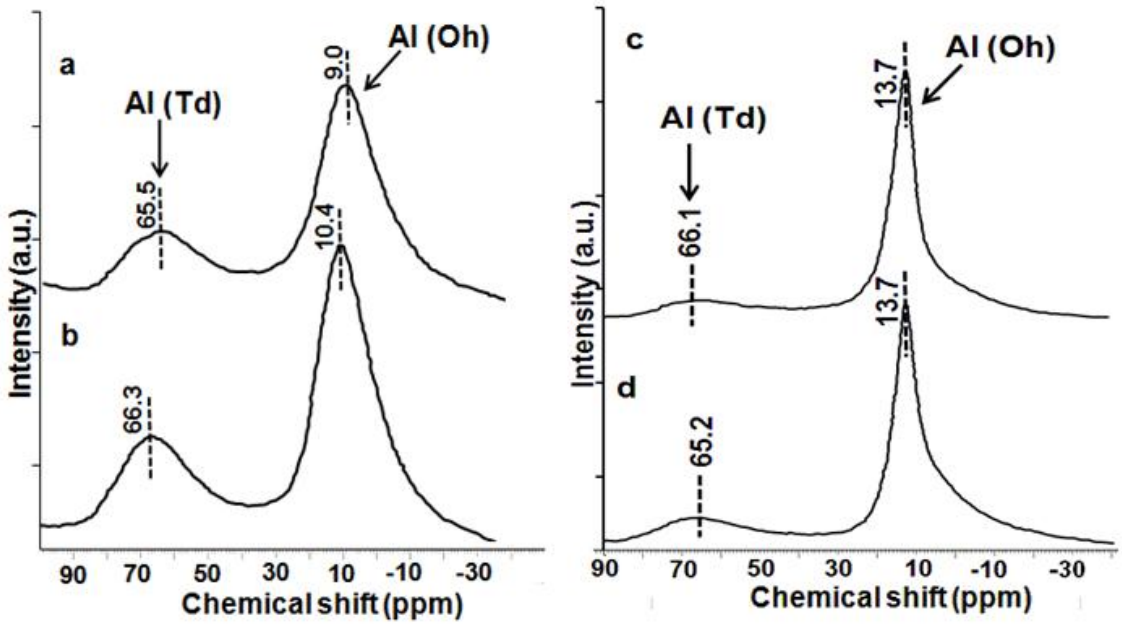

Figure 5-5 ^{27}Al-MAS NMR data for (a) NA; (b) γ-Al_2O_3; (c) NLA; (d) $LaAlO_3$-Al_2O_3

Ni is a paramagnetic nuclei, and a loss of signal is observed when a paramagnetic ion is near the NMR nucleus [49]. Reduction of signal intensity indicates the proximity of the compounds to the Ni ions [50]. Numerical approximation of the peak area shows that the catalyst/support ratios for the O_h/T_d+O_h sites for both NA and NLA are 1.55 and 2 respectively. This indicates that upon Ni impregnation, the O_h sites are more prominently observed the NLA catalyst compared to the NA catalyst. For the NA catalyst-support pair, a reduction of intensity was observed for both Oh and T_d sites. However, for the

NLA catalyst-support pair, only the T_d sites show reduction in intensity coupled with chemical shifts. Furthermore from the numerically approximated site ratios, it is evident that Ni ions in NLA have higher affinity towards T_d sites compared to Ni ions NA catalyst. This therefore confirms that in the NLA catalyst, the Ni^{2+} ions have indeed interacted and diffused into the surface lattice vacancies of the alumina [48] to form inverse spinel with the Al^{3+}cations in T_d coordination, hence confirming all our previous postulations and findings above.

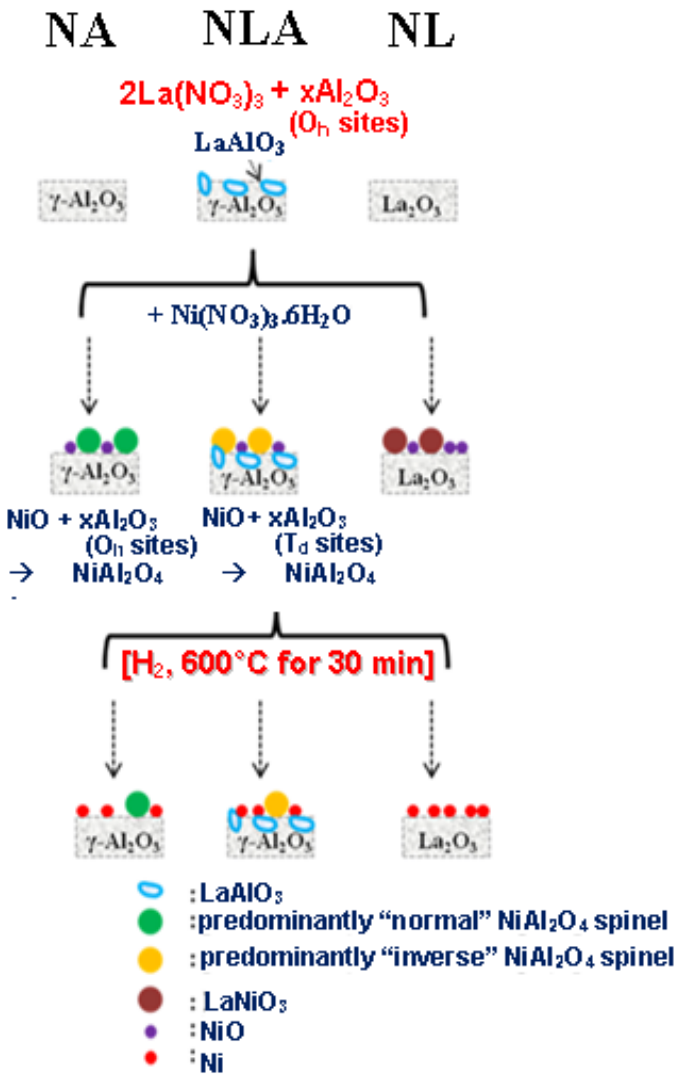

Figure 5-6 Proposed schematic for NA, NLA and NL catalyst synthesis

Figure 5-6 shows the proposed schematic for the NA, NLA and NL catalyst synthesis. For the catalyst support of NLA, as explained previously, the La and Al precursors initially react via solid state reaction (in O_h sites of Al^{3+}) due to the high temperature calcinations to form $LaAlO_3$ nanocrystallites on the alumina support. Upon impregnation with Ni the sintering conditions enables the Ni^{2+} to interact strongly with the supports. In this regard, the Ni^{2+} preferentially interacts with the Al^{3+} in O_h coordination forming $NiAl_2O_4$ for the NA catalyst. However, for the NLA catalyst, the dominant availability of Al^{3+} in T_d coordination due to the presence of the $LaAlO_3$ species, results in formation of the inverse $NiAl_2O_4$ spinel structure. When the Al^{3+} sites are exhausted, the other Ni^{2+} intercalates between the $LaAlO_3$ and the inverse $NiAl_2O_4$ in the form of NiO species. Finally for the NL catalyst, the Ni interacts to form $LaNiO_3$ in the presence of other NiO species. However, upon reduction at 600°C, the spinel structures in both NA and NLA catalysts do not decompose readily and are still partially present. On the other hand, the NL catalyst undergoes near-complete reduction to free Ni and La_2O_3 oxide.

5.2.7. *In-situ* Py-FTIR for NA and NLA catalyst

Alumina generally possesses both weak Bronsted (proton donor) acidity, originating from isolated surface hydroxyl groups, and when partially dehydroxylated, Lewis (electron acceptor) acidity in the form of cus surface Al^{3+} sites, created by the removal of Al–OH groups [51]. In order to determine the change in acidity with La introduction, Py FTIR was carried out for both the NA and NLA catalysts as shown in Figure 5-7. For the NA catalysts, upon evacuation at room temperature, peaks at positions

1445, 1492 and 1594 cm^{-1} can be observed. The sharp peak at 1445 is related to physisorbed Py which overlaps with the Lewis acid sites of the alumina. With increasing temperature, a shift towards higher wavenumber corresponding to Lewis acid sites can be clearly observed. The weak peak at 1492 correspond to both Bronsted and Lewis acid sites and were easily removed at above 100°C, whereas the peak at 1594 correlate to physisorbed Py [51-54].

On the other hand, for the NLA catalysts, the peaks are less distinguishable compared to the NA catalyst. The peaks at 1443 and 1590 cm^{-1}, ascribed to physisorbed Py was easily removed at temperatures above 100°C. It is apparent the Lewis acidity visible in the NA catalyst at temperatures greater than 100°C, was not detected in the NLA catalyst. However, presence of both Bronsted and Lewis acid sites can be discerned from the weak peak at 1490 cm^{-1}. Therefore, it is certain that incorporation of La in the alumina framework of the support clearly aids in reducing the acidic strength of the support.

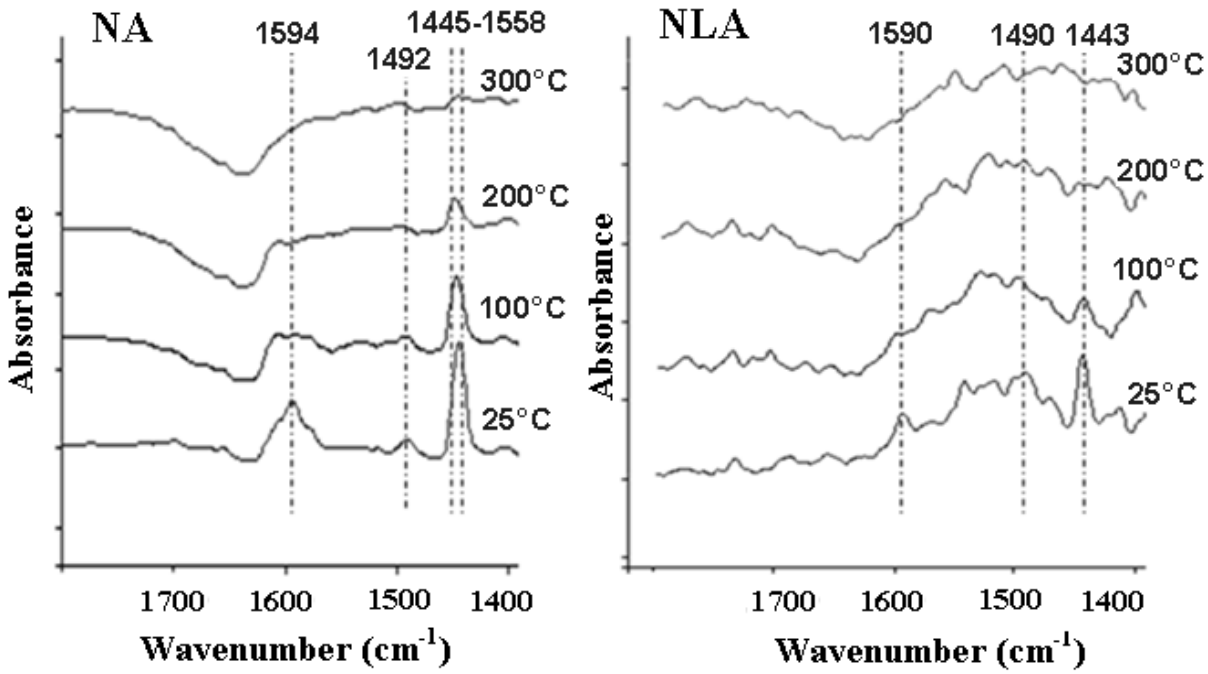

Figure 5-7 *In-situ* Py FTIR for NA and NLA catalyst

5.2.8. Catalytic activity and stability for DRM

Figure 5-8 (a) and (b) show the CH_4 and CO_2 conversions respectively via the catalytic DRM reaction over the NA, NLA and NL catalysts. DRM reaction was chosen as the probe reaction which can effectively utilize both CO_2 and CH_4 greenhouse gases. The NLA catalyst shows the most stable performance despite lower initial conversions compared to the NA catalyst. This is followed by the performances of NA and NL catalysts.

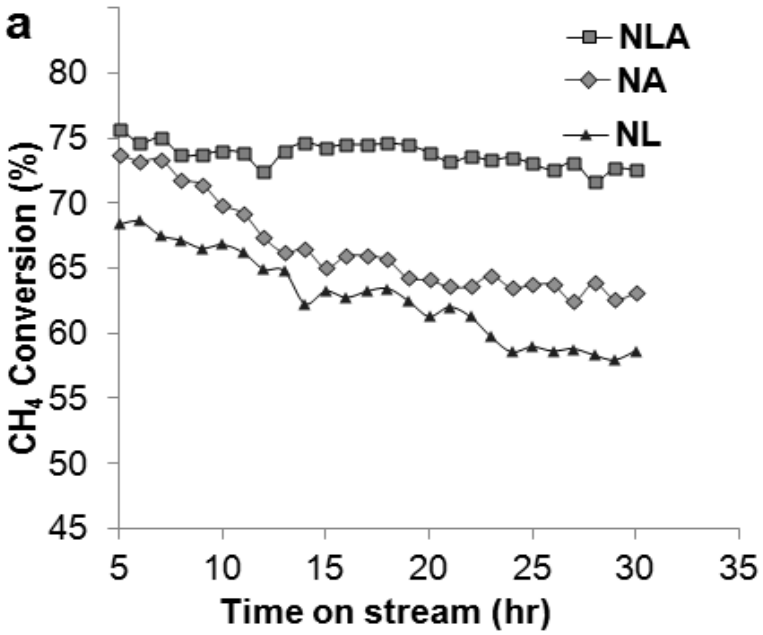
a
NLA
NA
NL
80
75
70
65
60
55
50
45
CH_4 Conversion (%)
5
10
15
20
25
30
35
Time on stream (hr)

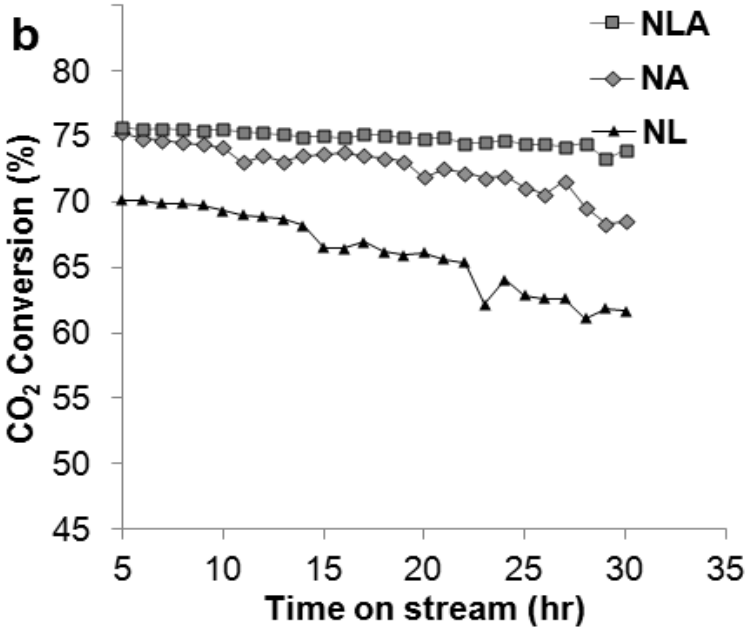
b
NLA
NA
NL
80
75
70
65
60
55
50
45
CO_2 Conversion (%)
5
10
15
20
25
30
35
Time on stream (hr)

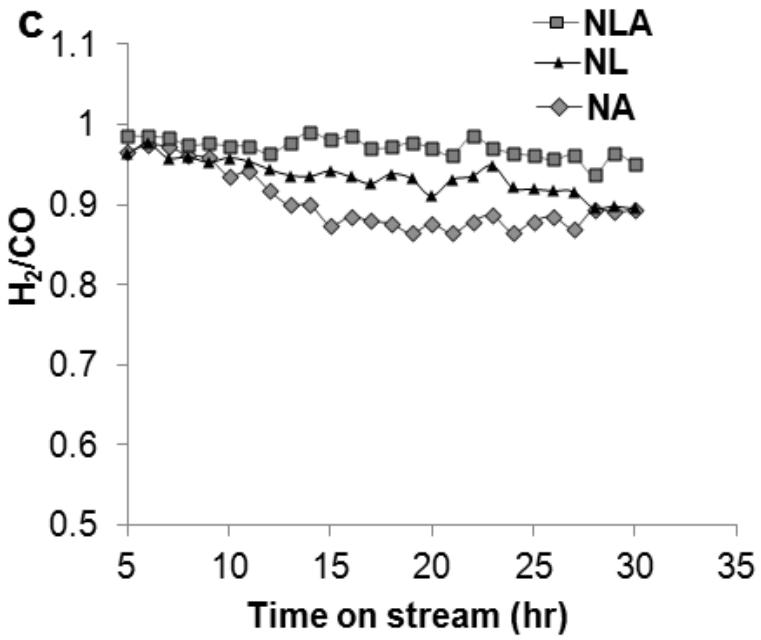

Figure 5-8 DRM catalytic performances at 700°C (a) CH_4 conversion; (b) CO_2 conversion; and (c) H_2/CO ratio

The deactivation of NA catalyst was less severe compared to the NL catalyst. NLA catalyst, on the other hand, showed relatively stable reactant conversions for both CH_4 and CO_2. In terms of selectivity in the form of H_2/CO ratio (as shown in Figure 5-8 (c)), all the catalysts exhibit values lower than the stoichiometric ratio of 1, suggesting the occurrence of reverse water gas shift (rWGS) side reactions. On the other hand, NA catalyst had the lowest overall H_2/CO ratio. This suggests greater tendency to reverse water gas shift (rWGS) reaction on the alumina supported catalyst due to the dehydration and dehydroxylation which prominently occurs on aluminium hydroxide. Possible presence of higher coverage of surface hydroxyls on the alumina support favors formation of carboxyl species, which will dissociate to form CO. Consequently, this higher coverage of surface hydroxyls favors the rWGS reaction [55].

Figure 5-9 shows the TGA profiles for the 30 hours of DRM reaction. Generally, three kinds of carbonaceous species have been found over Ni catalysts designated as C_α (removed at 150-220^{o}C), C_β (removed at 530-600^{o}C), and C_γ (removed at >650^{o}C). C_β and C_γ increase during prolonged exposure under reaction conditions [56]. Based on the carbon deposition rate, the amount of carbon was found to increase in the order of NLA (18 mgC/gcat.hr) < NA (21 mgC/gcat.hr) < NL (47 mgC/gcat.hr). It is worth noting that this order is in general agreement with the order of catalytic activity based on Figure 5-9, i.e., NLA>NA> NL.

Removal of the carbon species usually occur above 700°C for alumina supported Ni- catalysts [57]. The high gasification temperature of 695°C observed in the NA catalyst indicates pyrolytic type of carbon which is highly inert. Presence of pyrolytic carbon correlates to the higher acid strength of the support compared to NLA catalyst as shown from Py-FTIR results. For the NLA catalyst, the carbon gasification temperature is in the intermediate region of C_β and C_γ indicating more filamentous or fibrous type of carbon. It was reported that the more graphitic carbon is seen as an increase in chain length, and with a decrease in activity implies that carbon formation has a deactivating effect compared to the fiber type of carbon [58]. However, the deactivation effect was most severe for NL catalyst even though DTA profile in Figure 5-9 (c) indicates presence of fiber type of carbon formation. Explicitly, the small endothermic peak above 700°C is not due to graphitic carbon formation as in the case of NA, but is attributed to the decomposition of La carbonates, (i.e. $La_2O_2CO_3$ oxycarbonate species) as La carbonates decompose *ca.* 1000°C [59].

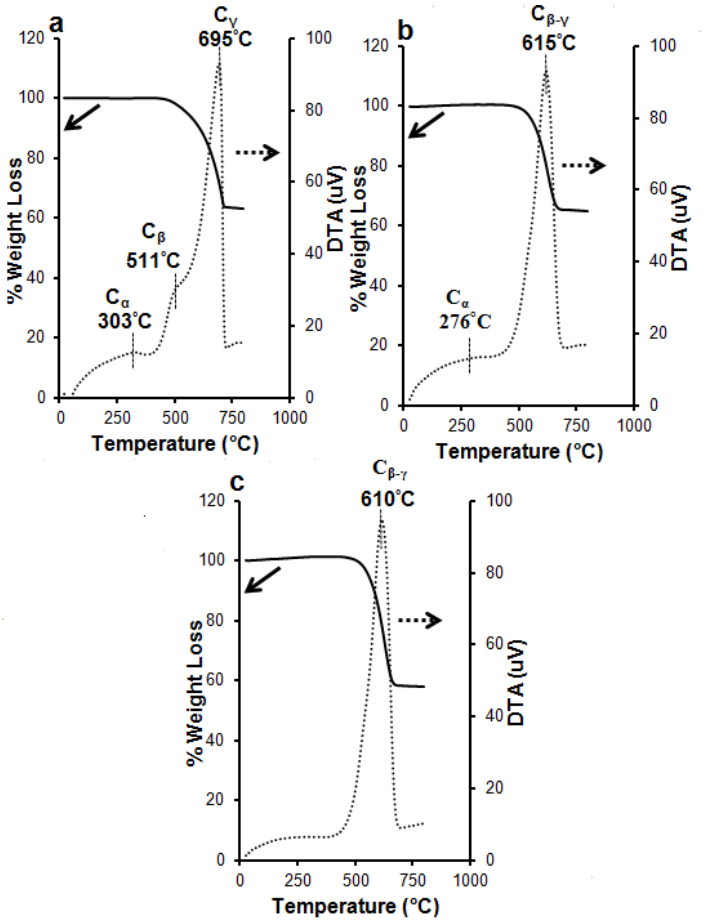

Figure 5-9TGA-DTA profiles of the spent catalysts after DRM reaction at 700°C for (a) NA, (b) NLA and (c) NL

In general alumina based catalysts are known to have the serious problem of carbon deposition; however, in this case, for both the NA and NLA catalysts, the amount of carbon decomposition seems to be lower than NL catalyst due to formation of surface nickel aluminate spinel structures, leading to stronger interaction between catalyst and the support. Hence, the regenerability of Ni on the surface by CO_2 is enhanced by the dispersing ability for Ni ions in ionic supports like alumina [60]. As a result; the amount of deposited carbon is lower for both NA and NLA catalysts compared to NL catalyst.

However, in terms of overall catalytic activity and stability, the performance of NLA catalyst is the best.

Furthermore progressive encapsulation of crystallites puts an end to filament growth, rendering the active site inaccessible. SEM images in Figure 5-10 shows that the NL catalyst exhibit more amorphous and agglomerated encapsulating type of carbon compared to the other spent catalysts. Due to its lower surface area, large particles become favorable sites for formation of carbon-encapsulating particles, which decrease the yield of nanotubes and is responsible for catalyst deactivation [61].

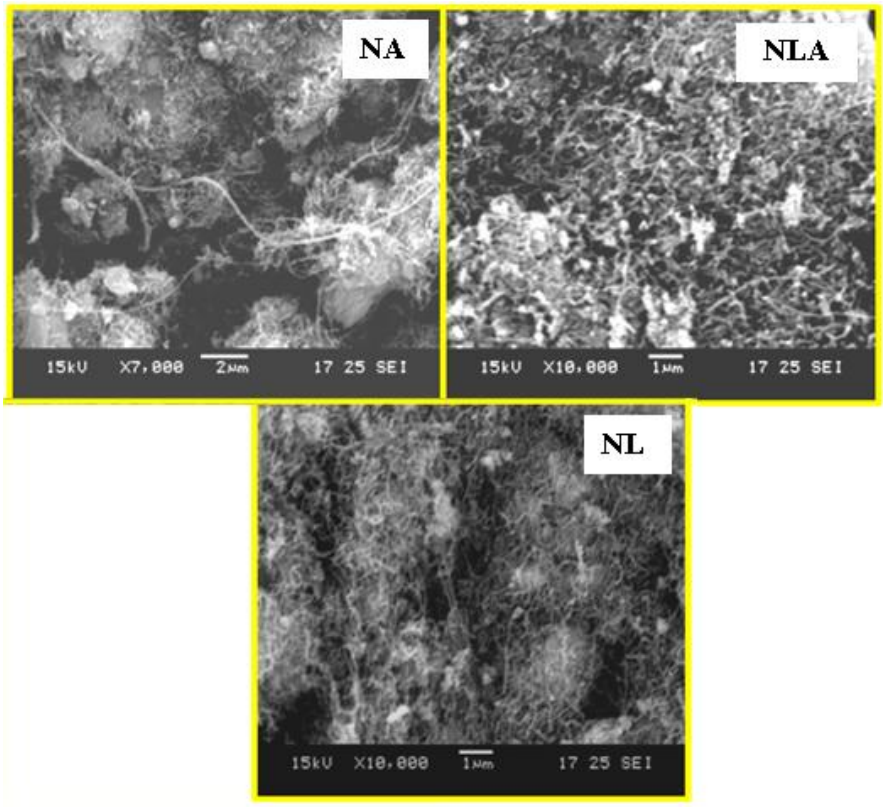

Figure 5-10 SEM images of spent catalysts after DRM reaction

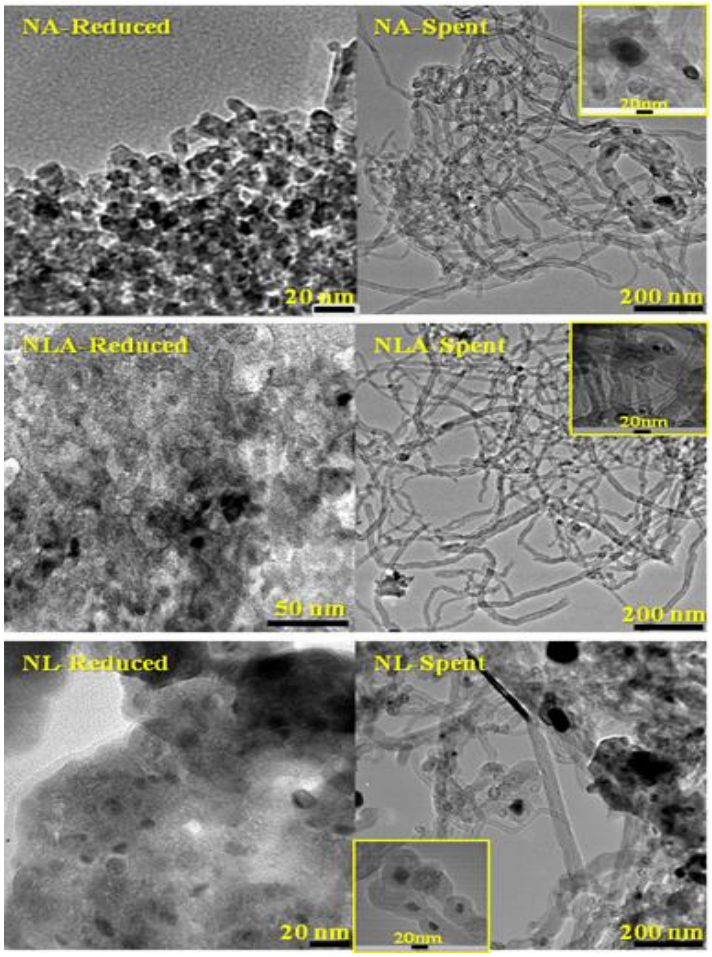

Figure 5-11 TEM images of reduced (left) and spent catalysts after DRM reaction at 700°C for 30 h (right)

It has been suggested that existence of nanotubes compared to amorphous type of carbon can enhance Ni catalyzed DRM reactions [15]. Furthermore, the spinel structure is able to yield bound state Ni-species after reduction which therefore decreases the available sites for carbon-encapsulating particles. Rostrup-Nielsen has demonstrated that lower coking rates can be expected if the metal is stabilized [62]. Thus, it can be deduced that the formation of surface spinel structures on both NLA and NA catalysts contribute to maintaining the catalytic performance with higher stability compared to NL catalyst.

However, from Figure 5-12 based on the particle size distribution of the spent catalysts shown, (obtained from TEM images, Figure 5-11), sintering on NA catalyst was much greater as compared to NLA catalyst, which explains the deactivation observed on NA catalyst during the 30 hours of DRM activity. For the NA catalyst, the Ni° particle size increased from 5.2 to 20.8 nm, whilst for the NLA catalyst, the Ni° particle size increased from 8.4 to 15.5 nm. Therefore, the sintering of nickel clusters occurred under reaction conditions. Sintering is an important route for the deactivation of Ni-based dry reforming catalysts [63].

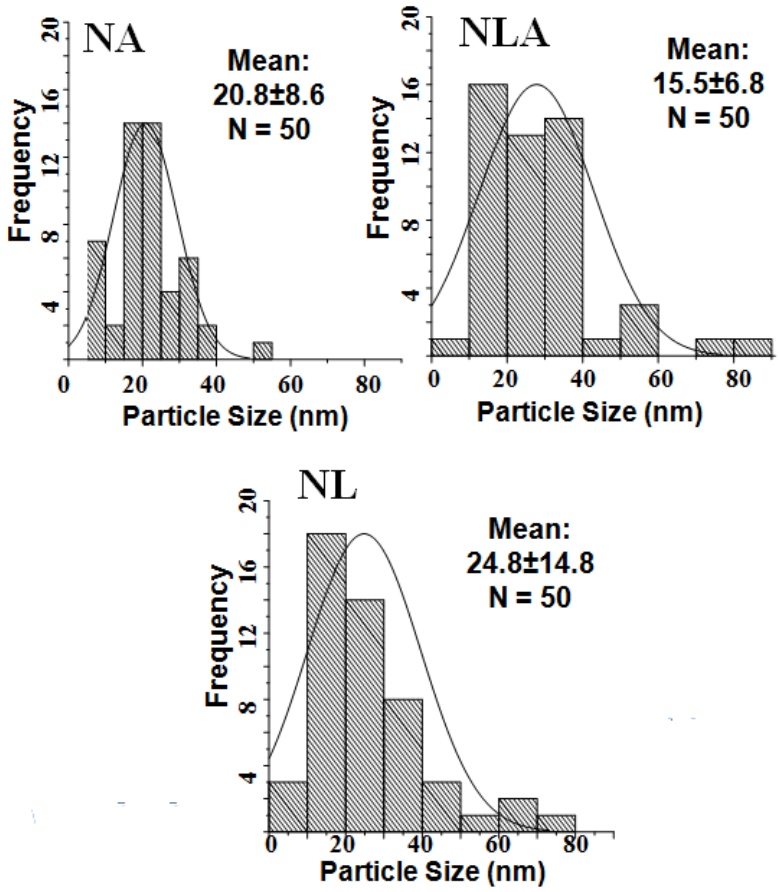

Figure 5-12 Ni° particle size distribution of spent catalysts after DRM reaction at 700°C

In order to further investigate the cause of this phenomenon, XRD profiles of spent NA and NLA catalysts are shown in Figure 5-13 using the reduced form as reference. Besides the additional graphite peak *ca.* 26°, presence of α-Al_2O_3 (306) at 77° can be observed as well on the XRD spectra of NA catalyst in Figure 5-13. This is surprising since transformation of γ-Al_2O_3 to α-Al_2O_3, which is the major cause of activity loss, generally occurs at sintering temperatures above 1200^{o}C [64]. Some studies have attributed this phase transformation phenomena to the cause of deactivation of $NiAl_2O_4$ species in the DRM reaction [65-67]. This occurs because Ni^{2+} in spinel structure which has been reduced to metallic Ni during reaction, falls out of the spinel structure, causing the nickel-less lattice conversion of the more reactive Al^{3+} in the Oh site from γ to α-alumina [67]. Bhattacharyya and Chang [67] have confirmed based on their previous studies that presence of alpha alumina in the system is not good for DRM reaction. In our case, besides formation of the alpha type of alumina species, some peaks which appear to be split are also observed on the main alumina structure. In fact, Gadalla and Bower [68] have found Ni/γ-Al_2O_3 displayed 20% higher activity compared to Ni/α-Al_2O_3. They attributed this to the stable allotrophic form of α-Al_2O_3 and its lower surface area which decreased the amount of contact that the gas had with the catalyst surface, thus resulting in lower conversion. In our case, besides the formation of the alpha type of alumina species, some peaks which appear to be split are also observed on the main alumina structure. Hence the catalyst deactivation on NA catalyst occurs due to gradual transformation to the alpha-type phases. However, the NLA catalyst did not exhibit any phase changes as shown in XRD spectra in Figure 5-13 because inverse spinel lattice has

the ability to impart extra stability to the catalyst so that the system can have sustained activity for longer durations [69].

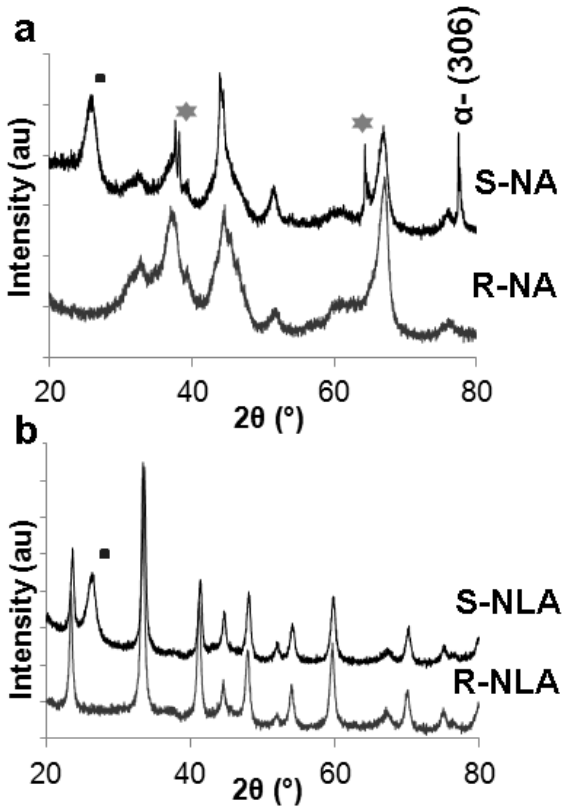

Figure 5-13 XRD patterns for comparison of reduced (R) and spent (S) catalysts, (a) NA and (b) NLA upon DRM at 700°C; The symbols represent: ■ : graphite peak at 26°; ✸ split peaks from reduced catalyst; α- (306) : alpha-alumina at (306) crystal plane

This proves that stabilization of the octahedral Al^{3+} ions in the $LaAlO_3$ matrix which forces the tetrahedral Al cations to react with the metallic active site to form inverse spinel structure can indeed prevent transformation into the undesirable α-Al_2O_3 phase. The phase transformation process from γ to α-Al_2O_3 leads to a loss of surface area and thus the sintering phenomenon was further induced on the NA catalyst during the prolonged DRM reaction. Furthermore, as explained by Oudet and Vejux [67] based on

their study on the sintering effect on La doped Pt/Al_2O_3 as automotive exhaust catalyst, the $LaAlO_3$ microdomains may be considered as physically impassable barriers delimiting areas within which metal sintering can take place, hence referring to contribution of the $LaAlO_3$ nanocrystallites on the alumina support.

In addition, UV-DRS spectra of the spent NA and NLA catalysts after DRM reaction at 700°C was conducted and shown in Figure 5-14. From here, it is evident that for the NA catalyst, a singular peak *ca*. 729 nm associated with Ni^{2+} on O_h sites was detected. This could be related to the presence of NiO in the catalyst, due to the oxidation of the metallic Ni species present in the catalyst after reaction. The peaks related to Ni^{2+} in T_d sites as found in the fresh NA catalyst (Figure 5-4) was not detected in the spent NA catalyst implying the destruction of the surface spinel structure due to the prolonged reaction at high temperature of 700°C. However, for the NLA catalyst, the features of the spent catalyst are rather similar to the fresh catalyst, with the presence of peaks at 669 and 731 nm is much greater than that of the NA catalyst. This suggests that besides NiO, the presence of Ni^{2+} in the form of the inverse $NiAl_2O_4$ surface spinel structure contributed to the much enhanced band intensity with a similar trend to that of the fresh catalyst. Therefore, the formation of inverse spinel structure helps to stabilize the catalytic performance since the tetrahedrally coordinated Al^{3+} possesses extra stability imparted by the inverse spinel configuration as compared to the octahedrally coordinated Al^{3+}.

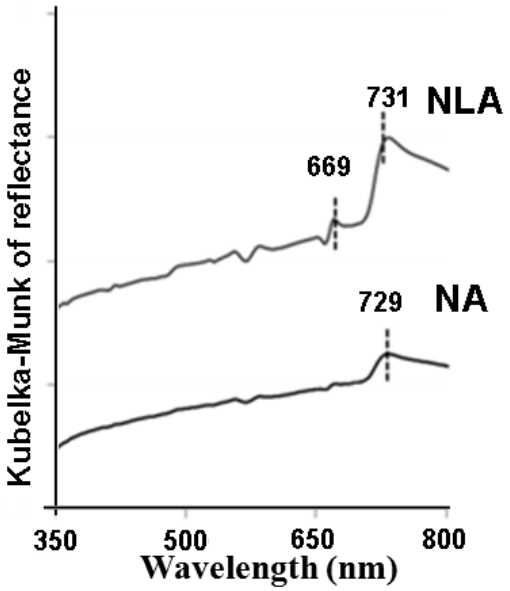

Figure 5-14 UV-DRS data for spent NA and NLA catalysts after DRM reaction at 700°C

In order to elucidate the most distinguishing factor in terms of deactivation observed on NA catalyst, the catalytic behaviours of NA and NLA catalysts were further investigated by operating the DRM reaction at 800°C. This is because at higher temperatures, thermodynamic constraints caused by diffusion limitations leads to low rate of carbon formation [71].

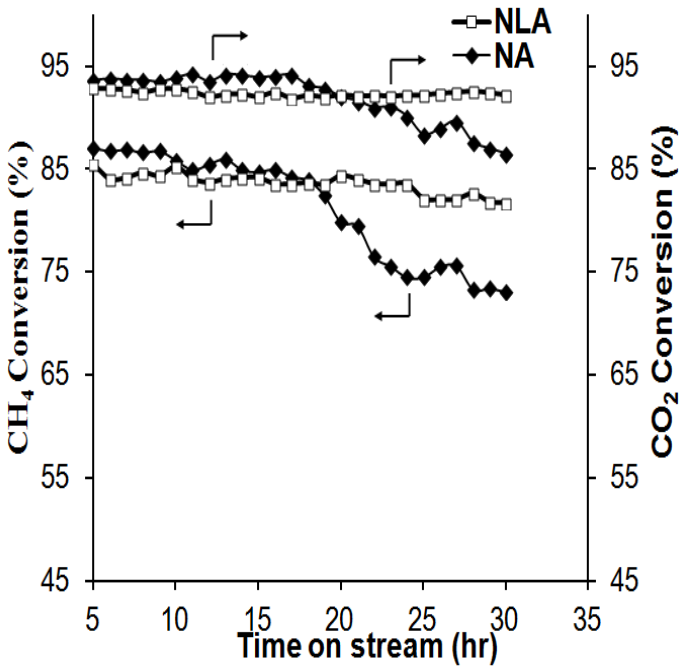

Figure 5-15 DRM catalytic performances at 800°C for NA and NLA catalysts

From Figure 5-15, after 19 hours of operation, the conversions of NA catalyst start to drop leading to loss of stability. The coking rate calculated from TGA is considerably lower at 9.1 and 9.3 mg C/g cat.hr for the NA and NLA catalyst respectively. This shows that effect of carbon amount for catalytic deactivation at the higher operating temperature can be eliminated.

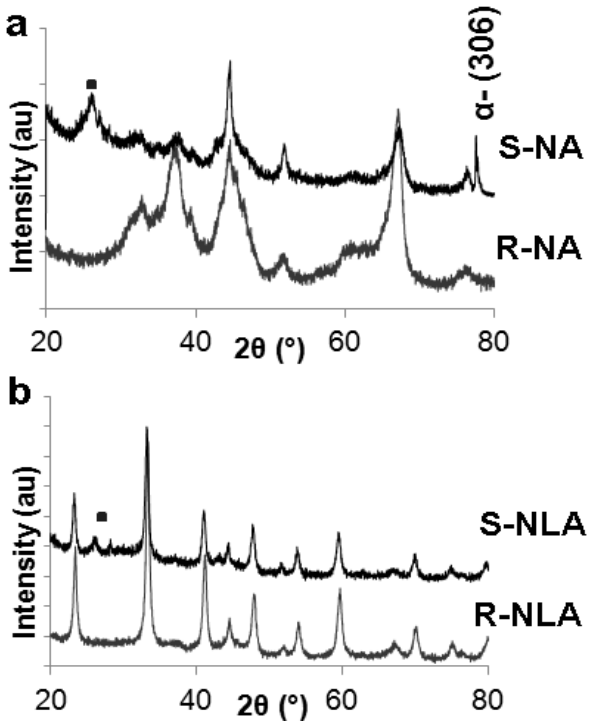

Figure 5-16 XRD patterns for comparison of reduced (R) and spent (S) catalysts, (a) NA and (b) NLA upon DRM at 800°C; The symbols represent: ■ : graphite peak at 26°; α- (306) : alpha-alumina at (306) crystal plane

Figure 5-16 shows the XRD of the spent NA and NLA catalysts after DRM at 800°C confirming that the alpha phase of alumina is still present in the NA catalyst and not on the NLA catalyst. Furthermore, the sintering is more pronounced for the Ni° particle sizes of the spent NA compared to spent NLA catalyst as shown in Figure 5-17. Hence, from these results, we can conclude that the cause of deactivation for NA catalyst at reaction temperature of 700°C could be due to formation of the more pyrolytic type of carbon as well as sintering associated with phase transformation from γ to α-Al_2O_3. However, upon increase in reaction temperature to 800°C, it took a much longer time for

loss in catalytic activity to take place and this is mainly attributed to the phase transformation of from γ to α-Al_2O_3.

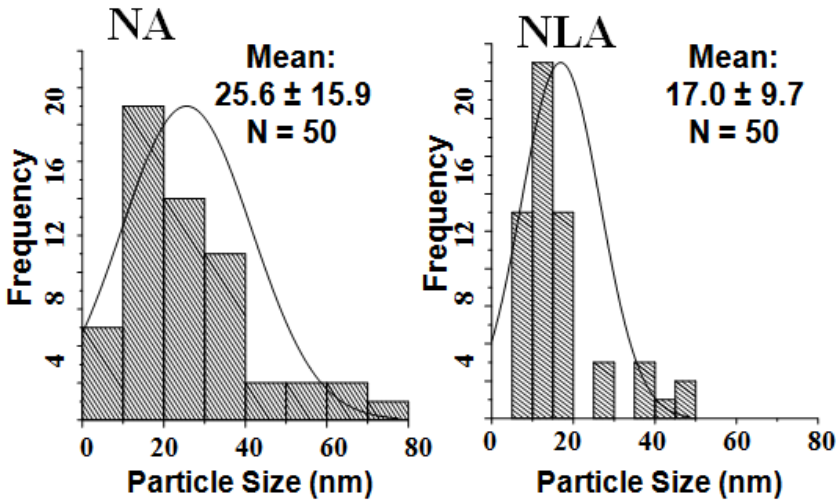

Figure 5-17 Ni° particle size distribution of spent catalysts after DRM reaction at 800°C

Most importantly, in order to elucidate the role of the inverse spinel structure, 5%Ni was impregnated on the $LaAlO_3$-Al_2O_3 support and is designated as 5%NLA. As we know from Figure 5-6, the NLA catalyst consists of both the free-form Ni and Ni in inverse spinel structure. Figure 5-18 (a) shows that the XRD profile of 5% NLA signifies dominant presence of $LaAlO_3$ with Al_2O_3 phases. NiO reflections were not observed. Furthermore, the H_2-TPR profile (shown in Figure 5-18 (b)) clearly suggests that most of the Ni has migrated to form strong interaction with the support, in the form of amorphous surface spinel structure. Therefore, based on this predominant inverse spinel structure, its role in catalyzing the reaction could be investigated. For comparison purposes, 5%Ni supported on γ-Al_2O_3 (5%NA) was also prepared and tested. As such, DRM activity was also performed at 700°C using 5% NLA and 5%NA to compare the specific activity (i.e. based on Ni loading) of the catalyst.

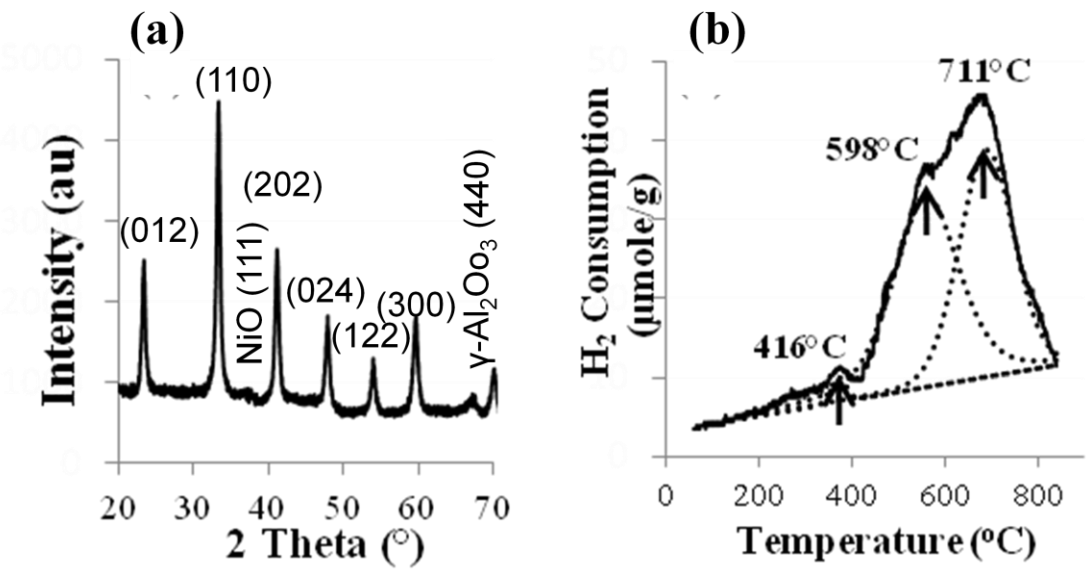

Figure 5-18 (a) XRD profile, (b) H_2-TPR profile of 5% NLA catalyst

From the catalytic activity results shown in Figure 5-19, we have confirmed that 5% NLA catalyst indeed is more stable than 5% NA, emphasizing the more specific role of the extra stability imparted by the inverse spinel structure. Table 5-3 shows a summary of the surface area and coking rate of the spent 5% NA and NLA catalysts. It can be concurred that although the differences in coking rate (12 mgC/gcat.hr for 5%NLA and 13.5 mgC/gcat.hr for 5% NA) is much lower compared to the 10%Ni loading. However, the CO_2 conversion achieved is much higher compared to the 10%Ni loading which explains the lower coking rate observed for the catalysts with 5% Ni loading.

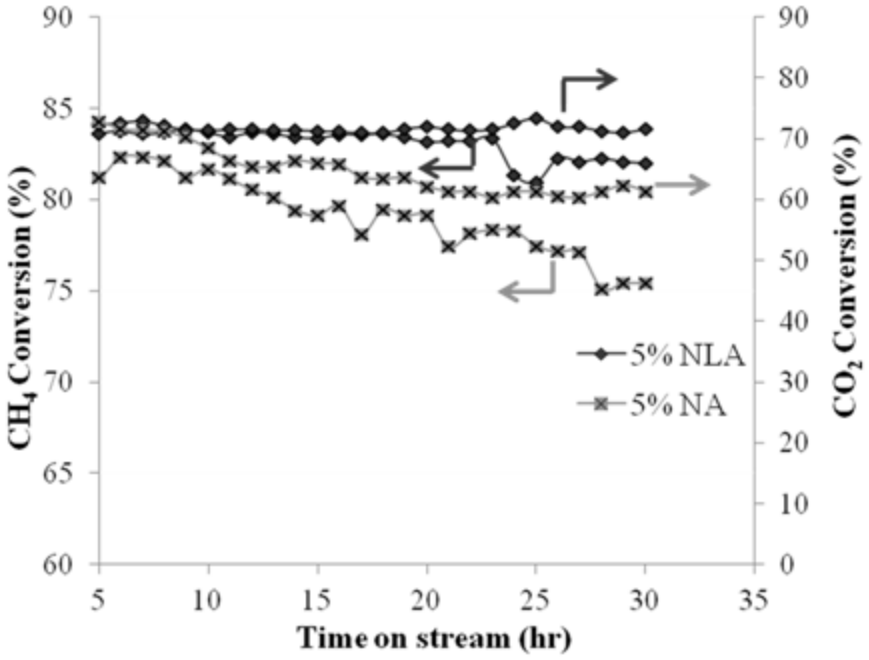

Figure 5-19 Catalytic CH_4 and CO_2 conversions for DRM of 5% NLA and 5% NA catalysts at 700°C

Table 5-3 Surface area and coking rate summary for 5% NLA and 5%NA catalysts

Sample	S_{BET}[a] (m^2/g) (Fresh Catalysts)	S_{BET}[a] (m^2/g) (Spent Catalysts)	Coking rate (mgC/g cat.hr)
5% NA	88	60	13.5
5% NLA	33	31	12

a) Determined from application of BJH method to experimental isotherms

5.3. Conclusion

In this study, the DRM catalytic behavior of Ni supported on *in-situ* formed $LaAlO_3$-Al_2O_3 (NLA) was investigated and compared with Ni supported on γ-Al_2O_3 (NA) and La_2O_3 (NL) oxides. Compared to the other supports, the NLA catalyst was found to exhibit active and stable performance for 30 hours of DRM operation. Based on several characterizations, we have confirmed presence of surface "inverse" spinel structure formation on NLA catalyst due to the interaction of La with the octahedral Al^{3+} sites forming *in-situ* $LaAlO_3$ –Al_2O_3. This phenomenon inadvertently induces the tetrahedrally coordinated Al^{3+} to react with the Ni^{2+} to form a predominantly inverse Ni aluminate spinel configuration. The forcible interaction of the tetrahedral sites to form the inverse spinel configuration in the NLA catalyst is one of the major reasons which hindered the catalytic deactivation compared to NA catalysts (where the γ-Al_2O_3 support underwent phase transformation to α-Al_2O_3) besides the presence of less graphitic carbon. As a result, the NLA catalyst stability can be maintained throughout the prolonged DRM reaction via the enhanced lattice stability proffered by the inverse spinel structure.

REFERENCES

[1] Guo, J.; Hou, Z.; Gao, J.; Zheng, X. *Fuel* **2008**, *87*, 1348-1354.

[2] Pan, W.; Song, C. *Catal. Today* **2009**, *148*, 232-242.

[3] Sutthiumporn, K.; Kawi, S. *Int. J. Hydrogen Energy* **2011**, *36*, 14435-14446.

[4] Sutthiumporn, K.; Maneerung, T.; Kathiraser, Y.; Kawi, S. *Int. J. Hydrogen Energy* **2012**, *37*, 11195-11207.

[5] Zhu, T.; Flytzani-Stephanopoulos, M. *Appl. Catal. A:Gen.* **2001**, *208*, 403-417.

[6] Zhu, X.; Huo, P.; Zhang, Y.P.; Cheng, D.G.; Liu, C.J. *Appl. Catal. B: Environ.* **2008**, *81*, 132-140.

[7] Pan, Y.X.; Liu, C.J.; Cui, L. *Catal. Lett.* **2008**, *123*, 96-101.

[8] Sun, G.B.; Hidajat, K.; Wu, X.S.; Kawi, S. *Appl. Catal. B: Environ.* **2008**, *81*, 303-312.

[9] Du, X.; Zhang, D.; Shi, L.; Gao, R.; Zhang, J. *J. Phys. Chem. C* **2012**, *116*, 10009-10016.

[10] Gates, B.C.; Lamb, H.H. *J. Mol. Catal.* **1989**, *52*, 1-18.

[11] Chase, G.C.; Espe, M.P.; Evans, E.A.; Ramsier, R.D.; Reneker, D.H.; Tuttle, R.W.; Rapp, J. *US Patent 20100009267* **2010**.

[12] Yan, Q.; Toghiani, H.; White, M.G. *J. Phys. Chem. C* **2007**, *111*, 18646-18662.

[13] Xu, J.; Chen, L.; Tan, K.F.; Borgna, A.; Saeys, M. *J. Catal.* **2009**, *261*, 158-165.

[14] Zhang, Z.; Verykios, X.E.; MacDonald, S.M.; Affrossman, S. *J. Phys. Chem.* **1996**, *100*, 744-754.

[15] Amin, M.H.; Mantri, K.; Newnham, J.; Tardio, J.; Bhargava, S.K. *Appl. Catal. B: Environ.* **2012**, *119-120*, 217-226.

[16] Hu, Y.H.; Ruckenstein, E. *Adv. Catal.* **2004**, *48*, 297-345.

[17] Cheng, Z.; Wu, Q.; Li, J.; Zhu, Q. *Catal. Today* **1996**, *30*, 147-155.

[18] Juan-Juan, J.; Roman-Martinez, M.C.; Illan-Gomez, M.J. *Appl. Catal. A: Gen.* **2004**, *264*, 169-174.

[19] Nikolla, E.; Holewinski, A.; Schwank, J.; Linic, S. *J. Am. Chem. Soc.* **2006**, *128*, 11354-11355.

[20] Bengaard, H.S.; Nørskov, J.K.; Sehested, J.; Clausen, B.S.; Nielsen, L.P.; Molenbroek, A.M.; Rostrup-Nielsen, J.R. *J. Catal*. **2002**, *209*, 365-384.

[21] Slagtern, A.; Olsbye, U.; Blom, R.; Dahl, I.M.; Fjellvåg, H. *Appl. Catal. A: Gen.* **1997**, *165*, 379-390.

[22] Kumagai, M.; Messing, G.L. *J. Amer. Ceram. Soc.* **1985**, *68*, 500-505.

[23] Kobayashi, H.; Tadanaga, K.; Minami, T. *J. Mater. Chem.* **1998**, *8*, 1241-1244.

[24] Schaper, H.; Doesburg, E.B.M.; van Reijen, L.L. *Appl. Catal.* **1983**, *7*, 211-220.

[25] Oudet, F.; Courtine, P.; Vejux, A. *J. Catal.* **1988**, *114*, 112-120.

[26] Beguin, B.; Garbowski, E.; Primet, M. *Appl. Catal.* **1991**, *75*, 119-132.

[27] Gao, W.; Li, M.; Klie, R.; Altman, E.I. *J. Elec. Spec. Related Phenom.* **2006**, *150*, 136-149.

[28] Bettman, M.; Chase, R.E.; Otto, K.; Weber, W.H. *J. Catal.* **1989**, *117*, 447-454.

[29] Imai, H.; Tagawa, T.; Kamide, N. *J. Catal.* **1987**, *106*, 394-400.

[30] Yang, X.D. *US Patent 7504085 B2*, **2009**, BASF.

[31] Powder Diffraction File-2 Release 2005; International Centre for Diffraction Data: Newton PA **2005.**

[32] Li, G.; Hu, L.; Hill, J.M. *App. Catal. A: Gen.* **2006**, *301*, 16-24.

[33] Yang, Z.; Bian, M.; He, A. *Appl. Catal. A: Gen.* **2001**, *205*,159-172.

[34] Pan, Y.X.; Liu, C.J.; Shi, P. *J. Power Sources* **2008**, *176*, 46-53.

[35] Maneerung, T.; Hidajat, K.; Kawi, S. *Catal. Today* **2011**, *171*, 24-35.

[36] Scheffer, B.; Molhoek, P.; Moulijn, J.A. *Appl. Catal.* **1989**, *46*, 11-30.

[37] Mortola, V.B.; Damyanova, S.; Zanchet, D.; Bueno, J.M.C. *Appl. Catal. B: Environ.* **2011**, *107*, 221-236.

[38] Boukha, Z.; Fitian, L.; Haro, M.L.; Mora, M.; Ruiz, J.R.; Jimenez-Sanchidrian, C.; Blanco, G.; Calvino, J.J.; Cifredo, G.A.; Trasobares, S.; Bernal, S. *J. Catal.* **2010**, *272*, 121-130.

[39] Chen, Y.; Liu, Y.; Niu, G.; Yang, Z.; Bian, M.; He, A. *Appl. Catal. A:Gen.* **2001**, *205*, 159-172.

[40] Haack, L.P.; de Vries, J.E.; Otto, K.; Chatta, M.S. *Appl. Catal. A: Gen*. **1992**, *82*, 199-214.

[41] Barrera, A.; Fuentes, S.; Viniegra, M.; , M.; Bogdanchikova, N.; Campa-Molina, J. *Mater. Res. Bull.* **2007**, *42*, 640-648.

[42] Priecel, P.; Kubicka, D.; Capek, L.; Bastl, Z.; Rysanek, P. *Appl. Catal. A: Gen.* **2011**, *397*, 127-137.

[43] Cimino, A.; Lo Jacomo, M.; Schiavello, M. *J. Phys. Chem.* **1971**, *75*, 1044-1050.

[44] Pompeo, F.; Nichio, N.N.; Souza, M.M.V.M.; Cesar, D.V.; Ferretti, O.A.; Schmal, M. *Appl. Catal. A: Gen.* **2007**, *316*¸175-183.

[45] Kim, P.; Kim, H.; Joo, J.B.; Kim, W.; Song, I.K.; Yi, J. *J. Mol. Catal. A: Chem.***2006**, 256, 178-183.

[46] Halevy, I.; Dragoi, D.; Ustundag, E.; Yue, A.F.; Arrendondo, E.H.; Hu, J.;

Somayazulu, M.S. *J. Phys. Condens. Matter*. **2002**, *14*, 10511-10516.

[47] Pergamon Materials Series, *Multinuclear Solid-State NMR of Inorganic Materials*, **2002,** *6*, 271.

[48] Kim, Y.; Kim, P. Kim, C.; Yi, J. *J. Mater. Chem.* **2003**, *13*, 2353-2358.

[49] La Mar, G.N.; Horrocks Jr, W.D.; Holm, R.H. NMR of Paramagnetic Molecules; Academic Press: New York, **1973**, 86.

[50] Zhang, W.; Sun, M.; Prins, R. *J. Phys. Chem. B.* **2003**, *107*, 10977-10982.

[51] Ballinger, T.H.; Yates, J.T. *Langmuir*, **1991**, *7*, 3041-3045.

[52] Busch, O.M.; Brijoux, W.; Thomson, S.; Schüth, F. *J. Catal.* **2004**, *222*, 174-179.

[53] Zaki, M.I.; Hasan, M.A.; Al-Sagheer, F.A.; Pasupulety, L. *Colloid. Surface. A*, **2001**, *190*, 261-274.

[54] Leydier, F.; Chizallet, C.; Chaumonnot, A.; Digne, M.; Soyer, E.; Quoineaud, A.A.; Costa, D.; Raybaud, P. *J. Catal.* **2011**, *284*, 215-229.

[55] Pan, Y.X.; Liu, C.J.; Ge, Q. *J. Catal.* **2010**, *272*¸ 227-234.

[56] Liu, D.; Quek, X.Y.; Cheo, W.N.E.; Lau, R.; Borgna, A.; Yang, Y. *J. Catal.* **2009**, *266*, 380-390.

[57] Luo, J.Z.; Yu, Z.L.; Ng, C.F.; Au, C.T. *J. Catal.* **2000**, *194*, 198-210.

[58] Chen, H.W.; Wang, C.Y.; Yu, C.H.; Tseng, L.T.; Liao, P.H. *Catal. Today* **2004**, *97*, 173-180.

[59] Shirsat, A.N.; Ali, M.; Kaimal, K.N.G.; Bharadwaj, S.R.; Das, D. *Thermochim. Acta*, **2003**, *399*, 167-170.

[60] Garcia-Dieguez, M.; Finocchio, E.; Larrubia, M.A.; Alemany, L.J.; Busco, G. *J. Catal.* **2010**, *274*, 11-20.

[61] Pena, J.A.; Herguido, J.; Guimon, C.; Monzon, A.; Santamaria, J. *J. Catal.* **1996**, *159*, 313-322.

[62] Zhu, X.; Zhang, Y.P.; Liu, C.J. *Catal. Lett.* **2007**, *118*, 306-312.

[63] Wang, J.; Wang, Y.; Wen, J.; Shen, M.; Wang, W. *Micropor. Mesopor. Mater.* **2009**, *121*, 208-218.

[64] Zhang, Y.; Xiong, G.; Sheng, S.; Yang, W. *Cat. Today* **2000**, *63*, 517-522.

[65] Bhattacharyya, A.; Chang, V.W. *Stud. Surf. Sci. Catal.* **1994**, *88*, 207-213.

[66] Nishamol, K.; Rahna, K.S.; Sugunan, S. *J. Mol. Catal. A: Chem.* **2004**, *209*, 89-96.

[67] Oudet, F.; Vejux, A. *Appl. Catal.* **1989**, *50*, 79-86.

[68] Hansen, J.R.; Christensen, C.H.; Sehested, J.; Helveg, S.; Rostrup-Nielsen, J.R.; Dahl, S. *Green Chem.* **2007**, *9*, 1016-1021.

CHAPTER 6

Oxygen permeation and stability study of $La_{0.6}Sr_{0.4}Co_{0.8}Ga_{0.2}O_{3-\delta}$ (LSCG) hollow fiber membrane with exposure to CO_2, CH_4 and He

$La_{0.6}Sr_{0.4}Co_{0.8}Ga_{0.2}O_{3-\delta}$ (LSCG) perovskite material has been synthesized and fabricated into oxygen permeating hollow fiber membranes. Oxygen permeation from 100 $mL \cdot min^{-1}$ of air at 650°C to 950°C were tested with 100$mL \cdot min^{-1}$ of pure He, CH_4 and CO_2 as sweep gases. The maximum O_2 permeation flux at 950°C was in the order of CH_4 followed by He and CO_2 at 7.45, 3 and 2.4 $mL.min^{-1}.cm^{-2}$. Sweeping with CH_4 resulted in the highest flux due to increase in surface exchange reaction whereas the lowest flux was attained for CO_2 sweep due to formation of $SrCO_3$. An 80 h CO_2-stability test was then conducted at 900°C and 800°C. In this CO_2-stability study, He and CH_4 were intermittently used as sweep gases in order to study their effect on the O_2 flux of the CO_2 swept LSCG membrane. Interestingly, the fluxes improved upon exposure to He and CH_4. However, after being switched back to CO_2 from He sweep, the flux slightly improved initially before stabilizing again to the value prior to He sweep. The impact of switching back from CH_4 showed insignificant changes in the stabilized flux compared to the initial value. SEM-EDX characterization of the membrane from the CO_2-stability study shows considerable erosion at the wall structure with indication of $SrCO_3$, SrO and CoO phases. However, this did not impede the stability of the fluxes or the integrity of the membrane throughout the 80-hour study. In fact, XRD shows that the perovskite structure is maintained despite having lower crystallinity.

6.1. Introduction

CO_2 is a notorious greenhouse gas which attracts great attention worldwide in view of its effect on global climate change [1]. Utilization of CO_2 in order to reduce its emission has been the focus of numerous studies recently [2-4]. For example, CO_2 capture from coal-fired power plants via enrichment of oxygen feedstock in oxyfuel technology is gaining prominence [5]. Another research area which has garnered substantial interest in recent years is the enhancement of partial oxidation of methane via oxidative CO_2 reforming of methane (OCRM) reaction [6]. This reaction is of particular interest since both CH_4 and CO_2 are greenhouse gas contributors. However, the conventional method of oxygen production for the above-mentioned processes via cryogenic technology is expensive and energy intensive [7].

In order to mitigate the costs associated with pure O_2 production, several excellent efforts on the development of mixed ionic and electronic conducting membranes (MIECM) have been undertaken [8-13]. Dense ceramic membranes exhibiting perovskite structure generally exhibit the greatest oxygen flux [14]. The advantages of the MIECM membrane are the dual conductivity of both electrons as well as oxygen ions, without a need for external circuitry like the solid oxide fuel cells [3]. When integrated into systems such as oxyfuel power plants, the energy penalty for CO_2 capture is significantly reduced by 50% [15]. MIEC membranes in hollow fiber configuration generally exhibit many advantages compared to planar and tubular membranes, such as higher surface area/volume ratio and facile high temperature sealing [16].

In general, catalytic membrane reactor systems are not considered ideal since perovskite materials are apt to deteriorate due to unstable phase structure under reducing, CO_2 containing or low oxygen pressure atmospheres [17]. There are several problems

associated with introduction of CO_2 for application with oxygen permeation membranes. CO_2 is known to be a sensitive gas to most of the MIEC materials due to the presence of alkaline earth elements in these materials [18, 19]. As such, CO_2 tends to corrode and poison the membrane surface via formation of carbonates [20, 21]. For example, it was found that presence of CO_2 greatly reduced the flux of $BaCo_{0.4}Fe_{0.4}Zr_{0.2}O_{3-\delta}$ membrane, leaving the permeate side Ba enriched [20]. Yi et al. [21] studied the effect of CO_2 exposure on sweep gas for $BaCo_{0.4}Fe_{0.4}Nb_{0.2}O_{3-\delta}$ membrane and found that the oxygen permeation performance deteriorated significantly. They further observed that a porous zone comprising CoO and Co-depleted Ba(Co, Fe, Nb)$O_{3-\delta}$ perovskite phase was formed upon exposure to pure CO_2. On the other hand, Arnold et al. [22] have found that pure CO_2 as sweep gas for high performance membranes such as BSCF have resulted in immediate stagnation of oxygen permeation at 1148 K. However, the flux could be recovered under He [22]. A strong decline in permeation flux was also observed for $Sr_{0.95}Co_{0.8}Fe_{0.2}O_{3-\delta}$ based membranes after treatment in CO_2 and or H_2O containing atmospheres [23]. Likewise, Yaremchenko et al. [24] have observed that upon exposure to CO_2 a significant decrease in O_2 flux through $SrCo_{0.8}Fe_{0.2}O_{3-\delta}$- $SrAl_2O_4$ composite membranes existed due to strontium carbonate formation.

Tan et al. [25] have reported that when $La_{0.6}Sr_{0.4}Co_{0.8}Fe_{0.2}O_{3-\delta}$ LSCF was exposed to high concentration of CO_2, Sr segregation and formation of surface carbonates resulted in surface erosion which was limited to 1.4μm. However, the stable performance with a flux of circa 0.79 $mL \cdot cm^{-2} \cdot min^{-1}$ at 950°C can be achieved [25]. In order to improve resistance of perovskite materials under CO_2 containing atmospheres, some recent studies have focused on the effect of cation substitution. These include introduction of Ca to

$(La_{1-x}Ca_x)FeO_{3-\delta}$ and $(La_{1-x}Ca_x)(Co_{0.8}Fe_{0.2})O_{3-\delta}$ [26] structures as well as Ti [27] and Ta [28] to the $SrCo_{0.8}Fe_{0.2}O_{3-\delta}$ structure. Other types of structures that have been explored to improve CO_2 resistance include $La_{0.6}Sr_{0.4}CoO_{3-\delta}$ coated on the dual phase of 40wt% Fe_2O_3-60wt% $Ce_{0.9}Gd_{0.1}O_{2-\delta}$. With pure CO_2 sweep at 1000°C, a stable flux *ca.* 0.2 $mL \cdot min^{-1} \cdot cm^{-2}$ could be maintained [13].

In terms of effect of CH_4, it has been reported that presence of pure CH_4 at the sweep side of LSCF membrane greatly improved the oxygen flux at higher temperatures [17, 29]. This was attributed to the surface etching resulting in membrane surface deterioration, hence leading to enhanced surface area to facilitate oxygen exchange [17]. Pei et al. [30], on the other hand, observed serious degradation when CH_4 was applied for POM reaction from oxygen permeated from $Sr(Co,Fe)O_x$ membrane. This could be due to instability caused by absence of La^{3+} in the A-site of the $Sr(Co,Fe)O_x$ system [29, 31].

Generally, doped lanthanum cobaltites, $La_{1-x}Sr_xCoO_{3-y}$ (LSC) based perovskites are known to possess mixed ionic–electronic conducting properties and high catalytic reactivities for oxygen reduction [32]. It was reported that CO_2 tolerance of perovskite oxides doped with different B-site elements was in the order of Ga > Cr >Mn > Fe > Co [33]. Therefore, presence of Ga in the LSCO membrane has good potential in terms of CO_2 resistivity. Furthermore, Co-containing perovskite materials are quite susceptible for decomposition under corrosive or reducing environments [34, 35]. In order to improve the stability of the Co-containing perovskite materials, doping of Ga has been studied by various researchers [32, 36, 37] in order to make it viable as a cathode for intermediate temperature SOFC. Even though presence of Ga in the LSCO compound leads to lower amount of electronic conductivity, Ga as a dopant has the distinction of imparting stability to the compound due to its fixed 3+ valence [38]. It was reported that the composition of

$La_{0.6}Sr_{0.4}Co_{0.8}Ga_{0.2}O_{3-\delta}$ was found to be ideal as doping of Ga above 0.2 leads to formation of unknown phases which were postulated to be $LaSrGaO_4$ [36]. Furthermore, at this low level of Ga doping, the decrease in electronic conductivity can be anticipated to be within tolerable limits.

Therefore based on the above considerations, the aim of this present work is to study the CO_2 tolerance of $La_{0.6}Sr_{0.4}Co_{0.8}Ga_{0.2}O_{3-\delta}$ (hereafter called LSCG) oxygen permeating hollow fiber membranes. Oxygen permeation of LSCG was firstly tested under various conditions and sweep gases such as He, CH_4 and CO_2. Finally, we report the stability for high flow rates of pure CO_2 as sweep gas for the LSCG hollow fiber membrane with intermittent exposure to He and CH_4 in order to explore the feasibility of CH_4 and He in terms of membrane regeneration upon CO_2 exposure.

6.2. Results and discussion

6.2.1. Morphology of LSCG hollow fiber membrane

Figure 6-1 shows the SEM image of the dense LSCG hollow fiber membrane after calcination at 1180°C for 5 h. From the cross section of the hollow fiber image shown in Figure 6-1 (a) and (c), an asymmetric membrane configuration is observed. According to Tan and Li [39], when a mixture of solvent (i.e. NMP) and non-solvent (such as deionised water) is used as the internal coagulant, with water as external coagulant, a highly asymmetric structure comprised of a dense outside layer integrated with an inside porous structure can be obtained. Furthermore, it can be observed that the relatively dense region (sponge-like before calcination) in the asymmetric structure shown in Figure 6-1 (c) is well defined due to the low air gap of 2 cm used. It has been reported that reduction in air gap leads to increase in thickness of sponge-like region [40, 41].

Figure 6-1 (b) show presence of little micropores formed on the external surface of the LSCG hollow fiber. However, these pores are mainly disconnected pore networks which explain the gas-tightness of the LSCG hollow fiber membrane. Furthermore, magnification of the dense section in the wall structure as in Figure 6-1 (d) shows merged crystallites confirming the denseness of the membrane.

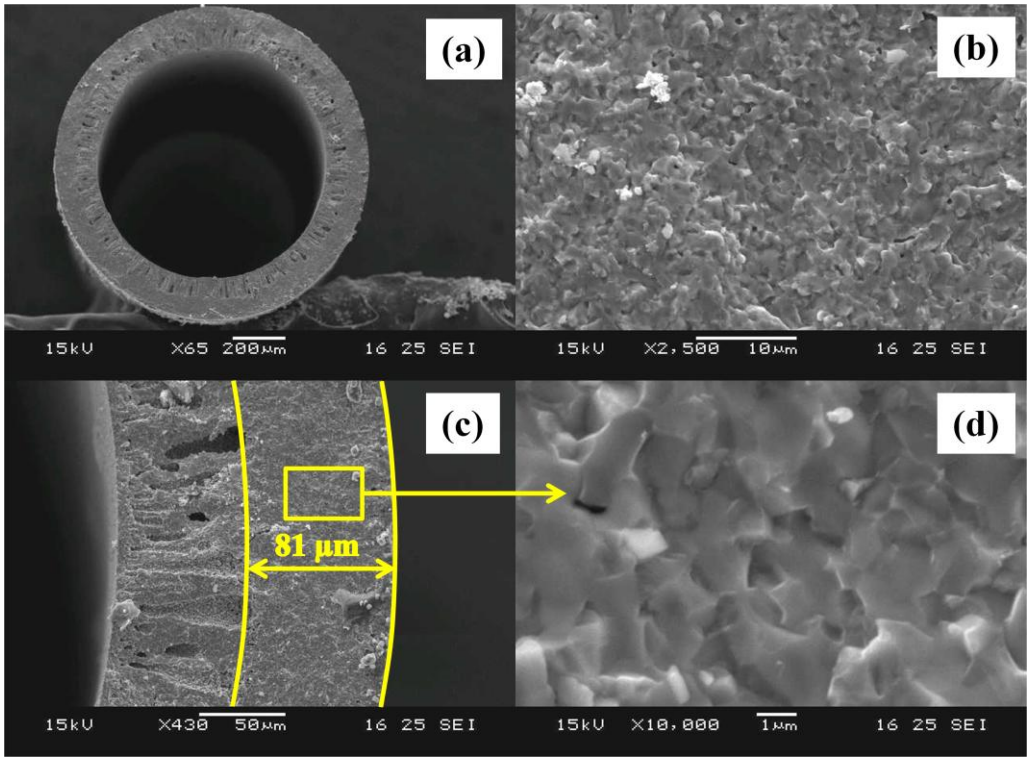

Figure 6-1 SEM images of LSCG hollow fiber membrane calcined after 1180 °C for 5 h: (a) cross section; (b) external surface; (c) wall structure; (d) dense layer.

6.2.2. Oxygen permeability of LSCG hollow fiber membrane

6.2.2.1. Oxygen permeability at various temperatures and flow under He sweep

In order to gauge the inherent permeability of LSCG hollow fiber membranes, a preliminary study was conducted with He as sweep gas. Figure 6-2 shows the oxygen permeability of the LSCG hollow fiber membrane swept by helium from 950°C to 650°C.

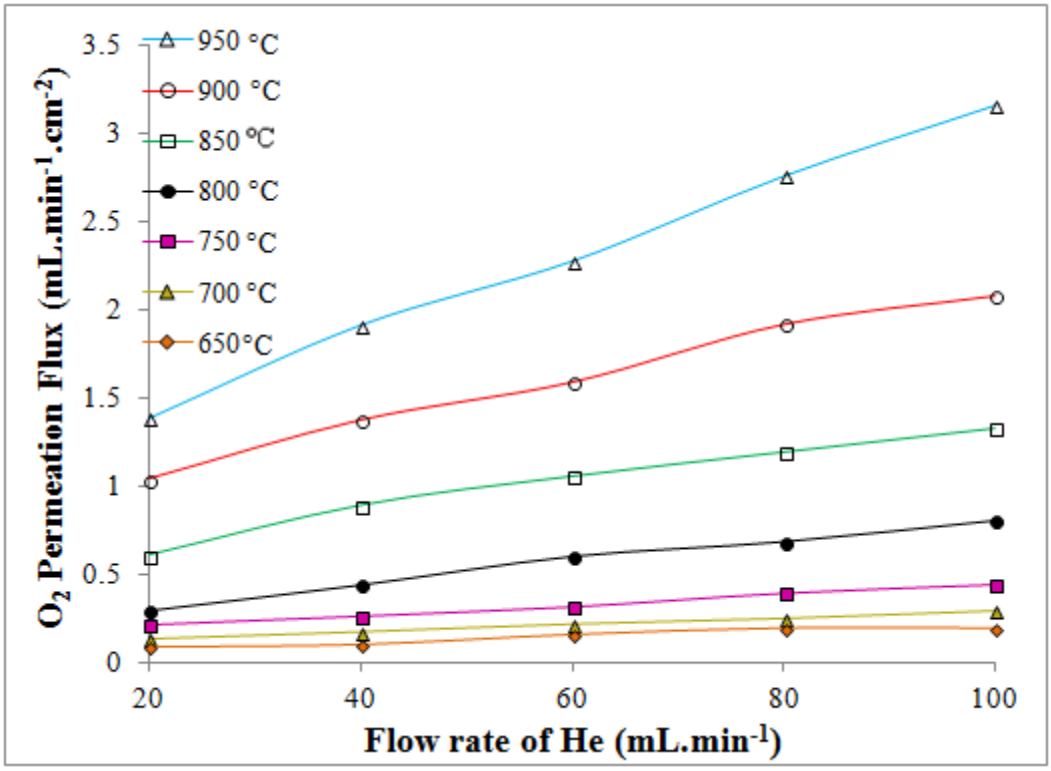

Figure 6-2 O_2 permeation flux through LSCG hollow fiber membrane swept by He from 950°C to 650°C (f_{air} =100 mL·min^{-1}, membrane area = 1.28 cm^2).

From Figure 6-2, it is clear that at higher temperatures, enhancement in permeability is observed. This can be attributed to the increase in diffusion rate and oxygen vacancies at higher temperatures, leading to membrane activation [42, 43]. At permeation temperature of 950°C, the oxygen flux is appreciably high at around 3 mL·min^{-1}·cm^{-2} (under He sweep of 100 mL·min^{-1}). This value is significantly high when compared to several other materials in the LSCO family [44, 45]. Another reason for the higher permeability is attributed to the advantageous structure of the hollow fiber membrane which provides thin effective thickness and higher effective area for surface exchange reactions compared to disk shaped membranes. The effect of increasing sweep

gas is more prominent at higher temperatures, whereby acceleration in permeation fluxes can be observed especially from 850°C onwards. Therefore, in order to minimize the effects of sweep gas flow rates, and to determine O_2 fluxes under CH_4 and CO_2 sweep at different temperatures, experiments were carried out using flow rates of 100 $mL \cdot min^{-1}$ and reported in the following subsection.

6.2.2.2. Effect of CH_4, CO_2 and He as sweep gases

Figure 6-3 shows the effect of different sweep gases of CH_4, CO_2 and He on the oxygen permeation flux of LSCG hollow fiber membrane at temperatures varied from 950°C to 650°C. The effect of the different sweep gases can be distinguished more clearly especially at higher temperatures. With 100 $mL \cdot min^{-1}$ of CH_4 as a sweep gas at a temperature of 950°C, the permeation can increase to 7.45 $mL.min^{-1}.cm^{-2}$, a value which is more than twice that of He and CO_2 as sweep gases. At the same conditions, the LSCG membrane swept by He and CO_2 resulted in significantly lower permeation of 3 and 2.4 $mL \cdot min^{-1} \cdot cm^{-2}$ respectively.

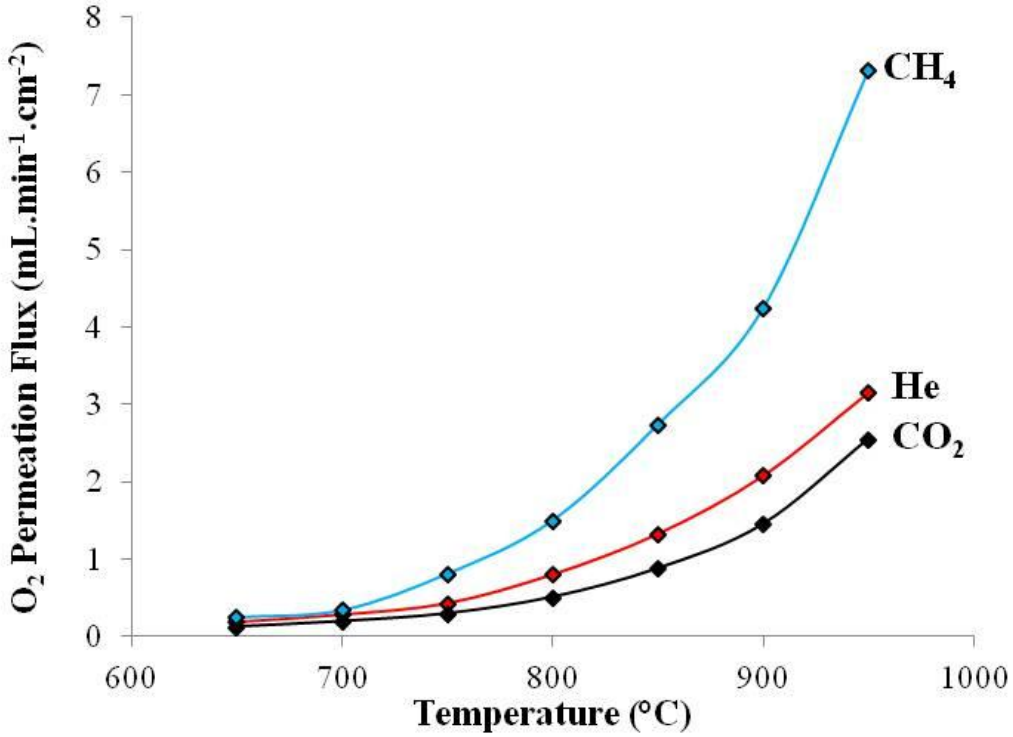

Figure 6-3 O_2 permeation flux through LSCG hollow fiber membrane swept by different sweep gases from 950°C to 650°C ($f_{air} = f_{He} = f_{CH4} = f_{CO2}$ =100 mL·min^{-1}, S.A.= 1.28 cm^2).

Figure 6-4 shows the Arrhenius plots for the activation energies of the different sweep gases. Generally, it is known that there exist two mechanisms that can kinetically control the oxygen permeation process. Firstly, it is the surface exchange reaction (where dissociation of O_2 molecule at feed side to oxygen ions and association of oxygen ions to O_2 molecule at permeate side take place) and secondly, it is the bulk-diffusion process (where oxygen ions diffuse through oxygen vacancies and electron through electron holes) [46, 47]. However, only a single activation energy can be identified for each sweep gas within the testing conditions. Helium has the lowest activation energy (39.23 kJ·mol^{-1}) followed by CO_2 (41.13 kJ·mol^{-1}) and CH_4 (47.40 kJ·mol^{-1}). This single activation energy

for oxygen permeation provides evidence for the structural stability of the membranes [13, 42]. It is not possible to distinguish clearly the limiting step of oxygen flux between surface exchanges and oxygen diffusion. Generally, it was reported that a change in activation energy usually occurs from surface reaction controlled to bulk diffusion controlled at higher temperatures. Based on the single activation energy slope, the calculated activation energy (E_A) may be reflective of a mixed state of bulk diffusion and surface reaction [13].

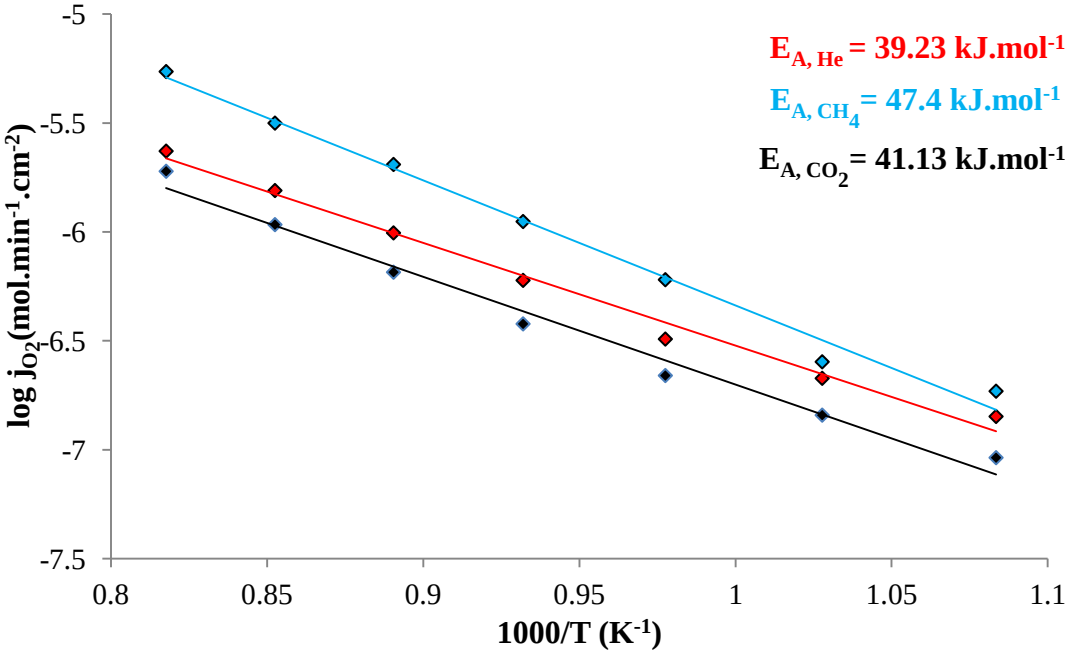

Figure 6-4 Arrhenius plot of O_2 permeation flux through LSCG hollow fiber membrane swept by different sweep gases (f_{air} = f_{He} = f_{CH4} = f_{CO2} =100 mL·min^{-1}, S.A.= 1.28 cm^2).

However, as can be observed from Figure 6-4, even though CH_4 recorded the highest flux at the higher temperatures, it has the highest activation energy compared to the other sweep gases. Figure 6-3 shows that a distinctive leap in permeation under CH_4 occurs more prominently at the higher temperature region. This indicates that the dominance of surface exchange reaction becomes increasingly important at higher temperatures. According to Xu and Thomson [29], a great increase in flux is indicative of more surface exchange reaction taking place. The reaction of CH_4 (with reducing property) with the surface of the membrane increases the oxygen partial pressure gradient across the membrane. With this, the driving force for O_2 permeation increases. This effect is even more apparent at higher temperatures, indicating greater reducibility of CH_4 with increasing temperatures. Therefore, this is the reason for greater flux observed when swept with CH_4. However, the higher E_A obtained for CH_4 sweep is due to the enhancement in CH_4 reducibility at higher temperature which can drastically elevate the fluxes compared to the lower temperatures. Hence, due to the higher E_A for CH_4, its role in increasing the flux was more prominent at the higher temperatures.

Helium being an inert gas displayed the lowest E_A as it did not take part in surface exchange reaction on the membrane. Rather, its role in maintaining the O_2 partial pressure gradient at the tested temperature range of 650°C to 950°C could ensure stable increase in O_2 fluxes which further emphasizes the stability of the LSCG structure.

The E_A for CO_2 as sweep gas is slightly higher than E_A for He as sweep gas, and the fluxes of O_2 under CO_2 was also lower than He. As explained by several researchers, CO_2 maybe chemically adsorbed on the membrane surface with the oxygen ions of CO_2 occupying the oxygen vacancy sites of the membrane [25, 48]. Hence, this leads to reduced driving force for oxygen permeation to occur. But evidently, CO_2 adsorption on

LSCG is not severe since the difference of E_A was rather marginal at *ca.* 2 kJ·mol^{-1} compared to He sweep. Likewise, for CO_2 sweep, a stable increase in O_2 fluxes across the temperature range studied could be maintained.

6.2.3. Surface morphology analysis after He, CH_4 and CO_2 sweep

From Figure 6-5, the surface morphology of the hollow fiber membranes after being swept by the different gases (He: (a) and (b); CH_4 (c) and (d); CO_2 (e) and (f)) between 650°C to 950°C can be observed by SEM. Figure 6-5 (a) shows that the dense region from the edge to the mid-wall of the cross section is clearly visible despite presence of slight jaggedness at the outer edge of the wall. However, high magnification of the external surface of the membrane in Figure 6-5 (b) clearly shows that exposure to He could still maintain the clear perovskite crystal morphology. Only small disconnected pores are observed on the surface.

Figure 6-5 (c) however, shows a very clear patch of eroded region at the wall structure upon being swept by CH_4. The surface etching caused by the exposure to CH_4 concurs with the findings of Liu et al. [17] and Xu and Thomson [29]. According to Xu and Thomson [29], the surface reduction from CH_4 reaction that occurs at points of localized stress causes the surface to "de-sinter" and attrition takes place leaving the etched surface. The highly etched membrane surface appears to increase both CH_4 activation and facilitate oxygen exchange leading to dramatic increases in O_2 flux. The external surface of the membrane swept with CH_4 and shown in Figure 6-5 (d) shows that, unlike the clean surface features observed on Figure 6-5 (b) for the He swept membrane, the particles appear more disintegrated. This is attributed to the extensive surface reaction which took place on the membrane as a result of CH_4 sweep. Furthermore, EDX analysis

revealed that most of the element on the surface comprise of C, due to the thermal decomposition of CH_4 [31]. Presence of other elements could not be accurately determined due to the high amount of carbon deposition.

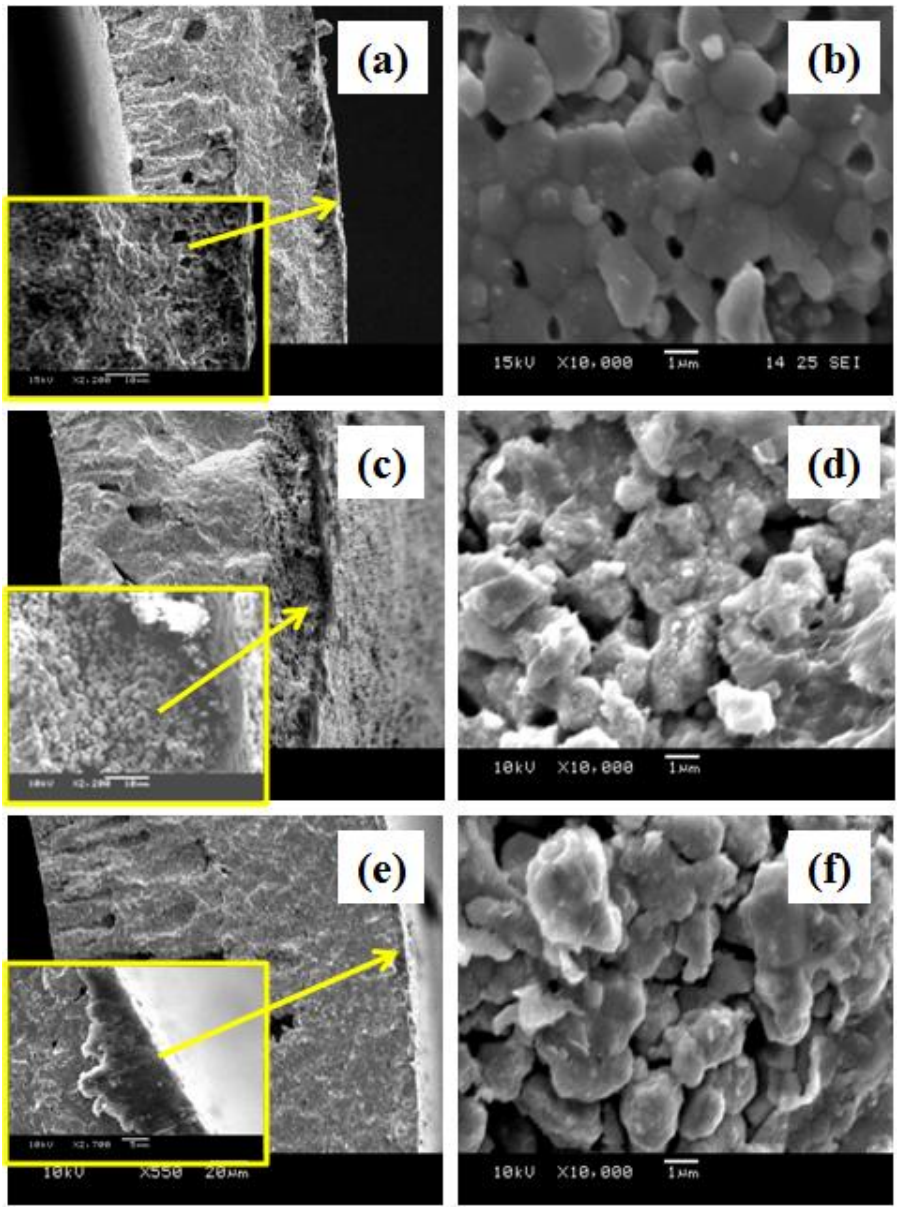

Figure 6-5 SEM images of LSCG hollow fiber membranes: (a) cross section and (b) external surface after He sweep; (c) cross section and (d) external surface after CH_4 sweep; (d) cross section and (e) external surface after CO_2 sweep

Figure 6-5 (e) shows that there are not much visible changes on the wall section of the membrane exposed to CO_2 sweep. However, a zoom-in of the wall edges as shown on the inset of Figure 6-5 (e) clearly shows a formation of a very thin and uneven layer. The external membrane surface in Figure 6-5 (f) shows the presence of particle clusters and debris more alike to Figure 6-5 (d) with CH_4 sweep. However, these clusters are clearly not as rough as observed for the membrane swept with CH_4. From EDX elemental analysis, this region appears to have higher elemental composition of Sr, suggesting presence of $SrCO_3$ due to surface interaction with CO_2 [25]. The formation of these carbonates which are electronically insulating is the reason of slightly lower fluxes as observed in Figure 6-3. Furthermore, the slightly higher activation energy for CO_2 sweep compared to He sweep is also attributed to these carbonate layers. However, since only a thin layer was formed, the flux was not greatly affected and was only *ca*. 15% lower than He sweep at 950°C. At lower temperatures, the differences in permeation were much smaller.

6.2.4. Stability under CO_2 sweep with intermittent exposure to CH_4 and He

Figure 6-6 shows the oxygen permeation results conducted with 100 $mL \cdot min^{-1}$ of pure CO_2 at 900°C and 800°C with intermittent exposure to He and CH_4. The flux steadily increased from *ca*. 1.45 $mL \cdot min^{-1} \cdot cm^{-2}$ to a steady-state value of 2.40 $mL \cdot min^{-1} \cdot cm^{-2}$ within the first 3 hours. The O_2 flux was constant until He introduction at 900°C, where the O_2 flux appear to be steadily increasing. After 2.5 hours, the sweep gas was switched back to CO_2 before steady state was attained. Remarkably after this first He introduction, a slight leap in flux to 2.67 $mL \cdot min^{-1} \cdot cm^{-2}$ under CO_2 atmosphere was observed before it slowly decreased to the pre-He sweep value. When CH_4 was then introduced, the flux

instantaneously increased up to a maximum of 5.87 $mL \cdot min^{-1} \cdot cm^{-2}$. However, upon switching back to CO_2, the flux gradually declined and stabilized at *ca.*2.22 $mL \cdot min^{-1} \cdot cm^{-2}$. When the temperature was lowered to 800°C, the flux of O_2 was rather steady at *ca.* 0.75 $mL \cdot min^{-1} \cdot cm^{-2}$. Upon switching to He sweep, the flux instantaneously reached stabilization *ca.* 1.06 $mL \cdot min^{-1} \cdot cm^{-2}$. A switch back to CO_2 led to the flux stabilizing at *ca.* 0.66 $mL \cdot min^{-1} \cdot cm^{-2}$. Again, introduction of CH_4 brought an immediate flux increase at *ca.* 2.55 $mL \cdot min^{-1} \cdot cm^{-2}$ and switching back to CO_2 brought the flux back to around 0.64 $mL \cdot min^{-1} \cdot cm^{-2}$. This flux was quite stable for the remaining 15 hour of study before the experiment was voluntarily stopped.

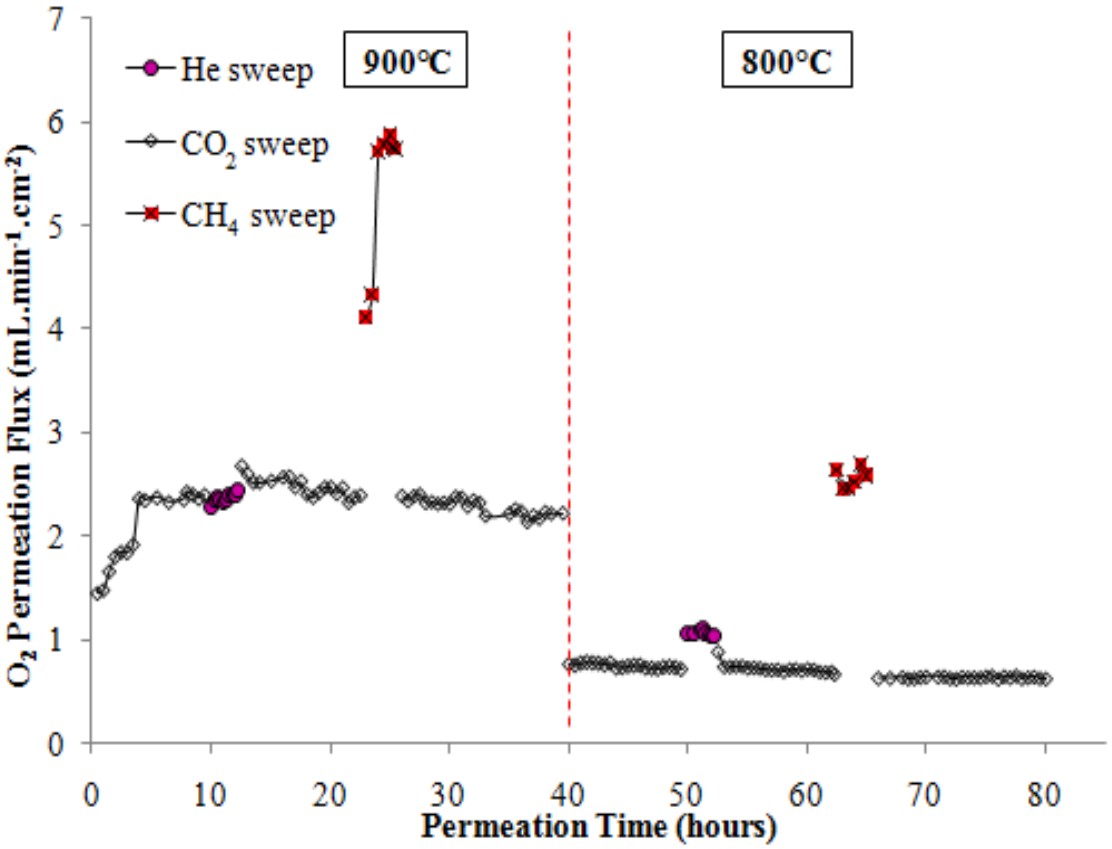

Figure 6-6 Stability study of LSCG hollow fiber membrane swept with CO_2 with intermittent exposure to He and CH_4

The above observations indicate that the LSCG hollow fiber membrane is able to withstand being swept such high flow rates of pure CO_2 and is able to deliver a stable O_2 permeation flux. More importantly is that, at the higher temperature of 900°C, upon being switched to He, steady increase in flux was observed. Thereupon, switching back to CO_2 sweep, appear to have regenerated the surface producing higher O_2 fluxes before finally stabilizing to its original value. This showed that the exposure to He was rather too short, and hence the complete steady state recovery under He flux could not be attained, even though the stable CO_2 flux could be still achieved. However, since our purpose was to minimize complete surface regeneration (thus preventing He from completely decomposing the surface carbonates) and to observe immediate effects of the sweep gas switch, the sweep gas switch duration was limited to 2.5 hours. Introduction of CH_4 shows that even though the flux can be remarkably improved, however, upon switching back to CO_2, the flux was restored to the initial value.

There have been several studies that indicated the role of He in regenerating the membrane surface poisoned by CO_2 [20-22]. In these studies, O_2 permeation was restored via surface carbonate decomposition after the O_2 fluxes showed significant deterioration under CO_2 atmosphere. However, in this study, a stable performance was achieved and there were no imminent deterioration observed in terms of O_2 fluxes under CO_2 sweep. Introduction of He and CH_4 did however, bring about an enhancement effect whereby the fluxes were improved under both He and even tremendously under CH_4 sweep. However, upon switching back to CO_2 sweep, the O_2 fluxes returned to their original values prior to He and CH_4 introduction.

Liu et al. [17] have observed that after activation of LSCF membrane with CH_4 at 900°C to 1000°C for 1-2 hours, the O_2 fluxes improved tremendously under He sweep.

For instance, the fluxes rose from 0.0177 (without activation) to 0.466 $mL \cdot min^{-1} \cdot cm^{-2}$ (after activation) at 800°C under He sweep. This phenomenon was attributed to the increase in surface area for surface exchange reaction caused by the surface deterioration from the CH_4 activation. In this study, however, the same effect of CH_4 activation observed for the LSCF membrane under He sweep could not be applied to the LSCG membrane swept under CO_2. Generally, when CH_4 reacts on the surface of the membrane, it will compete to consume oxygen ions and decompose to CH_3^* methyl radicals according to the following equation [29]

$$2CH_4 + 2h^* + O_O^x \rightarrow 2CH_3^* + H_2O + V_O^{**} \quad (2)$$

$$2O_O^x + 4h^* \rightarrow O_2 + 2V_O^{**} \quad (3)$$

Where h* represents electron holes, O_O^x for lattice oxygen, CH_3^* for methyl radicals and V_O^{**} refers to oxygen vacancies.

The above reaction leads to greater difference in oxygen partial pressure gradient resulting in higher fluxes observed. As discussed earlier in Section 6.2.3, as a result of CH_4 sweep, complete decomposition of CH_4 finally leads to C formation on the surface (confirmed by EDX analysis). However, it was reported by ten Elshof et al. [31] that upon decomposition of CH_4, segregated Sr from the CH_4 exposed side of the $La_{0.6}Sr_{0.4}Co_{0.8}Fe_{0.2}O_{3-\delta}$ (LSCF) membrane can react with the decomposed C to form $SrCO_3$. From our previous observations in Figure 6-5, CO_2 sweep resulted in Sr-enrichment, suggesting presence of $SrCO_3$ which concur with the finding of Tan et al. [25]. Therefore, from this discussion, we can postulate that formation of $SrCO_3$ is a result of both CH_4 and CO_2 exposure.

Therefore, upon introduction of CO_2 as sweep gas (post-CH_4 exposure), there are 3 reactions that can possibly occur due to the favorable thermodynamics under the high temperature region (800-900°C) of study:

i) Surface cleaning of carbon from permeated oxygen forming CO_2;

ii) Thermal decomposition of $SrCO_3$ (from CH_4 sweep) under CO_2 atmosphere to SrO species [49]; and

iii) Formation of $SrCO_3$ species due to chemical absorption of CO_2 on oxygen vacancy sites [25]

Hence, this reveals that possibility of an equilibrating balance between CO_2 adsorption and desorption on the surface was taking place post-CH_4 exposure due to the $SrCO_3$ carbonate species. In this regard, flux enhancement was not observed. Since He is an inert gas, it can readily decompose any carbonates present at high temperatures, and furthermore with the presence of extra surface area caused by the surface etching [17, 29], enhanced flux can be achieved. However, CO_2 can react with the surface to form the carbonate species, while simultaneously decomposing the carbonate species from the CH_4 sweep leading to insignificant changes in flux. In order to analyze further and elucidate the surface elements of the post-CO_2-stability analysis, SEM-EDX characterizations were done and discussed in the following section.

6.2.5. Surface morphology of LSCG membrane after CO_2-stability test

Figure 6-7 shows the SEM image of the membrane after the CO_2-stability test. From here, it is quite apparent that considerable surface erosion has taken place. Figure 6-7 (a) shows that only a thin dense layer bridged between the eroded surface and the asymmetric structure exists. This erosion is a result of exposure to high flow rates of CO_2

and CH_4 and is thus no surprise that during CH_4 sweep, remarkably high fluxes were achieved. However, as was discussed earlier, for the post-CH_4 sweep, the O_2 fluxes were not enhanced nor deteriorated during CO_2 sweep. In fact, it did not have any impact on the O_2 permeation under CO_2 sweep. EDX analysis of the mid-wall structure of the hollow fiber membrane shown in Figure 6-7 (b) indicates that the elements were slightly Co-enriched at 53%, compared to the theoretical 40%. Yi et al. [21] have indicated the presence of CoO on $BaCo_{0.4}Fe_{0.4}Nb_{0.2}O_{3-\delta}$ membrane upon CO_2 exposure.

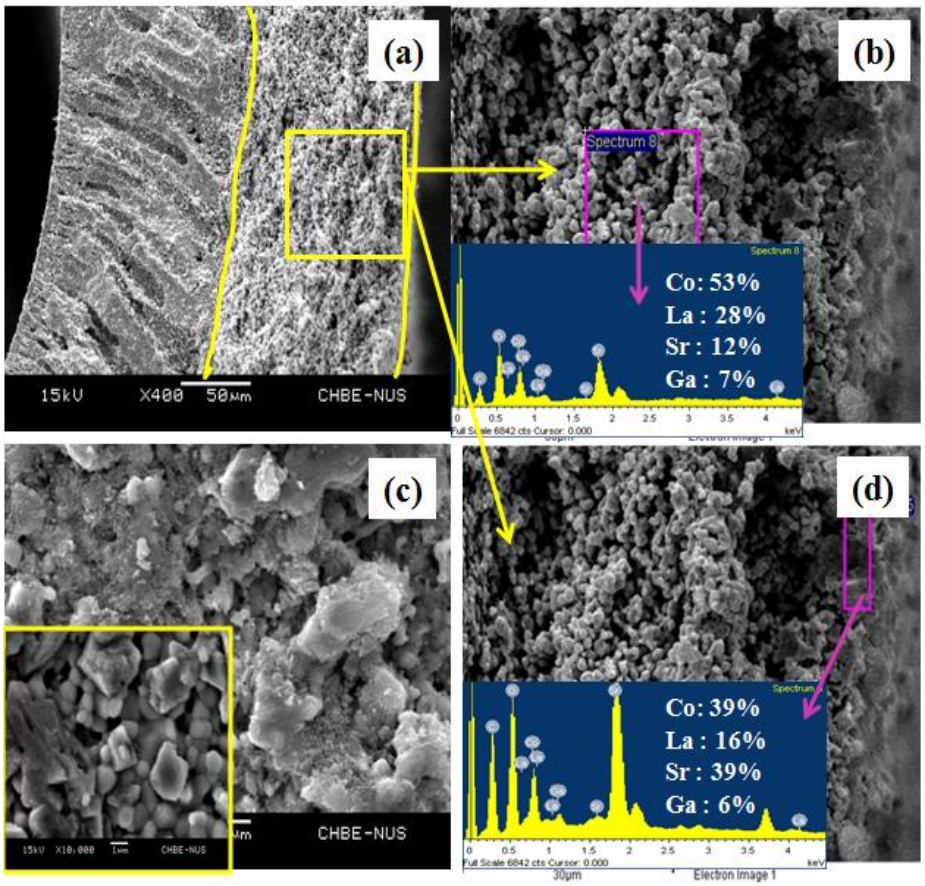

Figure 6-7 SEM images of LSCG hollow fiber membrane after CO_2-stability study: (a) cross section; (b) wall structure (mid-wall elemental composition); (c) external surface (inset: internal surface); (d) wall structure (external layer elemental composition)

On the other hand, EDX analysis of the irregularly formed thin layer shown in Fig Figure 6-7 (d) (similar to Figure 6-7 (e)), were Sr-enriched. From our discussion in section 6.2.4, this Sr-enriched region could be due to $SrCO_3$ and/or SrO (from $SrCO_3$ decomposition under CO_2). The C and O composition could not be accurately determined as the ratio of C:O was nearly similar to that of fresh membrane and hence was not included in the quantification. Therefore, we can deduce that segregated phases of $SrCO_3$, SrO and CoO could have been formed. Figure 6-7 (c) shows the presence of segregated particle clusters on the external surface of the membrane surface. However, the inset image of internal surface (air side) shows that the crystalline structures of the perovskite particles are still intact and well-coalesced despite the presence of some crystallite debris.

However, even in the presence of these phases, there was no adverse impact in O_2 flux under CO_2 sweep and the fluxes were generally stable. Although the membrane was considerably eroded from exposure to high flow rates of CH_4 and CO_2, the membrane integrity was still retained after the 80-hour CO_2 stability test.

6.2.6. Crystalline phases on LSCG membrane

Figure 6-8 shows the XRD analysis of the LSCG perovskite powder and LSCG hollow fiber membranes (fresh and post-reaction). Cubic perovskite phase with the characteristic *d*-spacing values in accordance to the literature was obtained and identified on the perovskite powder phase [32, 36, 37]. The crystallinity of the fresh membrane (as seen from the peak intensity) was the highest compared to the post-reaction membranes. Upon exposure to He, CH_4 and CO_2, the crystalline intensity was in the decreasing trend of He > CH_4 > CO_2 sweep. This implies the deterioration of crystal ordering which took place during the O_2 permeation testing [25].

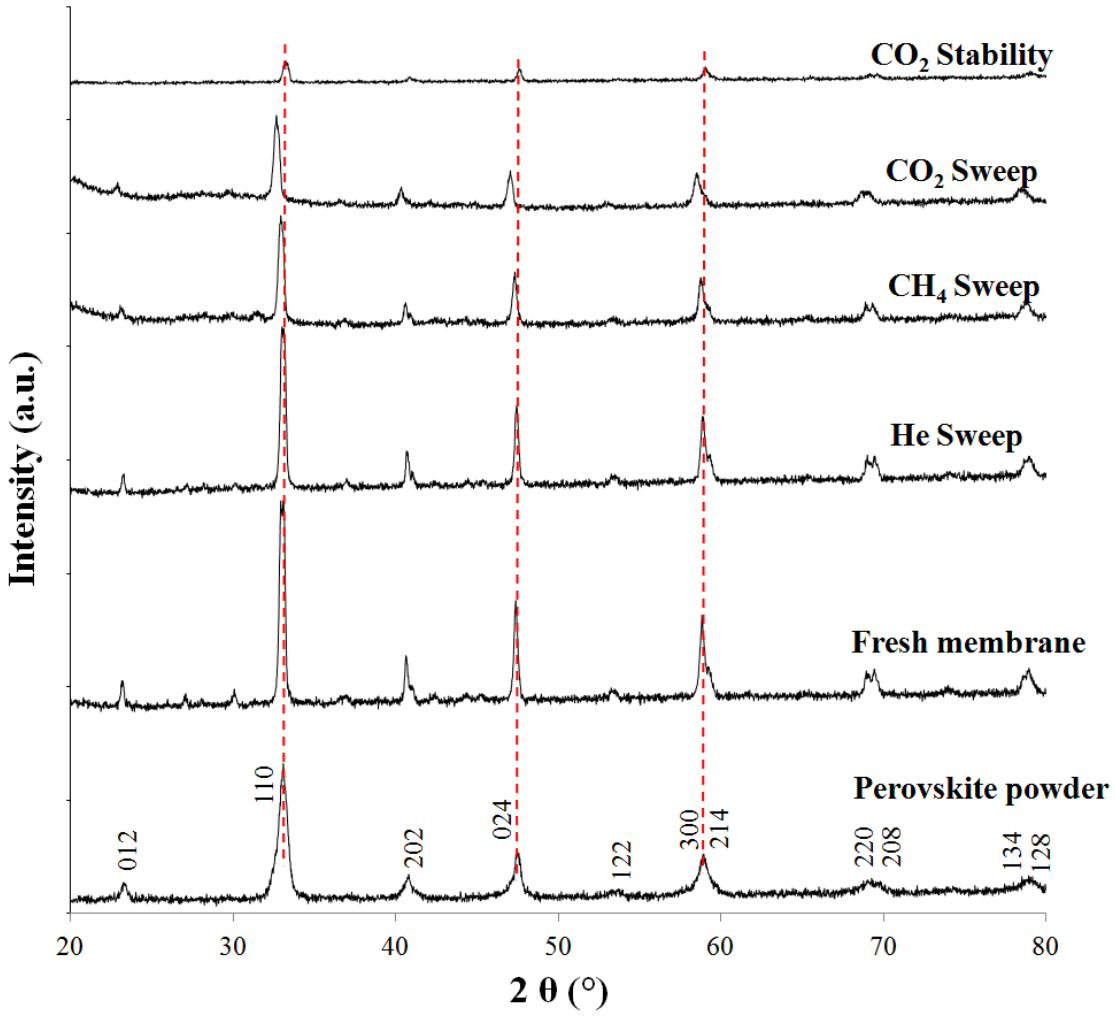

Figure 6-8 XRD spectra of LSCG perovskite and hollow fiber membranes with exposure to different sweep gases and after CO_2- stability test

The crystalline lattice structure was maintained for the He swept membrane. However, a slight peak shift to the left was observed for the CH_4 swept membrane and more obviously for the CO_2 swept membrane. This shift to the lower degree could be due to displacement of the Sr phase to form the $SrCO_3$ species as discussed earlier. However, the characteristic carbonate peaks could not be observed. Generally, Sr based metal oxides have a very weak Madelung constant and can donate electrons easily, which contribute to

their basic properties [50]. It is possible that presence of the stable Ga^{3+} element in the LSCG perovskite have contributed to an increase in relative acidity of the perovskite structure. This is because based on Sanderson's relative acidity scale, the relative acidity of Ga^{3+} is more than double of La^{3+} and Sr^{2+} [51, 52]. Therefore, there is tendency for lower affinity for $SrCO_3$ formation for the Ga-doped membrane due to the increased resistance of the membrane towards CO_2 adsorption (even though the presence of $SrCO_3$ is found on the membrane surface as deduced from EDX analysis). This is attested further by the fact that differences in flux between He and CO_2 sweep was *ca.* 15% -25% only. Furthermore, the fixed valence state of Ga further enhances structure stabilization of the perovskite.

Surprisingly, the crystalline phases of the membrane from CO_2-stability test exactly matches the original perovskite structure, without signs of shifting or presence of other phases. This correlates with our earlier discussion with regards to the equilibrium adsorption and desorption of CO_2, forming $SrCO_3$ during CO_2 sweep and decomposing $SrCO_3$ from CH_4 sweep and He sweep. However, the crystalline peak reflections were rather weak, indicating severe deterioration of the crystalline ordering as a result of the harsh reaction conditions.

6.2.7. O_2-TPD analysis

Figure 6-9 displays the O_2-TPD profile of the LSCG hollow fiber membrane. O_2-TPD is a very important study in order to ascertain the oxygen mobility of the perovskite structure. In the perovskite ABO_3 structure, the reduction of unstable B^{4+} to B^{3+} with O_2 desorption and vacancy generation first occurs on the surface, whilst lattice oxygen diffuse from bulk to surface [53]. Generally, for Co (B site) containing materials, desorption

peaks between 200 and 600°C relate to reduction of Co^{4+} to Co^{3+} and the higher temperature desorption peaks are associated to reduction of Co^{3+} to Co^{2+} to release O^{2-} from the lattice of the crystalline structure [42, 54].

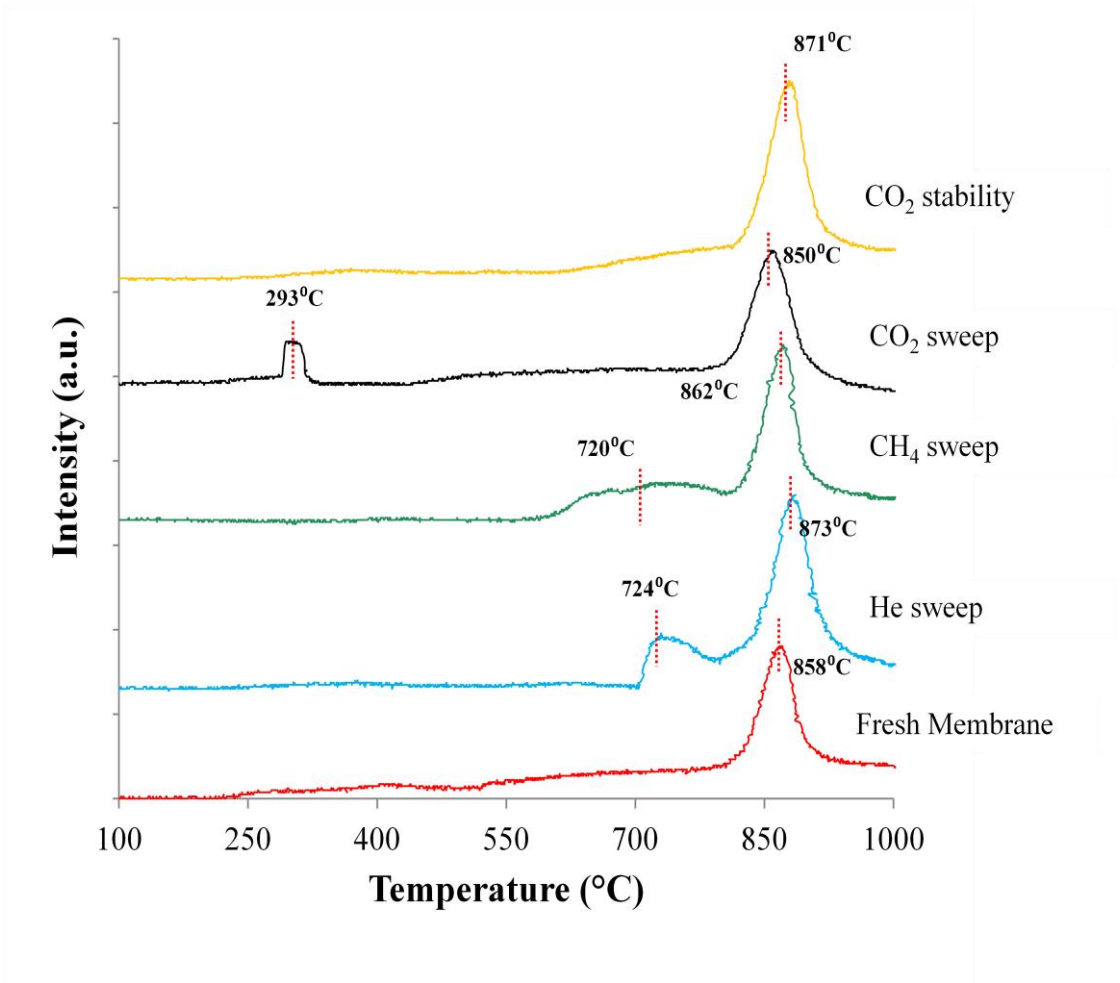

Figure 6-9 O_2-TPD of LSCG hollow fiber membranes: fresh and upon exposure to different sweep gases and after CO_2- stability study

From this analysis, fresh membrane shows an O_2 desorption peak at *ca.* 858°C due to release of O^{2-} species from the crystalline lattice. Absence of the other peaks associated with the valence change of the Co species, indicates clearly that the presence of Ga with fixed valence, provides an important stabilization effect in terms of inherent structural property, characterized by the single O^{2-} release peak. However, upon exposure to He and

CH_4, an additional broad peak *ca*. 720°C was observed, in addition to the peak from the oxygen lattice. It is postulated that the increase in surface roughness and segregated phase destabilized the membrane structure, and as such, could have resulted in reduction of the segregated CoO species due to a less compact perovskite structure. This less compactness upon reaction weakened the bonding energy and migration barrier [53].

As for the membrane exposed to CO_2, two peaks were observed at *ca.* 293°C and 850°C. This could be due to formation of $SrCO_3$, which resulted in less Sr presence in the LSCG structure. As such, this enables to Co phase to undergo transition to Co^{4+} in order to maintain the oxygen stoichiometry of the perovskite. Therefore, the reduction at the lower temperature is related to the Co^{4+} reduction to Co^{3+}.

Remarkably, for the membrane from post-CO_2-stability analysis, only a single desorption peak at *ca.* 871°C was observed. The peak had a narrower full width at half maximum (FWHM) of 40°C compared to the peak from the fresh membrane with FWHM of 47°C. The narrower FWHM is an indication of further absence of re-adsorption and mass transport limitations [55]. This finding indicates supports the results from XRD which show significant deterioration in the crystal ordering leading to smaller crystallites and more compact lattice structure.

6.3. Conclusion

$La_{0.6}Sr_{0.4}Co_{0.8}Ga_{0.2}O_{3-\delta}$ (LSCG) hollow fiber membranes have been successfully fabricated and tested for oxygen permeation under He, CH_4 and CO_2 atmospheres. It was found that exposure to CH_4 resulted in greater enhancement of O_2 flux followed by He and CO_2. The greater flux from CH_4 sweep is due to the enhanced surface exchange reaction due to membrane surface deterioration by the CH_4 gas. The lower flux for CO_2

swept membrane was due to the formation of the insulating $SrCO_3$ species. As such, an 80h CO_2-stability test with intermittent exposure to He and CH_4 was then conducted. It was remarkable to find that the O_2 flux was rather stable and could maintain significant fluxes at final values of 2.22 $mL \cdot min^{-1} \cdot cm^{-2}$ (for 900°C) and 0.63 $mL \cdot min^{-1} \cdot cm^{-2}$ (for 800°C). This enhanced stability was attributed to incorporation of Ga which has a fixed valence state which stabilized the Co-O structure and higher relative acidity (compared to Sr) resulting in reduced affinity for $SrCO_3$ formation. Considerable erosion was observed from SEM, with EDX analysis indicating presence of $SrCO_3$, SrO and CoO phases. However, XRD analysis shows that the phase microstructure and the crystalline lattice structure could be maintained. Significantly, even after 80 hours of operation under the harsh CO_2 environment, the integrity of the LSCG membrane could be maintained with stable O_2 permeation fluxes.

REFERENCES

[1] Stadler, H.; Beggel, F.; Habermehl, M; Persigehl, B.; Kneer, R.; Modigell, M.; Jeschke, P. *Int. J. Greenhouse Gas Con.* **2011**, *5*, 7-15.

[2] Zhu, X.; Liu, H.; Cong, Y.; Yang, W. *Chem. Commun.* **2012**, *48*, 251-253.

[3] Slade, D.A.; Duncan, A.M.; Nordheden, K.J.; Stagg-Williams, S.M.; *Green Chem.* **2007**, *9*, 577-581.

[4] Zhang, C.; Chang, X.; Fan, Y.; Jin, W.; Xu, N. *Ind. Eng. Chem. Res.* **2007**, *46*, 2000-2005.

[5] Carbo, M.C.; Jansen, D.; Hendriks, C.; de Visser, E.; Ruijg, G.J.; Davison, J. *Energy Procedia* **2009**, *1*, 487-494.

[6] Foo, S.Y.; Cheng, C.K.; Nguyen, T.H.; Adesina, A.A. *Ind. Eng. Chem. Res.* **2010**, *49*, 10450-10458.

[7] Leo, A.; Liu, S.; da Costa, J.C.D. *Int. J. Greenhouse Gas Con.* **2009**, *3*, 357-367.

[8] Tan, X.; Wang, Z.; Meng, B.; Meng, X.; Li, K. S. *J. Memb. Sci.* **2010**, *352*, 189-196.

[9] Balachandran, U.; Dusek, J.T.; Maiya, P.S.; Ma, B.; Mieville, R.L.; Kleefisch, M.S.; Udovich, C.A. *Catal. Today* **1997**, *36*, 265-272.

[10] Zeng, Y.; Lin, Y.S.; Swartz, S.L. *J. Memb. Sci.* **1998**, *150*, 87-98.

[11] Wang, H.; Tablet, C.; Feldhoff, A.; Caro, J. *J. Memb. Sci.* **2005**, *262*, 20-26.

[12] Chen, Z.; Ran, R.; Shao, Z.; Yu, H.; da Costa, J.C.D. *Ceram. Int.* **2009**, *35*, 2455-2461.

[13] Luo, H.; Jiang, H.; Efimov, K.; Liang, F.; Wang, H.; Caro, J. *Ind. Eng. Chem. Res.* **2011**, *50*, 13508-13517.

[14] Bouwmeester, H.J.M., Burggraaf, Dense ceramic membranes for oxygen separation, in: A.J. Burggraaf and L. Cot (Eds.), Fundamentals of inorganic membrane science and technology, *Elsevier Sci.* **1996**, 435.

[15] Stadler, H.; Beggel, F.; Habermehl, M; Persigehl, B.; Kneer, R.; Modigell, M.; Jeschke, P. *Int. J. Greenhouse Gas Con.* **2011**, *5*, 7-15.

[16] Liu, S.; Tan, X.; Shao, Z.; da Costa, J.C.D. *AIChE J.* **2006**, *52*, 3452-3461.

[17] Liu, H.; Pang, Z.; Tan, X.; Shao, Z.; Sunarso, J.; Ding, R.; Liu, S. *Ceram. Int.* **2009**, *35*, 1435-1439.

[18] Dong, X.; Jin, W.; Xu, N. *Chem. Mater.* **2010**, *22*, 3610-3618.

[19] Jin, W.Q.; Zhang, C.; Chang, X.F.; Fan, Y.Q.; Xing, W.H.; Xu, N.P. *Environ. Sci. Technol.* **2008**, *42*, 3064-3068

[20] Czuprat, O.; Arnold, M.; Schirrmeister, S.; Schiestel, T.; Caro, J. *J. Memb. Sci.* **2010**, *364*, 132-137.

[21] Yi, J.; Schroeder, M.; Weirich, T.; Mayer, J. *Chem. Mater.* **2010**, *22*, 6246–6253.

[22] Arnold, M.; Wang, H.; Feldhoff, A. *J. Memb. Sci.* **2007**, *293*, 44-52.

[23] Yi, J.; Feng, S.; Zuo, Y.; Liu, W.; Chen, C. J. *Chem. Mater.* **2005**, *17*, 5856-5861.

[24] Yaremchenko, A.A.; Kharton, V.V.; Avdeev, M.; Shaula, A.L.; Marques, F.M.B. *Solid State Ionics* **2007**, *178*, 1205-1217.

[25] Tan, X.; Liu, N.; Meng, B.; Sunarso, J.; Zhang, K.; Liu, S. *J. Memb. Sci.* **2012**, *389*, 216– 222.

[26] Efimov, K.; Klande, T.; Juditzki, N.; Feldhoff, A. *J. Memb. Sci.* **2012**, *389*, 205-215.

[27] Zeng, Q.; Zu, Y.B.; Fan, C.G.; Chen, C.S. *J. Memb. Sci.* **2009**, *335*, 140-144.

[28] Chen, W.; Chen, C.S.; Winnubst, L. *Solid State Ionics* **2011**, *196*, 30–33.

[29] Xu, S.J.; Thomson, W.J. *Ind. Eng. Chem. Res.* **1998**, *37*, 1290-1299.

[30] Pei, S.; Kleefisch, M.S.; Kolylinski, T.P.; Faber, J.; Udovich, C.A. *Catal. Lett.* **1995**, *30*, 201-212.

[31] ten Elshof, J.E.; Bouwmeester, H.J.M.; Verweij, H. *Appl. Catal. A.* **1995**, *130*, 195-212.

[32] Matsuda, M.; Ihara, K.; Miyake, M. *Solid State Ionics* **2004**, *172*, 57–61.

[33] Sirman, J. The evolution of materials and architecture for oxygen transport membranes, in: A.F. Sammells, M.V. Mundschau (Eds.), Nonporous Inorganic Membranes, *Wiley*-VCH, **2006**,165-184.

[34] Luo, H.; Wei, Y.; Jiang, H.; Yuan, W.; Lv, Y.; Caro, J.; Wang, H. *J. Memb. Sci.* **2010**, *350*, 154-160.

[35] Kniep, J.; Lin, Y.S. *Ind. Eng. Chem. Res.* **2011**, *50*, 7941-7948.

[36] Wang, S.; Zheng, R.; Suzuki, A.; Hashimoto, T. *Solid State Ionics* **2004**, *174*, 157–162.

[37] Yan, B.; Zhang, J.; Liu, J.; Liu, G. *Mater. Lett.* **2005**, 59, 3226-3229.

[38] Kharton, V.V.; Viskup A.P.; Naumovich, E.N.; Lapchuk, N.M. *Solid State Ionics* **1997**, *104*, 67–78.

[39] Tan, X.; Li, K. Engineering aspects of MIEC hollow fiber membranes for oxygen production membrane engineering for the treatment of gases, Volume 2: Gas-separation Problems Combined with Membrane Reactors, Eds. E. Drioli and G. Barbierir, *Royal Society of Chemistry*, **2011**, 253-278.

[40] Kingsbury, B.F.K.; Zhentao, W.; Li, K. *Catal. Today* **2010**, *156*, 306-315.

[41] Widjojo, N.; Chung, T.S. *Ind. Eng. Chem. Res.* **2006**, *45*, 7618-7626.

[42] Tong, J.; Yang, W.; Zhu, B.; Cai, R. *J. Memb. Sci.* **2002**, *203*, 175-189.

[43] Acharya, M.; Raich, B.A.; Foley, H.C. *Ind. Eng. Chem. Res.* **1997**, *36*, 2924-2930.

[44] Teraoka, Y.; Nobunaga, T.; Yamazoe, N. *Chem. Lett.*, **1988,** *17*, 503-506.

[45] Zhang, K.; Sunarso, J.; Shao, Z.; Zhou, W.; Sun, C.; Wang, S.; Liu, S. *RSC Adv.* **2011**, *1*, 1661-1676.

[46] Zhu, H.; Liu, H.; Li, Q.; Cong, Y.; Yang, W. *Solid State Ionics* **2011**, *185*, 27-31.

[47] Sunarso, J.; Baumann, S.; Serra, J.M.; Meulenberg, W.A.; Liu, S.; Lin, Y.S.; da Costa, J.C.D. *J. Memb. Sci.* **2008**, *320*, 13-41.

[48] Nomura, K.; Ujihira, Y.; Hayakawa, T.; Tekehira, K. *Appl. Catal. A: Gen*, **1996**, *137*, 25-36.

[49] Scholten, M.J.; Schoonman, J. *Solid State Ionics* **1993**, 61, 83-91.

[50] Zhou, W.; Liang, F.; Shao, Z.; Zhu, Z. *Scientific Reports*, 2, doi:10.1038/srep00327.

[51] Sanderson, R.T. *J. Inorg. Nuc. Chem.* **1966**, *7*, 1553-1565.

[52] Jeong, N.C.; Lee, J.S.; Tae, E.L.; Lee, A.J.; Yoon, K.B. *Angew. Chem. Int. Ed.* **2008**, *47*, 10128-10132

[53] Zhang, G.; Liu, Z.; Zhu, N.; Jiang, W.; Dong, X.; Jin, W. *J. Memb. Sci.* **2012**, *405-406*, 300-309.

[54] Shao, Z.; Yang, W.; Cong, Y.; Dong, H.; Tong, J.; Xiong, G. *J. Memb. Sci.* **2000**, *172*, 177-188.

[55] Busser, G.W.; Hinrichsen, O.; Muhler, M. *Catal. Lett.* **2002**, *79*, 49-54.

CHAPTER 7

$La_{0.6}Sr_{0.4}Co_{0.8}Ga_{0.2}O_{3-\delta}$ (LSCG) hollow fiber membrane reactor: Partial oxidation of methane at medium temperature

In this study, $La_{0.6}Sr_{0.4}Co_{0.8}Ga_{0.2}O_{3-\delta}$ (LSCG) hollow fiber membrane reactor was integrated with $Ni/LaAlO_3$-Al_2O_3 catalyst for the catalytic partial oxidation of methane (POM) reaction. The process was successfully carried out in the medium temperature range (600-800°C) for reaction of blank POM with bare membrane, catalytic POM reaction and swept with H_2:CO gas mixture. For the catalytic POM reaction, enhancement in selectivity to H_2 and CO is obtained between 650°C-750°C when O_2:CH_4 <1. High CH_4 conversion of 97% is achieved at 750°C with corresponding H_2 and CO selectivity of *ca.* 74% and 91%. The oxygen flux of the membranes also increased with the increase in oxygen partial pressure gradient across the membrane. The post-reacted membranes were tested via XRD and FESEM-EDX for their crystallinity and surface morphology. XPS analysis was further used to investigate the Co 2p and Sr 3d binding energies of the segregated elements from the reducing reaction environment.

7.1. Introduction

Synthesis gas (syngas) production (a mixture of H_2 and CO) is important in chemical industries as it can be easily converted to chemicals and fuels (via Fischer-Tropsch synthesis) and used for hydrogen production [1-2]. Production of syngas via catalytic hydrocarbon conversion reactions such as partial oxidation of methane (POM) and steam reforming of methane (SRM) have been widely investigated since CH_4, the main component of natural gas, is readily accessible [3]. The POM reaction appears to be

an attractive alternative to SRM for hydrogen production due to its mild exothermicity, as compared to the highly endothermic nature of the SRM reaction which renders it a capital and energy intensive process [4]. The main difficulty for POM reaction, however, stems from the requirement of the costly cryogenic air separation process for oxygen supply [5].

Several research developments focusing on integrated catalytic membrane reactor systems with mixed ionic and electronic conducting (MIEC) membranes capable of selective oxygen production from air have been carried out [6-11]. The synergic effects of coupling separation and reaction in a single unit are expected to play a decisive role in the area of sustainable energy technologies by allowing a process design without the cost intensive (cryogenic) oxygen separation unit [12-13]. Hence, the optimal process design can minimize energy consumption [14].

According to Balachandran et al. [6], direct contact of the membrane with the reducing gases of H_2 and CO from the reaction may cause the oxide phase to lose the lattice oxygen, resulting in decomposition of the perovskite structure. Hence, immediate replenishment of the lattice oxygen through thinner wall structure is crucial. In this regard, hollow fiber membrane configuration has distinct advantages over disc or tubular membranes as it can provide larger area per unit volume and enables facile high temperature sealing [15].

Despite structural optimization, phase decomposition of membranes under syngas producing conditions is a prevalent issue due to the large oxygen partial pressure gradient from the air and permeate (reaction) side. Since Teraoka et al. [16] firstly reported on perovskite oxides such as $La_xSr_{1-x}Co_yFe_{1-y}O_{3-\delta}$ with high oxygen permeability, cobalt-based perovskite materials have been widely investigated [17-18]. However, Co-based materials are also known for their limited chemical stability [19]. Pei et al. [20] reported

the failure mechanism on $SrCo_{0.8}Fe_{0.2}O_x$ (SCFO) membranes which fractured under POM conditions due to crystal lattice mismatch caused by high oxygen chemical potential gradient across the membrane. In order to improve the stability of membrane materials, cations with constant valence (Zr^{4+}, Ga^{3+} and Al^{3+}) were used as a partial substitution for the B-site cations (Co^{4+}/Co^{3+} and/or Fe^{4+}/Fe^{3+}) [19,21,22].

We have recently tested the Ga-doped $La_{0.6}Sr_{04}Co_{0.8}Ga_{0.2}O_{3-\delta}$ (LSCG) hollow fiber membranes for CO_2 stability with intermittent exposure to CH_4 and He as sweep gas [23]. Therefore, in this contribution, we explore the feasibility of incorporating a Ni based catalyst and assembling a LSCG catalytic hollow fiber membrane reactor for POM reaction. Valuable insights on the morphological changes which took place on the membrane surface upon POM reaction, as well as upon exposure to H_2 and CO gases are discussed based on data from elemental analysis techniques such as energy dispersive spectroscopy (EDX) and X-ray photoelectron spectroscopy (XPS). The medium temperature range of 600°C to 800°C was chosen for study since a suitable operation temperature is an important criterion for POM reaction. The reason being, too low a temperature leads to insufficient oxygen permeation thereby limiting the methane conversion, whereas too high a temperature leads to deep oxidation thus compromising on product selectivity [24]. Furthermore, too high a temperature also results in catalyst sintering and deactivation which is not practical for the system [9]. Based on the results of POM reaction, the possible reaction pathways were postulated and compared with previous studies which were mainly conducted at 800°C and above.

7.2. Results and discussion

7.2.1. Blank POM reaction with bare membrane

The inherent catalytic property of the LSCG hollow fiber membrane was measured first without catalyst in order to elucidate the effect of catalyst in the membrane reactor for the POM reaction. In this blank experiment conducted at the medium temperature of 600°C to 800°C, 25% CH_4/He (10mL.min^{-1}) was introduced on the shell side with air flow rate of 100 mL.min^{-1} in the lumen side of the membrane reactor. Analysis of the product gas from the GC shows that the main composition of the effluent stream consists of CO_2 and CO as well as un-reacted CH_4. Since the steam from the effluent of the membrane reactor is condensed prior to introduction in the GC, therefore H_2O peak is not detected. On the other hand, H_2 could barely be detected throughout the duration of the reaction.

Figure 7-1 shows the oxygen permeation fluxes for the blank POM experiment on the bare membrane, catalytic POM reaction and the exposure 50% H_2:CO (in helium) sweep gas. The blank POM experiment on the bare membrane has the lowest O_2 permeation flux at *ca.* 0.2 mL.min^{-1}.cm^{-2} at 600°C and barely reaching *ca*. 0.3 mL.min^{-1}.cm^{-2} at 800°C. Based on the POM reaction results shown in Figure 7-2, it is apparent that the LSCG hollow fiber membrane has inherently poor catalytic activity with a rather low CH_4 conversion of about 23-25% from 600 to 800°C. Furthermore, without presence of catalyst, deep oxidation is favored based on the stealthy decrease in CO selectivity from *ca.*17% to 8% at 700°C and after which a rapid decline to *ca.* 2% at 800°C. This rapid decline above 700°C is consistent with the obvious increase in O_2 permeation flux from 700°C onwards, as shown in Figure 7-1. O_2 was not detected in the product stream even though there is low conversion of CH_4. In this regard, without the presence of catalyst,

oxidation of methane proceeded rather slowly throughout the experiment. This clearly indicates the crucial presence of a suitable catalyst in order to catalyze the reaction.

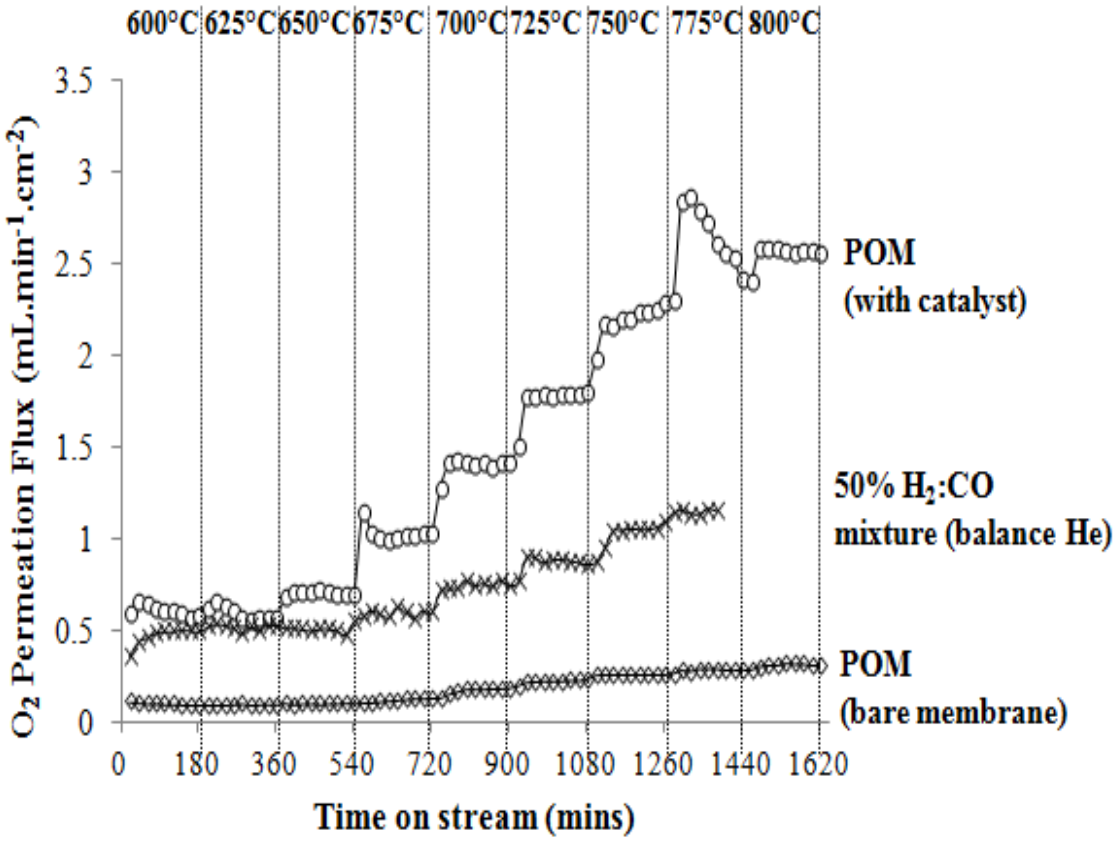

Figure 7-1 Oxygen permeation flux of LSCG hollow fiber membrane under blank POM with bare membrane, POM with catalyst and with 50%H_2:CO (in He) sweep. (For POM: F_{air}=100 mL·min^{-1}, F_{CH4}=2.5 mL·min^{-1}, F_{He}=7.5 mL·min^{-1} and for 50%H_2:CO: F_{air}=100 mL·min^{-1}, F_{H2}=2.5 mL·min^{-1}, F_{CO}=2.5 mL·min^{-1}, F_{He}= 5 mL·min^{-1}).

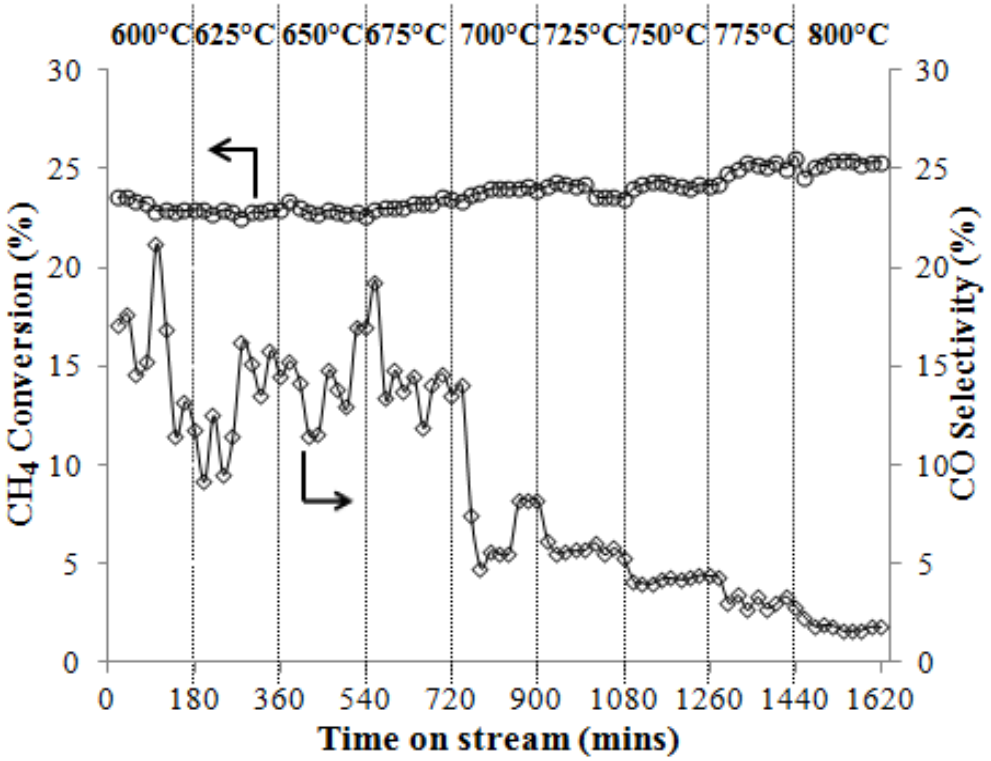

Figure 7-2 %CH_4 conversion and % CO selectivity for blank POM with bare membrane (F_{air}=100 mL·min^{-1}, F_{CH4}=2.5 mL·min^{-1}, F_{He}=7.5 mL·min^{-1}, S_A= 1.28 cm^2).

Hence, in the next section, we provide the results of the catalytic membrane reaction. Generally for POM reactions, Ni based catalysts is the preferable choice, owing to its comparable methane reforming activity with noble metals, wide availability and low cost which is more appealing and practical from an industrial standpoint [25]. As such, we used a methane reforming catalyst developed by our research group (5% Ni/$LaAlO_3$-Al_2O_3) to be packed in the catalytic membrane reactor.

7.2.2. POM reaction in catalytic membrane reactor

The 5% Ni/$LaAlO_3$-Al_2O_3 catalyst was initially reduced at 600°C for 30 minutes, in order to activate the metallic Ni^0 responsible for providing active sites for the catalytic

transformation of methane to syngas in the presence of oxygen. 0.2g of the pre-reduced catalyst was then packed in the catalytic hollow fiber membrane configuration. From the results shown in Figure 7-1 and Figure 7-3, presence of the active Ni based catalyst greatly improves the O_2 permeation flux as well as the catalytic activity for POM reaction.

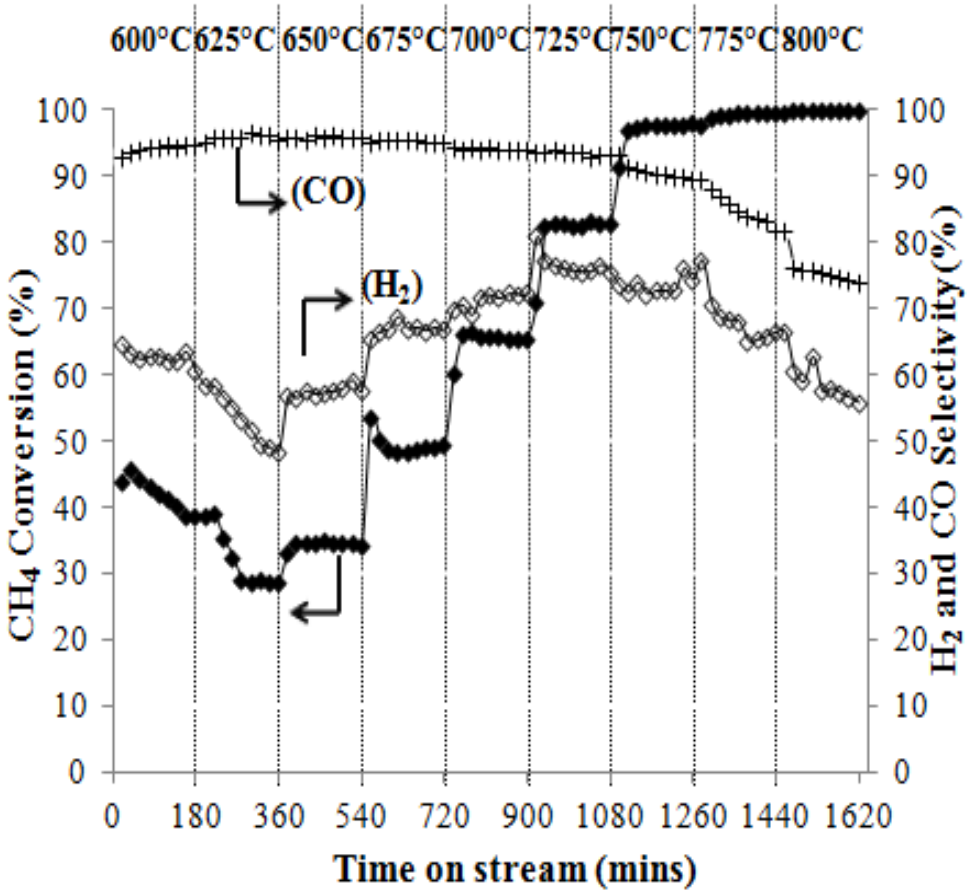

Figure 7-3 Catalytic performance for POM in membrane reactor (F_{air}=100 mL·min^{-1}, F_{CH4}=2.5 mL·min^{-1}, F_{He}=7.5 mL·min^{-1}, 0.2g 5%Ni/$LaAlO_3$-Al_2O_3, S_A= 1.28 cm^2).

The O_2 permeation flux greatly improved especially from 675°C onwards and reached a maximum of *ca.* 2.5 mL.min^{-1}.cm^{-2} at 800°C. The temperature-accelerated O_2

permeation flux played a major role in improving the CH_4 conversion for the POM reaction. From Figure 7-3, a slight drop in CH_4 conversion can initially be observed with gradual improvement from 650°C onwards. This result correlates with the O_2 permeation flux which shows an increase in flux from 650°C onwards. Generally, oxygen surface exchange reaction mechanism becomes activated with increasing temperature. More than 97% of CH_4 conversion is achieved from 750°C onwards. This immense improvement in CH_4 conversion is due to the fact that in the presence of catalyst, the selectivity towards H_2 and CO production increases. Hence, at the interface of the catalyst layer on the membrane surface, the presence of highly reducing syngas creates a low oxygen partial pressure atmosphere. This leads to a large differential pressure gradient across the membrane. According to Zhu et al. [26], oxygen exchange reaction becomes complicated in the presence of catalyst. This is because the reductive un-reacted CH_4, as well as product H_2 and CO gases formed from POM reaction on the Ni catalyst, can, through mass transfer diffusion from catalyst to membrane surface, react with permeated lattice oxygen and adsorbed oxygen species (O^{2-}, O^-, O_2^{2-}, O_2^- etc.). Likewise this reaction can also happen with the desorbed gaseous oxygen from the membrane surface. By further removal of the oxygen from the membrane surface (which on its own is rate limiting without the presence of sweep/reactive gases) with the gases from the catalyst bed-interface, this results in increased O_2 permeation for further catalytic conversion to syngas. Therefore, the increase in O_2 permeation flux correlates with the rate of catalytic POM reaction.

However, H_2 selectivity is relatively much lower than CO selectivity especially at temperatures < 675°C. With the increase in temperature, H_2 selectivity increases and reaches a maximum of *ca.* 75% at the temperature range of 700°C to 750°C. This result

correlates with the findings of Yin et al. [27] where significant differences in both H_2 and CO selectivities were observed at the lower temperatures. The continual oxidizing of accumulated carbon at the lower temperature could be a contributing factor in maintaining the markedly higher CO selectivity compared to H_2 selectivity at the lower temperatures [27]. As aforementioned, as the reaction temperature increases, the O_2 flux increases and therefore more CH_4 is consumed. CO product selectivity is above 90% and markedly decreases at temperatures above 750°C onwards when the O_2 flow rate (O_2 flux ($mL.min^{-1}.cm^{-2}$) *x* membrane surface area, (S_A, cm^2)) begins to approach the CH_4 feed flow rate, leading to excess O_2 (O_2:CH_4 >1). Likewise at the temperatures above 750°C, the H_2 selectivity also begins to decline in a similar pace with the decline in CO selectivity in favor of H_2O and CO_2 production from total combustion.

7.2.3. Sweep with 50% H_2/CO (in helium) gas mixture

Upon exposure to 50% H_2:CO (in helium) as sweep gas, as shown in Figure 7-1, a noticeable increase in O_2 permeation flux is evident compared to the blank POM reaction with bare membrane. This is due to the presence of strong H_2 and CO reducing gases resulting in enhanced surface reactions, due to immediate conversion of the permeated O_2, resulting in lower O_2 partial pressure, thereby leading to greater driving force [28, 29]. The O_2 flux under exposure to 50%H_2:CO (in helium) is comparable to the O_2 flux from the catalytic POM reaction at temperatures lower than 675°C. Above this temperature, the flux begins to increase steadily but at a lower magnitude than the increase in O_2 flux experienced by the catalytic POM reaction. This is because as shown in Figure 7-1, with increase in temperature, greater catalytic activity in the POM reaction results in greater

amount of H_2 production. Stoichiometrically, 1 mole of CH_4 is capable of producing 2 moles of H_2 and 1 mole of CO from subsequent oxidation and reforming reactions. Hence a greater volumetric flow of the reducing gases are a consequence of the catalytic POM reaction, compared to the equivolume H_2 and CO sweep gas mixture.

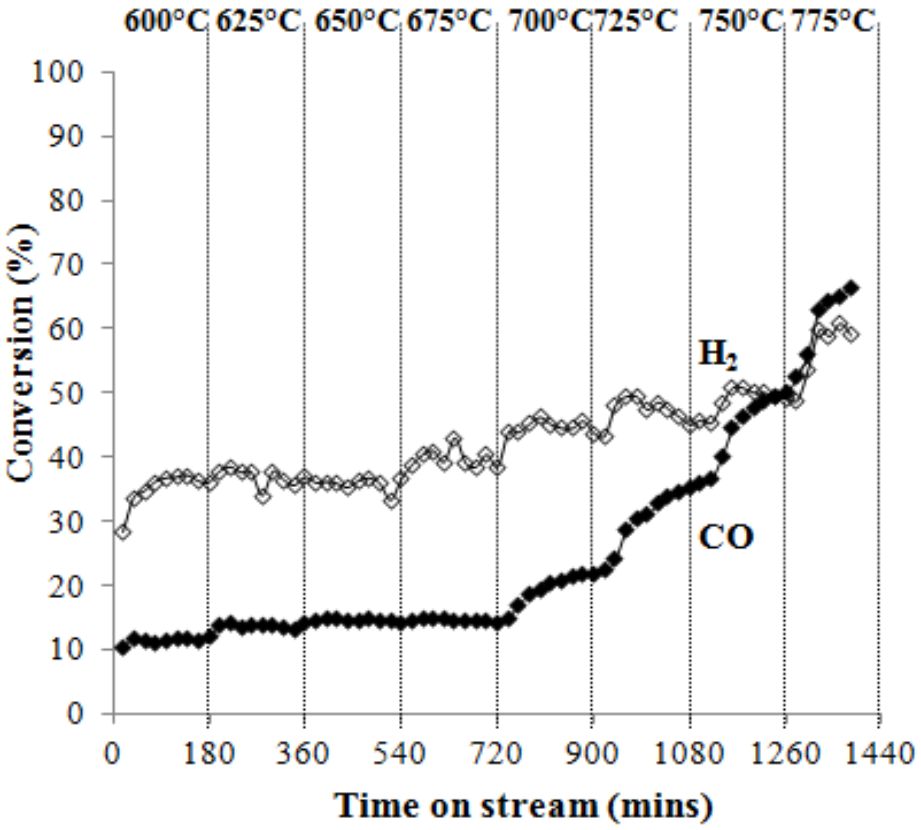

Figure 7-4 H_2 and CO_2 conversions in membrane exposed to 50% H_2:CO (in He) (F_{air}=100 mL·min^{-1}, F_{H_2}=2.5 mL·min^{-1}, F_{CO}=2.5 mL·min^{-1}, F_{He}= 5 mL·min^{-1}, S_A= 1.28 cm^2)

Figure 7-4 shows the %H_2 and %CO conversions from 600°C to 775°C. The only reactions that can take place are basically oxidation of the reactants, hence the equations

pertaining to the H_2 and CO conversions are shown as Equations 7-1 and 7-2 as follows [30]:

$$CO + O^{2-} \rightarrow CO_2 + 2e^- \quad (7\text{-}1)$$

$$H_2 + O^{2-} \rightarrow H_2O + 2e^- \quad (7\text{-}2)$$

Due to the steep increment in terms of temperature-accelerated conversions of both H_2 and CO, the immense surface reaction activity and excess water production led to stress and fracture of the membrane at the reactor cold zone near the exit. This disrupted the experiment leading to discontinuation of study just before the last data point could be collected at 775°C. However, the trend can still be observed, whereby it is evident that at lower temperatures (< 700°C), CO oxidation was rather steady with only marginal improvement from 650°C. A dramatic increase in conversion begin to be apparent at the higher temperatures, whereby from 750°C onwards, CO conversion begin to surpass H_2 conversion. Generally CO_2 desorption is the rate limiting step in CO oxidation reactions. Furthermore, CO_2 preferentially adsorbs on the perovskite surface to form carbonates such as $SrCO_3$. However, with increasing temperature, these carbonates can easily undergo thermal desorption, hence with more vacant sites, therefore, the rate for CO oxidation increases as well. Increase in activation of lattice oxygen due to thermal activation of the membrane also contributes to more oxygen vacancy. Increase in oxygen vacancy (especially at temperatures above 750°C) also contributes to increase in selectivity for CO oxidation especially with increasing temperature [31].

It has been reported that oxidation kinetic sequence in the presence of reducing gases is in the order of H_2>CO>CH_4 and this order correlates with the tendency of the reducing gases to react with surface oxygen ions [32-34]. Our results correlate to this

sequence and are distinguished by the H_2 and CO conversions especially in the lower temperatures. However, opposed to previously reported data, this study was conducted in the presence of both H_2 and CO due to their merit of being simultaneously produced during POM reactions. Previous studies were conducted on individual gas exposures and it was shown that for membranes such as $Ba_{0.5}Sr_{0.5}Co_{0.8}Fe_{0.2}O_{3-\delta}$, the membrane material reacts more readily with H_2 compared to CO [34]. From the results shown in Figure 7-4, this trend is quite evident from the $\%H_2$ and %CO converted at the lower temperatures. As mentioned earlier, with increasing temperature, rate of CO oxidation increases due increase in CO_2 desorption (as surface carbonates), hence CO conversion increases as well. Also at increasing temperatures, the CO polarization enhances the affinity with perovskite surface, thus restraining the adsorption of H_2 on the membrane surface [32].

7.2.4. POM reaction pathways occurring on catalyst surface in catalytic LSCG membrane reactor

Many studies have been devoted in contemplating over the reaction pathways involved in the POM reaction. Two types of main reaction pathways on the catalyst bed as shown below have been generally proposed [35]:

(i) direct partial oxidation (DPO) where both CH_4 and O_2 adsorb on the catalyst surface producing H_2 and CO according to reaction (Equation 7-3) [36]:

$$\textbf{POM: } CH_4 + \tfrac{1}{2}\, O_2 \leftrightarrow 2H_2 + CO \qquad \Delta H^o_{298} = -35 \text{ kJ/mol} \qquad (7\text{-}3)$$

(ii) combustion-reforming reaction (CRR), where the reactant undergoes complete combustion (Equation 7-4) and the resulting water undergoes steam reforming of methane (SRM) (Equation 7-5) and CO_2 undergoes dry reforming of methane (DRM) (Equation 7-6) as follows [37]:

Total Combustion: $CH_4 + 2O_2 \leftrightarrow CO_2 + 2H_2O$ $\Delta H^o_{298} = -801$ kJ/mol (7-4)

SRM: $H_2O + CH_4 \leftrightarrow 3H_2 + CO$ $\Delta H^o_{298} = +206$ kJ/mol (7-5)

DRM: $CO_2 + CH_4 \leftrightarrow 2H_2 + 2CO$ $\Delta H^o_{298} = +261$ kJ/mol (7-6)

It has been generally categorized that at high space velocities ($>10^5$ $L.kg^{-1}.h^{-1}$), DPO mechanism is favorable and at low space velocities ($<10^5$ $L.kg^{-1}.h^{-1}$), CRR is more likely to proceed [38]. In this catalytic membrane reactor system, the calculated space velocity is 750 $L.kg^{-1}.h^{-1}$, and this may indicate that CRR is more likely to take place. Hereby, the lower space velocity requires longer residence times for complete O_2 conversion, allowing more H_2O to adsorb and provide additional adatoms for oxidation of carbon adatoms [39].

As observed from the results from the oxygen flux from H_2:CO as sweep gas, the O_2 flux begin to increase due to the dramatic increase in CO conversion at temperatures above 700°C alongside with CO conversion to CO_2. Therefore, if direct POM was reaction pathway, the CO and H_2 selectivity should start dropping from 700°C because at this stage, the O_2:CH_4 ratio was more than 0.5 and less than 1. For direct POM reactions, O_2:CH_4 ratio of 0.5 is stoichiometrically advantageous for optimal reaction. However, the temperature region of 700°C to 750°C showed the best H_2 and CO selectivities from the catalytic POM reaction. Henceforth, the reaction pathway at this alludes with the theory of total oxidation followed by reforming with steam and CO_2 produced from the combustion. This was also observed by several other researchers who studied POM in a catalytic membrane reactor [38, 40, 41]. Even though the H_2 selectivity improves with increasing temperature up to 750°C, however, the H_2 selectivity is still lower than CO selectivity. Therefore, this leads us to believe that a possibility of reverse water gas shift (RWGS)

reaction to take place at the same time, since RWGS reaction is prevalent between 700°C to 800°C [42]. Furthermore, as discussed earlier for the effect of H_2:CO mixture sweep gas, based on the oxidation kinetic sequence, H_2 is more readily oxidizable to H_2O. Equation 7-7 below shows the RWGS reaction:

$$\textbf{RWGS: } CO_2 + H_2 \leftrightarrow CO + H_2O \qquad \Delta H^o_{298} = +41 \text{ kJ/mol} \qquad (7\text{-}7)$$

Therefore, we summarize below the proposed reaction pathways which take place on the catalyst bed of the LSCG catalytic hollow fiber membrane system during POM in the medium temperature of 600°C - 800°C.

i) Low temperature region (600°C -650°C), where O_2 permeation is negligible:

- Methane decomposition on Ni based catalyst (Equation 7-8):

$$CH_4 \rightarrow C + 2H_2 \qquad (7\text{-}8)$$

ii) Medium temperature region (650°C -750°C), where O_2 :CH_4 < 1 :

Carbon oxidation: $C_{ads} + O_{ads} \rightarrow CO_{ads} \rightarrow CO$ (7-9)

- CRR pathway (Equations 7-4 to 7-6), in which total combustion is followed by SRM and DRM reactions, proceeds at a higher pace with increasing temperatures due to the endothermic nature of these reactions.
- Simultaneous occurrence of RWGS (700°C -750°C) (Equation 7-7) which is attributed to lower H_2 selectivities compared to CO selectivities.

iii) Medium – high temperature region (> 750°C), where O_2:CH_4 >1:

- Increase in dominance of deep oxidation reactions to produce more H_2O and CO_2 as deduced from similar declining pace of H_2 and CO selectivities.

The above summary can be analogous to general POM reactions which occur in the catalyst bed in catalytic membrane reaction systems. However, temperature shifts can occur depending on the amount of CH_4 feed as well as the permeating ability of the membrane, whereby membranes with better inherent properties can induce permeation at lower temperatures. The catalytic configuration, type and amount also play a role in changing the reaction pathways involved in the catalytic POM membrane reaction systems. In general, CH_4 reacts differently with different catalyst. For example, with an oxidation catalyst, such as another type of perovskite, it is possible that different kinds of oxidation products, such as C_2 and CO_x species could be formed. Hence, the main reaction pathway involved in the POM reaction largely depends on the catalyst property and the membrane material (which determines the oxygen permeation capacity) as well as the temperature regime of the reaction.

7.2.5. Crystalline phase structure analysis

Figure 7-5 shows the XRD crystalline structure analysis of the LSCG hollow fiber membranes (fresh and post-reaction). The standard cubic perovskite phases with the corresponding *d*-spacing values were identified accordingly [18, 43]. The only differences between the fresh and post-reacted membranes are the reduction in peak intensity as well as slight increase in peak widths. This indicates that deterioration of the initial crystal ordering has taken place to form amorphous debris [44]. Furthermore, the increase in peak width is indicative of the decrease in crystalline size which may be caused by the decomposition due to the reductive environment. The membrane from the blank POM reaction (without catalyst) has the least crystalline deterioration compared to the membrane from the catalytic POM reaction as well as the membrane which has been

exposed to the 50% H_2:CO mixture (in helium). This is evidently due to the greater concentration gradient imposed on the membrane due to the presence of the reducing gases of H_2, CO compared to just CH_4 only. In order to gain a deeper insight on the composition of these amorphous debris, FESEM-EDX and XPS analysis were conducted and reported as follows.

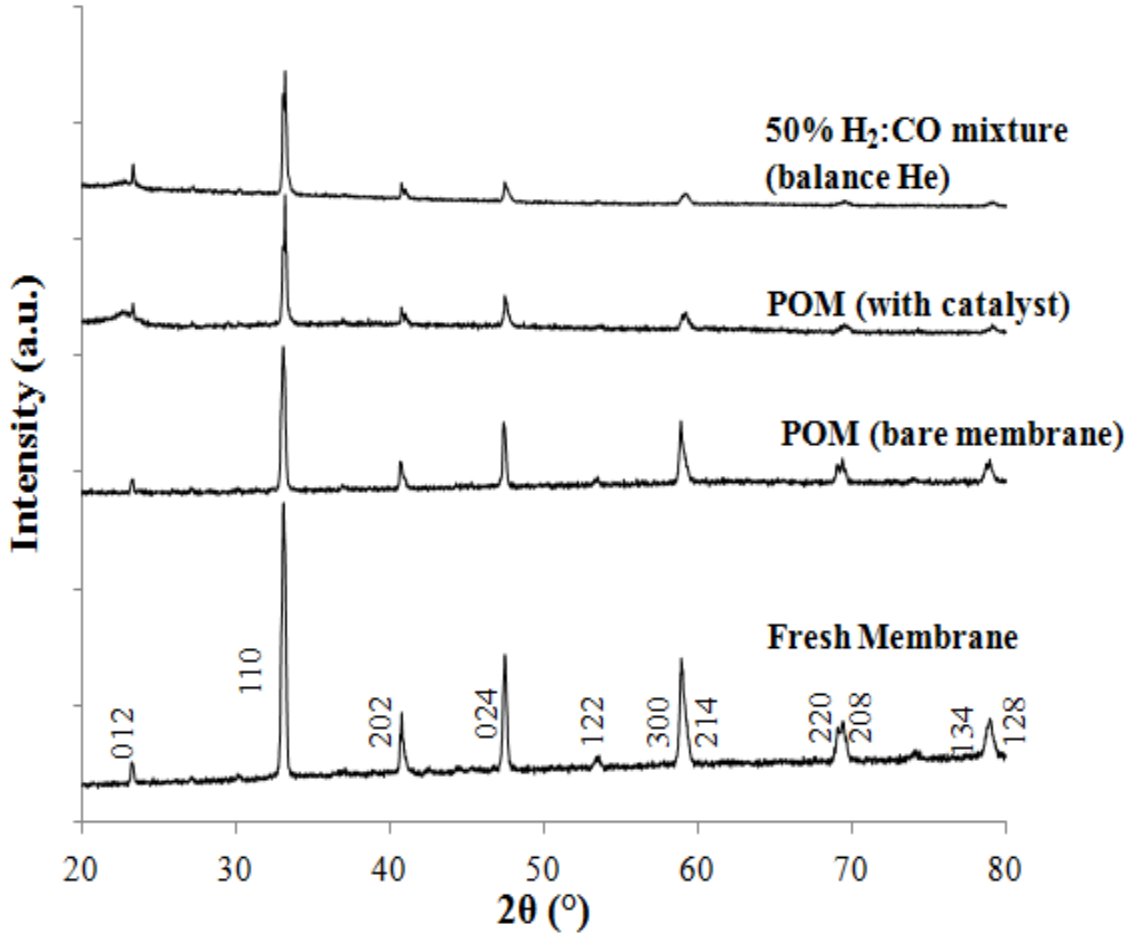

Figure 7-5 XRD profiles of fresh and post-reacted LSCG hollow fiber membranes upon reaction under POM conditions and after 50% H_2:CO (in He) sweep

7.2.6. Surface morphology and elemental distribution via FESEM-EDX

Figure 7-6 shows the FESEM images with the corresponding EDX spectra for the external (reaction side - left) and internal (air side - right) surfaces of the membrane after blank POM reaction (Figure 7-6 (a)), catalytic POM reaction (Figure 7-6 (b)) and exposure to 50% H_2:CO mixture (in helium) (Figure 7-6 (c)). The values denoted in the brackets after each element show the % difference from the stoichiometric amounts.

Based on morphological observation by FESEM, it can be seen that the changes in the structure and composition of the membrane correlates to the surface reaction activity caused by the presence of reducing gases. In other words, the O_2 permeation flux results correspond to the extent of morphological changes observed on the membrane surface. The surface of Figure 7-6 (a) is rather intact with isolated lumps present on the surface due to the presence of mainly CH_4 which is the least reducing gas when compared to H_2 and CO. Figure 7-6 (b) shows the greatest amount of amorphous debris and surface erosion due to the catalytic POM reaction, followed by Figure 7-6 (c). The macrovoids on the permeate-interface are opened upon exposure to reducing gases, hence simultaneously promoting surface exchange kinetics and reducing the membrane effective thickness [44]. On the other hand, no such trend can be distinguished from observation of the internal surfaces of all the post-reacted membranes. They all look similar and structurally intact, and the impact of the different surface reactions cannot be differentiated by visual observation of the internal surfaces. The morphological similarity for the internal surfaces of all the post-reacted membranes shows that the surface near the reaction side was affected by the reducing atmosphere, while the rest of membrane was stabilized by oxygen transport from air side [7].

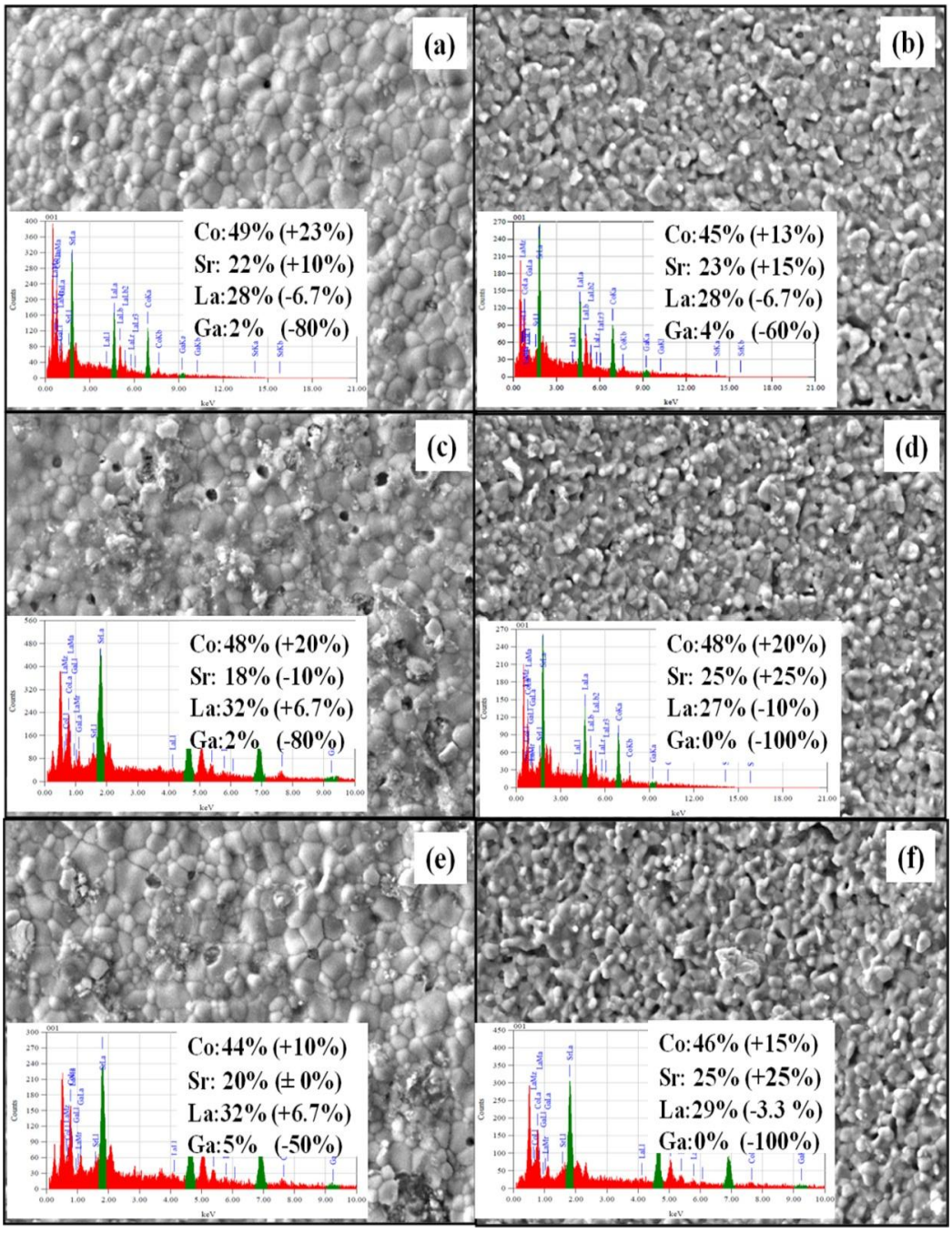

Figure 7-6 FESEM images of LSCG hollow fiber membranes (inset: EDX summary): (a) external and (b) internal surface after blank POM with bare membrane; (c) external and (d) internal surface after POM with catalyst; and (e) external and (f) internal surface after 50% H_2:CO (in He) sweep

However, corresponding EDX spectral information on the inset of the figures gives more detailed information on the extent of phase segregation. All the samples (both internal and external surfaces) show that Co is present a little in excess. Co-enriched surface phases whose large grains were broken to finer grains have been reported on permeate sides of membrane surfaces due to the erosion caused by the reducing atmosphere [7, 33, 45, 46]. Further, Sr enrichment is observed more clearly on the internal surfaces of all the post reacted membranes. Sr-enrichment in the form of $SrCO_3$ has also been observed by ten Elshof et al. [47] who conducted experiments of oxidative coupling of methane in a $La_{0.6}Sr_{0.4}Co_{0.8}Fe_{0.2}O_3$ membrane reactor.

In general, slight La loss could be observed on all the membrane surfaces with the exception of external surface of membrane after catalytic POM reaction and exposure to H_2/CO mixture in helium, where minor La enrichment is present. On the other hand, Ga deficiency is observed on all the post-reacted membranes, especially on the internal surfaces, due to both Co and Sr enrichment. Thus, the La and Ga elements may have tendency to diffuse inwardly towards the membrane bulk. This is due to the intense surface exchange reaction activity which resulted in Sr and Co-enriched phases which have greater mobility to segregate out of the perovskite structure. XPS analysis results are discussed in the next section in order to gain a deeper insight of the segregated Sr and Co elements on the membrane surface.

7.2.7. XPS analysis

As a follow up from the FESEM-EDX results discussed previously, photoemission spectra was recorded for both the external and internal surfaces of the LSCG hollow fiber membranes before and after reaction. Figure 7-7 and Figure 7-8 show the representative

Sr3d and Co2p photoemission spectra respectively for the fresh LSCG hollow fiber membranes and the post-reacted membranes. These spectra are chosen due to their complexities and changeable states especially after reaction under the reducing environment which leads to segregated phases. Table 7-1 gives a summary of the peaks and the composition of the states for the respective elemental spectra for both the external (reaction side) and internal (air side) surface.

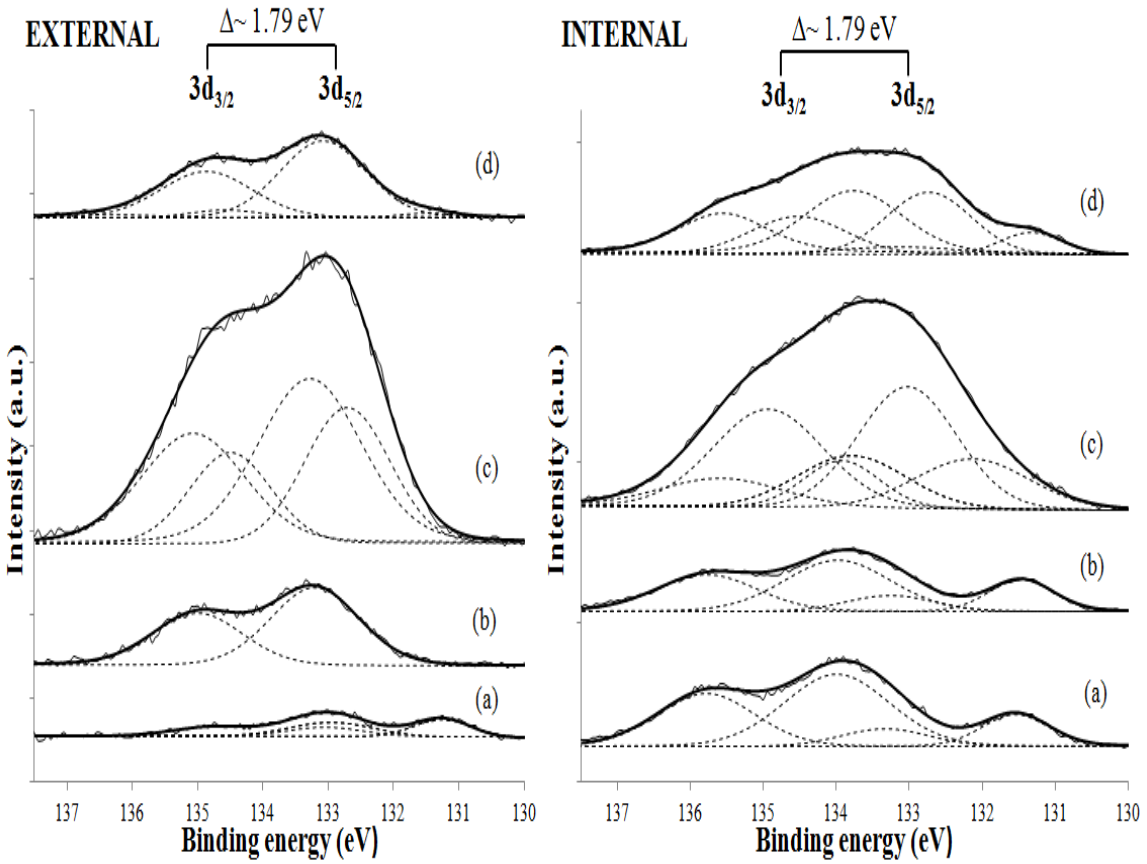

Figure 7-7 Sr 3d XPS spectra for (a) fresh LSCG membrane; (b) after blank POM with bare membrane; (c) after POM with catalyst; and (d) after 50% H_2:CO (in He) sweep

In terms of Sr 3d spectra, as revealed by FESEM-EDX analysis, surface enrichment from Sr can be observed on nearly all the post reacted samples. In order to perform curve fitting for the Sr 3d spectra, a set of criterions were adhered to such as using a splitting energy of 1.79 eV for the Sr doublets, and a Sr $3d_{3/2}$:Sr $3d_{5/2}$ peak area ratio of 2:3[48]. As summarized in Table 7-1, the lower BE of 131.5-132.1 eV correspond to Sr^{2+} existing in the perovskite structure [49]. At the slightly higher BE values ranging from 132.1-132.7 eV may be due to presence of Sr in the low oxidation state such as SrO_{1-x} suboxide on the surface [50]. These are basically Sr^{2+} ions surrounded by vacancies in the oxygen-deficient perovskite structure [51]. BE values *ca*. 133.0 – 133.7 eV coincides well with the $SrCO_3$ component [52, 53]. The higher BE *ca*. 133.8-135.8 eV suggests presence of SrO species [53, 54].

Based on Figure 7-7 and Table 7-1, for the fresh LSCG hollow fiber membrane, the external surface shows that the Sr element exists mainly in the form of $SrCO_3$ (due to atmospheric contamination) and Sr^{2+}. The internal surface however, consists mainly of SrO species with a lesser percentage of Sr^{2+} in the perovskite phase. Upon blank POM reaction (bare membrane), the external surface consists only of $SrCO_3$ species and the internal surface is quite similar to that of the fresh membrane. This is largely due to the CH_4 oxidation activity on the membrane surface, whereby the produced CO_2 reacts with the surface Sr and adsorbs in the form of $SrCO_3$ on the external surface.

Table 7-1 XPS binding energy summary of Sr 3d and Co 2p elements for fresh and post-reacted LSCG hollow fiber membranes

Element	State	Fresh Membrane				Blank POM (Bare Membrane)				Catalytic POM (Membrane + Catalyst)				50% H_2:CO (in He) sweep gas			
		Outer		Inner		Outer		Inner		Outer		Inner		Outer		Inner	
		BE (eV)	Area (%)	BE (eV)	Area (%)	BE (eV)	Area (%)	BE (eV)	Area (%)	BE (eV)	Area (%)	BE (eV)	Area (%)	BE (eV)	Area (%)	BE (eV)	Area (%)
Sr $3d_{5/2}$	Sr^{2+}	131.3	45	131.5	22			131.5	27			132.1	24	131.3	10	131.5	4
	SrO_{1-x}									132.7	39			132.7	41		
	$SrCO_3$	133	55			133.2	100			133.3	61	133	52			133.1	88
	SrO			134	78			133.9	73			133.8	24	133.8	49	134.6	8
Co $2p_{3/2}$	Co^{3+}	780.1	70	780	70	779.7	45	779.7	56	779.5	49	779.3	56	780.3	60	779.6	43
	CoO/Co_3O_4	782.3	30	781.8	22	781.5	40	780.9	24	781.2	39	781.1	44	782.1	40	781	35
	Co^{4+}			783.6	8	784.2	15	782.5	20	783.7	12					782.7	22

On the other hand, presence of $SrCO_3$ carbonate species is more prominent on the LSCG membrane after catalytic POM reaction and exposure to H_2:CO mixture. Even more significantly, for the membrane exposed to the H_2:CO mixture, all the $SrCO_3$ exists in the internal surface. Due to the presence of CO, it is well known that the only reaction that can take place is reaction of CO with the adsorbed O_2 to form CO_2. CO_2 desorption is the rate limiting step from this reaction since it reacts strongly with the Sr to form $SrCO_3$ which adheres more strongly on the internal surface. Even though the membrane from the catalytic POM reaction also has presence of $SrCO_3$, however, due to the effect of catalyst, the formation of CO_2 is suppressed with higher selectivity for CO formation which can desorb more easily compared to the carbonate species. The presence of carbonate on the external surface can also be attributed to the surface contamination. It can also be observed that with presence of both H_2 and CO reducing agents (i.e. from POM catalytic reaction and exposure to H_2:CO mixture), transformation to SrO_{1-x} is more evident. Again, this is ascribed to the intense surface oxygen reaction activity leading to more oxygen vacancies contributed by the presence of these highly reducing gases. However, in all cases, presence of Sr^{2+} in perovskite form especially in the internal surface shows that even in the presence of the Sr-enriched segregates as confirmed by EDX and XPS analysis, the inherent perovskite structure is still maintained, thereby enabling the oxgyen reduction reactions to take place.

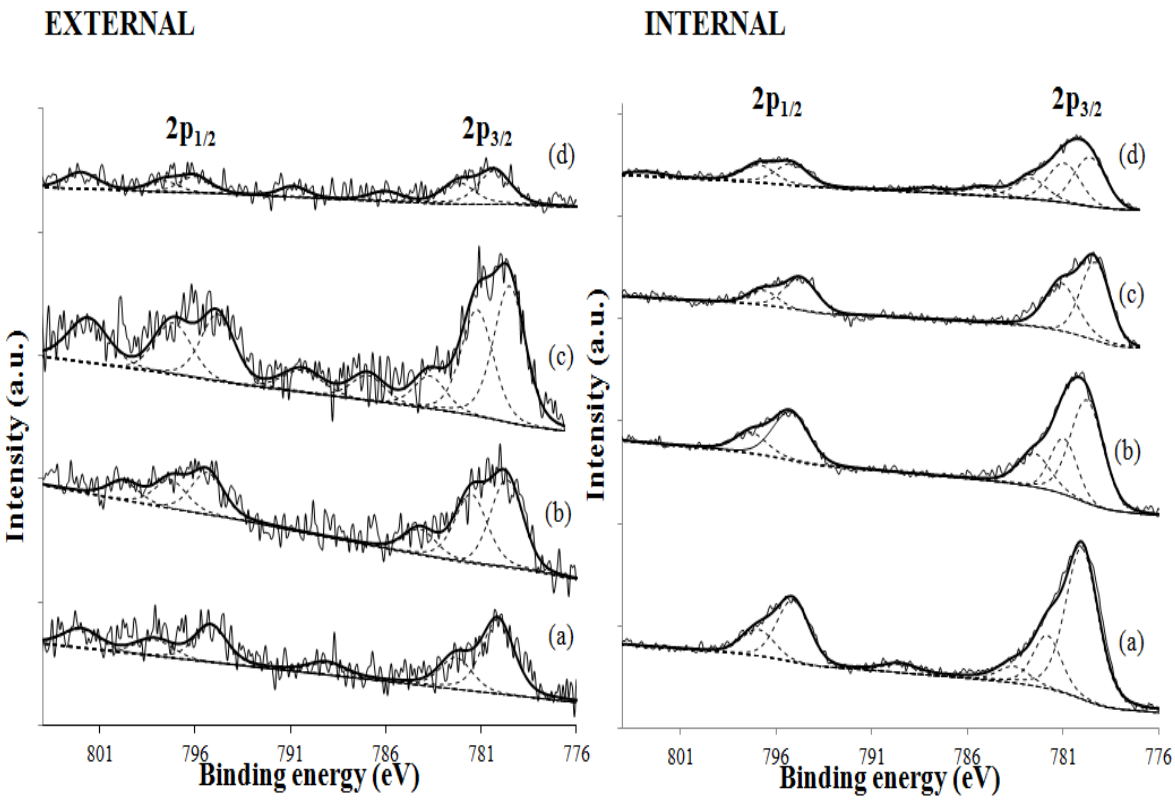

Figure 7-8 Co 2p XPS spectra for (a) fresh LSCG membrane; (b) after blank POM with bare membrane; (c) after POM with catalyst; and (d) after 50% H_2:CO (in He) sweep

In terms of the Co 2p photoemission spectra, XPS analysis provides much insight on the complex Co metal reduction and its state of existence. For the fresh LSCG membrane, as shown in Figure 7-8 (a), the Co $2p_{3/2}$ main spectra can be observed *ca.*780 eV for both the internal and external surfaces with a weak shake up peak *ca.*789 eV. The presence of the weak shake up peak indicate presence of low spin Co^{III} corresponding to octahedral Co^{3+} [55]. The corresponding energy difference arising from the Co $2p_{3/2}$ - Co $2p_{1/2}$ splitting of *ca.* 15 eV further indicates the presence of Co^{3+} [56]. However, for the external surface of the fresh membrane an additional satellite peak at 802 eV can be observed. Peak deconvolution shows another set of Co $2p_{3/2}$ – Co $2p_{1/2}$ doublets at *ca.* 782

and 797 eV respectively. As summarized in Table 7-1, the contribution of the Co $2p_{3/2}$ state at the higher binding energy of *ca.* 782 eV in the fresh membrane is nearly one third of total Co element contribution. These peaks can be assigned to Co^{2+} state [57]. Generally, substitution of Sr^{2+} into La^{3+} results in charge imbalances which are compensated by oxidation of Co^{3+} to the Co^{4+}, or by formation of oxygen holes. The Co^{4+} (d^5) ion however, is not readily stabilized and would be expected to be paramagnetic, giving rise to a shake-up satellite [58]. In order to achieve goodness of fit, the peak at the higher binding energy prior to the satellite region, in the range of 782.5 to 784.2 eV can be ascribed to Co^{4+}.

During the POM reaction, the reducing nature of the permeate side can cause the membrane to undergo deleterious changes to its surface structure [54]. This leads to enhanced electronic activity due to the hydrocarbon degradation taking place, whereby the strongly reducible nature of Co^{3+} will induce transformation to Co^{2+} which has stable half-filled orbits containing stable electron distribution of $t_{2g}^5 e_g^2$ [59]. As can be observed from Figure 7-8 and Table 7-1, upon exposure to the reducing gases, the Co $2p_{3/2}$ peak appear to shift to lower binding energies, indicating the presence of Co^{2+}/Co^{3+}. The presence of shake up peaks at 785 and 802 on the external surface of the of the membrane as shown in Figure 7-8 (c) and Figure 7-8 (d) confirm the presence of CoO and Co_3O_4 surface oxide species [60]. A shift towards lower BE (*ca.* 779 eV) have also been observed by Petunchi and Lombardo during reduction of $LaCoO_3$ under H_2 [61]. The XPS data correlate with the EDX data shown in Figure 7-6, and gives greater insight on the elemental existence of the Co-species on the membrane surface.

7.3. Conclusion

In this study, medium temperature operation of LSCG catalytic hollow fiber membrane reactor packed with 5%Ni/$LaAlO_3$-Al_2O_3 catalyst has been investigated. Based on the results of blank POM reaction (bare membrane), catalytic POM reaction (membrane with catalyst) and sweep with 50%H_2/CO (in helium), it is evident that with presence of larger amount of H_2 and CO gases, higher oxygen flux can be attained. The oxygen permeation flux from the catalytic membrane reactor reached *ca.* 2.5 $mL.min^{-1}.cm^{-2}$ compared to only 0.3 $mL.min^{-1}.cm^{-2}$ for the blank POM reaction (without catalyst) at 800°C. Based on the catalytic POM reaction, at the optimal temperature of 750°C, CH_4 conversion of 97% is achieved with high H_2 and CO selectivity of *ca.* 74% and 91% were obtained. Based on the FESEM-EDX and XPS spectral analysis, presence of $SrCO_3$, CoO and Co_3O_4 can be detected on the external surface of the membrane after catalytic POM reaction, whereas the internal surface of the membrane is enriched with SrO, SrO_{1-x}, CoO and Co_3O_4 phases. Nevertheless, the crystalline perovskite structure and its inherent properties are retained and hence enabling oxygen permeability in the highly reducing environment.

REFERENCES

[1] Sutthiumporn, K.; Maneerung, T.; Kathiraser, Y.; Kawi, S. *Int. J. Hydrogen Energy* **2012**, *37*, 11195-11207.

[2] Sutthiumporn, K.; Kawi, S. *Int. J. Hydrogen Energy* **2011**, *36,* 14435-14446.

[3] Wang, W.; Ran, R.; Shao, Z. *J. Power Sources* **2011**, *196*, 90-97.

[4] Mateos-Pedrero, C.; Duquesne, S.; Carrazán, S.R.G.; Soria, M,A.; Ruíz, P. *Appl. Catal. A Gen*. **2011**,*394*, 245-256.

[5] Li, Q.; Zhu, X.; He, Y.; Yang, W. *Catal. Today*. **2010**,*149*, 185-190.

[6] Balachandran, U.; Dusek, J.T.; Mieville, R.L.; Poeppel, R.B.; Kleefisch, M.S.; Pei, S.; Kobylinski, T.P.; Udovich, C.A.; Bose, A.C. *Appl. Catal. A Gen*. **1995,** *133*,19-29.

[7] Tsai, C.Y.; Dixon, A.G.; Moser, W.R.; Ma, Y.H. *AIChE J*. **1997**, *43*, 2741-2750.

[8] Wang, H.; Feldhoff, A.; Caro, J.; Schiestel, T.; Werth, S. *AIChE J*. **2009**, *55*, 2657-2664.

[9] Tan, X.; Li, K. *AIChE J*. **2009**, *55*, 2675-2685.

[10] Dong, H.; Shao, Z.; Xiong, G.; Tong, J.; Sheng, S.; Yang, W. *Catal. Today*. **2001**, *67*, 3-13.

[11] Jin, W.; Li, S.; Huang, P.; Xu, N.; Shi, J.; Lin, Y.S. *J. Membr. Sci*. **2000**, *166*, 13-22.

[12] Zhang, K.; Sunarso, J.; Shao, Z.; Zhou, W.; Sun, C.; Wang, S.; Liu, S. *RSC Adv.* **2011**, *1*, 1661-1676.

[13] Wang, H.; Tablet, C.; Feldhoff, A.; Caro, J. *J. Membr. Sci*. **2005**, *262*, 20-26.

[14] Raich, B.A.; Foley, H.C. *Ind. Eng. Chem. Res*. **1998**, *37*, 3888-3895.

[15] Tan, X.; Pang, Z.; Gu, Z.; Liu, S. *J. Membr. Sci.* **2007**, *302*,109-114.

[16] Teraoka, Y.; Zhang, H.M.; Furukawa, S.; Yamazoe, N. *Chem. Lett*. **1985**, *11*, 1743–1746.

[17] Sunarso, J.; Baumann, S.; Serra, J.M.; Meulenberg, W.A.; Liu, S.; Lin, Y.S.; da Costa, J.C.D. *J. Membr. Sci*. **2008,** *320*, 13-41.

[18] Liang, F.; Jiang, H.; Luo, H.; Caro, J.; Feldhoff, A. *Chem. Mater*. **2011,** *23*, 4765-4772.

[19] Yang, N.T.; Kathiraser, Y.; Kawi, S. *J. Membr. Sci.* **2013**, *428*, 78-85.

[20] Pei, S.; Kleefisch, M.S.; Kobylinksi, T.P.; Faber, J.; Udovich, C.A.; Zhang-McCoy V.; Dabrowski, B.; Balachandran, U.; Mieville, R.L.; Poeppel, R.B. *Catal. Lett*. **1995**, *30*, 201-212.

[21] Luo, H.; Tan, B.; Wei, Y.; Wang, H.; Jiang, H.; Caro, J. *AIChE J*. **2010**, *56*, 604-610.

[22] Kharton, V.V.; Tsipis, E.V.; Marozau, I.P.; Yaremchenko, A.A.; Valente, A.A.; Viskup, A.P.; Frade, J.R.; Naumovich, E.N.; Rocha, J. *J. Solid State Electrochem*. **2005,** *9*, 10-20.

[23] Kathiraser, Y.; Wang, Z.; Yang, N.T.; Zahid, S.; Kawi, S. *J. Membr. Sci.* **2013**, *427*, 240-249.

[24] Wu, Z.; Wang, B.; Li, K. *Int. J. Hydrogen Energy* **2011**, *36*, 5334-5341.

[25] Oemar, U.; Hidajat, K.; Kawi, S. *Appl. Catal. A Gen*. **2011,** *402*,176-187.

[26] Zhu, X.; Li, Q.; He, Y.; Cong, Y.; Yang, W. *J. Membr. Sci.* **2010,** *360*, 454-460.

[27] Yin, X.; Hong, L.; Liu, Z. *J. Membr. Sci.* **2008**, *311*, 89-97.

[28] Zhang, W.; Smit, J.; Annaland, M.V.S.; Kuipers, J.A.M. *J. Membr. Sci.* **2007,** *291*, 19-32.

[29] Zeng, Y.; Lin, Y.S. *AIChE J*. **2001**, *47*, 436-444.

[30] Ikeguchi, M.; Mimura, T.; Sekine, Y.; Kikuchi, E.; Matsukata, M. *Appl. Cat. A: Gen*. **2005**, *290*, 212-220.

[31] Gosavi, P.V.; Biniwale, R.B. *Int. J. Hydrogen Energy* **2012**, *37*, 3958-3963.

[32] Shen, P.; Ding, W.; Zhou, Y.; Huang, S. *Appl. Surf. Sci*. **2010**, *256*, 5094-5101.

[33] Zhang, Y.; Liu, J.; Ding, W.; Lu, X. *Fuel* **2011**, *90*,324-330.

[34] Jiang, Q.; Faraji, S.; Slade, D.A.; Stagg-Williams, S.M. *Membr. Sci. Technol*. **2011**, *14*, 235-273.

[35] Dissanayake, D.; Rosynek, M.P.; Kharas, K.C.C.; Lunsford, J.H. *J. Catal*. **1991**, *132*, 117–127.

[36] Hickman, D.A.; Schmidt, L.D. *J. Catal*. **1992**, *138*, 267–282.

[37] Prettre, M.; Eichner, Ch.; Perrin, M. *Trans. Faraday Soc*. **1946**, *43*, 335b-340.

[38] Wang, H.; Cong, Y.; Yang, W. *Catal. Today* **2003**, *82*, 157-166.

[39] Hickman, D.A.; Schmidt, L.D. *AIChE J*. **1993**, *39*, 1164-1177.

[40] Chen, C.S.; Feng, S.J.; Ran, S.; Zhu, D.C.; Lin, W.; Bouwmeester, H.J.M. *Angew. Chem. Int. Ed*. **2003**, *42*, 5106-5112.

[41] Caro, J.; Caspary, K.J.; Hamel, C.; Hoting, B.; Kölsch, P.; Langanke, B.; Nassauer, K.; Schiestel, T.; Schmidt, A.; Schomäcker, R.; Seidel-Morgenstern, A.; Tsotsas, E.; Voigt, I.; Wang, H.; Warsitz, R.; Werth, S.; Wolf, A. *Ind. Eng. Chem. Res*. **2007**, *46*, 2286-2294.

[42] Fan, M.S.; Abdullah, A.Z.; Bhatia, S. *ChemCatChem*, **2009**,*1*, 192-208.

[43] Wang, S.; Zheng, R.; Suzuki, A.; Hashimoto, T. *Solid State Ionics.* **2004**,*174*, 157-162.

[44] Tan, X.; Shi, L.; Hao, G.; Meng, B.; Liu, S. *Sep. Purif. Technol*. **2012**, *96*, 89-97.

[45] Gu, X.; Jin, W.; Chen, C.; Xu, N.; Shi, J.; Ma, Y.H. *AIChE J*. **2002**, *48*, 2051-2060.

[46] Xu, S.J.; Thomson, W.J. *AIChE J*. **1997,** *43*, 2731-2740.

[47] ten Elshof, J.E.; Bouwmeester, H.J.M.; Verweij, H. *Appl. Catal. A: Gen*. **1995**, *130*, 195-212.

[48] van der Heide, P.A.W. *Surf. Interface Anal*. **2002**, *33*, 414-425.

[49] Yamazoe, N.; Teraoka, Y.; Seiyama, T. *Chem. Lett*. **1981**, *12*, 1767-1770.

[50] Kozhukharov, V.; Machkova, M.; Ivanov, P.; Bouwmeester, H.J.M.; Van Doorn, R. *J. Mater. Sci. Lett.* **1996**, *15*, 1727-1729.

[51] Polini, R.; Falsetti, A.; Traversa, E.; Schäf, O.; Knauth, P. *J. Europ. Cer. Soc*. **2007**, *27*, 4291-4296.

[52] Liu, B.; Zhang, Y.; Tang, L. *Int. J. Hydrogen Energy* **2009**, *34*, 435-439.

[53] Natile, M.M.; Poletto, F.; Galenda, A.; Glisenti, A.; Montinini, T.; De Rogatis, L.; Fornasiero, P. *Chem. Mater*. **2008**, *20*, 2314-2327.

[54] Norman, C.; Leach, C. *J. Membr. Sci.* **2011**, *382*, 158-165.

[55] Marcos, J.A.; Buitrago, R.H.; Lombardo, E.A. *J. Catal.* **1987**, *105*, 95-106.

[56] Natile, M.M.; Ugel, E.; Maccato, C.; Glisenti, A. *Appl. Catal. B: Environ*. **2007**, *72*, 351-362.

[57] Prasad, D.H.; Park, S.Y.; Oh, E.O.; Ji, H.; Kim, H.R.; Yoon, K.J.; Son, J.W.; Lee, J.H. *Appl. Catal. A: Gen*. **2012**, *447-448*, 100-106.

[58] Bocquet, A.E.; Chalker, P.; Dobson, J.F.; Healy, P.C.; Myhra, S.; Thompson, J.G. *Physica C*. **1989**, *160*, 252-258.

[59] Sun, M.; Jiang, Y.; Li, F.; Xia, M.; Xue, B.; Liu, D. *Mater. Trans.* **2010**, *51*, 2208-2214.

[60] Mota, N. Navarro, R.M.; Alvarez-Galvan, M.C.; Al-Zahrani, S.M.; Fierro, J.L.G. *J. Power Sources* **2011**, *196*, 9087-9095.

[61] Petunchi, J.O.; Lombardo, E.A. *Catal. Today* **1990**, *8*, 201-219.

CHAPTER 8

Oxidative CO_2 reforming of methane in

$La_{0.6}Sr_{0.4}Co_{0.8}Ga_{0.2}O_{3-\delta}$ (LSCG) hollow fiber membrane reactor

CO_2 utilization in catalytic membrane reactors for syngas production is an environmentally benign solution to counter the escalating global CO_2 concerns. In this study, integration of $La_{0.6}Sr_{0.4}Co_{0.8}Ga_{0.2}O_{3-\delta}$ (LSCG) hollow fiber membrane reactor with $Ni/LaAlO_3$-Al_2O_3 catalyst for the oxidative CO_2 reforming of methane (OCRM) reaction was successfully tested for 160h of reaction. High CH_4 and CO_2 conversions of ca. 94% and 73% were obtained with O_2 flux ca. 1 $mL.min.^{-1}.cm^{-2}$ at 725°C for the 160-h stability test. Surface temperature programmed desorption studies of the membrane was conducted with H_2, CO and CO_2 as probe gases. SEM-EDX, XPS and FTIR analysis of the post reacted membrane after long term stability tests suggests Sr-enriched phases with presence of adsorbed carbonate and hydrogenated carbon. This shows subsequent reactant spillover on the membrane surface from the catalyst bed took place due to the reaction occurring on the catalyst. However, XRD analysis of the bulk structure does not show any phase impurities, thus confirming the structural integrity of the LSCG hollow fiber membrane.

8.1. Introduction

The rising levels of anthropogenic emissions of CO_2 and CH_4, two major greenhouse gases, contributes to alarmingly dangerous climate change [1-3]. In view of the serious environmental implications, many investigations have been carried out for the CO_2 (dry) reforming of methane (DRM) reaction as a means to utilize and transform these two major greenhouse gases into more valuable products, i.e. syngas and hydrogen. This

will improve further the efficiency and economics of overall processes for power generation and CO_2 sequestration [4]. Syngas serves as the building block for numerous chemicals such as ammonia and methanol [5]. However, the major drawbacks of DRM include high energy requirements owing to its endothermicity (ΔH^o_{298K} = 247 kJ.mol^{-1}) as well as the high carbon deposition on Nickel based catalysts associated with the DRM process [6]. Hence, in order to compensate for the energy extremes of the endothermic DRM process, an alternative process which can be considered is via oxidative CO_2 reforming of methane (OCRM). This process is highly beneficial since by introducing some exothermicity, via addition of oxygen, the energy requirement can be minimized and the syngas ratio can be tailored by adjusting the feed proportions of oxygen, methane and CO_2. Furthermore, presence of oxygen also enables carbon gasification from the catalyst, thus preventing reactor blockage [7].

Use of dense oxygen mixed ionic and electronic oxygen conducting (MIEC) ceramics as an environmentally benign process to supply oxygen from air for either syngas or hydrogen production have received significant attention in recent years [8, 9]. Integration of catalytic membrane reactor system with the oxygen-permeable MIEC membrane for partial oxidation of hydrocarbons has been widely explored in view of its immense benefits of sustainable production via minimizing unit operation and energy costs [10-16]. Besides serving as sustainable oxygen sources for POM process, integration of MIEC membrane provide selective permeation barriers to N_2, which eliminates the formation of environmental pollutants (e.g., NOx) during high-temperature reactions [17].

Slade et al. [18] successfully incorporated $SrFeCo_{0.5}O_x$ (SFC) disc membrane to supply oxygen for CO_2 reforming of methane. They demonstrated that the lattice oxygen supplied from the membrane is more beneficial in terms of giving higher reactant

conversions compared to co-fed molecular gas phase oxygen for the methane reforming. On the other hand, Wei et al. [19] showed that with presence of a small amount of CO_2 (*ca.* 5% of methane feed), the methane conversion can be drastically increased from 55% to 92% especially at the lower temperature of their study, i.e. at 850°C) using the $BaCo_{0.6}Fe_{0.2}Ta_{0.2}O_{3-\delta}$ (BCFT) membrane packed with a Ni-based catalyst. Besides, in a study carried out by Jin et al. [20] on CO_2 decomposition using perovskite membranes, increase in oxygen permeation rate is found to be beneficial to the decomposition of CO_2 to CO and lattice oxygen. Hence, when applied for the OCRM reaction, this inadvertently increases the syngas product selectivity, besides gasifying the deposited carbon as a result of methane decomposition. However, very few studies have been reported on this reaction branch, and in all cases, disc configurations were used [8, 19, 21].

On the other hand, MIEC membranes in the form of hollow fiber membrane configuration exhibit several advantages such as higher surface area/volume ratio with facile sealing [22]. Using this principle, our group has recently published our findings of using $La_{0.6}Sr_{0.4}Co_{0.8}Ni_{0.2}O_{3-\delta}$ (LSCN) hollow fiber membrane configuration for the OCRM reaction. The comparison between DRM and OCRM reactions were carried out at 800°C. The benefits of OCRM reaction in terms of higher methane conversions as well as lower catalyst carbon deposition were demonstrated [23].

In this study, an integrated OCRM reaction using the Ga-doped $La_{0.6}Sr_{0.4}Co_{0.8}Ga_{0.2}O_{3-\delta}$ (LSCG) hollow fiber membrane coupled with a Nickel based catalyst (5% $Ni/LaAlO_3$-Al_2O_3) developed by our research group is carried out. Here we report the long-term stability (160 h) results for the OCRM reaction at the intermediate temperature of 725°C with further analyses on the post-reacted membrane. In this study, surface studies on the fresh LSCG membrane using CO, H_2 and CO_2 as probe gases were

firstly conducted in order to facilitate further understanding on the interaction of the LSCG membrane with the highly reducing product gases of H_2 and CO, as well as CO_2 reactant gas. The LSCG membrane has been found to be stable under CO_2 atmosphere [24], which is an important criterion for the OCRM reaction. Furthermore, the integrated catalytic LSCG membrane reactor has also been studied for POM reaction, which is a pre-requisite for studying the OCRM reaction [25]. Hence the study of OCRM reaction using hollow fiber membrane reactor for long-term stability and the associated morphological changes in the membrane has great potential for utilization of CO_2 in an environmentally sustainable reaction process.

8.2. Results and discussion

8.2.1. TPD of H_2 and CO on LSCG membrane surface

Figure 8-1 shows the TPD profiles from the crushed LSCG hollow fiber membranes upon adsorption of H_2 and CO respectively for 1 hour at room temperature. TPD of CO and H_2 yielded CO_2 and H_2O species respectively upon increase in temperature. Since La^{3+} is partially replaced with Sr^{2+}, hence charge compensation is achieved via oxidation of Co^{3+} to Co^{4+}, and by formation of an oxygen deficient perovskite. Therefore, presence of the Co^{4+} (unstable) and oxygen vacancies facilitates diffusion of lattice oxygen from bulk to surface [26]. Thus, upon thermal activation, this leads to oxidation of adsorbed CO and H_2 species with increase in temperature.

Based on the TPD profiles, it can be inferred that the LSCG membrane has greater affinity towards H_2 compared to CO. Both the onset temperatures for CO_2 and H_2O desorption begin around the same temperature, *ca.* 325°C. However, for the CO_2 peaks formed from the TPD-CO experiment, a sharp peak at 437°C followed by a smaller

shoulder peak at 600°C was observed. It has been proposed by several researchers that CO adsorbs on surface O^{2-} ions by interacting with the adsorbed atomic oxygen, producing a more labile monodentate carbonate species (corresponding to its low desorption temperature) that decomposes, yielding CO_2 and oxygen [26-27].

On the other hand, for the H_2O peak formed from the TPD-H_2 experiment, a low and broad peak showing a very mild H_2O desorption with a shoulder at 760°C is observed, before finally evolving into a sharp peak at 862°C. This sharp peak coincides with the reduction of Co^{3+} to Co^{2+} in the LSCG perovskite [22]. Reaction of H_2 and lattice oxygen has been reported to be promoted with increasing temperature [28-29]. Based on our previous study [23], and similar findings reported by other groups [30-31], the membrane surface has been found to react more readily with H_2 followed by CO. However, as observed in this study, upon desorption of H_2 and CO, the release of H_2 as H_2O is much slower than desorption of CO as CO_2. It has been proposed by Tejuca et al. [29] that H_2 is adsorbed on Co^{n+} sites, and with increasing temperature, reduction takes place. Hence, increase in H_2O formation intensity shows that oxide surface undergoes reduction, which is substantially lower than what is required for bulk reduction. As such based on our data, it is possible that both H_2 and CO adsorb at different sites, with respect to the different desorption temperatures. Therefore, in order to elucidate more understanding on the carbonate decomposition on the LSCG perovskite, CO_2-TPD was conducted at various CO_2 adsorption temperatures.

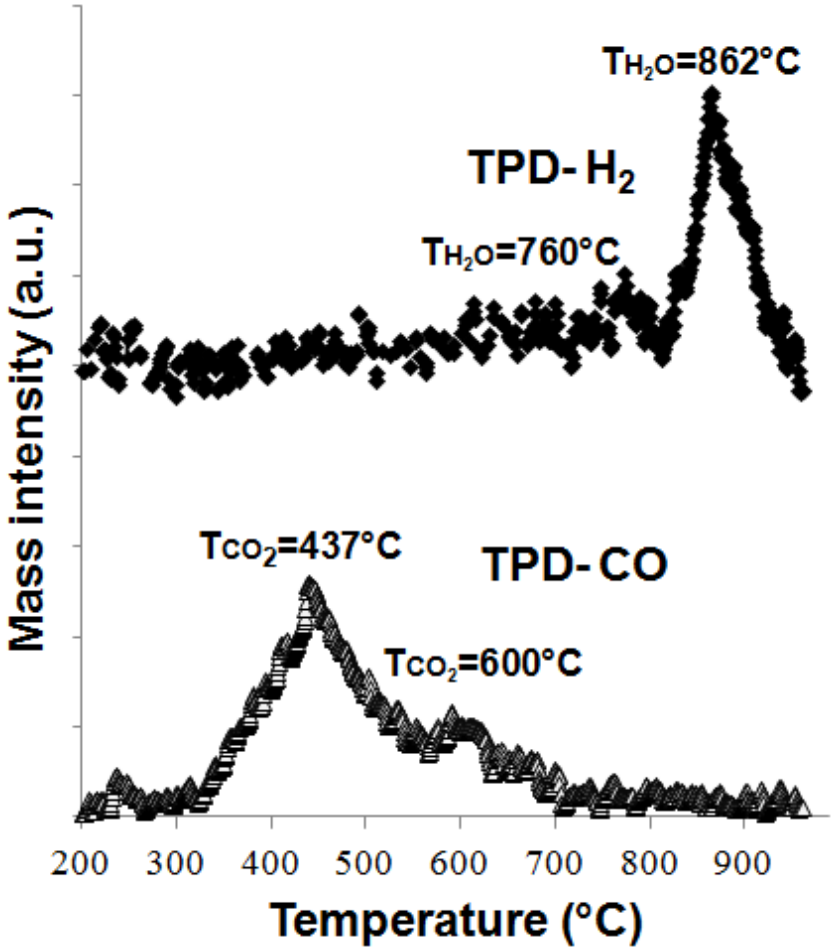

Figure 8-1 H_2 and CO-TPD analysis for fresh LSCG membrane

8.2.2. TPD of CO_2 on LSCG membrane surface

Figure 8-2 shows the CO_2-TPD profiles of the crushed LSCG hollow fiber membranes after pre-treatment for 1 hour under CO_2 at various temperatures. For the samples pre-treated at room temperature, 100°C and 300°C, almost similar profiles can be observed. A wide first peak (with an onset temperature of 327°C (for T_{ads}= 25, 100 and 300°C) and a second sharper peak (at *ca.* 626°C for T_{ads} = 25°C; 618°C for T_{ads} = 100°C and 635°C for T_{ads} = 25 and 300°C) are formed. Another observation is that as the temperature of adsorption increases from 25 to 300°C, the strength of the first desorption

peak begin to diminish, whilst the second sharper peak has comparable adsorption strength. Conversely, upon increase in the adsorption temperature to 450 and 650°C, a change in pattern can be observed. The first peak is similarly shaped as the second peak formed from CO_2 adsorption at the lower temperatures. Also, the second peak formed from CO_2 adsorption at 450 and 650°C, although sharper, is broader than the former peak. With increase in CO_2 adsorption temperature from 450-650°C, the desorption temperatures of both peaks gradually shifted to higher temperatures. The first peak shows a 50°C shift (from 640°C at T_{ads}= 450°C to 690°C at T_{ads}= 650°C). On the other hand, the second peak show a 37°C shift (717°C at T_{ads}= 450°C to 754°C at T_{ads}= 650°C).

The overall peak shifts towards higher temperatures observed on all samples, with increase in CO_2 adsorption temperature imply strengthening of CO_2 reactivity of CO_2 on the LSCG basic sites with increasing temperature. This is more evident with its more distinctive desorption (i.e. sharper peaks and higher desorption temperatures, especially for T_{ads} = 450 and 650°C). This shift in adsorption was also observed by Yan et al. [32] who studied the adsorption of CO_2 at various temperatures on $Ba_{0.5}Sr_{0.5}Co_{0.8}Fe_{0.2}$ (BSCF). Adsorption of CO_2 leads to formation of carbonates which form a resistance layer on the perovskite surface as compared to O_2 adsorption which helps stabilize the perovskite structure [32]. Based on the two desorption peaks from CO_2-TPD, by taking into account the basic character of La and Sr in the LSCG, it is reasonable to suppose that the main cause of carbonate formation is due to lanthanum and strontium [33]. In fact cobalt has been observed to not interact with CO_2 [34]. Regarding the different desorption peaks, it has been reported that generally desorption of CO_2 peaks at different temperatures refer to different distribution of the carbonate species, i.e. monodentate, bidentate or bulk types [33].

By comparing the first desorption peak T_{ads} = 25, 100 and 300°C, and the second desorption peak of T_{ads} = 450 and 650°C, it is possible to assign the former to monodentate carbonates, while the latter could be assigned to the transformation of the monodentate carbonates to the higher thermal stability bidentate carbonates. The monodentate carbonate species is derived from the interaction of CO_2 with oxygen anions near neighbours of La^{3+} or Sr^{2+} cations. The bidentate carbonate from CO_2 takes place on pairs of surface sites composed of lattice oxygen and an anionic vacancy [29]. It is more thermally stable compared to the monodentate carbonate as it requires destruction of oxygen-oxide bond structure [27]. As for the small sharper peak which appear *ca.* 600-700°C (i.e. the second desorption peak for T_{ads} = 25, 100 and 300°C and the first desorption peak for T_{ads} = 450 and 650°C), it is possible to attribute it to decomposition of surface strontium carbonate crystallites on the perovskite oxide. This is deduced based on the similarities in peak appearance from all the TPD profiles, even though desorption at higher temperatures take place corresponding to increasing CO_2 adsorption temperature. Strontium is prone to form segregated phases and react readily with CO_2 forming surface $SrCO_3$ crystallites which decompose at temperatures between 600-900°C [32, 35, 36].

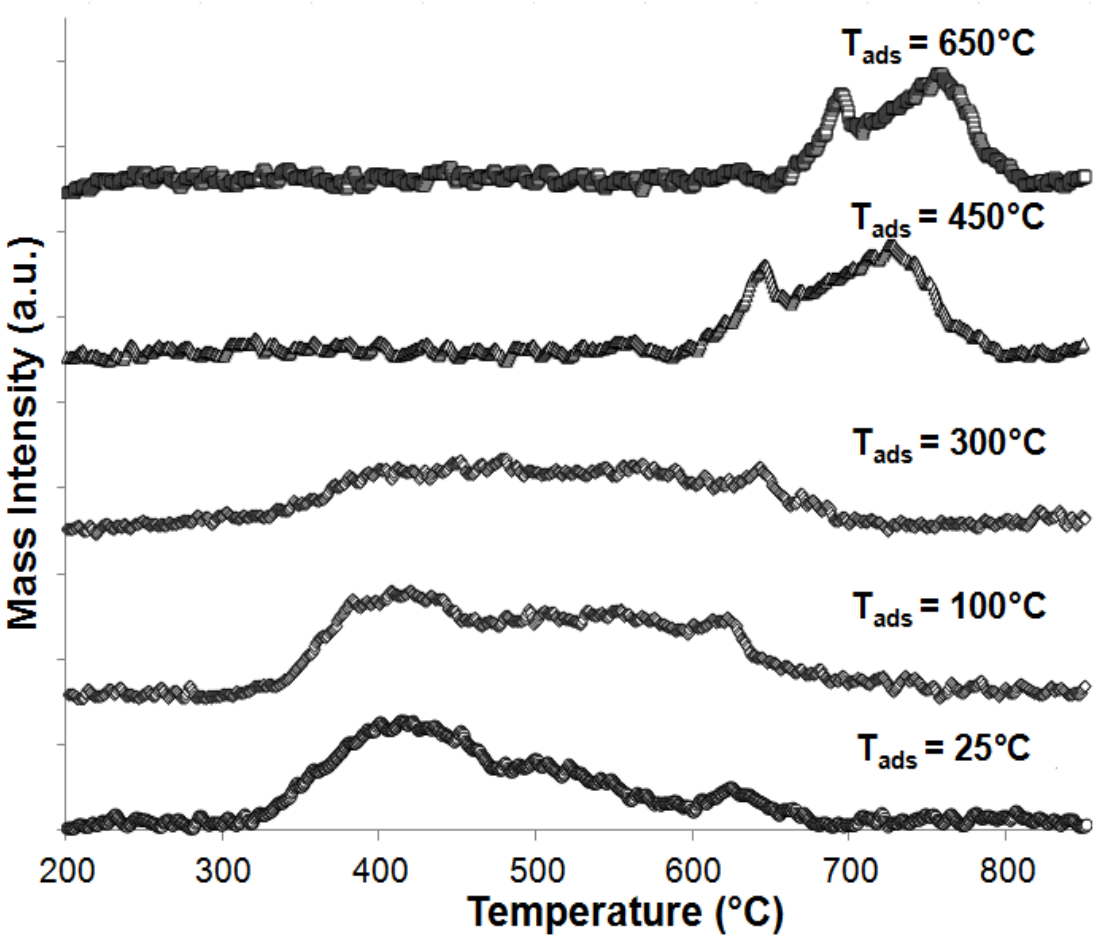

Figure 8-2 CO_2-TPD for various adsorption temperatures on fresh LSCG membrane

8.2.3. OCRM reaction with varying temperature

8.3.3.1. Effect of temperature on O_2 permeation

Figure 8-3 shows the O_2 permeation flux (coupled with the reactant conversions) during the course of the OCRM reaction with increasing temperature from 650-800°C. The O_2 permeation flux was calculated using Equations 4-5 to 4-7. Data was collected every 180 mins for an interval of 25°C. Based on Figure 8-3, the oxygen permeation flux showed a steady increase from *ca*. 0.8 $mL.min^{-1}.cm^{-1}$ (650°C) to 1.4 $mL.min^{-1}.cm^{-1}$ (800°C). Most other oxygen membrane reactors reported in literature are those usually

used for partial oxidation of hydrocarbons such as methane in POM. These reactions deliver significant increment in oxygen fluxes with increasing temperature due to the reducing nature of methane and its product gases of H_2 and CO which aid in increasing the O_2 partial pressure gradient across the membrane.

We have found in our previous study that even though the LSCG membrane is stable in concentrated CO_2 atmosphere, however, the O_2 flux does not improve in the presence of CO_2, despite having been exposed to CH_4 (tremendous flux enhancement observed during CH_4 exposure) [22]. This is because presence of CO_2 can lead to carbonate formation, which can block the membrane surface and provide some resistance to oxygen permeation [37]. However, in this study, with increasing temperature, some improvement in flux can be observed, aided by the presence of the reaction product gases, i.e H_2 and CO. In other words, upon reaction of CH_4, CO_2 and O_2 on the catalyst bed, the produced syngas results in a very reducing atmosphere which lowers significantly the oxygen partial pressure especially on the interface of the catalyst bed and membrane surface. Hence, this creates a large differential pressure gradient across the membrane, which becomes a driving force in ensuring O_2 flux enhancement [8, 21].

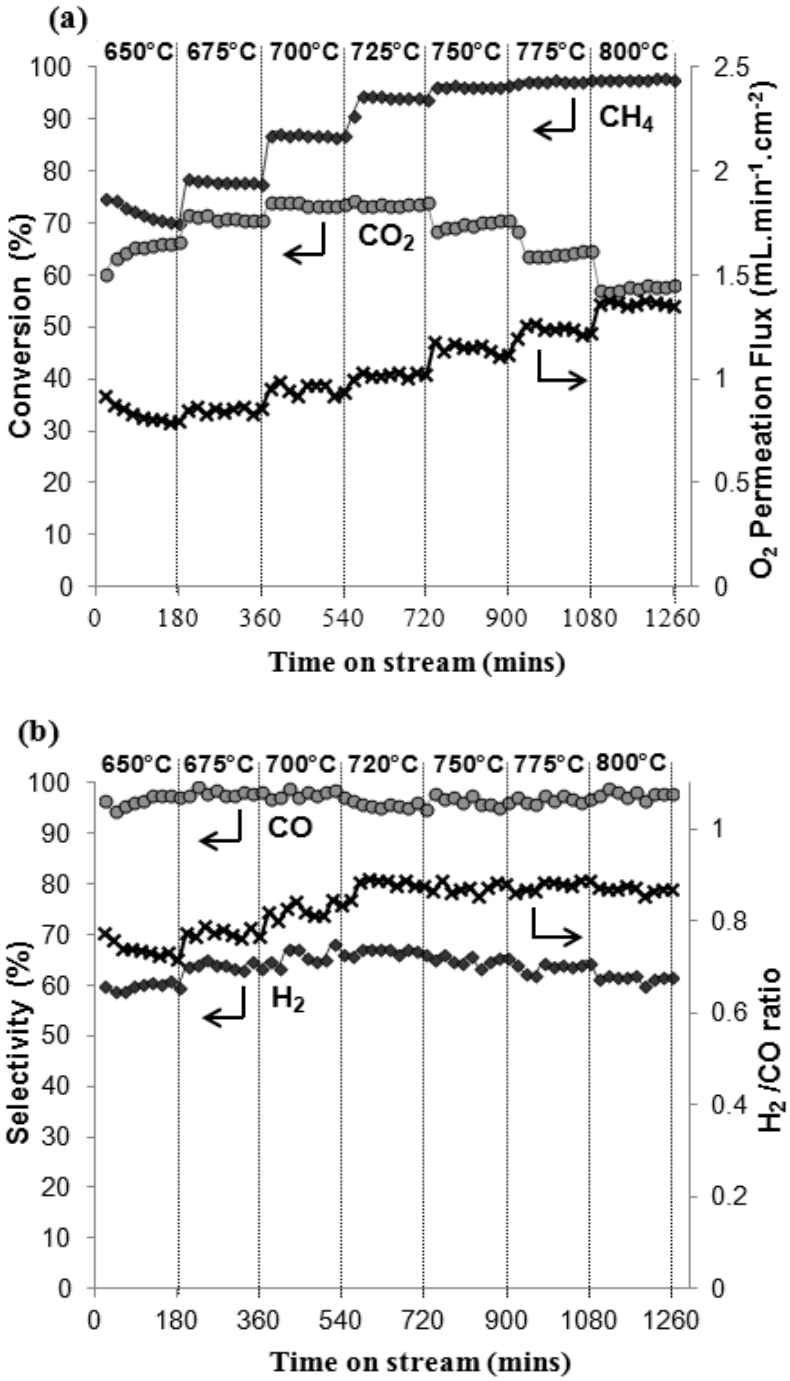

Figure 8-3 Oxygen permeation and catalytic OCRM reaction in LSCG hollow fiber membrane reactor from 650°C-800°C. (a) O_2 supply, $\%CH_4$, CO_2 conversions; (b) H_2&CO selectivity, H_2/CO ratio. (F_{air}=100 mL·min^{-1}, F_{CH4}=3.2 mL·min^{-1}, F_{CO2}=2.7 mL·min^{-1}, F_{He}=6.8 mL·in^{-1}, 0.18g 5%Ni/$LaAlO_3$-Al_2O_3, S_A=1.52 cm^2).

8.3.3.2. Effect of O_2 permeation flux on OCRM catalytic performance

Based on the reactant conversions shown in Figure 8-3 (a), it can be seen that increase in O_2 permeation flux (with increasing temperature) is beneficial in enhancing CH_4 conversion in the OCRM reaction, especially when the LSCG membrane is thermally activated at temperatures exceeding 675°C. During the OCRM testing at 650°C, a slight drop in CH_4 conversion (from *ca*. 75% to 70%) is attributed to low O_2 permeation as well as insufficient activation of CO_2 reforming to take place. The temperature-accelerated O_2 permeation flux is crucial for improving CH_4 conversion from *ca.* 80% (at 675°C) to 98% (at 800°C). In fact, 95% methane conversion is achieved from 750°C onwards.

On the other hand, in terms of CO_2 conversion, steady improvement from *ca*. 65% (at 650°C) to 73% (at 725°C) was observed. However, further increase in temperature leads to considerable decrease in conversion of CO_2 which reaches about 58% (at 800°C). This shows that with a marked improvement in O_2 permeation flux from 750°C onwards, the major reactions of both the CO_2 reforming and partial oxidation of methane competes with each other. Since both these reactions consume CH_4, hence with increasing temperature, CH_4 conversion continues to ascend and maintain near complete conversion.

As shown in Figure 8-3 (b), CO selectivity is maintained throughout the temperature range of 650-800°C from 95-98%. On the other hand, gradual increase in H_2 selectivity takes place from 60% (at 650°C) to 68% (at 725°C). Above this temperature, a very mild decrease in H_2 selectivity begins to take place reaching 63% (at 800°C). The lower H_2 selectivity indicates presence of water which cannot be detected by the GC. However, there are no other side product formations apart from water in this reaction. In terms of H_2/CO ratio, from an initial value of *ca.* 0.75, the ratio gradually increased and maintained around 0.88 from 725°C onwards. This shows that despite slight decrease in

H_2 selectivity, the H_2/CO ratio is not affected and can be maintained. The greater increase in CH_4 conversion, explains the reason H_2/CO ratio can be maintained, whereby at temperatures above 725°C, POM begin to exert a greater influence in the OCRM reaction owing to the increase in O_2 flux, and therefore subsequent decrease in CO_2 conversions.

Our previous finding in POM reaction [23] showed that higher O_2 flux could be attained compared to OCRM reaction leading to dominance of combustion especially at the higher temperatures which contribute to drop in both H_2 and CO selectivities. Hence, in this OCRM study, presence of CO_2 can be considered to control the O_2 permeation ($O_{2,\ permeated}$:$CH_{4,\ feed}$ <1) thus enabling the permeated O_2 to be more selective in its methane conversion especially at higher temperatures. As discussed earlier based on the results of H_2 and CO TPD studies, it can be inferred that the slightly lower H_2 selectivity can be attributed to the LSCG membrane's affinity towards H_2 compared to CO. As discussed earlier based on H_2 TPD results, H_2 is more likely to have higher affinity to adsorb on Co^{n+} sites of the LSCG membrane compared to CO. Hence, the continuous presence of highly reducing gases with increasing reaction temperature results in a more reduced Co state which in turn enables it to more easily oxidize the adsorbed H_2 to H_2O, thus resulting in lower H_2 in the permeate stream. In addition, unlike our previous study on POM reaction, where RWGS and combustion reactions dominate at the higher temperatures, in this study, direct POM is a significant reaction pathway together with DRM, due to the controlled oxygen permeation in the presence of CO_2 as a co-reactant.

8.2.4. Examination of chemical stability for OCRM reaction

It is crucial to examine the durability of the LSCG membrane for the OCRM reaction for an extended period of time.

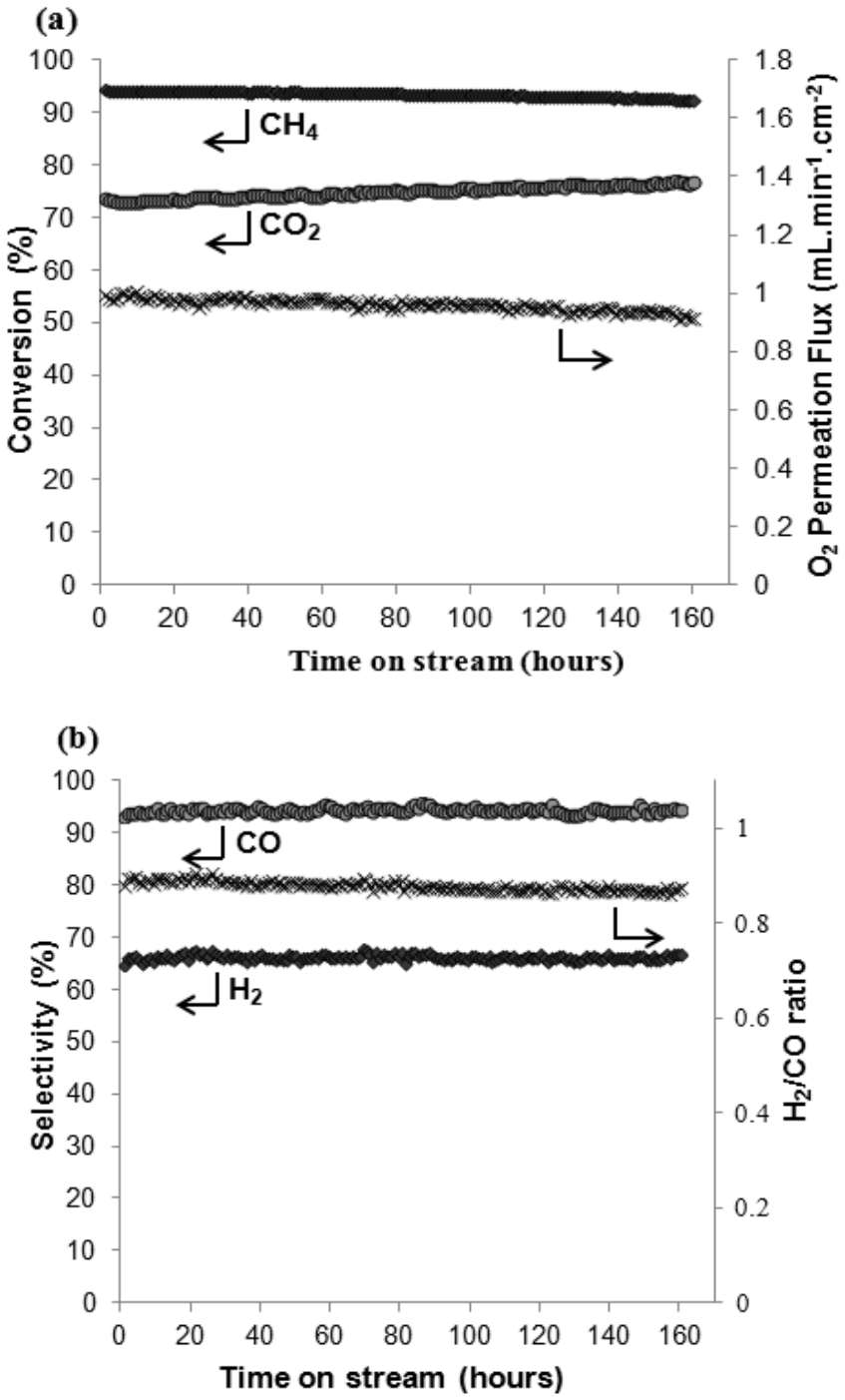

Figure 8-4 160-hour stability study for O_2 permeation and OCRM reaction at 725°C in LSCG hollow fiber membrane reactor. (a) O_2 supply, $\%CH_4$, CO_2 conversions; (b) H_2&CO selectivity, H_2/CO ratio. (F_{air}=100 mL·min^{-1}, F_{CH4}=3.2 mL·min^{-1}, F_{CO2}=2.7 mL·min^{-1}, F_{He}=6.8 mL·min^{-1}, 0.18g catalyst, S_A= 1.52 cm^2)

The OCRM stability test was conducted at the optimal reactant conversion and product selectivities which occur 725°C as determined in Figure 8-3. The OCRM stability test was carried out for 160 h before it was voluntarily terminated. As shown in Figure 8-4 (a), a stable CH_4 conversion is maintained with just a 1% drop to *ca*. 93% at the end of the 160 h. Coincidentally at the end of the 160 h, the O_2 flux also dropped from 1 to 0.92 mL.min $^{-1}$.cm^{-2}. On the other hand, the CO_2 conversion had a 3% conversion increment towards the end of the study due to the lower O_2 flux. However, in terms of product selectivity, the H_2 and CO selectivity, as well as H_2/CO ratio is maintained throughout the study. Overall it can be surmised that based on the conditions employed, steady and stable OCRM performance can be achieved using the LSCG hollow fiber membrane. The used membranes were further analyzed and discussed in the following section.

8.2.5. Post-reaction characterization after stability test

8.2.5.1. Crystalline phase structure and structural morphology

Figure 8-5 shows the XRD analysis of the post-reacted membrane after OCRM stability test of 160 hours. The membrane crystalline phases are still intact and match the lattice structure of the fresh LSCG hollow fiber membrane. This explains the stable performance achieved during the OCRM stability test. The only obvious difference in the XRD pattern is that the crystalline intensity of the post-reacted membranes are lower than the fresh membrane thus indicating deterioration of crystal ordering which took place during the OCRM reaction [21, 37]. However, presence of any segregated phases could not be discerned based on bulk XRD analysis of the post-reacted membrane. Hence, in order to further ascertain any possible changes on the membrane surface, SEM-EDX analysis was conducted.

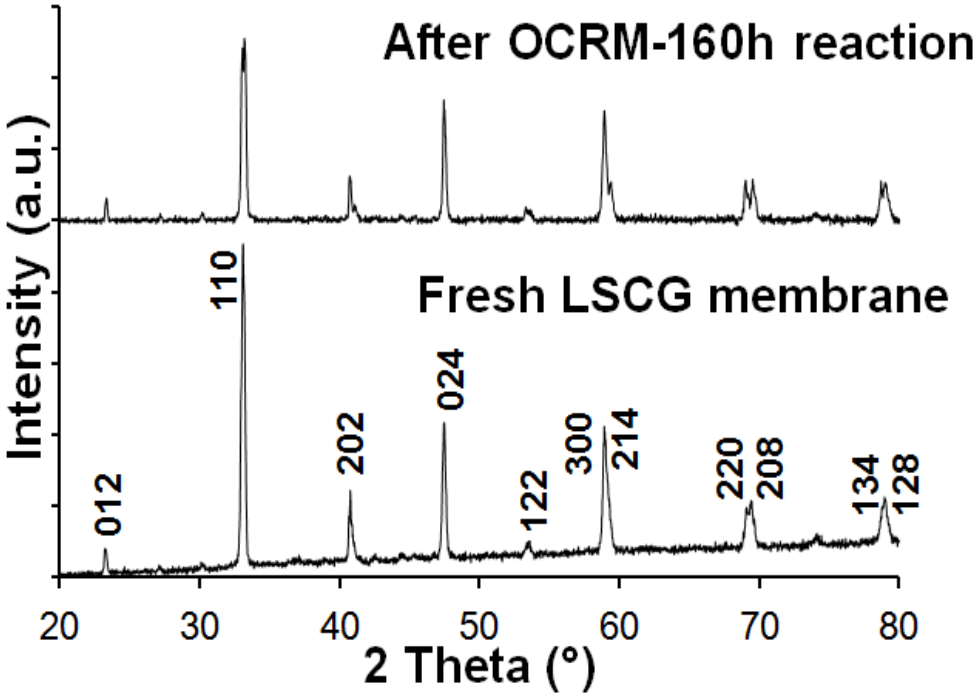

Figure 8-5 XRD profiles of fresh and post-reacted LSCG hollow fiber membranes after 160-h OCRM stability study

Figure 8-6 shows the SEM-EDX analysis of inner (air side) and outer (reaction side) surfaces of the post-reacted membranes. The morphological structure of inner surface looks intact and well-coalesced compared to the outer surface, where surface erosion is observed. Depletion of Co elements can be discerned on both inner and outer surfaces based on EDX analysis. However, this is in contrast with our previous study conducted for POM reaction, where Co enrichment was found on the membrane internal and external surfaces, in the form of CoO and Co_3O_4 species [23]. Hence, in this case, depletion of Co can be attributed to migration of Co to the lamellae grain boundary [38]. The main reason of the Co extraction and migration is attributed to the reduction of cobalt cations due to the highly reducing atmosphere [39]. Therefore, even though the long term

presence of the membrane in the simultaneous corrosive and reducing atmosphere enhanced migration of Co species from the membrane surface towards the grain boundary, however, this did not affect the bulk perovskite structure, retaining its structural integrity.

On the other hand, Sr-enrichment occur on both the outer (low partial pressure) and inner (high partial pressure) side of the membrane, especially on the inner air-side membrane surface. Strontium segregation towards the membrane surface occurs as opposed to cobalt inward diffusion due to greater mobility exhibited by strontium [40]. The Sr-enrichment phenomena have been observed by several studies related to presence of destructive gases such as CH_4 [41] and CO_2 [37] on the permeate side of the membrane.

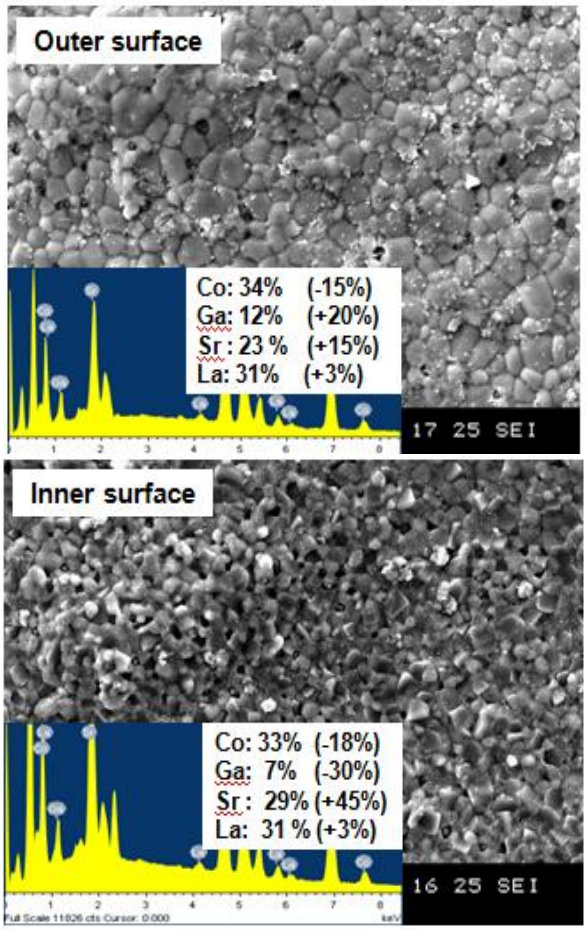

Figure 8-6 SEM images of inner and outer surfaces of post-reacted LSCG hollow fiber membranes after 160-h OCRM stability study (inset: EDX summary)

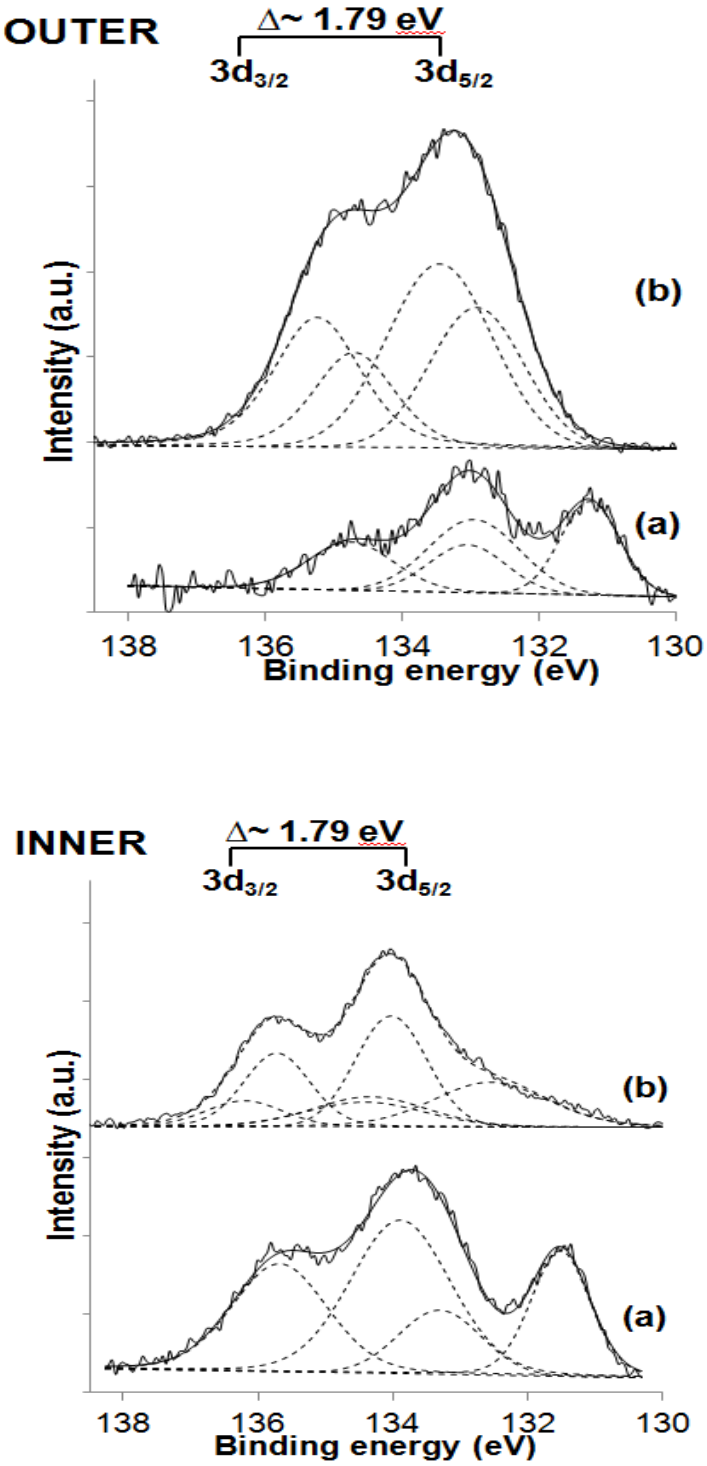

Figure 8-7 Sr 3d XPS spectra for inner and outer surfaces of (a) fresh LSCG membrane; (b) after160-h stability study under OCRM conditions.

Table 8-1 XPS binding energy summary of Sr 3d elements for fresh and post-reacted LSCG hollow fiber membranes

Element	State	Fresh Membrane				Post-reacted (OCRM)			
		Outer		Inner		Outer		Inner	
		BE (eV)	Area (%)	BE (eV)	Area (%)	BE (eV)	Area (%)	BE (eV)	Area (%)
Sr 3d$_{5/2}$	Sr^{2+}	131.3	42	131.5	27				
	SrO_{1-x}							132.4	28
	$SrCO_3$	133.2	58			133.4	60		
	SrO			133.9	73	134.7	40	134.1	72

In order to gain deeper insight on the compositional fractions of Sr segregated phases on the membrane surface, XPS analysis of the post-reacted LSCG membrane (after 160-h OCRM stability study) was conducted and compared with the fresh membrane. Figure 8-7 and Table 8-1 summarizes the compositional fractions of the Sr elements based on XPS analysis of the LSCG hollow fiber membranes. Based on the summary and description of the Sr states provided in Table 8-1, the lower BE of 131.5-132.1 eV is attributed to Sr^{2+} existing in the perovskite structure. BE values ranging from 132.1-132.7 eV correspond to presence of Sr in the low oxidation state such as SrO_{1-x} suboxide on the surface, whereas higher BE *ca*. 133.8-135.8 eV are correlated to SrO species. $SrCO_3$ components are marked with BE values *ca*. 133.0 – 133.7 eV [23, 42, 43].

It is evident that the outer surface (reaction side) of the LSCG membrane comprise mainly of $SrCO_3$ (60%) and SrO (40%) phases. Even the fresh membrane displays significant amounts of $SrCO_3$ (55%) on the outer surface (due to atmospheric contamination, resulting in carbonate formation). However, the remainder Sr elements in the fresh membrane comprise of the Sr^{2+} in the perovskite lattice, unlike the segregated strontium oxides present on the post-reacted membrane. As for the inner membrane surface (air side), transformation of Sr species to the SrO_{1-x} suboxide is shown, whereas the remaining species comprise of strontium oxides, in a similar composition to the fresh membranes. Hence, it can be surmised that the intense surface reaction reactivity on the membrane surface result in transformation of Sr^{2+} in perovskite phase to SrO and to a lesser extent in the internal air side to SrO_{1-x} species.

8.2.5.2. FTIR analysis and *in-situ* DRIFTS of CO and CO_2 desorption

FTIR analysis of the post-reacted LSCG hollow fiber membranes shown in Figure 8-8 (a) indicates that the surface is populated with strong peaks associated to carbonate and CH_x species. The bands at 1560, 1450, 1267, 1181, 1010 and 903 cm^{-1} are attributed mainly to carbonates, presumably produced in a reaction of CO_2 with surface oxide ions, such as lanthanum oxycarbonate species [44-47]. The low polarization power of highly basic metal cations such as La^{3+} and Sr^{2+} bind to bidentate carbonates and are identified with the band at 1560 and 1267 (due to their low splitting of 193 cm^{-1}) [48]. The band at 1384 cm^{-1} is due to adsorbed gaseous CO_2. On the other hand, doublet bands at 2920 and 2851 cm^{-1} are assigned to asymmetric and symmetric C-H stretching [49] respectively, most likely CH_x species adsorbed on the surface. The formation of this species is

attributed to spillover from methane C-H splitting on the catalyst bed to the membrane surface [49].

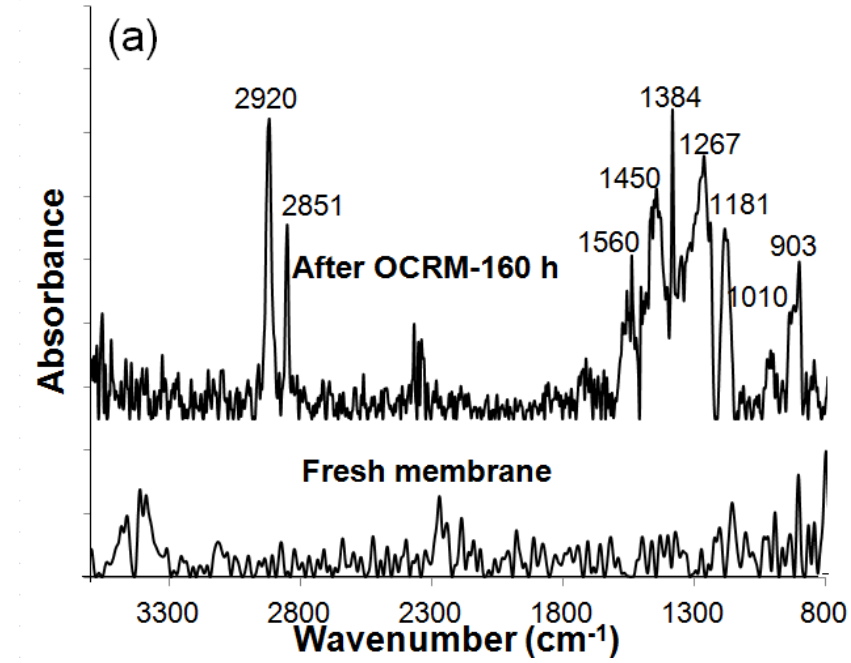

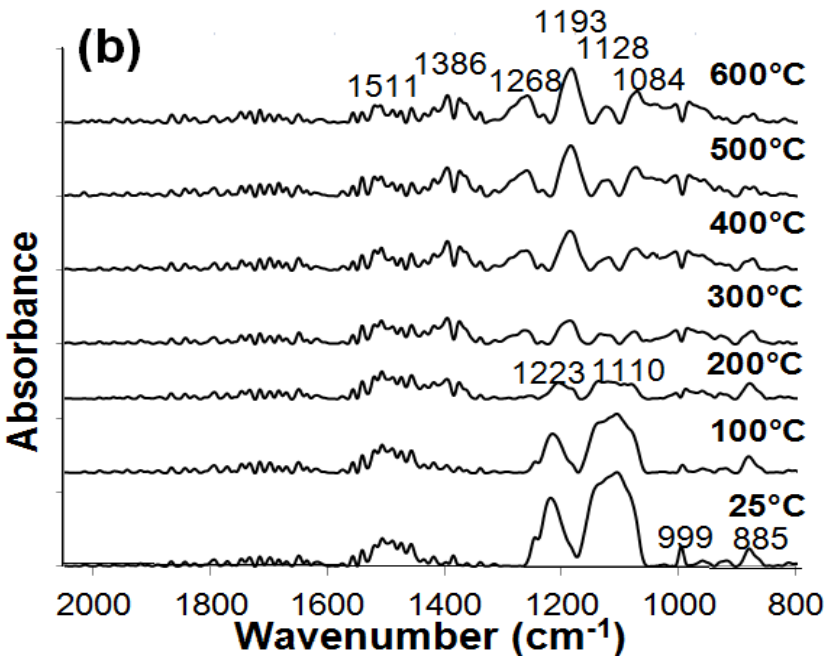

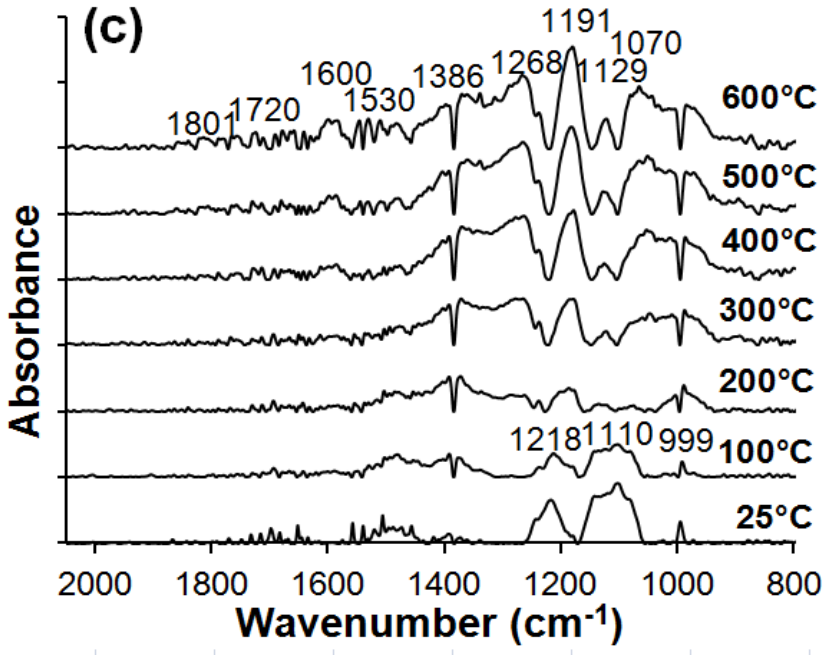

Figure 8-8 FTIR spectra of (a) fresh and post-reacted LSCG hollow fiber membrane; (b) *in-situ* DRIFTS of desorption after CO_2 adsorption on post-reacted LSCG hollow fiber membrane; (c) *in-situ* DRIFTS of desorption after CO adsorption on post-reacted LSCG hollow fiber membrane

CO_2 and CO adsorption at 600°C was conducted on the post-reacted LSCG hollow fiber membranes (diluted with KBr) in the Harricks dome cell. This analysis was carried out to probe the reactivity of the membrane surface. Figure 8-8 (b) and (c) shows the *in-situ* DRIFTS spectra of dynamic variation in desorption temperature under He flow. For CO_2 as probe gas, peaks at 885, 999, 1115, 1221 and 1511 cm^{-1} are formed. The higher intensity of peaks in the region between 800-1200 cm^{-1} are due to adsorbed carbonates (νCO_3^{2-}) [50]. The peaks at 999 1115 and 1221 start to reduce in intensity and disappear from 200°C. Above 200°C, a shift towards the peak at *ca.*1268, 1195, 1128 and 1084 cm^{-1} are observed. The peaks at the lower temperatures can be attributed desorption of more labile carbonate species such as the monodentate carbonate which are formed on the

surface of the perovskite, and likewise the peaks at higher temperatures, can be assigned to the bidentate carbonates [26, 27].

The lack of bands betweem 1300-1600 makes it difficult to ascertain the type of carbonates formed. In any case, it has been suggested in several studies that most of the residual carbonates, mainly monodentate carbonate, derives from interaction of CO_2 oxygen anions near neighbours of lanthanum or strontium cations [33, 51]. The peaks at *ca.* 1084 and 885 cm^{-1} point out to the reactivity of CO_2 to form $La_2O_2CO_3$ and $SrCO_3$ which all fall at the same range, but the greater intensity of the peak at 885 cm^{-1} suggests that presence of $SrCO_3$ is more likely [52]. This again correlates to the presence of segregated SrO and SrO_{1-x} phases on the membrane surface which are reactive to CO_2 forming $SrCO_3$ phases.

As for the reactivity of CO, as shown in desorption spectra in Figure 8-8 (c), similar profile with CO_2 desorption spectra can be observed. However, the peak at 885 cm-1 attributed to $SrCO_3$ cannot be clearly identified. Bidentate carbonates are more visible at the higher temperatures *ca.* 1600 and 1720 cm^{-1}. A weak band at 1801cm^{-1} is discernible and can be attributed to CO on metal cobalt sites [53]. This could be attributed to surface reduced Co element which may have formed on the grain boundaries due to the long-term exposure of the membrane in the reaction environment. However, the strong CO-metal bound carbonyl peaks either in linear or bridged form (identifiable between 1900-2100 cm^{-1}) are absent [54]. *In-situ* DRIFTS study further confirms that both CO and CO_2 compete for the same adsorption sites of La^{3+}/ Sr^{2+} for carbonate formation on the LSCG membrane surface. Therefore, this further attests to the structural integrity of the membrane after the stability test since structural decomposition would entice CO-metal bonding to the reduced Co^{n+} sites.

8.3. Conclusion

In this study, oxidative CO_2 reforming of CH_4 has been successfully carried out in a $La_{0.6}Sr_{0.4}Co_{0.8}Ga_{0.2}O_{3-\delta}$ (LSCG) hollow fiber membrane reactor packed with 5%Ni/$LaAlO_3$-Al_2O_3 catalyst. Successful long-term durability of the LSCG hollow fiber membrane under simultaneous corrosive and reducing environments of the OCRM reaction was achieved at the reaction conditions employed throughout the 160-h stability test at 725°C. Analysis of the reaction results shows that high CH_4 and CO_2 conversions of *ca.* 94% and 73% were obtained with O_2 flux *ca*. 1 $mL.min.^{-1}.cm^{-2}$. Surface interaction using H_2, CO and CO_2 as probe gases for adsorption at room temperature were analyzed via TPD method. H_2 has higher affinity to the Co^{n+} sites of the perovskite, compared to CO. Adsorption of CO_2 is further carried out at various temperatures and indicates shift in desorption peak towards higher temperature due to the increased basic strength. TPD-CO_2 further suggests a transformation from monodentate to bidentate carbonate species with increasing adsorption strength. SEM-EDX, XPS and FTIR analysis of the post reacted membrane suggests Sr-enriched phases with presence of hydrogenated carbon and carbonate due to the reaction which occur on the catalyst, and reactant spillover on the membrane from the catalyst bed. *In-situ* DRIFTS study of CO and CO_2 adsorption at high temperature, and subsequent desorption at various temperatures confirm that both CO and CO_2 compete for the same adsorption sites of La^{3+}/ Sr^{2+} for carbonate formation, albeit with higher intensity with regards to CO_2. However, XRD analysis of the bulk structure does not show any phase impurities, thus confirming the structural integrity of the LSCG hollow fiber membrane. The structural integrity of the hollow fiber membrane is certainly encouraging in promoting application of hollow fiber membrane reactors for the environmentally benign OCRM reaction.

REFERENCES

[1] Xie, K.; Zhang, Y.; Meng, G.; Irvine, J.T.S. *J. Mater. Chem.* **2011**, *21*, 195-198.

[2] James, O.O.; Maity, S.; Mesubi, M.A.; Ogunniran, K.O.; Siyanbola, T.O.; Sahu, S.; Chaubey, R. *Green Chem.* **2011**, *13*, 2272-2284.

[3] Ha, K.S.; Bae, J.W.; Woo, K.J.; Jun, K.W. *Environ. Sci. Technol.* **2010**, *44 (4)*, 1412-1417.

[4] Ida, J.I.; Lin, Y.S. *Environ. Sci. Technol.* **2003**, *37 (9)*, 1999-2004.

[5] Asadullah, M.; Ito, S.I.; Kunimori, K.; Yamada, M.; Tomishige, K. *Environ. Sci. Technol.* **2002**, *36 (20)*, 4476-4481.

[6] Zhu, X.; Huo, P.; Zhang, Y.P.; Cheng, D.G.; Liu, C.J. *Appl. Catal. B:Environ.***2008**, *81*, 132-140.

[7] Oemar, U.; Hidajat, K.; Kawi, S. *Appl. Catal. A:Gen.* **2011**, *402*, 176-187.

[8] Faraji, S.; Nordheden, K.J.; Stagg-Williams, S.M. *Appl. Catal. B: Environ.* **2010**, *99*, 118-126.

[9] Sunarso, J.; Baumann, S.; Serra, J. M.; Meulenberg, W. A.; Liu, S,; Lin, Y. S.; Diniz da Costa, J. C. *J. Membr.Sci.* **2008**, *320*, 13–41.

[10] Shao, Z.; Dong, H.; Xiong, G.; Cong, Y.; Yang, W. *J. Memb. Sci*. **2001**, *183*, 181-192.

[11] Jin, W.; Li, S.; Huang, P.; Xu, N.; Shi, J.; Lin, Y.S. *J Membr Sci*. **2000**, *166*, 13-22.

[12] Tan, X.; Li, K. *AIChE J*. **2009**, *55*, 2675-2685.

[13] Wang, H.H.; Tablet, C.; Schiestel, T.; Caro, J. *Catal. Today*, **2006**, *118*, 98-103.

[14] Chen, C.S.; Feng, S.J.; Ran, S.; Zhu, D.C.; Lin, W.; Bouwmeester, H.J.M. *Angew Chem Int Ed*. **2003**, *42*, 5106-5112.

[15] Tan, X.; Pang, Z.; Gu, Z.; Liu, S. *J Membr Sci*. **2007**, *302*, 109-114.

[16] Caro, J.; Wang, H.H.; Tablet, C.; Kleinert, A.; Feldhoff, A.; Schiestel, T.; Kilgus, M.; Kölsch, P.; Werth, S. *Catal. Today*, **2006**, *118*,128-135.

[17] Balachandran, U.; Dusek, J.T.; Sweeney, S.M.; Poeppel, R.B.; Mieville, R.L.; Maiya, P.S.; Kleefisch, M.S.; Pei, S.; Kobylinski, T.P.; Udovich, C.A.; Bose, A.C. *Am. Ceram. Soc. Bull.* **1995,** *7 4*, 71-75.

[18] Slade, D.A.; Duncan, A.M.; Nordheden, K.J.; Stagg-Williams, S.M. *Green Chem.* **2007**, *9*, 577-581.

[19] Wei, Y.Y.; Huang, L.; Tang, J.; Zhou, L.Y.; Li, Z.; Wang, H.H. *Chin. Chem. Lett.* **2011**, *22*, 1492-1496.

[20] Jin, W.; Zhang, C.; Chang, X.; Fan, Y.; Xing, W.; Xu, N. *Env. Sci. Technol.* **2008**, *42*, 3064-3068.

[21] Jiang, Q.; Faraji, S.; Nordheden, K.J.; Stagg-Williams, S.M. *J. Memb. Sci*. **2011**, *368*, 69-77.

[22] Liu, S.; Tan, X.; Shao, Z.; Diniz da Costa, J.C. *AIChE J.* **2006**, *52*, 3452-3461.

[23] Yang, N.T.; Kathiraser, Y.; Kawi, S. *Int. J. Hyd. Energ.* **2013**, *38 (11)*, 4483-4491.

[24] Kathiraser, Y.; Wang, Z.; Yang, N.T.; Zahid, S.; Kawi, S. *J Membr Sci*. **2013**, *427*, 240-249.

[25] Kathiraser, Y.; Kawi, S. *AIChE J.* In revised version.

[26] Tejuca, L.G.; Fierro, J.L.G. *Advances in Catalysis*, **1989**, *36*, 237-327.

[27] Jung, H.J.; Lim, J.T.; Lee, S.H.; Kim, Y.R.; Choi, J.G. *J. Phys. Chem.* **1996**, *100*, 10243-10248.

[28] Tan, X.; Shi, L.; Hao, G.; Meng, B.; Liu, S. *Sep. Purif Technol*. **2012**, *96*, 89-97.

[29] Tejuca, L.G.; Bell, A.T.; Fierro, J.L.G.; Tascón, *J. Chem. Soc. Faraday Trans. I.* **1987**, *83*, 3149-3159.

[30] Jiang, Q.; Faraji, S.; Slade, D.A.; Stagg-Williams, S.M. *Memb. Sci. Technol.* **2011**, *14*, 235-273.

[31] Shen, P.; Ding, W.; Zhou, Y.; Huang, S. *Appl Surf Sci*. **2010**, *256*, 5094-5101.

[32] Yan, A.; Liu, B.; Dong, Y.; Tian, Z.; Wang, D.; Cheng, M. *Appl. Catal. B:Environ.* **2008**, *80*, 24-31.

[33] Galenda, A.; Natile, M.M.; Nodari, L.; Glisenti, A. *Appl. Catal. B:Environ.* **2010**, *97*, 307-322.

[34] Galenda, A.; Natile, M.M.; Krishnan, V.; Bertagnolli, H.; Glisenti, A. *Chem. Mater.* **2007**, *19*, 2796-2808.

[35] Shao, Z.P.; Xiong, G.X.; Ren, Y.J.; Cong, Y.; Yang, W.S. *J. Mater. Sci.* **2000**, *35*, 5639-5644.

[36] Ryu, K.H.; Haile, S.M. *Solid State Ionics* **1999**, *125*, 355-367.

[37] Tan, X.; Liu, N.; Meng, B.; Sunarso, J.; Zhang, K.; Liu, S. *J. Memb. Sci.* **2012**, *389*, 216– 222.

[38] Efimov, K.; Xu, Q.; Feldhoff, A. *Chem. Mater.* **2010**, *22*, 5866-5875.

[39] Li, Y.; Zhao, H.; Xu, N.; Shen, Y.; Lu, X.; Ding, W.; Li, F. *J. Memb. Sci.* **2010**, *362*, 460-470.

[40] van der Heide, P.A.W. *Surf. Interface Anal.* **2002**, *33*, 414-425.

[41] ten Elshof, J.E.; Bouwmeester, H.J.M.; Verweij, H. *Appl Catal A Gen*. **1995**, *130*, 195-212.

[42] Liu, B.; Zhang, Y.; Tang, L. *Int J Hydrogen Energy* **2009**, *34*, 435-439.

[43] Natile, M.M.; Poletto, F.; Galenda, A.; Glisenti, A.; Montinini, T.; De Rogatis, L.; Fornasiero, P. *Chem Mater*. **2008**, *20*, 2314-2327.

[44] Zhou, W.; Liang, F.; Shao, Z.; Zhu, Z. *Sci. Reports.* **2012**, *2 (327)*, 1-6.

[45] Wovchko, E.A.; Yates Jr, J.T. *J. Am. Chem. Soc.* **1998**, *120*, 7544-7550.

[46] Klingenberg, B.; Vannice, M.A. *Chem. Mater.* **1996**, *8*, 2755-2768.

[47] Zhang, Z.; Verykios, X.E.; MacDonald, S.M.; Affrossman, S. *J. Phys. Chem.* **1996,** *100*, 744-754.

[48] Tejuca, L.G.; Rochester, C.H.; Fierro, J.L.G.; Tascon, J.M.D. *J. Chem. Soc. Faraday Trans. I*, **1984**, *80*, 1089-1099.

[49] Schweicher, J.; Bundhoo, A.; Frennet, A.; Kruse, N.; Daly, H.; Meunler, F.C. *J. Phys. Chem. C.***2010**, *114*, 2248-2255.

[50] Jung, J.I.; Edwards, D.D. *J. Solid State Chem.* **2011**, 184, 2238-2243.

[51] Ferri, D.; Forni, L. *Appl. Catal. B* **1998,** *16*, 119.

[52] Leo, A.; Liu, S.; Diniz da Costa, J.C. *Sep. Purif. Technol.* **2011**, *78*, 220-227.

[53] Cai, Z.; Li, J.; Liew, K.; Hu, J. *J. Mol. Catal. A:Chem.* **2010**, *330*, 10-17.

[54] Gamarra, D.; Martinez-Arias, A. *J. Catal.* **2009**, *263*, 189-195.

CHAPTER 9

Conclusions and Recommendations

9.1 Conclusions

CO_2 and CH_4 utilization for valuable syngas/hydrogen production via DRM reaction provides a sustainable solution in view of the escalating global concerns on the climate change phenomena. On another note, syngas/hydrogen production in a MIEC membrane reactor is a promising process, which constitutes a reasonable compromise between the product yield and energy efficiency. Hence, in a nutshell, the achievements of this thesis are firstly, the development of an active and thermally stable Ni supported on $LaAlO_3$-Al_2O_3 perovskite oxide (NLA) catalyst for DRM reaction. The second milestone is the development of the $La_{0.6}Sr_{0.4}Co_{0.8}Ga_{0.2}O_{3-\delta}$ (LSCG) hollow fiber membrane, which was found to display high chemical stability under CO_2 and CH_4 environments. Finally, integration of this LSCG membrane with the NLA catalyst was realised, firstly for POM reaction, and secondly for the OCRM reaction. Long term stability of the OCRM reaction was successfully conducted with minimal consequence on the membrane properties, hence making this process a suitable alternative worth exploring for future sustainable energy production with the utilization of both CO_2 and CH_4.

In terms of catalyst development, it has been noted from several studies that catalyst thermal stabilization of conventional Ni supported on alumina is an important material property which can be capitalized to enhance catalytic performance in terms of activity and stability. In this context, lanthanum nitrate was used to react with Al_2O_3

(*ca.*1:4 mol ratio) and calcined at high temperature of 900°C in order to form the thermally stable $LaAlO_3$ support. Upon Ni impregnation and further calcinations, the synthesized NLA catalyst was tested for DRM was investigated and compared with Ni supported on γ-Al_2O_3 (NA) and La_2O_3 (NL) oxides. Compared to the other supports, the NLA catalyst was found to exhibit active and stable performance for 30 hours of DRM operation. Based on several characterizations, the presence of surface "inverse" spinel structure formation on NLA catalyst was postulated due to the interaction of La with the octahedral Al^{3+} sites forming *in-situ* $LaAlO_3$ –Al_2O_3. This phenomenon inadvertently induces the tetrahedrally coordinated Al^{3+} to react with the Ni^{2+} to form a predominantly inverse Ni aluminate spinel configuration. The forcible interaction of the tetrahedral sites to form the inverse spinel configuration in the NLA catalyst is one of the major reasons which hindered the catalytic deactivation compared to NA catalysts (where the γ-Al_2O_3 support underwent phase transformation to α-Al_2O_3) besides the presence of less graphitic carbon. As a result, the NLA catalyst stability can be maintained throughout the prolonged DRM reaction via the enhanced lattice stability proffered by the inverse spinel structure. The development of this catalyst provided a stepping stone for further venture into integrated MIEC catalytic membrane reactor systems, since the presence of oxygen offers a less severe reaction environment for the catalyst compared to just DRM alone.

Hence, the next goal was to develop a chemical stable membrane capable of withstanding the harsh reaction environment, especially from CO_2, since CO_2 has been known to notoriously result in the MIEC perovskite decomposition via carbonate formation. Generally, lanthanum strontium cobaltite ($La_{0.6}Sr_{0.4}CoO_{3-\delta}$) are known to possess mixed ionic–electronic conducting properties and high catalytic reactivities for

oxygen reduction. Besides, they are also known to be are quite susceptible for decomposition under corrosive or reducing environments. Therefore, in order to take advantage of the inherent permeation property of the LSCO material, Ga was doped to form the $La_{0.6}Sr_{0.4}Co_{0.8}Ga_{0.2}O_{3-\delta}$ (LSCG) material. This composition has been found by several researchers to be optimal in order to ensure that excessive Ga doping does not lead to formation of unknown segregated phases as well as compromise on the electronic conductivity. The hollow fiber configuration was chosen in view of its high surface area/volume ratio as well as facile sealing at high temperatures. Oxygen permeation from 100 $mL \cdot min^{-1}$ of air at 650°C to 950°C were tested with 100$mL \cdot min^{-1}$ of pure He, CH_4 and CO_2 as sweep gases. The maximum O_2 permeation flux at 950°C was in the order of CH_4 followed by He and CO_2 at 7.45, 3 and 2.4 $mL.min^{-1}.cm^{-2}$. Sweeping with CH_4 resulted in the highest flux due to increase in surface exchange reaction whereas the lowest flux was attained for CO_2 sweep due to formation of $SrCO_3$. Furthermore, the LSCG membrane could retain its integrity even after 80h of CO_2 stability test, of which negligible decrease in fluxes were observed.

Upon successful fabrication of the chemically stable LSCG hollow fiber membrane, the next step was to test it for POM reaction and integrated with the NLA catalyst. The process was successfully carried out in the medium temperature range (600-800°C) for reaction of blank POM with bare membrane, catalytic POM reaction and swept with H_2:CO gas mixture. For the catalytic POM reaction, enhancement in selectivity to H_2 and CO is obtained between 650°C-750°C when O_2:CH_4 <1. High CH_4 conversion of 97% is achieved at 750°C with corresponding H_2 and CO selectivity of *ca.* 74% and 91%. The oxygen flux of the membranes also increased with the increase in

oxygen partial pressure gradient across the membrane. The presence of the Ni based NLA catalyst is shown to be crucial for syngas generation, since the membrane inherently has low catalytic activity. Based on the FESEM-EDX and XPS spectral analysis, presence of $SrCO_3$, CoO and Co_3O_4 can be detected on the external surface of the membrane after catalytic POM reaction, whereas the internal surface of the membrane is enriched with SrO, SrO_{1-x}, CoO and Co_3O_4 phases. Nevertheless, the crystalline perovskite structure and its inherent properties are retained and hence enabling oxygen permeability in the highly reducing environment.

Finally, the LSCG membrane was integrated once again with the NLA catalyst and was tested successfully for 160-h OCRM reaction, in the presence of both the environmentally debilitating CO_2 and CH_4 gases for syngas generation. High CH_4 and CO_2 conversions of *ca.* 94% and 73% were obtained with O_2 flux *ca*. 1 $mL.min.^{-1}.cm^{-2}$ at 725°C for the 160-h stability test. Post-reaction characterizations of the LSCG hollow fiber membranes confirm surface structural changes due to the intense oxygen reduction activity for the OCRM reaction. *In-situ* DRIFTS study of CO and CO_2 adsorption at high temperature, and subsequent desorption at various temperatures confirm they compete for the same adsorption sites of La^{3+}/ Sr^{2+} for carbonate formation. However, XRD analysis of the bulk structure does not show any phase impurities. The structural integrity of the hollow fiber membrane is certainly encouraging in promoting application of hollow fiber membrane reactors for the environmentally benign OCRM reaction.

9.2 Recommendations for future prospects

Based on the research outcomes in the process of preparing this thesis, several recommendations are proposed for future work in order to realize the commercialization of this process. Firstly, in terms of catalyst synthesis, the utilization of lanthanum, being a rare earth element, increases the catalyst cost. Hence, other materials which can form perovskite-oxide phases can be considered such as ceria. Another aspect which requires study is the presence of other gases together with the reactants such as steam and sulfur. This is because at the moment it is not practical to capture 100% CO_2 from the sources such as flue gas. Hence, further study on the feed stream consisting of various components is quite important to enable commercialization feasibility for DRM technology.

On another note, despite the attainment of a thermally stable and active catalyst for the DRM reaction, however, upon integration with the hollow fiber membrane, the feed of the reactant gases have to be regulated. This is because direct contact of the catalyst and membrane causes fracture from mechanical stress when carbon forms on the thin-wall structure of the hollow fiber membrane. Hence, study of reaction kinetics is an important aspect (covered in Chapter 2) which should be carried out in order to optimize the catalytic performance and test commercialization feasibility of the catalyst for reforming of methane. Without doubt that in order to integrate catalyst and optimize the membrane functionalities for large scale industrial use, it is important that large quantities of feed can be processed at the same time.

The second issue is improvement in the fabrication of the LSCG hollow fiber membrane. In order to enhance the oxygen permeating property of the membrane, surface

modifications via acid etching or coating with a highly conductive porous layer are possible solutions to enhance the surface area for oxygen reduction reaction. Another way, is to use a dual layer spinneret, of which one inner coagulant has high level of porosity (probably from pore enhancers such as activated carbon), and the other middle coagulant is for the dense layer formation. Therefore, using the dual layer concept, a higher performance membrane can be achieved.

Thirdly, in order to test for commercialization feasibility, it is not so feasible to pack the catalyst with the hollow fiber membrane. For large scale O_2 production, hollow fibers have to be assembled in a membrane module as bundles. For simultaneous use as an integrated catalytic membrane reactor, it would be more desirable to pre-coat the membrane with catalyst in order to render the membrane more feasible for commercial assembly.

APPENDIX

List of publications based on results obtained in this thesis

[1] **Y. Kathiraser**, J. Ni, U. Oemar, E.T. Saw, S. Kawi, Mechanistic and kinetic aspects for CO_2 reforming of methane over Ni based catalysts, *Submitted to Industrial and Engineering Chemistry Research.* [Parts of this review paper forms Chapter 2].

[2] **Y. Kathiraser**, W. Thitsartarn, K. Sutthiumporn, S. Kawi, Inverse $NiAl_2O_4$ on $LaAlO_3$ –Al_2O_3: Unique catalytic structure for stable CO_2 reforming of methane, *Journal of Physical Chemistry C*, **2013**, Accepted [Chapter 4].

[3] **Y. Kathiraser**, Z. Wang, N.T. Yang, S. Zahid, S. Kawi, Oxygen permeation and stability study of $La_{0.6}Sr_{0.4}Co_{0.8}Ga_{0.2}O_{3-\delta}$ (LSCG) hollow fiber membrane with exposure to CO_2, CH_4 and He, *Journal of Membrane Science*, **2013**, *427*, 240-249 [Chapter 5]

[4] **Y. Kathiraser**, S. Kawi, $La_{0.6}Sr_{0.4}Co_{0.8}Ga_{0.2}O_{3-\delta}$ (LSCG) hollow fiber membrane reactor: Partial oxidation of methane at medium temperature, *AIChE Journal*. In revised version [Chapter 6]

[5] **Y. Kathiraser**, Z. Wang, S. Kawi, Oxidative CO_2 reforming of methane in $La_{0.6}Sr_{0.4}Co_{0.8}Ga_{0.2}O_{3-\delta}$ (LSCG) hollow fiber membrane reactor, *In preparation for submission to Environmental Science and Technology*. [Chapter 7]

List of publications relevant to this thesis

[1] K. Sutthiumporn, T. Maneerung, **Y. Kathiraser**, S. Kawi, *International Journal of Hydrogen Energy*, **2012**, *37*, 11195-11207.

[2] N.T. Yang, **Y. Kathiraser**, S. Kawi, *Journal of Membrane Science*, **2013**, *428*, 78-85.

[3] Z. Wang, **Y. Kathiraser**, S. Kawi, *Journal of Membrane Science*, **2013**, *431*, 180-186.

[4] N.T. Yang, **Y. Kathiraser**, S. Kawi, *International Journal of Hydrogen Energy*, **2013**, *38 (11)*, 4483-4491.